Characterization of nucleolus-associated chromatin domains during cellular aging and upon genetic inactivation of the Upstream Binding Factor protein

DISSERTATION ZUR ERLANGUNG DES DOKTORGRADES
DER NATURWISSENSCHAFTEN (DR. RER. NAT.)
DER FAKULTÄT FÜR BIOLOGIE UND VORKLINISCHE MEDIZIN DER
UNIVERSITÄT REGENSBURG

vorgelegt von

Stefan Dillinger

aus Kelheim

im Jahr 2016

Das Promotionsgesuch wurde eingereicht am:
08.01.2016

Die Arbeit wurde angeleitet von:
PD Dr. Attila Németh

Regensburg, 08.01.2016

Stefan Dillinger

Contents

Summary viii

Zusammenfassung x

List of abbreviations xii

1 Introduction 1

1.1 Nuclear and nucleolar organization in mammalian cells 1

1.1.1 General principles of nuclear organization 1

1.1.2 Nucleolar structure and function - a historical overview 4

1.1.3 Perinucleolar heterochromatin 8

1.1.4 Repetitive DNA in the nucleolus-associated genome 8

1.1.5 Chromosomal organization of ribosomal DNA repeat clusters 10

1.2 Cellular aging 14

1.2.1 Cellular senescence 14

1.2.2 Changes in nuclear architecture during cell cycle and cellular aging . 17

2 Results 19

2.1 Analyses of nucleolus-associated chromatin in human cells and its changes during cellular aging 19

2.1.1 Isolation of nucleolar DNA from IMR90 cells for array CGH analyses 19

2.1.1.1 Controls of the cellular aging process 19

2.1.1.2 Controls of nucleolus isolation 21

2.1.1.3 Microarray analysis of NADs in proliferating and senescent IMR90 cells 24

2.1.2 Isolation of nucleolar DNA from K562 cells using different fractionation procedures 25

2.1.3 Isolation of nucleoli to analyze histone post-translational modifications (PTM) from HeLa cells 29

2.1.4 Single-cell analyses of nucleolar morphology and nucleolus-associated tandem repeats in proliferating and senescent IMR90 cells 31

2.1.4.1 Changes in nucleolar morphology during replicative senescence 31

2.1.4.2 Qualitative analyses of the nuclear distribution of histone PTMs during replicative senescence by immunofluorescence 35

2.1.4.3 Quantitative immunofluorescence analysis of H3K9me3 in replicative senescence . . . 39
2.1.4.4 3D-FISH analysis of tandem repeat arrays in replicative senescence . . . 44
2.1.5 3D-FISH analysis of NADs in proliferating and senescent cells . . . 49
2.2 Changes in nucleolus-associated chromatin upon UBF knock-out in mouse embryonic fibroblasts (MEF) . . . 56
2.2.1 Controls of the UBF knock-out system . . . 56
2.2.2 Isolation of nucleolus-associated DNA before and after induction of UBF knock-out . . . 58
2.2.3 Analysis of rDNA and major satellite reorganization upon UBF depletion by 3D immuno-FISH in MEF cells . . . 62

3 Discussion **67**
3.1 Nucleolus-associated chromosomal domains in proliferating and senescent IMR90 cells . . . 67
3.2 Comparison of experimental procedures for the analysis of nucleolus-associated chromatin . . . 69
3.3 Single-cell analyses of nucleolar morphology and nucleolus-associated tandem repeats . . . 70
3.3.1 Global nucleolar morphology dynamics during replicative senescence 71
3.3.2 Nuclear distribution of histone PTMs in proliferating and senescent cells . . . 72
3.3.3 Large-scale spatial rearrangements of tandem repeat arrays in replicative senescence . . . 74
3.3.4 NAD dynamics in replicative senescence . . . 76
3.4 Changes in nucleolus-associated chromatin upon UBF knock-out in MEF cells . . . 79

4 Materials **81**
4.1 Instruments . . . 81
4.2 Software and online tools . . . 82
4.3 Consumables and Chemicals . . . 83
4.4 Buffers, Solutions and Media . . . 84
4.5 Enzymes . . . 86
4.6 Kits . . . 86
4.7 Standard DNA and protein weight markers . . . 86
4.8 Antibodies . . . 87
4.8.1 Primary antibodies . . . 87
4.8.2 Secondary antibodies . . . 88
4.9 Bacterial strains . . . 88

4.10 Mammalian cell lines . . . 89
4.11 Oligonucleotides . . . 90
4.11.1 Genotyping primer . . . 90
4.11.2 qPCR primer . . . 90
4.11.3 BAC clones . . . 91
4.11.4 Biotinylated oligonucleotides . . . 91
4.12 Plasmids . . . 92

5 Methods **93**
5.1 DNA methods . . . 93
5.1.1 Isolation of genomic DNA from human cells . . . 93
5.1.2 Isolation of plasmid DNA from bacteria . . . 93
5.1.3 Isolation of nucleolar DNA and array CGH experiments . . . 93
5.1.3.1 Isolation of nucleolar DNA after formaldehyde cross-linking from human cells . . . 93
5.1.3.2 Isolation of nucleolar DNA after formaldehyde cross-link from MEF cells . . . 94
5.1.3.3 Isolation of nucleolar DNA without formaldehyde cross-linking from human cells . . . 95
5.1.3.4 Microarray experiments . . . 95
5.1.4 DNA agarose gel electrophoresis . . . 96
5.1.5 Measurement of DNA concentration . . . 96
5.1.6 PCR genotyping of MEF cells . . . 96
5.1.7 Quantitative PCR (qPCR) . . . 97
5.2 Protein methods . . . 99
5.2.1 SDS polyacrylamide gel electrophoresis . . . 99
5.2.2 Western blot . . . 99
5.2.2.1 Semi-dry blotting . . . 99
5.2.2.2 Ponceau S staining . . . 100
5.2.2.3 Immunodetection . . . 100
5.3 Mammalian cell culture . . . 101
5.3.1 Maintenance . . . 101
5.3.2 Freezing and thawing of cells . . . 101
5.3.3 Determining the cell number . . . 102
5.3.4 Preparation of quiescent cell populations . . . 102
5.3.5 Preparation of senescent cell populations . . . 102
5.3.6 Senescence test . . . 102
5.3.7 Knock-out of UBF in MEFs . . . 103
5.4 Immunfluorescence . . . 103
5.4.1 Fixation and immunostaining of mammalian cells . . . 103
5.4.2 Immunostaining of nucleoli after isolation . . . 103

5.4.3 Quantitative immunofluorescence . . . 104
5.4.3.1 Determination of relative immunofluorescence intensities in the ROIs . . . 104
5.4.3.2 Determination of the heterogeneity of staining in the ROIs 106
5.4.3.3 Determination of the subnuclear distribution of the 10% brightest pixels . . . 106
5.4.4 Determining number and volume of nucleoli . . . 108
5.5 FISH-techniques . . . 108
5.5.1 Preparation of hybridization probes . . . 108
5.5.1.1 Amplification of DNA . . . 108
5.5.1.2 Nick-translation . . . 109
5.5.1.3 Hybridisation mix preparation . . . 109
5.5.2 Fixation of cells for 3D-FISH . . . 110
5.5.3 Immunostaining . . . 110
5.5.4 Image acquisition settings . . . 111

6 Appendix **112**
6.1 Identification of NADs . . . 112
6.2 Quantitative immunofluorescence . . . 115
6.3 NADs and LADs of the genomic regions analyzed in 3D immuno-FISH experiments . . . 122

7 Acknowledgements **127**

List of Tables **128**

List of Figures **129**

Bibliography **132**

Summary

The nucleus of mammalian cells consists of several structural and functional domains, of which the nucleolus is the largest one. Although its primary function in the synthesis of ribosomal RNA and early steps of ribosome assembly is well characterized and its role in stress sensing, cell cycle regulation and RNA modification has been revealed, the involvement of the nucleolus in genome organization is less well understood. Nucleolus-associated chromosomal domains (NADs) were initially described independently by two different laboratories, providing a snapshot of the nucleolus-associated genome in HeLa and HT1080 human cancer cells (Németh et al., 2010; van Koningsbruggen et al., 2010). These investigations showed that NADs represent mainly a specific heterochromatin compartment. However, NADs have not been mapped in normal diploid cells and other species than human. Moreover, the dynamics of the nucleolus-associated chromatin during diverse cellular processes such as cellular aging, or after inhibition of nucleolar transcription remained largely unknown.

Here, the effect of different nucleolus isolation protocols on the mapping of NADs and on the identification of histone post-translational modifications (PTMs) by masss spectrometry were monitored first. The results revealed robust, comparable mappability of NADs under various conditions, but differences in the maintaining of PTMs depending on the nucleolus isolation procedure. Next, the dynamics of nucleolus-associated chromatin was investigated during replicative senescence in IMR90 human embryonic fibroblasts. *In vitro* human diploid fibroblasts stop dividing after a certain number of cell divisions (Hayflick, 1965), a process called replicative senescence. During this process the nuclear architecture and nucleolar morphology get largely rearranged (Bridger et al., 2000; Mehta et al., 2007; Hein et al., 2011). The nucleolar hallmarks of senescent cells include increased size and fusion of nucleoli, furthermore chromatin and DNA methylation changes of ribosomal DNA (rDNA) (Hein et al., 2011). In the course of this study the nucleolus association of chromosomal domains was mapped using comparative genomic hybridization on high-resolution microarrays. The initial analyses suggest that NADs are stable units and their genomic maps show only minor differences between the population of proliferating and senescent IMR90 cells. Three-dimensional analysis of nucleolar morphology provided quantitative data about the increase of nucleolar volume in senescent IMR90 cells and the accompanying decrease of their number per cell. Immunostaining of histone PTMs in proliferating and senescent IMR90 cells revealed that the distribution of a marker for constitutive heterochromatin, trimethylation of the lysine 9 of histone H3 (H3K9me3), exhibits the most remarkable changes at the nucleoli during cellular aging. In senescent cells this histone

modification was depleted in the perinucleolar space, whereas a notable alteration in its distribution, but only a minor change in its relative amount was visible at the nuclear periphery, another characteristic site of heterochromatin accumulation. Immuno-FISH experiments revealed firstly that the localization of rDNA arrays with respect to nucleoli does not change remarkably during cellular senescence, secondly that senescence-associated distension of satellites goes together with their disassociation from nucleoli, moreover that the localization of selected genomic regions frequently, but not completely corresponds to the nucleolus association states, which were observed in high-throughput genomic analyses.

Finally, nucleolus-associated DNA was isolated from mouse embryonic fibroblast cells, in which inhibition of ribosomal RNA transcription was achieved by induced depletion of the Upstream Binding Factor (UBF) protein, an essential factor of nucleolar RNA polymerase I transcription *in vivo* (Hamdane et al., 2014). Here again data were collected in high-resolution comparative genomic hybridization experiments for future bioinformatic analyses. In addition, 3D immuno-FISH experiments were performed to monitor large-scale alterations of nuclear and nucleolar architecture. The results illustrated, that the rDNA tends to form discrete foci, which get condensed and co-localized with major satellite repeat clusters at the centromeres.

In summary, in this study nucleoli were isolated from different human and mouse cells and their DNA and protein content was subjected to high-throughput genomic and mass spectrometry analyses, respectively. In addition, the dynamics of the nucleolus-associated chromatin was investigated in replicative senescence in human embryonic fibroblasts. The results shed new light on the role of the nucleolus in genome organization during these processes and provide a basis for further investigations.

Zusammenfassung

Der Nukleolus ist die Größte von verschiedenen strukturellen und funktionellen Domänen im Kern von Säugetierzellen. Obwohl seine primäre Funktion, die Synthese ribosomaler RNA und frühe Schritte der Ribosomenassemblierung gut beschrieben sind und seine Rolle in der Stresswahrnehmung, Zellzyklusregulierung und RNA Modifikation beschrieben wurde, ist wenig über seine Rolle im Bezug auf die Genomorganisierung bekannt. Nukleolus-assoziierte Chromosomendomänen (NADs) wurden erstmals unabhängig in zwei unterschiedlichen Laboren indentifiziert und lieferten einen Überblick über das nukleolus-assoziierte Genom in HeLa und HT1080 Zellen (Németh et al., 2010; van Koningsbruggen et al., 2010). Diese Experimente zeigten, dass NADs hauptsächlich heterochromatische Regionen beinhalten. Jedoch wurden NADs bisher nicht in normalen diploiden Zellen sowie anderen Spezies ausser dem Menschen identifiziert. Außerdem blieb die Dynamik von nukleolusassoziertem Chromatin während zellulärer Prozesse wie der zellulären Alterung oder nach der Inhibierung nukleolärer Transkripition weitgehend unbekannt.

Hier wurden zuerst Effekte von verschiedenen Protokollen zur Nukleolusisolierung auf die Identifizierung von NADs und der Identifizierung von post-translationalen Histonmodifikationen (PTMs) mit Massenspektrometrie untersucht. Ergebnisse zeigten eine vergleichbare Identifizierung von NADs unter verschiedenen Bedingungen, aber auch Unterschiede in der Erhaltung von PTMs abhängig von der Art der Nukleolusisolierung. Als nächstes wurde die Dynamik von nukleolus-assoziiertem Chromatin während replikativer Seneszenz in IMR90 humanen embryonischen Fibroblasten untersucht. *In vitro* hören humane diploide Fibroblasten nach einer bestimmten Anzahl an Zellteilungen auf sich zu teilen (Hayflick, 1965), dieser Prozess ist bekannt als replikative Seneszenz während dessen die nukleäre Architektur und nukleoläre Morphologie einer umfangreichen Umorganisierung unterliegen (Bridger et al., 2000; Mehta et al., 2007; Hein et al., 2011). Nukleoli in seneszenten Zellen zeichnen sich durch ihre erhöhte Größe und ihr Verschmelzen aus, außerdem verändert sich der Status der Methylierung von Chromatin und ribosomaler DNA (rDNA) (Hein et al., 2011). Im Verlauf dieser Arbeit wurden NADs mittels vergleichender genomischer Hybridisierung auf hochauflösenden Microarrays identifiziert. Vorläufige Analysen zeigten NADs als stabile Domänen und ihre genomische Kartierung ergab nur kleine Unterschiede zwischen proliferierenden und seneszenten Zellpopulationen. Dreidimensionale Analysen der nukleolären Morphologie lieferten quantitative Daten über die Zunahme des Volumens von Nukleoli in seneszenten IMR90 Zellen und die parallele Reduzierung ihrer Anzahl pro Zelle. Immunofärbungen von Histon PTMs in proliferierenden und seneszenten IMR90 Zellen zeigten, dass sich die Verteilung eines Markers für konstitutives Heterochromatin,

trimethylierung von Histon H3 an Lysin 9 (H3K9me3), während der zellulären Alterung am meisten am Nukleolus verändert. In seneszenten Zellen war diese Histonmodifikation abgereichert an Nukleoli, wohingegen eine veränderte Verteilung aber nur ein kleiner Unterschied in der relativen Häufigkeit an der Kernperipherie, einem weiteren typischen Bereich für die Akkumulierung von Heterochromatin, erkennbar war. Immuno-FISH Experimente zeigten einserseits, dass sich die Lokalisation von rDNA Arrays währen der zellulären Seneszenz im Bezug auf Nukleoli nicht entscheidend ändert, andererseits, dass die seneszenz-assoziierte Distension von Satelliten DNA mit ihrer Dissoziation von Nukleoli einhergeht. Außerdem, wurde gezeigt, dass die Lokalisierung ausgewählter genomischer Regionen häufig, aber nicht immer mit dem Status der Nukleolusassoziation übereinstimmt, welche in genomischen Hochdurchsatzanalysen ermittelt wurden.

Zuletzt wurde nukleolus-assoziierte DNA aus embryonischen Mausfibroblasten isoliert, in welchen eine Inhibierung von ribosomaler RNA Transkription durch die Depletion des Upstream Binding Factor (UBF) Proteins erreicht wurde, welches ein essentieller Bestandteil der nukleolären RNA Polymerase I Transkription *in vivo* ist (Hamdane et al., 2014). Auch hier wurden Daten von hochauflösender vergleichender genomischer Hybridisierung für künftige bioinformatische Analysen gesammelt. Zusätzlich wurden 3D immuno-FISH Experimente durchgeführt, um großräumige Veränderungen in der Kernarchitektur und der Morphologie von Nukeoli zu unterzuschen. Ergebnisse zeigten, dass die rDNA dazu tendiert diskrete Bereiche zu formen, welche dann kondensieren um dann mit Major Satelliten DNA Klustern an den Zentromeren zu kolokalisieren.

Zusammenfassend wurden in dieser Arbeit Nukleoli aus verschiedenen humanen und murinen Fibroblasten Zelllinien isoliert und ihre Protein- und DNA-Bestandteile wurden jeweils mittels Hochdurchsatzgenmomik und -spektrometrischen Methoden analysiert. Zusätzlich wurde die Dynamik von nukleolus-assoziiertem Chromatin in replikativer Seneszenz in humanen embryonischen Fibroblasten untersucht. Die Ergebnisse werfen neues Licht auf die Rolle des Nukleolus in der Genomorganisierung während dieser Prozesse and bieten eine Basis für zukünftige Analysen.

List of abbreviations

$°C$	degree Celsius
5mC	5 methyl cytosine
A_x	absorbance at x nm
aa	amino acid
Amp	ampicillin
APS	ammonium persulfate
bp	base pair
BSA	bovine serum albumine
CB	Cajal Body
CGH-array	Comparative genomic hybridisation
Da	Dalton
DDR	DNA damage response
DFC	Dense fibrillar component
DIC	Differential interference contrast
DIRS	Dictyostellum intermediate repeat sequence
DJ	Distal Junction
DMSO	Dimethylsulfoxide
DNA	deoxyribonucleic acid
dNTP	2'-deoxynucleotide triphosphate
EDTA	ethylenediaminotetraacetate
ENCODE	Enceclopedia of DNA elements
EtBr	Ethidium Bromide
FA	Formamide
FC	Fibrillar Center
FCS	fetal calf serum
FISH	Fluorescence in situ hybridization
g	gram or gravity
GC	Granular component

GF ..... Growth factor
h ..... hour
HDACi ..... Histone deacetylase inhibitor
HLB ..... Histone loclus
HSA18 ..... Human Chromosome 18
HSA19 ..... Human Chromosome 19
IF ..... Immunfluorescence
IGS ..... Intergenic spacer
kb ..... kilobases
kDa ..... Kilodalton
l ..... litre
LAD ..... Lamina-associated domain
LINE ..... Long interspersed elements
LTR ..... Long terminal repeats
M ..... molar
Mb ..... Megabases
min ..... minute
MOPS ..... 3-(N-morpholino)propanesulfonic acid
MW ..... molecular weight
NAD ..... nucleolus associated domain
No ..... nucleolus
NOR ..... Nucleolar Organizer Region
NT ..... nickt translation
nt ..... nucleotide
PAA ..... polyacrylamide
PBS ..... phosphate buffered saline
PBS-T ..... phosphate buffered saline with 0.1 % Tween20
PcG ..... Polycomb group
PCH ..... Pericentromeric heterochromatin
PCR ..... polymerase chain reaction
PDL ..... Population doubling level
PH ..... Peripheral Heterocrhomatin
PIC ..... Pre initiation complex

PJ ..... Proximal Junction
PLE ..... Penelope like elements
PML ..... Promyelocytic leukaemia
PNH ..... Perinucleolar heterochromatin
Pol I ..... RNA polymerase I
PSG ..... Pregnancy specific glycoproprotein
qPCR ..... quantitative PCR
rDNA ..... ribosomal DNA
RNA ..... ribonucleic acid
rpm ..... rounds per minute
rRNA ..... ribosomal RNA
SADS ..... Senescene Associated Distension of Satellites
SAHF ..... Senescence Associated Heterochromatin foci
SASP ..... Senescence Associated Secretory Phenotype
SDS ..... sodium dodecyl sulfate
SDS-PAGE ..... sodium dodecyl sulfate polyacrylamide gel electrophoresis
sec ..... second
SINE ..... Short interspersed elements
SL-1 ..... Selectivity Factor 1
snoRNP ..... small nucleolar ribonucleoparticles
snRNP ..... small nuclear ribonucleoparticles
Taq ..... Thermus aquaticus
TBE ..... tris borate EDTA
TE ..... Tris EDTA
TEMED ..... N,N,N',N'-tetramethylethylenediamine
Tip5 ..... TTF-I interacting protein 5
Tris ..... tris(hydroxymethyl)aminomethane
TSS ..... transcription start site
U ..... unit
UBF ..... upstream binding factor
UCE ..... Upstream Control Element
UV ..... ultra violett
WB ..... Western Blot

WCE ..... whole cell extract

X-gal 5-bromo-4-chloro-indolyl-β-D-galactopyranoside

1 Introduction

1.1 Nuclear and nucleolar organization in mammalian cells

1.1.1 General principles of nuclear organization

The DNA is wrapped around histone octameres to form nucleosomes, which are folded into higher order structures of chromatin and megabase-scale chromosomal domains. These form chromosomes, which appear in the interphase cell as nuclear chromosome territories (reviewed in Cremer and Cremer (2010)). This term was first described in the beginning of the 20^{th} century (Boveri, 1909), but a territorial organization of interphase chromosomes was originally observed earlier by Rabl (1885). Multicolor FISH experiments in human fibroblasts firmly confirmed the existence of chromosome territories which are largely separated spatially (Figure 1.1, Dietzel et al. (1998); Bolzer et al. (2005)).

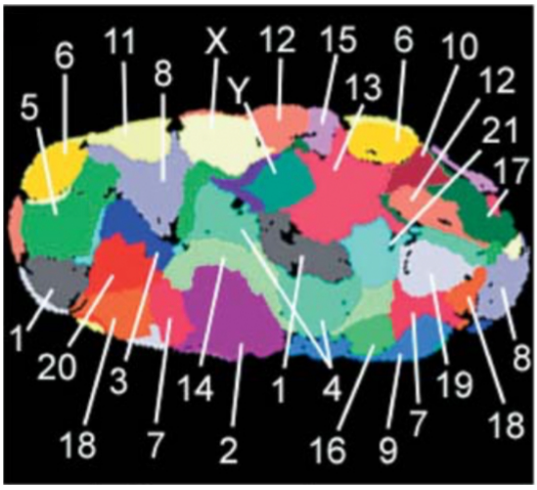

Figure 1.1 – Visualization of chromosome territories.
Chromosomes were stained with multicolour FISH and the results are displayed in false colours. Each area is marked with the respective chromosome number. Image taken from Bolzer et al. (2005)

In the last decade the spatial distribution of the genome in the nucleus has been analyzed using different high-throughput methods (Figure 1.2). For example, the interaction of different parts of the genome was analyzed with Chromosome Conformation Capture, also called 3C, and its derivatives (Dekker et al., 2002; Fraser et al., 2015). Such analyses revealed that the organization of the human genome can be modeled as a fractal

globule (Lieberman-Aiden et al., 2009). Subsequently, a high-resolution contact probability map of the human genome was constructed using Hi-C, resulting in high-resolution maps of chromosomal contact domains (Rao et al., 2014). Furthermore, the association of chromosomes with nuclear sub-compartments was analyzed using various methods. The interaction of the genome with the nuclear lamina was investigated using DamID. This is a technique, where DNA adenin methyltransferase (Dam), which methylates adenines in GATC sequences, is genetically fused to a protein and hence methylates the respective DNA sequences at the site of its localization. For instance Dam-LaminB1, digestion with DpnI and microarray analysis can be used to identify lamin-associated domains (Pickersgill et al., 2006; Guelen et al., 2008). A second method to map contacts with the nuclear lamina and also the nuclear pore complexes (NPC) is chromatin immunoprecipitation (ChIP). In ChIP experiments protein-DNA interactions are fixed by formaldehyde cross-linking, which is followed by mechanical shearing of the DNA and subsequent immunoprecipitation of the cross-linked material with antibodies targeting proteins of interest. Then the DNA is analyzed on genome-wide tiling microarrays or by high-throughput sequencing (Johnson et al., 2007). The association of chromosomal domains with nucleoli can be investigated using another approach which includes cell fractionation and combined microarray and deep sequencing analysis of purified nucleolar DNA (Németh et al., 2010; van Koningsbruggen et al., 2010).

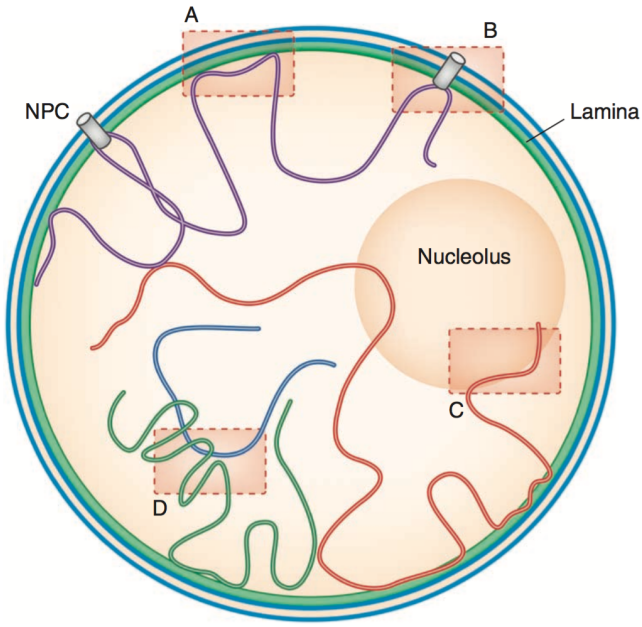

Figure 1.2 – Scheme depicting different interaction possibilities of chromosomal domains with nuclear subcompartments.
(A) Interaction with the nuclear lamina can be investigated with DamID, (B) interactions with the nuclear pore with DamID or ChIP, (C) association to nucleoli can be investigated using fractionation, (D) interactions between intra- and interchromosomal domains can be investigated with 3C and its derivatives. Adapted from van Steensel and Dekker (2010).

Nuclear bodies

Nuclear bodies are membrane-less nuclear substructures, which can be detected by different microscopy techniques (Spector, 2006). The most prominent of these structures is the nucleolus with its shell of perinucleolar heterochromatin (PNH), which is clearly visible under the light microscope. Further structures include Cajal bodies (CBs), Histone locus bodies (HLBs), Promyelocytic leukaemia (PML) bodies and Polycomb group (PcG) bodies (Figure 1.3). Nuclear bodies participate in diverse cellular functions. The primary function of the nucleolus is the synthesis of ribosomal RNA and assembly of pre-ribosomes. CBs are involved in snRNP and snoRNP biogenesis and post-transcriptional modification of snRNAs (Spector, 2006). HLBs are chromatin-associated nuclear bodies which assemble around the histone gene clusters and represent the sites of histone mRNA transcription and processing (Nizami et al., 2010). PML bodies contain the PML protein and are possibly involved in transcriptional regulation or nuclear protein sequestration, however their function is not entirely clear (Ching et al., 2013). PcG bodies contain the human polycomb repressive complex 1 and associate with heterochromatic regions (Saurin et al., 1998).

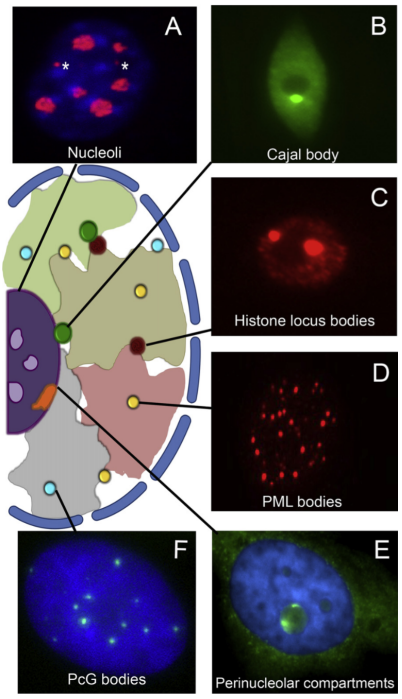

Figure 1.3 – Nuclear bodies.
The scheme in the middle illustrates the nucleus with large chromosomal domains and nuclear bodies, which are individually shown on the fluorescence microscopy images around the scheme. (A) Nucleoli of a MEF cell are stained for fibrillarin (red), DNA was counter-stained with DAPI (blue). (B) CB was stained using an antibody against the U2B protein (green) in an *Arabidopsis thaliana* nucleus. (C) HLBs are visualized with an anti-FLASH antibody in a *Drosophila* S2 cell nucleus. (D) PML-bodies stained in a mouse NIH 3T3 cell with an anti-PML antibody. (E) PNH stained with an oligo-nucleotide probe hybridizing against the hY1 RNA (green), DNA was counterstained with DAPI. (F) PcG bodies were labeled by transfecting a human cell line with YFP-tagged Bmi1. Adapted from Matera et al. (2009).

1.1.2 Nucleolar structure and function - a historical overview

The main function of the nucleolus is the synthesis of of ribosomal RNA, however it plays a role also in other cellular processes, such as stress response, cellular aging and cell cycle control (Pederson, 1998; Boisvert et al., 2007). The nucleolus was first observed by Fontana (1781) (Figure 1.4), but it took another 40 years until Wagner (1835) and Valentin (1836) discovered and originally described the nucleolus independently (reviewed by Mosgoeller (2004)).

Figure 1.4 – First illustration of the nucleolus.
a) Epidermal cell of an eel with nucleus and nucleolus. c) Red blood cell of the same species as scale. Figure adapted from Schwarzacher and Wachtler (1983), originally published by Fontana (1781).

In 1898 the first comprehensive review about the discoveries concerning nucleoli in the 18^{th} and 19^{th} century was published and it included 346 hand-drewn nuclei and nucleoli from a collection of biological material (Montgomery, 1898). Thirty years later Heitz (1931) and McClintock (1934) independently observed, that nucleoli form at specific chromosomal loci. Heitz hereby also noted, that nucleoli form at secondary constrictions and that the size of this secondary constriction is reflected by the size of the respective nucleolus. In addition, he also mentioned that nucleoli tend to fuse during the cell cycle, as nuclei contain only one nucleolus before cells entered mitosis. Furthermore, McClintock also initially described the nucleolar-organizing body, today known as nucleolar organizer region (NOR). This was the first time when the nucleolus was connected to a cytogenetic entity.

The first electron microscopic experiments shed light on the tripartite structure of the nucleolus in 1952, revealing that the nucleolus consists of the fibrillar center (FC), the dense fibrillar component (DFC) and the granular component (GC) (Figure 1.5, Bernhard et al. (1952); Swift (1963)).

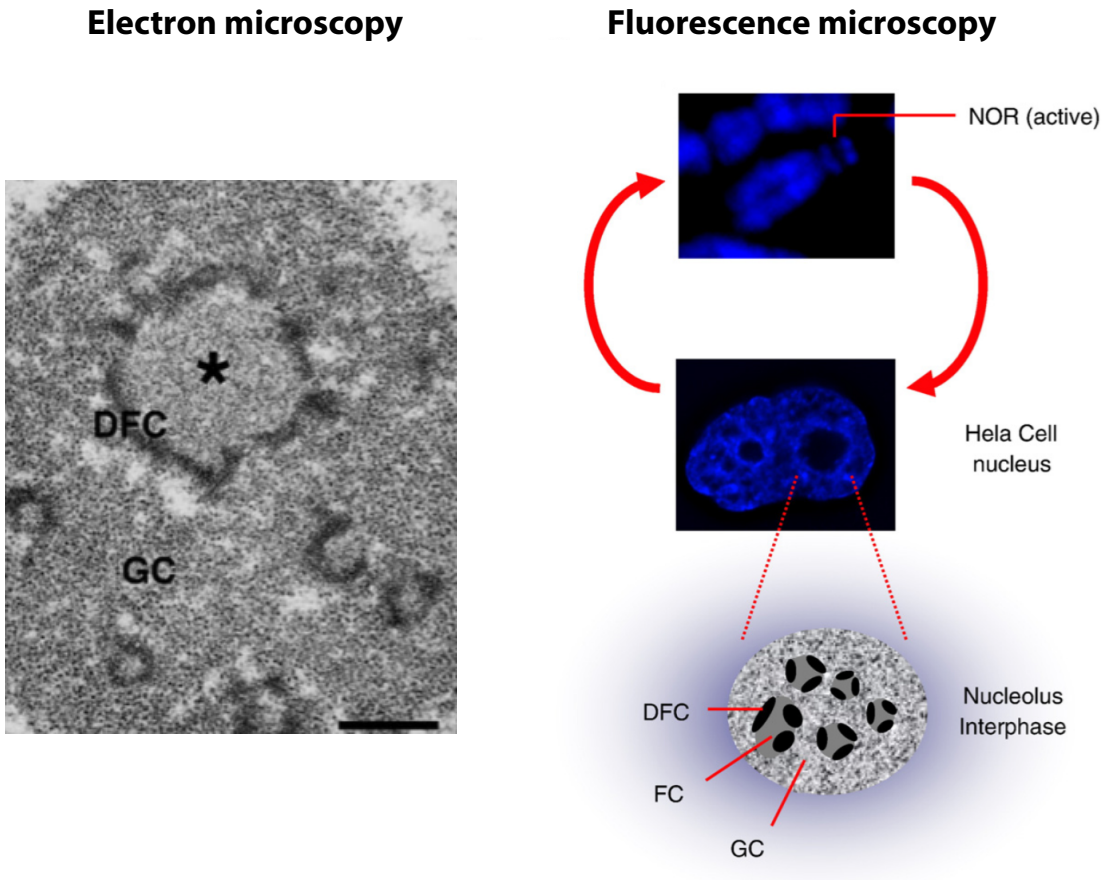

Figure 1.5 – Structural features of the human nucleolus on microscopy images. Electron microscopy image illustrating the three main parts of the nucleolus of a HeLa cell (on the left). The asterisk marks the fibrillar center, which is surrounded by the dense fibrillar component, which is enclosed by the granular component. Figure adapted from Sirri et al. (2007). Fluorescence microscopy images are shown on the right. Upper panel shows a DAPI stained human acrocentric chromosome with a NOR visible as secondary constriction (no DAPI staining). The middle panel depicts a DAPI stained HeLa cell nucleus. The density of DNA in the nucleolus is lower, therefore it appears as a black hole. Lower panel illustrates a nucleolus during the interphase with the three parts FC, DFC and GC. Adapted from Prieto and McStay (2008). Scale bar: 0.5 µm.

The following functions were assigned to the structural components of the nucleolus: The FC contains the ribosomal DNA and RNA polymerase I (Pol I), the transcription takes place at the border of FC and DFC, the nascent RNA grows into the DFC where also the early processing of rRNA takes place, while later rRNA processing and ribosome assembly steps occur in the GC (Recher et al., 1969; Raska et al., 1995; Sirri et al., 2002).

In the 50s and 60s protocols were developed to isolate nucleoli and analyze their molecular composition (Vincent, 1952; Monty et al., 1956; Muramatsu et al., 1963; Vincent et al., 1966). In these approaches nucleoli were purified by sequential cell fractionation and centrifugation. These protocols were then adapted in recent years to get deeper insights concerning molecular constitution and dynamics of nucleoli.

Later, various studies led to the conclusion, that a major component of the nucleolus is ribosomal RNA. First evidence came from *Xenopus* mutants which had no nucleoli due to a deletion of the NORs. In these mutants the tadpoles had a deficiency in ribosomal RNA synthesis (Brown and Gurdon, 1964; Birnstiel et al., 1966). Conclusive evidence came then from experiments with radioactively labeled rRNA. When the rRNA was hybridized on metaphase chromosomes it localized to the secondary constrictions on acrocentric chromosomes, and when it was hybridized in interphase cells it preferentially localized to nucleoli (Perry, 1962; McConkey and Hopkins, 1964; Spiegelman and Ritossa, 1965; Henderson et al., 1972). These experiments demonstrated that rRNA is synthesized in nucleoli and the rDNA is located at the NORs. Next, the synthesis of this RNA by the Pol I enzyme complex was shown (Roeder and Rutter, 1969; Reeder and Roeder, 1972). In 1969 O.L. Miller captured ribosomal genes during transcription and showed the heavy loading of the ribosomal genes with Pol I, which was the first in situ visualization of a transcribed gene. These electron micrographs became then famous under the term 'Miller spreads' (Miller and Beatty, 1969).

For transcription initiation on the rDNA several factors are necessary, which were discovered in the 1980s. The pre-initiation complex (PIC) has to form, in order to provide a binding platform for Pol I. Hence, the Upstream Binding Factor (UBF) and Selectivity Factor 1 (SL-1), which conveys species specificity, have to bind to the DNA (Learned et al., 1985; Jantzen et al., 1990). When this complex is formed, Pol I, which is associated to RRN3/TIF-IA (Moorefield and Greene, 2000; Bodem et al., 2000) is recruited to the promoter and transcription can initiate (reviewed in Moss and Stefanovsky (2002); Grummt (2003); Russell and Zomerdijk (2005)).

By the turn of the millennium it became more and more evident, that ribosomal RNA production is not the sole task of the nucleolus. The nucleolus also plays important roles in cell cycle regulation, stress response via p53 and the nucleolar protein p14ARF and in human diseases like viral infections (reviewed in Pederson (1998); Boisvert et al. (2007)).

With the rise of high-throughput methods and the already available purification protocols of nucleoli, new light was shed on the nucleolar proteome, genome and RNome. Characterization of the nuclear proteome revealed, that nucleoli feature a large protein complexity, harboring more than 700 different proteins (Scherl et al., 2002; Andersen et al., 2002; Couté et al., 2006). Furthermore, the genome of nucleolus-associated chromatin was characterized and the presence of specific gene families and the enrichment of satellite repeats was unveiled (Németh et al., 2010; van Koningsbruggen et al., 2010). The RNome of nucleoli was first explored in plants and later in the context of the ENCODE-project (Kim et al. (2009, 2010); Djebali et al. (2012), Figure 1.6). More recently other nucleolar non-coding RNAs were also characterized (Bai et al., 2014; Caudron-Herger et al., 2015).

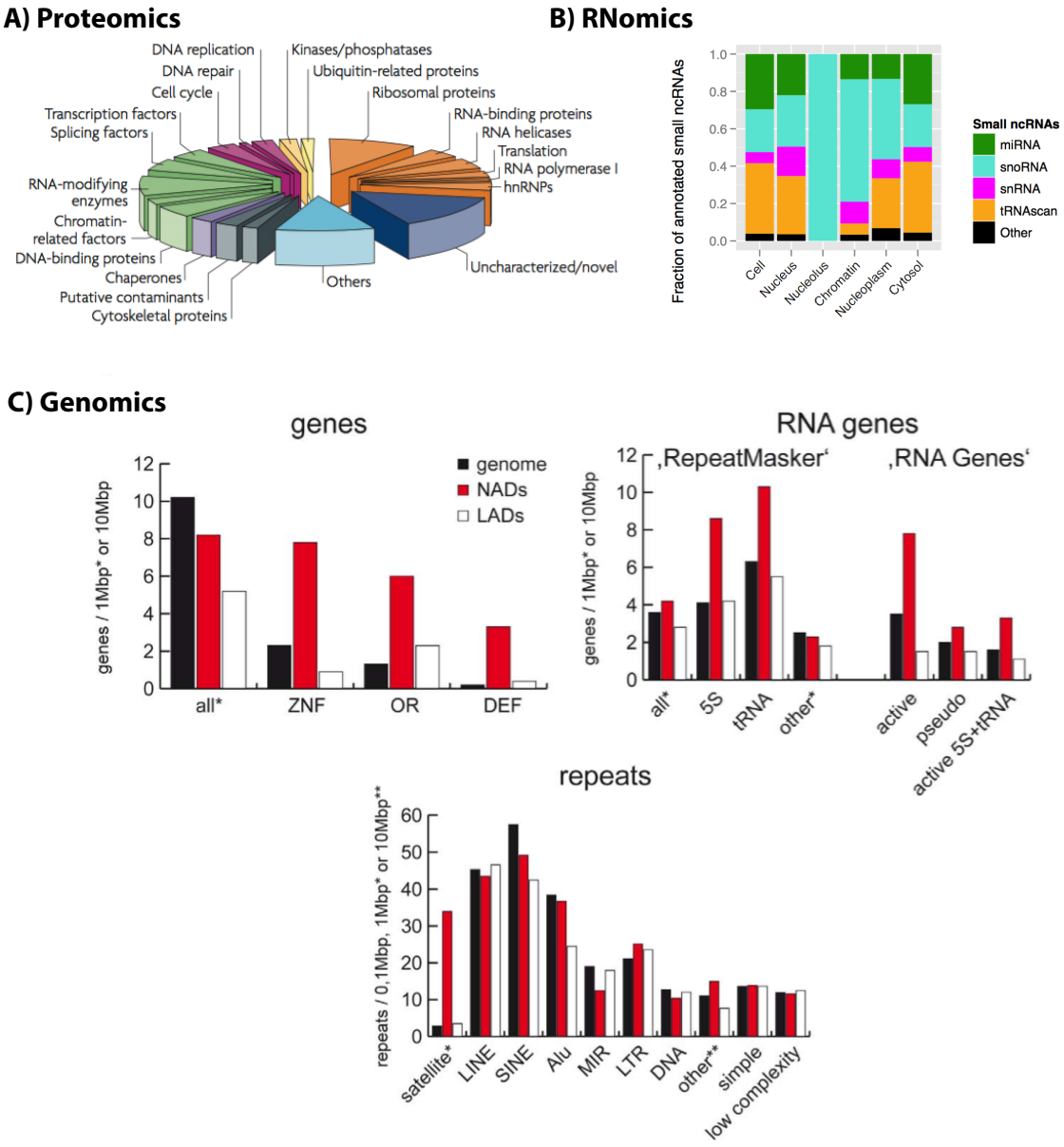

Figure 1.6 – The nucleolar '-omics'.
(A) Mass spectrometry revealed the presence of more than 700 proteins in the human nucleolus. Proteins are clustered according to their molecular functions and colour-coded for similar and related functions. Adapted from Boisvert et al. (2007). (B) RNA composition of different cellular and nuclear compartments. Adapted from Djebali et al. (2012). (C) Comparison of the content of genomic regions that are enriched in nucleolus-associated domains showing the enrichment of Zinc-finger genes (ZNF), olfactory receptor genes (OR), defensin genes (DEF) and satellite repeats. 5S and tRNA genes are also enriched in nucleolus-associated chromatin. NADs are depicted in red, LADs in white and the whole genome in black. Adapted from Németh et al. (2010)

1.1.3 Perinucleolar heterochromatin

Chromatin can generally be divided into transcriptionally active euchromatin, and transcriptionally repressed heterochromatin. Euchromatin is often referred to as 'open' chromatin and is more sensitive to DNase I digest. In contrast, heterochromatin is referred to as 'closed' chromatin and is associated with low sensitivity to DNase I digest. These two types of chromatin are associated with specific epigenetic modifications and histone variants (Even-Faitelson et al., 2015). The terms eu- and heterochromatin are used in this meaning hereafter. Furthermore, 'closed' chromatin can be further subdivided into facultative and constitutive heterochromatin that are characterized by the presence of H3K27me3/H3K9me2 and H3K9me3 histone PTMs, respectively (Kharchenko et al., 2011; Filion et al., 2010). Different studies analyzed the positioning of genes in the mammalian nucleus and found that it is probabilistic. Domains that are generally associated with heterochromatin tend to associate to the nuclear periphery, whereas domains that are actively transcribed are located to the nuclear interior (Bickmore, 2013; Cremer et al., 2001). However, first evidence for the presence of heterochromatic regions also around nucleoli came from studies in the 1960s and 1970s, where it was shown that heterochromatic regions of chromosome 1 and 9 associate with nucleoli (Gagné et al., 1973; Stahl et al., 1976). Then the genomic content of nucleoli and its adjacent perinucleolar heterochromatin was analyzed, which contained gene families that are organized in large clusters and are expressed in a tissue-specific manner like zinc finger, defensin, T-cell receptor and olfactory receptor genes. Furthermore, satellite repeats such as alpha, satellite-2, $(CATTC)_n/(GAATG)_n$, beta and others were also enriched in NADs. Another characteristic of this nuclear compartment is, that it is relatively gene poor and enriched in repressive histone marks, such as H3K27me3, H3K9me3 and H4K20me3 (Németh et al., 2010; van Koningsbruggen et al., 2010). A further site of heterochromatin accumulation is the nuclear periphery. Domains interacting with this nuclear region were identified using DamID (Guelen et al., 2008; Kind and van Steensel, 2010). Those domains feature a comparable domain size as NADs with about 0.1-1 Mb and are frequently overlapping with them (Németh and Längst, 2011). The perinucleolar heterochromatin (PNH) and the peripheral heterochromatin (PH) are functionally similar and domains are highly interchangeable. For instance, domains that were located at the nuclear periphery are found stochastically distributed between the PNH and PH in daughter cells after going through cell division (Kind et al., 2013; Ragoczy et al., 2015).

1.1.4 Repetitive DNA in the nucleolus-associated genome

An important part of the nucleolus-associated genome are repetitive DNA elements, which were first discovered in the 1960s (Britten and Kohne, 1968) and can be interspersed within the genome or form tandem repeats and in total span possibly over two thirds

of the human genome (Figure 1.7, (de Koning et al., 2011)). Besides the long tandem repeat clusters of ribosomal RNA genes other tandem repeats are also an integral part of the nucleolus-associated genome, as mentioned above. Elements of the tandem repeat family are satellite DNA, minisatellites and microsatellites, tandem gene paralogues and telomeric DNA (López-Flores and Garrido-Ramos, 2012).

Satellite DNA is characterized by tandemly repeated sequences, that are typically over 200 nucleotides in length and are organized in hundred or thousand repeated units in one cluster spanning up to several megabases in the genome. A key component of the PNH is satellite repeat DNA, originally discovered in 1961 by Saul Kit in a CsCl-gradient (Kit, 1961). Different types of satellites, such as alpha- and beta-, were discovered by digesting the genome with different restriction enzymes (Waye and Willard, 1989; Alexandrov et al., 1993). Besides the satellite DNA and subtelomeric regions, major parts of the nucleolus-associated genome are tandem gene paralogues, including the rDNA.

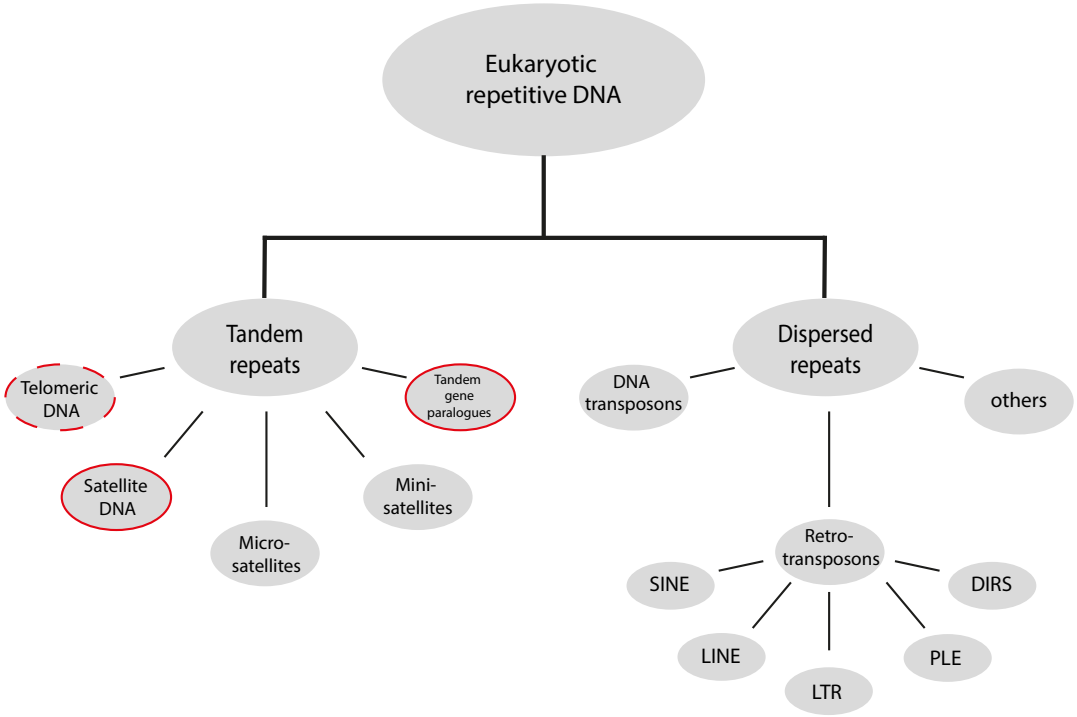

Figure 1.7 – Classification of the different types of repetitive DNA found in the genomes of eukaryotes.
Abbreviations: interspersed elements (SINE), long interspersed elements (LINE), long terminal repeats (LTR), Penelope-like elements (PLE) and Dictyostellum intermediate repeat sequence (DIRS). Tandem repeats enriched in nucleolus-associated DNA are encircled in red. Redrawn after (López-Flores and Garrido-Ramos, 2012).

1.1.5 Chromosomal organization of ribosomal DNA repeat clusters

NORs

In mammalian cells the nucleolus forms around transcriptionally active nucleolar organizer regions, which are embedded into a flanking heterochromatin context (Figure 1.8). *In situ* hybridization experiments unveiled, that those regions are located on the short arms of the human acrocentric chromosomes 13, 14, 15, 21 and 22 (Henderson et al., 1972) and murine chromosomes 12, 15, 16, 17, 18, 19 (Dev et al., 1977). Dynamic molecular combing experiments suggest that the human rDNA repeats are predominantly arranged in a head to tail fashion in humans, but a subset of repeats shows non-canonical arrangement (Caburet et al., 2005). The presence of 300-350 copies of the rDNA repeat unit per haploid genome was revealed by pulse-field gel electrophoresis (PFGE). Furthermore, the size of each individual NOR ranges between 50 kb and up to over 6 Mb (Schmickel, 1973; Sakai et al., 1995; Gonzalez and Sylvester, 1995; Stults et al., 2008). Satellite repeat regions create a heterochromatic epigenetic context at the centromeres and telomeres, and it has been proposed that they isolate the rDNA cluster from genes that are transcribed by Pol II and III (Greig and Willard, 1992; McStay and Grummt, 2008). Investigation of the direct flanking regions of the NORs, revealed that the proximal junction (PJ) consist mainly of segmental duplications, whereas the distal junction (DJ) contains a high portion of unique sequences, indicating functionality. Careful analysis of these newly identified sequences showed similarities to euchromatic regions. In addition, the DJ was shown to localize to the perinucleolar heterochromatin, providing an anchor for the active rDNA (Floutsakou et al., 2013).

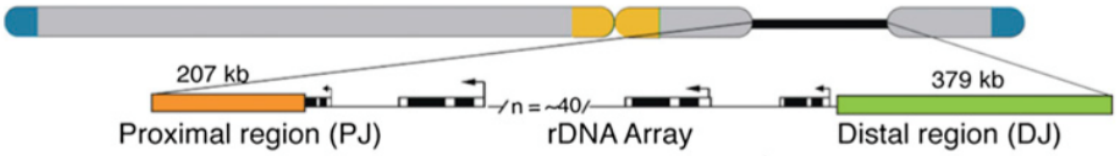

Figure 1.8 – Location of the rDNA arrays on human acrocentric chromosomes. The rDNA arrays is located between the distal junction in the direction of the telomeres and the proximal junction in the direction of the centromeres. Adapted from Floutsakou et al. (2013).

Nucleolar organizer regions can be found in an active and in an inactive state. Active NORs are less condensed during mitosis and have a distinct chromosome structure, giving rise to secondary constrictions on metaphase chromosomes, which can be visualized as a gap in a DNA staining due to their uncondensed state (Saitoh and Laemmli, 1994; Heliot et al., 1997). Furthermore, recent studies revealed in epi-combing experiments, that active non-methylated NORs can be interspersed with inactive methylated rDNA repeats in human cells (Zillner et al., 2015). The open, transcription competent state of chromatin

is maintained during mitosis, where the components of the Pol I transcription machinery including UBF stay associated to active parts of the rDNA (Roussel et al., 1993, 1996). In contrast to active NORs, inactive NORs are condensed and do not form secondary constrictions on metaphase chromosomes. They do no longer give rise to nucleoli and do not show any association with components of the Pol I transcription machinery, especially UBF (McStay and Grummt, 2008). For inactivation of the rDNA different mechanisms have been proposed, those include the elimination of rDNA by nonhomologous crossing over, and rRNA gene silencing due to DNA methylation at position five of the cytosine (5mC) (Guillén et al., 2004).

The rDNA repeats can be present in two different states as characterized by psoralen accessibility assays in yeast (Sogo et al., 1984). 'open' rDNA repeats are depleted of nucleosomes and transcriptionally active. 'closed' repeats are occupied by nucleosomes and transcriptionally inactive. Besides the 'open' and 'closed' the 'poised' state of rDNA is characterized by the presence of Pol I and UBF at the rDNA repeat in mitosis, which can be activated in the next interphase. In the 'closed' state, rDNA is always lacking Pol I and occupied by nucleosomes, but can be methylated or unmethylated. Unmethylated rDNA is embedded in chromatin that carries activating histone marks, whereas methylated DNA is embedded in chromatin carrying repressive ones. Presumably only rDNA units that do not carry DNA methylation and do carry activating histone marks can be activated for transcription again (reviewed in Németh and Längst (2011); Hamperl et al. (2013)).

The structural organization of the mammalian rDNA repeat unit

The rDNA repeat (Figure 1.9) spans 43 kb in humans and about 45 kb in mice and consists of the rRNA coding region and an intergenic spacer (IGS) (Gonzalez and Sylvester, 1995; Grozdanov et al., 2003). As mentioned above, Pol I transcribes exclusively the rRNA genes resulting in a 45S precursor rRNA. This is then processed into the 18S, 5.8S and 28S rRNA which are assembled into ribosomes together with the Pol III transcribed 5S RNA and about 80 ribosomal proteins. The three parts of the rDNA that encode the mature rRNA species are separated by two internal transcribed spacer regions (ITS1 and ITS2) and flanked by two external transcribed spacer regions at the 5' and 3' end (5'ETS and 3'ETS). The approximately 30 kb long IGS contains regulatory elements which are flanking the coding region and include the gene promoter, a spacer promoter, repetitive enhancer elements and transcription terminators (Haltiner et al., 1986; Gonzalez and Sylvester, 1995; McStay and Grummt, 2008). The rDNA promoter has a bipartite structure, composed out of an upstream control element (UCE) and the core promoter next to the transcription start site (Haltiner et al., 1986; Learned et al., 1986).

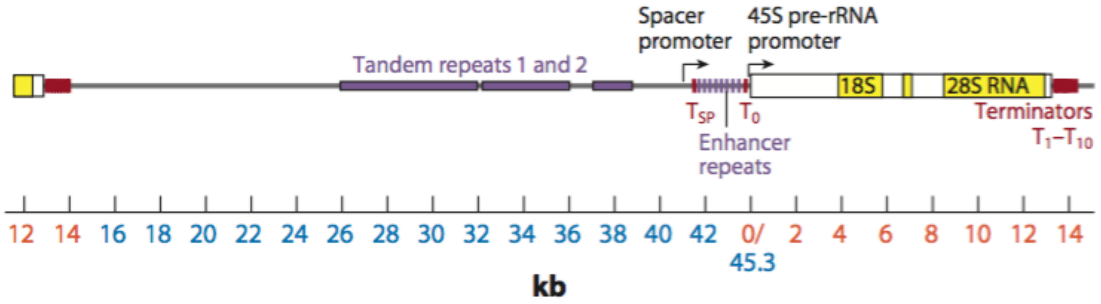

Figure 1.9 – Illustration of the rDNA repeat unit structure.
The structure of the murine rRNA gene is depicted. Arrows indicate the sites of transcription initiation of the 45S pre-rRNA and the intergenic spacer promoter. Locations of mature rRNA encoding regions are marked in yellow, terminator regions are marked in red, repetitive enhancer repeats are marked in purple and the locations of the promoters are indicated. A scale is shown below: numbers indicate kilobase pairs and the zero point represents the transcription start site of the rRNA gene. Adapted from McStay and Grummt (2008).

The role of UBF in rRNA transcription

The transcription of ribosomal RNA is facilitated by Pol I in combination with the pre-initiation complex (PIC) consisting of SL1 and UBF. The interaction of UBF and SL1 to form the PIC and activation of transcription was first shown by Tjian and colleagues (Bell et al., 1988). UBF is a highly abundant protein, which contains six HMG boxes and at least four of them are known to mediate DNA binding (Jantzen et al., 1990, 1992). UBF is a highly conserved protein, showing 73 % homology between mammals and *Xenopus* (Moss and Stefanovsky, 1995). Furthermore, two different splice-variants of UBF, UBF1 and UBF2, were found in humans with a size of 94 and 97 kDa (Figure 1.10).

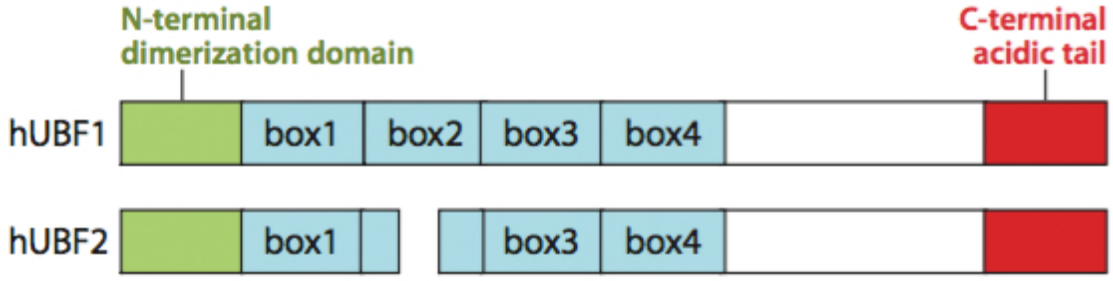

Figure 1.10 – Illustration of sequence conservation of UBF variants.
Schematic sequences of human UBF are illustrated. HMG-boxes 1-4, which mediate DNA binding (blue), the N-terminal dimerization domain (green) and the C-terminal acidic tail (red) are shown. Adapted from (McStay and Grummt, 2008).

In vivo UBF dimerizes and the presence of multiple HMG boxes enables this dimer to bend the DNA to a 360° loop. This structure resembles the loop structure of a nucleosome and was called enhancesome reflecting its activating effect on transcription initiation (McStay et al., 1991; Bazett-Jones et al., 1994; Putnam et al., 1994; Stefanovsky et al., 2001). In addition to this function, UBF plays a role also in defining the chromatin architecture of active rDNA repeat units. It binds all over the rRNA enhancer and coding regions and represents an essential structural component of the open rDNA chromatin conformation (O'Sullivan et al., 2002; Sanij et al., 2008; Zentner et al., 2011). This architectural role of UBF is supported by observations showing that new secondary constrictions as well as nucleoli form at sites where UBF binding sites of *Xenopus* are integrated into the human genome in a non NOR context. Remarkably, factors of the Pol I transcription and ribosomal RNA processing machinery are recruited to these sites called pseudo-NORs, although the inserted sequences lack the promoter sequences and are therefore not capable of transcription (Mais et al., 2005; Prieto and McStay, 2008). A possible mechanism for creating and maintaining the open chromatin structure of rDNA is that UBF competes with histone H1, leading to decompaction of chromatin. Recently evidence arised that besides playing a regulatory role in Pol I transcription UBF regulates also Pol II at highly transcribed histone genes, which is mediated by the shorter splice variant UBF2 (Sanij et al., 2015; Diesch et al., 2015). In order to further investigate the function of UBF *in vivo* a conditional gene-deletion system was established in mouse, which was used also in the presented work. This gene-deletion was achieved by placing two Lox recombination sites into intron 2 and 5 of the UBF gene and crossing such a recombinant mouse with a mouse carrying the ER-Cre recombinase. Hamdane et al. (2014) showed by using this system, that UBF defines the active chromatin domains of the rRNA genes and is essential for transcription of these genes. Furthermore, loss of UBF leads to the formation of a proteinaceous nucleolar precursor body containing rRNA synthesis and processing factors, which progressively separates from rDNA loci (Hamdane et al., 2014).

1.2 Cellular aging

1.2.1 Cellular senescence

Already 50 years ago Hayflick and Moorhead (1961) described that "there does exist a finite limit to the cultivation period of diploid cell strains", a phenomenon that is today known as the 'Hayflick limit'. This finding implied a replication-dependent molecular mechanism, which induces a stop in proliferation and the senescent status after a certain number of cell divisions.

In the early 1970s, five years prior to the discovery of telomeres (Blackburn and Gall, 1978), a model describing the shortening of the DNA template during each replication was already proposed (Olovnikov, 1973). Later, the varying length of telomeres in different cell types was discovered (Cooke and Smith, 1986). The shortening of the DNA template proposed by Olovnikov was then found to be associated with cessation of cell division in *in vitro* cultivated fibroblasts and the causal role for telomere shortening in cellular senescence was proposed (Harley et al., 1990; Bodnar et al., 1998). In the latter study two normal human cell types were transfected with a vector enconding the catalytic subunit of the telomerase, which lead to an extended replicative life-span compared to not transfected cells. More recently it was observed, that telomere shortening induces a DNA damage response (DDR), which is responsible for and maintains the senescence phenotype (d'Adda di Fagagna et al., 2003). Cellular senescence, which is caused by telomere shortening is called replicative senescence. Further causes of senescence include oxidative stress, activated oncogenes or other stresses such as inadequate growth conditions (Parrinello et al., 2003; Chen and Ames, 1994; McConnell et al., 1998; Ramirez et al., 2001). All these factors lead to a cessation of proliferation and an exit from the cell cycle. This exit can be mediated by a variety of molecular mechanisms and factors that regulate the cell cycle and control different cell cycle checkpoints (Kuilman et al., 2010; López-Otín et al., 2013; Salama et al., 2014; Muñoz-Espín and Serrano, 2014).

Senescence is a stable exit from the cell cycle

Progression through the cell cycle is crucial for eukaryotic cell growth and proliferation which is controlled at different stages by so called check-points. When cells exit mitosis, they progress to the G1 Phase where they synthesize proteins and their growth is dependent on extracellular signals such as growth factors (GF) and nutrients. The progression through S-Phase is controlled by a check-point in the cell cycle which is also called the restriction point. When a given cell passes this check-point it is committed to progressing through the cell cycle and is no longer dependent on external signals. If the amount of nutrients or GFs is not sufficient to pass this check-point, cells enter a quiescent state of halted proliferation. This state of dormancy can be overcome, when the amount of GFs

and nutrients increases and passes a certain threshold to proceed into the S Phase (Pardee, 1974). After cells passed the restriction point, they commence through S Phase to duplicate their DNA. The integrity of the produced DNA is then checked and repair mechanisms are eventually activated. When the amount and quality of the replicated DNA is sufficient, cells progress through G2 into M Phase. Here the alignment of the chromosomes to the middle axis of the cell is controlled and if microtubuli function is guaranteed cells progress through mitosis (Blagosklonny and Pardee, 2002).

Consecutive cell divisions cause telomere attrition, which leads to the activation of DDR and downstream DNA damage kinases ATM, ATR, CHK1 and CHK2. P53 gets phosphorylated and activates the expression of p21 which binds to and inhibits CDK-cyclin complexes. Finally, this leads to a hyperphosphorylation of the tumor suppressor RB and a proliferation arrest (Figure 1.11, rewieved in Muñoz-Espín and Serrano (2014); Moskalev et al. (2014); Salama et al. (2014)).

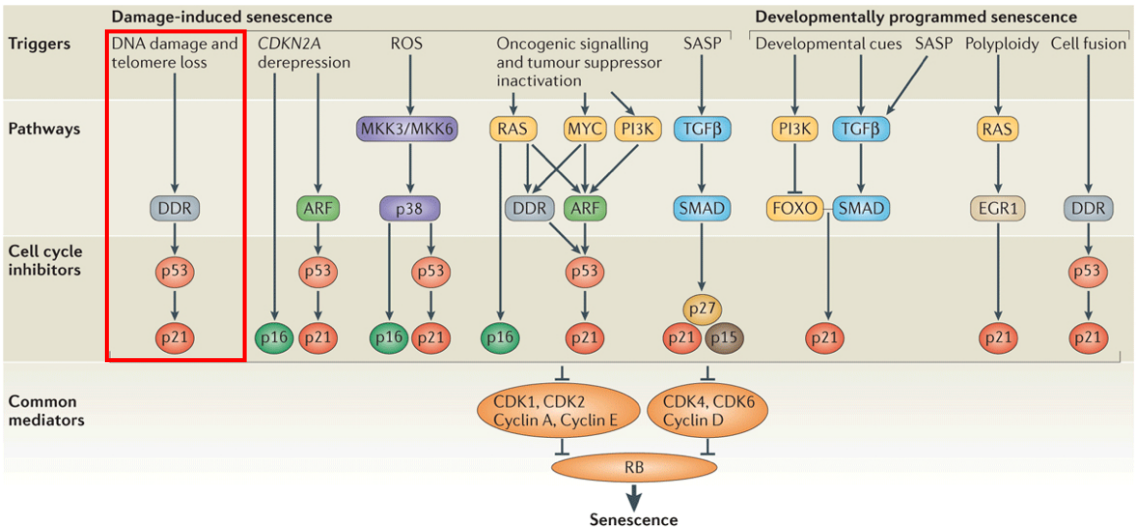

Figure 1.11 – Molecular mechanisms of cellular senescence.
Multiple external or internal signals (triggers) activate signaling cascades (pathways) that lead ultimately to the activation of cell cycle inhibitors and the tumor suppressor RB. Marked with the red rectangle is the pathway thats leads to replicative senescence by DNA damage and telomere attrition. This pathway directly activates p53 and its downstream target p21. Adapted from (Muñoz-Espín and Serrano, 2014).

Regarding the cell cycle exit point and DNA content of senescent cells it has been thought until very recently that they are arrested in G1 Phase of the cell cycle and possess accordingly a diploid (2n) genome. However, Mao et al. (2012) could show, that senescent IMR90 and WI-38 cell populations also contained cells with tetraploid (4n) DNA content suggesting that they originate from a G2 exit point. Those cells were found at a frequency

of 37 - 39 %. This is in agreement with another recent observation, that human cells can skip one mitosis before becoming senescent (Figure 1.12, Johmura et al. (2014)).

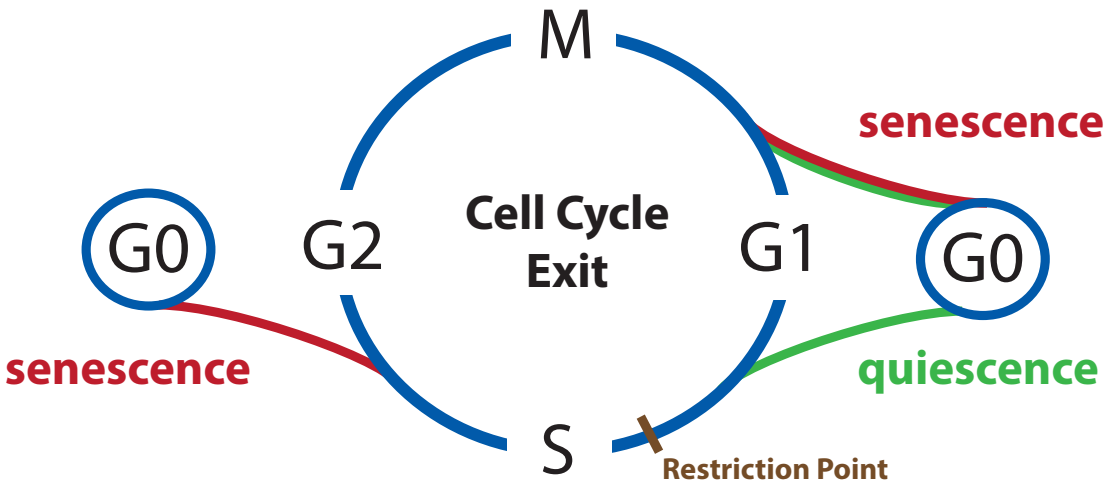

Figure 1.12 – Senescent and quiescent cells exit the cell cycle.
Human cells can reversibly exit the cell cycle at the restriction point at the end of G1 to enter cellular quiescence. In contrast, cellular senescence is a stable cell cycle arrest which can also be entered in parallel to G2 phase with cells being tetraploid (4n).

Alterations of cellular structure and function and nucleolar changes during cellular senescence

Besides flattening of the cell and cessation of proliferation, several markers of cellular senescence have been described in the past two decades, which allow the recognition of senescent cells in a cell population. Furthermore, a well established test to identify senescent cells was developed by Dimri et al. (1995). This test makes use of the overexpression of lysosomal β-galactosidase in senescent cells (Lee et al., 2006).

Moreover, senescent cells secrete certain molecules, a phenomenon called senescence associated secretory phenotype (SASP). SASP is coupled to DNA damage and is not found in all senescence types. Factors that are secreted include inflammatory factors such as IL-6 and IL-8, growth factors and receptor ligands (Rodier et al., 2009; Coppé et al., 2010). By emitting those compounds into their local environment, senescent cells induce a so called 'bystander effect', which causes cellular senescence in neighboring cells (Nelson et al., 2012).

1.2.2 Changes in nuclear architecture during cell cycle and cellular aging

Nuclear and nucleolar organization are prone to large rearrangements in cellular senescence and during the cell cycle, due to changes in gene expression and the connected potential re-localization of chromosomal domains. In fact, the repositioning of whole chromosome territories was observed during replicative senescence in human diploid fibroblasts (Bridger et al., 2000)

Further changes in the nuclear architecture in senescent cells include the formation of senescence associated heterochromatin foci (SAHF), which can be observed as punctuate DNA foci in senescent cells, whereas proliferating cells show a more homogeneous DAPI staining. This phenomenon was first described and characterized in Ras-induced senescence. SAHFs contain heterochromatic proteins, such as HP1 and repressive histone marks such as H3K9 methylation (Narita et al., 2003; Rai and Adams, 2012). However, this phenotype is not seen in every type of cellular senescence and occurs predominantly in oncogene-induced senescence (Kosar et al., 2014).

More recently, the senescence-associated distension of satellites (SADS) was discovered. This decondensation of pericentromeric and centromeric satellites, which mainly localize to nucleoli, occurs earlier and more consistently than SAHF formation. SADS is not restricted to a certain type of cellular senescence and occurs also in replicative senescence. Furthermore, SADS is not dependent on other chromatin changes such as SAHF and it is an early event in cellular senescence. The amount of H3K9 methylation and H3K27me3 associated to SADS does not change in senescent compared to proliferating cells, excluding a causal role for this heterochromatin mark and indicating that satellites are distended rather than decondensed. SADS was also found to be correlating with a downregulation of the structural protein lamin B1 (Swanson et al., 2013), which was described independently in several studies (Shimi et al., 2011; Freund et al., 2012; Sadaie et al., 2013).

Changes in nucleolar morphology that were observed during cellular aging, such as one larger nucleolus as measured by the dry mass was observed in senescent cells, resemble changes that were observed during progression through the cell cycle (Bemiller and Lee, 1978; Bemiller and Miller, 1979). Changes in nucleolar morphology, that happen during the cell cycle were already investigated during the 1970s. Human chromosomes contain 10 NORs on the acrocentric chromosomes, therefore 10 nucleoli should be present in each nucleus, but the maximum number of nucleoli was rarely observed (Hsu et al., 1975). Anastassova-Kristeva (1977) observed nuclei containing different amounts of nucleoli in mammalian cells, with nuclei containing 7, 8 or 9 nucleoli being less abundant, indicating a quick association of some loci. In the course of the cell cycle nucleoli fuse resulting in a single nucleolus at the end of interphase (Figure 1.13). More recently Brangwynne et al. (2011) proposed a physical model of nucleolar fusion. According to this, nucleoli behave

like liquid droplets that will fuse during the cell cycle.

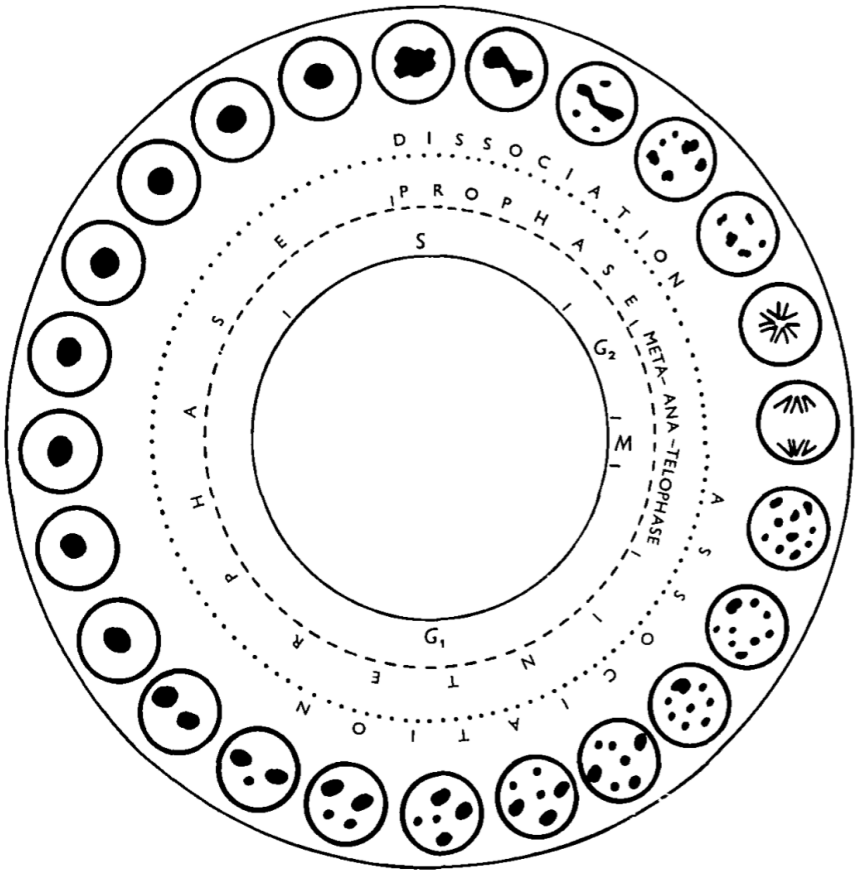

Figure 1.13 – Association and dissociation of nucleoli during the cell cycle. Nuclei are depicted as circles containing individual nucleoli. Association and dissociation of nucleoli during the cell cycle is depicted. Adapted from (Anastassova-Kristeva, 1977)

2 Results

2.1 Analyses of nucleolus-associated chromatin in human cells and its changes during cellular aging

2.1.1 Isolation of nucleolar DNA from IMR90 cells for array CGH analyses

Nucleolus-associated domains (NADs) were first described in 2010 in HeLa and HT1080 cells, providing a snapshot of genome organization in and around the nucleolus (Németh et al., 2010; van Koningsbruggen et al., 2010). In order to compare NADs of different human cell lines and obtain information about the nucleolus-associated chromatin in normal, non-transformed diploid cells, nucleoli were isolated from young, proliferating IMR90 fibroblasts.

Nuclear architecture is subjected to reorganization during physiological processes, such as cellular aging (Bridger et al., 2000). To get an insight in the dynamics of nucleolus-associated chromatin during these processes, nucleolus-associated DNA was isolated from quiescent and senescent IMR90 cells. In short, IMR90 cells were fixed on plates using 0.2 % formaldehyde and nucleoli were purified by sequential sonication in buffers containing high (12 mM) and a low concentrations (1 mM) of $MgCl_2$. Mg^{2+} compacts chromatin and therefore decreasing its concentration leads to decompaction of chromatin-structures and facilitates the purification of nucleoli by simultaneous depletion of loosely associated chromatin domains. Cross-linked nucleoli are very dense particles and separation after sonication was achieved by centrifugation in 0.88 mM sucrose solution. Finally, nucleolar DNA was isolated from purified nucleoli.

2.1.1.1 Controls of the cellular aging process

When primary cells are cultivated *in vitro* they stop dividing after a certain number of cell cycles, this is called the 'Hayflick limit' (Hayflick and Moorhead, 1961). In order to monitor whether the IMR90 cell-population was proliferating or senescent, four independent methods were used. Regular counting of cell numbers provided information about the proliferation status of the cell population at first. Then the over-expression of senescence-associated β-galactosidase was inspected using an enzyme activity assay and the level of the proliferation marker Ki-67 was detected by immunofluorescence-staining.

Furthermore, decondensation of satellite-2 was monitored in FISH-experiments during cellular senescence (see Section 2.1.4.4, Figure 2.28), since senescence-associated distension of satellites (SADS) is a stable and early marker for cellular senescence (Swanson et al., 2013).

Prior to nucleolus isolation from non-dividing, senescent cells the status of senescence was monitored. This was evaluated by the mean of β-galactosidase activity measurement according to a well-established assay (Dimri et al., 1995). In short, IMR90 cells were grown in 6-well plates, fixed with formaldehyde and a β-galactosidase activity measurement was performed. Senescent cells showed a characteristic intense blue staining, due to the cleavage of the X-gal substrate, whereas no staining was visible in proliferating and quiescent IMR90 cells (Figure 2.1).

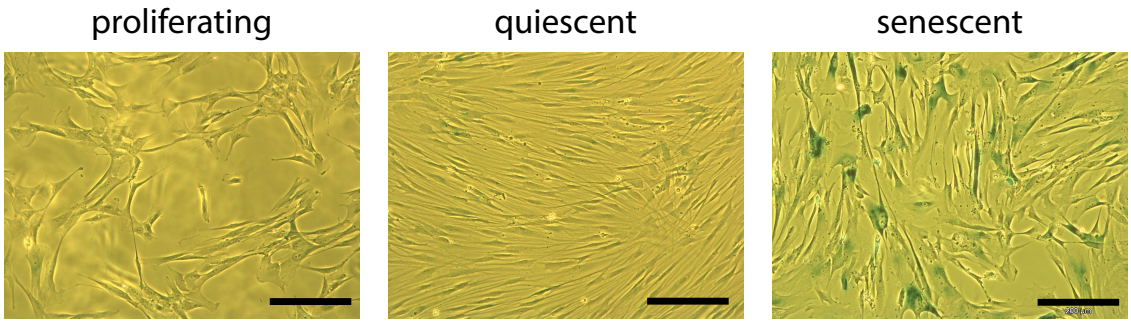

Figure 2.1 – β-galactosidase staining indicates senescence status.
IMR90 cells were fixed with formaldehyde and β-galactosidase activity assay was performed for proliferating, quiescent and senescent cells. Intense blue staining is characteristic for senescent cells. Scale-bar: 200 µm.

In order to quantify the amount of non-proliferating cells, Ki-67 staining was combined with DAPI staining in immunofluorescence experiments. Ki-67 is a protein, which is expressed predominantly in the S phase in cycling cells, where it localizes in nucleoli (Scholzen and Gerdes, 2000). Hence, a lack of this protein indicates cessation of proliferation as expected for senescent cells. The amount of proliferating and non-proliferating cells in the different cell populations was quantified. In total, 200 senescent cells were evaluated for the presence of Ki-67 and 90 % of them were Ki-67 negative, whereas in a proliferating cell population 84 % of 120 cells were positive. Representative fluorescence microscopy images illustrate that senescent cells do not show any Ki-67 staining (Figure 2.2, lower panel), whereas proliferating cells are Ki-67 positive (Figure 2.2, upper panel).

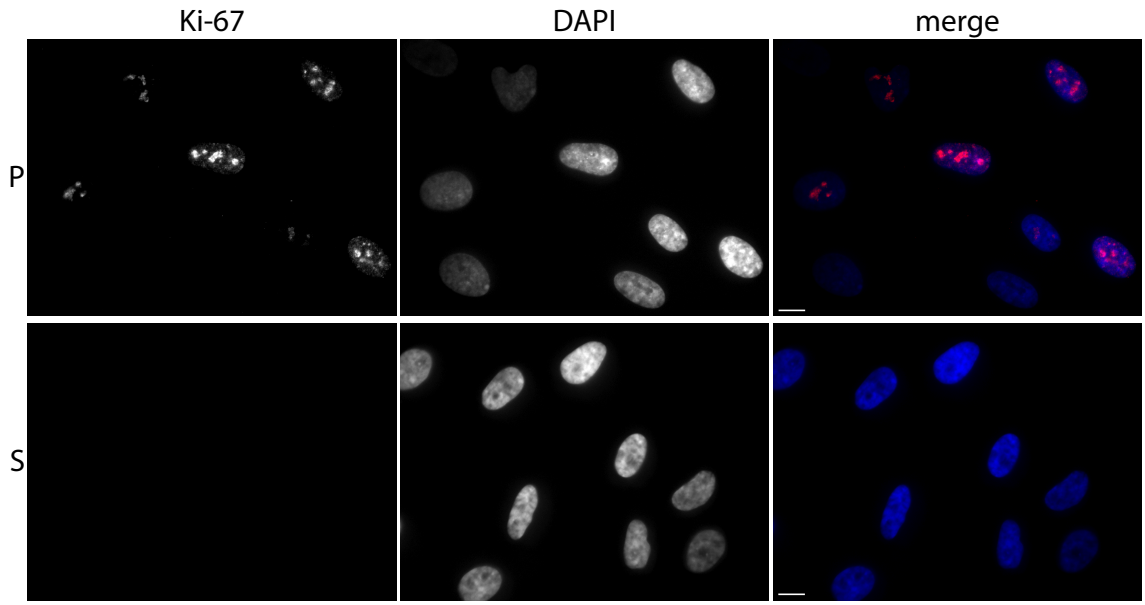

Figure 2.2 – Lack of Ki-67 staining indicates stop of proliferation.
Proliferating and senescent IMR90 cells were fixed with formaldehyde and stained for Ki-67 and DAPI. Upper panel (P): proliferating cells with positive Ki-67 staining. Lower panel (S): senescent cells with negative Ki-67 staining. Ki-67 staining is depicted in red, DNA in blue. Scale bar: 10 µm.

2.1.1.2 Controls of nucleolus isolation

The quality of nucleolus isolations was controlled using three independent methods. The enrichment of the nucleolar marker protein UBF and depletion of the cytoplasmatic factor tubulin in nucleolar fractions was monitored in western blot analysis. In addition, the size and shape of isolated nucleoli was analyzed with DIC microscopy and the enrichment of the 5' External Transcribed Spacer (5'ETS) and 28S rDNA in nucleolar fractions compared to gDNA was assayed by qPCR. The DNA was taken from nucleolus preparations that passed quality controls and hybridized on two-colour Human CGH 4.2M Whole Genome Tiling Arrays against non-nucleolar DNA. To complement these analyses with biological replicate experiments, nucleolus-associated DNA from proliferating, quiescent and senescent IMR90 cells was prepared by A. Németh and hybridized against genomic DNA on the same array type.

Monitoring the levels of UBF in isolated nucleolar fractions by western blot analysis

In order to control the quality of nucleolus isolations the enrichment of the nucleolar marker protein UBF, as well as the depletion of the cytoplasmatic marker protein tubulin was monitored. Therefore, three aliquots for western blot analysis were taken during the purification process. The first aliquot was taken from whole cell lysates before the purification (whole cell extract = 'wce'), to serve as an input control. Further aliquots were taken

after the first round of sonication, to yield unpure nucleoli (dirty nucleoli = 'dNo') and after the second round of sonication to yield the final nucleolar fraction (clean nucleoli = 'cNo').

To evaluate the quality of the purified nucleoli, the relative amount of UBF compared to tubulin was assessed in different fractions. As illustrated in Figure 2.3 enrichment of UBF compared to tubulin was observed in the 'cNo' fraction for all three purifications. For the isolation from senescent cells an additional aliquot was collected from the supernatant after the second round of sonication ('sNo'). The analysis of this fraction indicates, that only small amounts, if any, of nucleolar components are lost in this step, since no signal for UBF is visible.

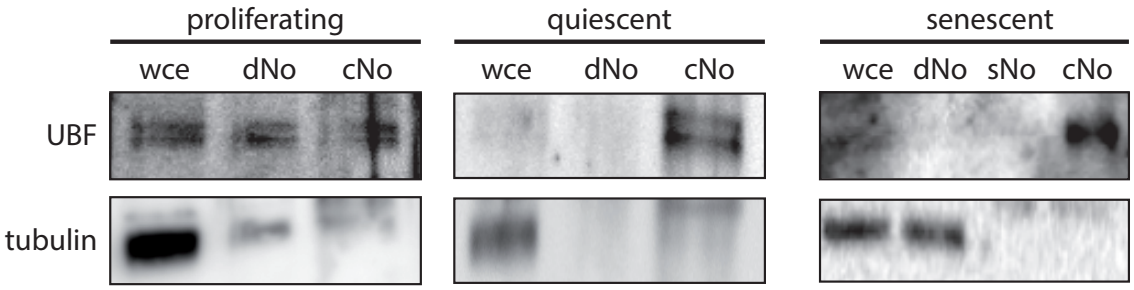

Figure 2.3 – Western blot detection of UBF and tubulin to monitor levels in different fractions of nucleolus preparations.
Fractions of nucleolus isolations of proliferating, quiescent and senescent IMR90 cells were analyzed by UBF and tubulin western blot. Enrichment of UBF compared to tubulin is visible in all purifications. wce = whole cell extract, dNo = dirty nucleoli, sNo = supernatant after second round of sonication, cNo = clean nucleoli.

Evaluation of the size and shape of isolated nucleoli with DIC microscopy

In order to evaluate purified nucleoli with respect to their size and the presence of nuclear remnants, differential interference contrast (DIC) microscopy was performed. Aliquots were taken from fixed cells, and from purified nucleoli prior to DNA precipitation. On the one hand, nucleoli were evaluated instantly during the purification process, to have an immediate quality control, on the other hand images were documented after the purification process from nucleoli that were stored at 4 $°C$.

Purified nucleoli should be visible as refractive, spheric bodies and no large nuclear remnants, should be present. Isolated nucleoli of proliferating and senescent IMR90 cells exhibit comparable morphology as nucleoli in the respective cells with no nuclear remnants visible. Furthermore, smaller particles, were also visible. These particles may be mitochondria as they can co-sediment with nucleoli (Figure 2.4).

On one image some areas with aggregated particles and also smaller particles were visible (see for instance Figure 2.4 right bottom image). This is due to the fact that nucleoli were stored at 4 $°C$ until the documentation and if the storage time was longer than a few hours it often led to aggregation and also partial disintegration of nucleoli in the sucrose-free Tris buffer, nevertheless the majority of the particles exhibit comparable morphology and size as nucleoli in the respective cells.

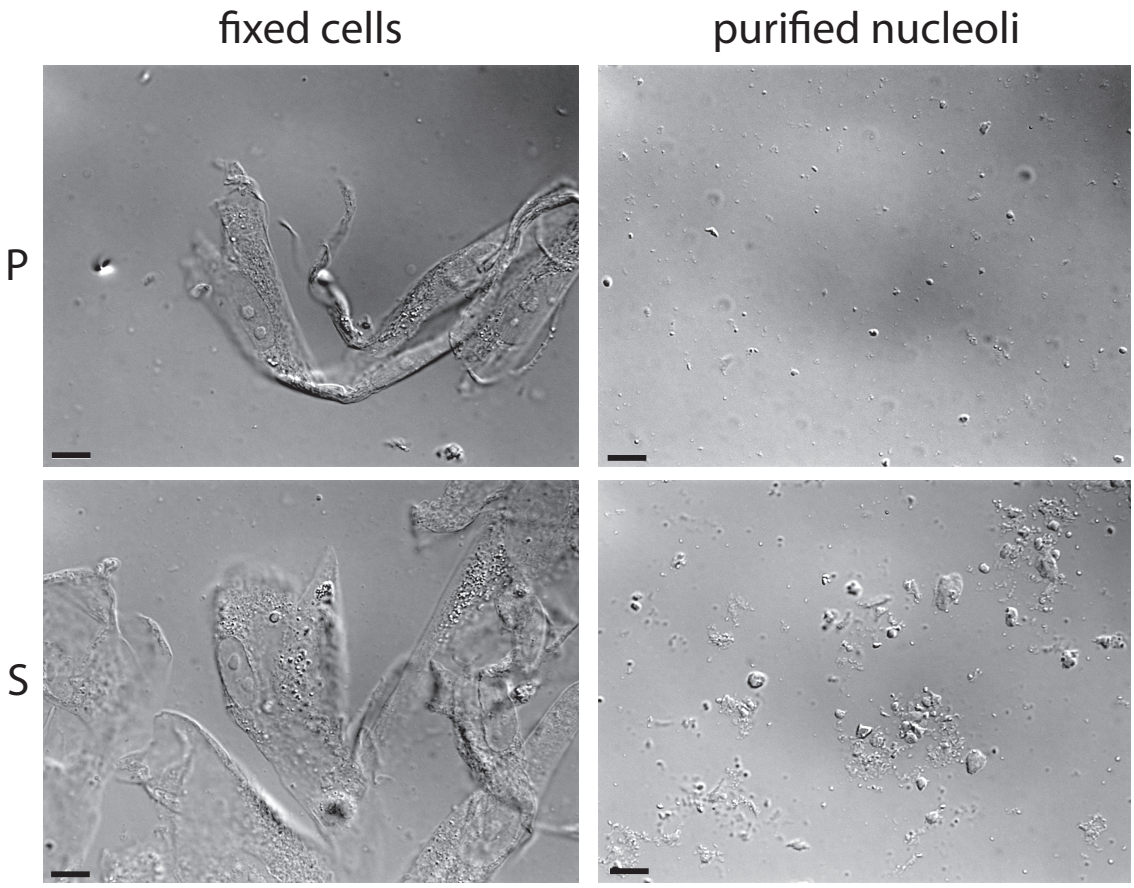

Figure 2.4 – Monitoring size and shape of isolated particles with DIC microscopy.
Fixed cells and isolated nucleoli were observed under a light microscope. Purified nucleoli (right panel) show similar size and shape as nucleoli in fixed cells (left panel). Upper panel: proliferating cells, lower panel: senescent cells. Scale bar: 10 µm.

Monitoring of the levels of rDNA in isolated nucleolar DNA with qPCR

Since the rDNA is the core DNA component of nucleoli, the amount of rDNA in isolated nucleolar DNA compared to genomic DNA was measured to evaluate the quality of nucleolus isolations. Hence, equal amounts of genomic DNA isolated from IMR90 cells

and isolated nucleolar DNA were subjected to qPCR analysis using TaqMan probes for detection. For amplification, oligonucleotides amplifying parts of the 5'ETS and the 28S rDNA were used in parallel.

Figure 2.5 illustrates the calculated values for the amount of both parts of the rDNA for nucleoli prepared from proliferating, senescent and quiescent cells. Enrichment of rDNA is clearly visible for the preparation from proliferating, quiescent and senescent IMR90 cells and is in the range of 100-fold, with the exception of the higher 5'ETS value in the quiescent sample.

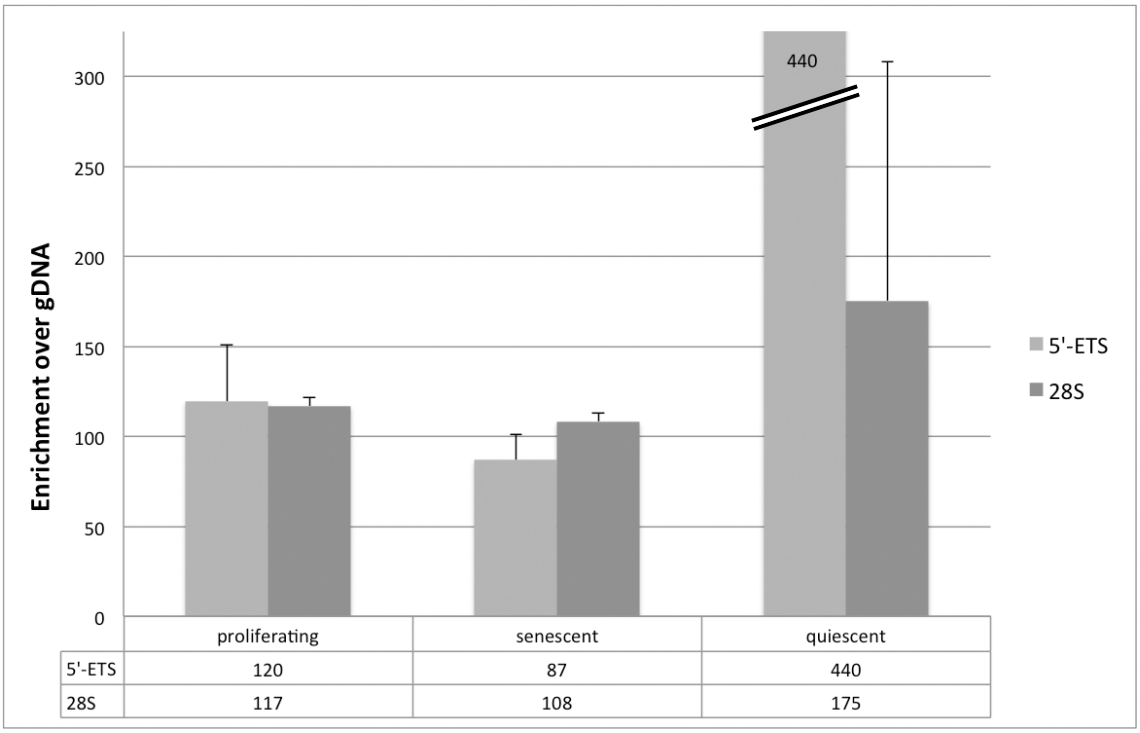

Figure 2.5 – qPCR analysis of rDNA amounts in isolated nucleolar DNA compared to genomic DNA.
Nucleolus-associated DNA from proliferating, quiescent and senescent IMR90 cells was analyzed in qPCR experiments. 5'-ETS (light grey) and 28S (dark grey) rDNA regions were analyzed. Enrichment was calculated as rDNA in nucleolar DNA divided by rDNA in the same amount (10 ng) of gDNA. Exact values are indicated in the table.

2.1.1.3 Microarray analysis of NADs in proliferating and senescent IMR90 cells

Nucleolus-associated DNA was fluorescently labeled and hybridized together with labeled, non-nucleolar DNA on two-colour Human CGH 4.2M Whole Genome Tiling Arrays with a median probe spacing of 284 bp. Visualization of the normalized microarray-data in

the Integrated Genome Browser (IGB) revealed a similar pattern of nucleolus-associated domains with no major differences in senescent cells compared to proliferating cells, suggesting that NADs are very stable during replicative senescence (Figure 2.6). However, the signal amplitude is lower in arrays that were hybridized with DNA from senescent cells.

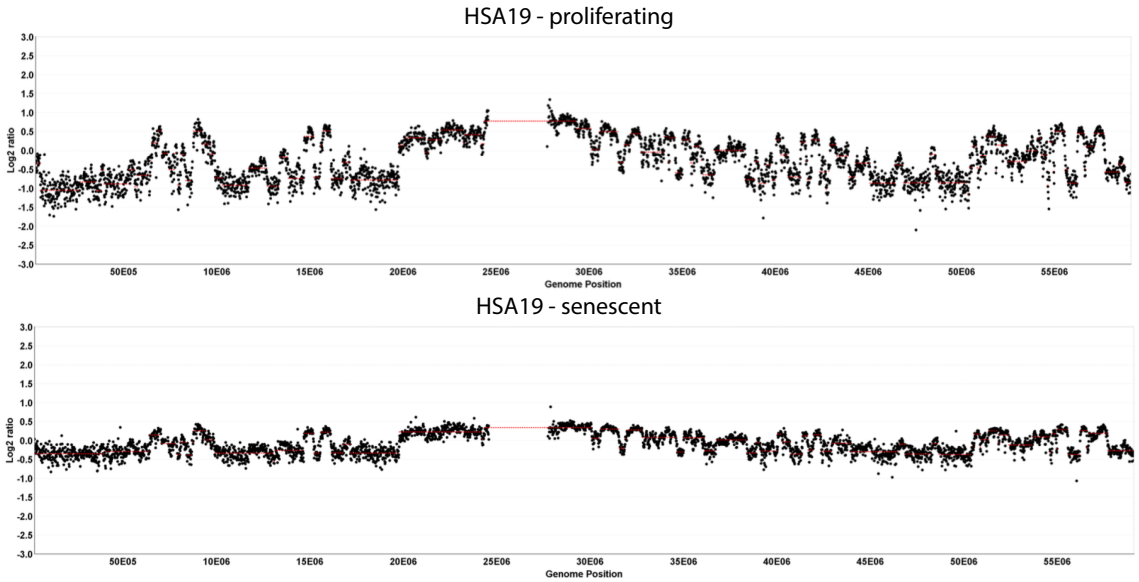

Figure 2.6 – Illustration of normalized data of CGH-microarrays.
Nucleolus-associated DNA was hybridized against non nucleolar-DNA. Positive values indicate an enrichment of the respective genomic region in nucleolus-associated DNA, negative values indicate a depletion. A snapshot from chromosome 19 is shown from proliferating (upper panel) and senescent (lower panel) IMR90 cells. The gap represents unmapped centromeric regions.

2.1.2 Isolation of nucleolar DNA from K562 cells using different fractionation procedures

Experimental procedures for isolating nucleoli were first developed in the 1950s and 1960s (Vincent, 1952; Monty et al., 1956; Busch et al., 1963). In the last decade, studies in three different laboratories have been performed using modified versions of those protocols. The outlines of the three approaches are as follows (see Methods Sections 5.1.3.1 and 5.1.3.3 for details):

(A) The laboratory of B. McStay used a cross-linking approach, where cells were fixed with 0.2 % formaldehyde and nucleoli were isolated using two sonication steps. Sonications were performed in buffers containing decreasing concentrations of $MgCl_2$ (12 mM and 1 mM) and 0.88M sucrose (Sullivan et al., 2001).

(B) The laboratory of A. Lamond made use of a native approach without cross-linking, where nuclei were first isolated using a dounce homogenizer and subsequently centrifuged two times on sucrose cushions (0.25 M and 0.35 M sucrose). Then nucleoli were isolated by sonication in a buffer containing 0.5 mM $MgCl_2$ followed by another centrifugation on a 0.88 M sucrose cushion (Andersen et al., 2002).

(C) The laboratory of T. Pederson, also made use of a native approach. This protocol was used also by the ENCODE consortium (Djebali et al., 2012). Here, cells were incubated in a hypotonic buffer and disrupted with a dounce homogenizer. Nucleoli were isolated after a sonication step followed by centrifugation through 1.1 M sucrose (Bhorjee and Pederson, 1973).

In order to compare the efficiency of these protocols with respect to identification of NADs, nucleoli were isolated from K562 human chronic myelogenous leukemia cells, a cell line from which large datasets of epigenetic analyses are available including RNomics of isolated nucleoli (Djebali et al., 2012). In the presented work, nucleoli were isolated from $1x10^8$ K562 cells using each of the three protocols (Figure 2.7, marked with ST). In parallel, isolations were also performed by an independent experimenter to investigate the robustness of the isolation procedures (marked with AN).

To control the quality of isolated nucleoli, the relative amount of the nucleolar marker protein UBF compared to tubulin in isolated nucleolar fractions was monitored in western blot. Figure 2.7 illustrates western blot controls for all three purifications performed in two independent experiments. For nucleoli isolated from cross-linked cells (protocol (A)) an enrichment of UBF compared to tubulin was observed in the fraction of clean nucleoli ('cNo') for both experiments. When nucleoli were isolated without formaldehyde cross-linking using a two-step protocol (protocol (B)) or a one-step protocol (protocol (C)) UBF was again enriched in the nucleolar fraction ('N4' and 'No') compared to tubulin.

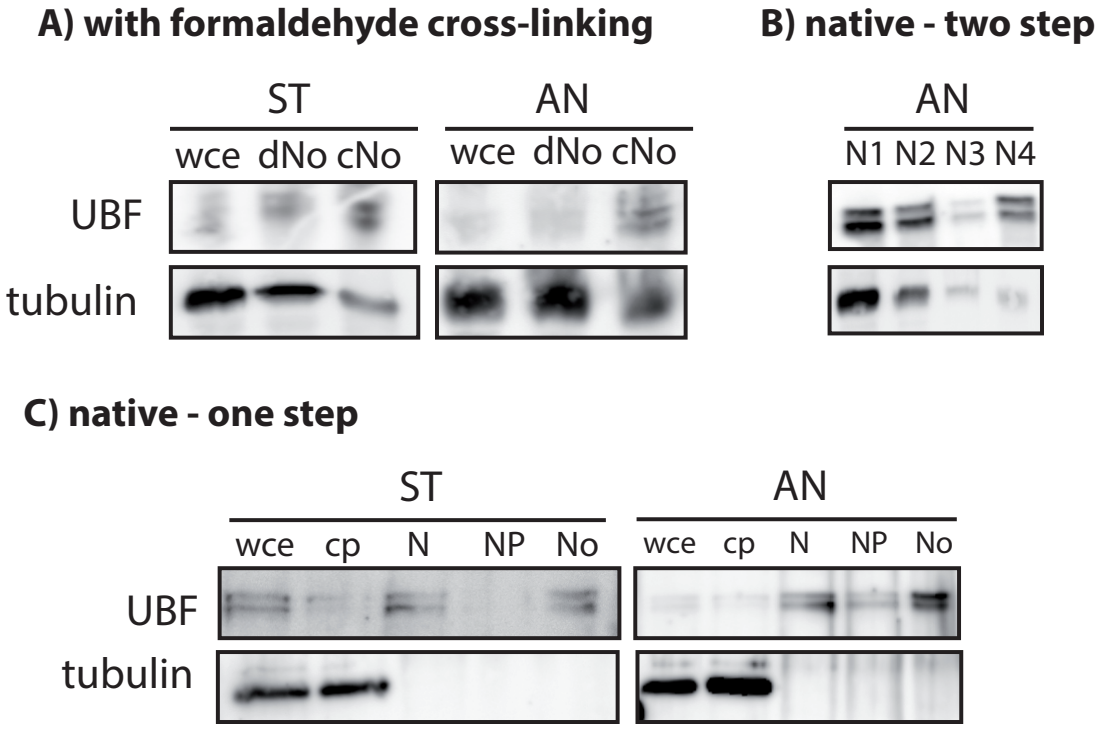

Figure 2.7 – Western blot detection of UBF and tubulin in K562 cellular fractions.
Fractions of the nucleolus purification process were analyzed using western blot and the level of UBF and tubulin was monitored. **(A)** Nucleolus isolation using formaldehyde cross-linked cells. UBF was enriched compared to tubulin in isolated clean nucleoli. wce = whole cell extract, dNo = dirty nucleoli, cNo = clean nuleoli. **(B)** Nucleolus isolation under native conditions including a nucleus isolation step. UBF was enriched compared to tubulin in the final nucleolar fraction. N1 = nuclei, N2 = dirty nuclei, N3 = nuclear plasma, N4 = clean nucleoli. **(C)** Nucleolus isolation using native conditions. UBF was enriched compared to tubulin in the nucleolar fraction. wce = whole cell extract, cp = cytoplasmic fraction, N = nuclei, NP = nuclear plasma, No = clean nucleoli.

Nucleolus-associated DNA was fluorescently labeled and hybridized together with labeled, non-nucleolar DNA on two-colour Human CGH 4.2M Whole Genome Tiling Arrays with a median probe spacing of 284 bp. Visualization of the normalized microarray-data in the IGB revealed comparable patterns for all three purification methods as illustrated by the example of chromosome 19 on Figure 2.8. For the native two-step preparation only one microarray hybridization was performed. The normalized microarray data indicated that patterns between biological replicates can exhibit larger differences than patterns between the different purification methods (compare panels A/B and D/E with A/C/D in Figure 2.8).

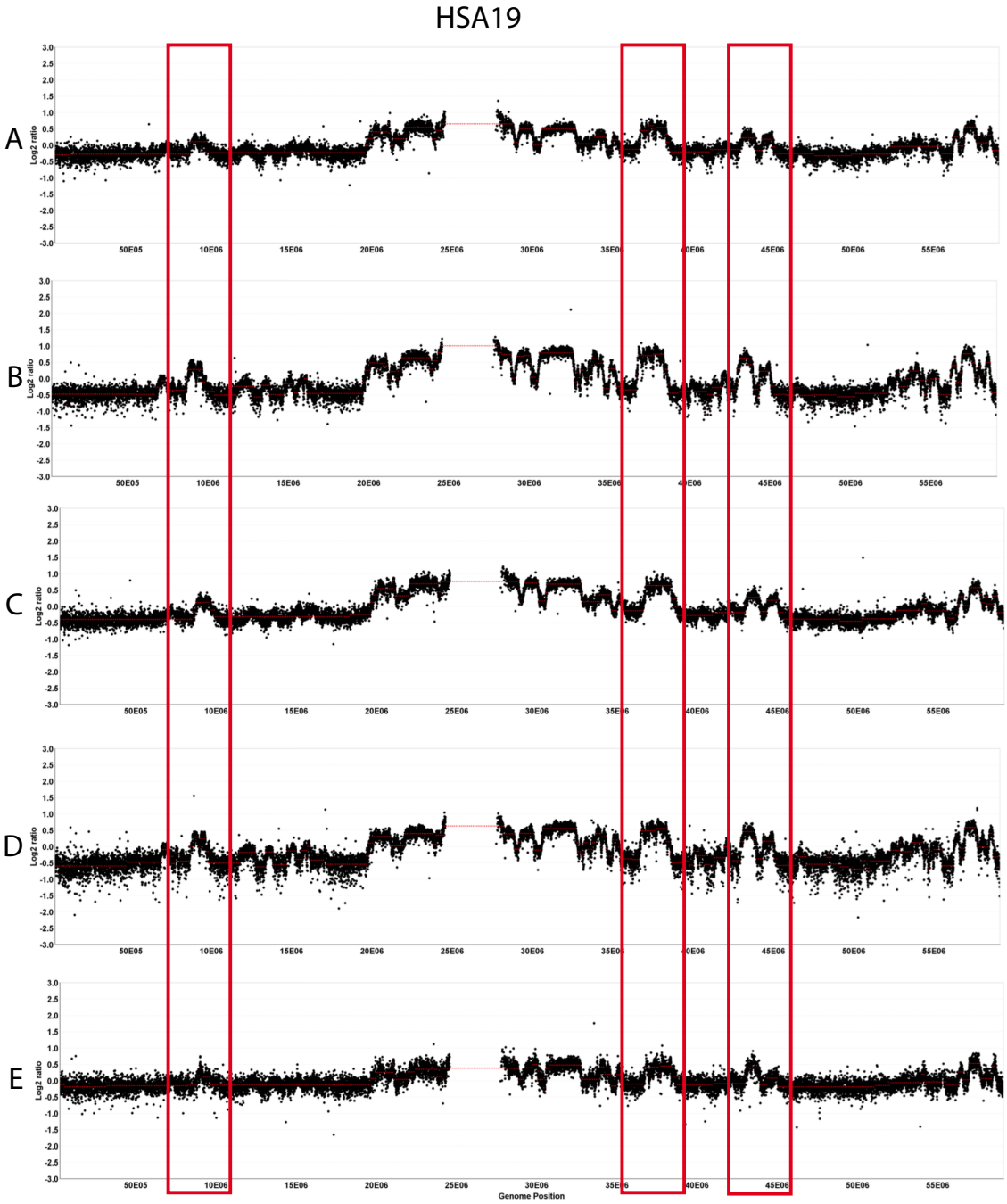

Figure 2.8 – Array CGH analysis of nucleolus-associated DNA prepared by using different nucleolus isolation methods.
Normalized microarray data from CGH arrays are illustrated. Nucleolus-associated DNA was hybridized against non nucleolar-DNA on two-colour Human CGH 4.2M Whole Genome Tiling Arrays. Positive values indicate an enrichment of this genomic region in nucleolus-associated DNA, negative values indicate a depletion. A snapshot from chromosome 19 is shown. Nucleoli were purified with cross-linking (A, B), or under native conditions using a two-step (C) or a one-step protocol (D, E). The gap represents unmapped centromeric regions. Red rectangles were added for orientation.

2.1.3 Isolation of nucleoli to analyze histone post-translational modifications (PTM) from HeLa cells

In order to characterize nucleolus-associated chromatin with respect to histone PTMs, nucleoli were isolated from HeLa cells in parallel with different approaches. The resulting nucleolar fractions containing the histones were analyzed by SDS-PAGE. On the one hand nucleoli were isolated from formaldehyde cross-linked cells and subsequent fractionation (protocol (A) in 2.1.2). There an aliquot was set aside after the first round of sonication (dirty nucleoli = 'dNo') and isolated nucleoli were also collected for subsequent analyses ('No'). On the other hand nucleoli were isolated under native conditions (protocol (B) described in 2.1.2). During this procedure one aliquot was set aside from purified nuclei ('N2') and clean nucleoli were also collected ('No'). All collected fractions were subjected first to SDS-PAGE and Coomassie staining.

Histones were clearly visible on a Coomassie stained SDS-polyacrylamid gel and no gross difference was observed concerning their quality (Figure 2.9).

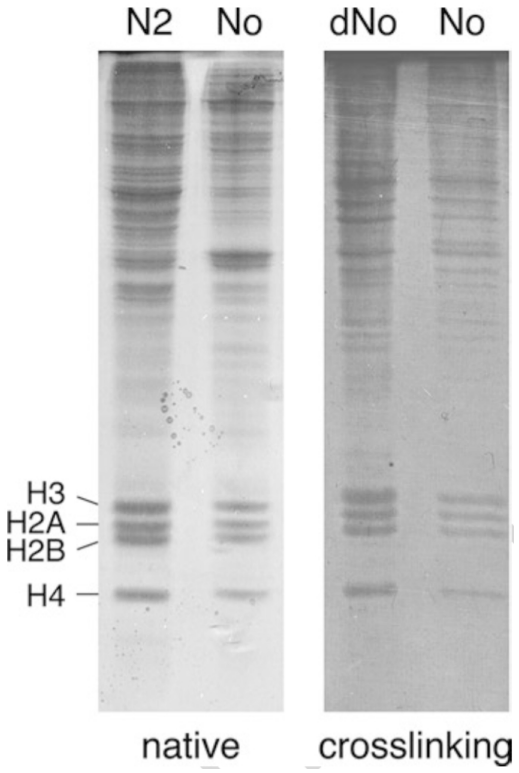

Figure 2.9 – Comparison of histones from different fractions of nucleolus preparations by Coomassie staining of SDS-polyacrylamide gels.
The protein fractions were separated on 17.5 % SDS-PAGE. Proteins from purified nuclear ('N2') and nucleolar ('No') fractions of nucleolus isolation under native condition are shown on the left side. Proteins from dirty nucleolar ('dNo') and nucleolar ('No') fractions of nucleolus isolation under cross-linking condition are shown on the right side. Histone proteins are indicated by their names.

This study focused on identifying the effects of the two different isolation procedures on the N-terminal tail of histone H4 with respect to their acetylation. Histone acetyltransferases and deacetylases are inactivated when cells are fixed with formaldehyde and their diffusion is limited in cross-linked cells, but may be still active during native preparations. This is why purifications were also performed in the presence of sodium butyrate, an inhibitor of histone deacetylases (Candido et al., 1978).

In addition, the effect of heat-mediated reversal of the cross-linking was tested. Formaldehyde is a cross-linking reagent, which works at short distances (down to 2 Å) and its interaction with proteins and nucleic acids is reversible by heat. It efficiently cross-links protein with DNA, protein with RNA and protein with protein. It is therefore very suitable to analyze histone PTMs at different genomic loci. It is important to revert the cross-link at 65 $°C$ before mass spectrometry analysis are performed, to obtain identifiable peptides after protease digestions and thus interpretable data. This incubation will also lead to an induction of heat-mediated loss or change of histone PTMs and a balance of reverting the cross-link and maintaining PTMs must be achieved. To test this, the final nucleolar fraction was split into five different aliquots which were incubated at 65 $°C$ for 0h, 1h, 2h, 4h and 8h.

Isolated nucleolar fractions were subjected to SDS-PAGE and stained with Coomassie. Then the effects of both isolation procedures, the effect of the inhibitor of histone deacetylases and of different times of heat-induced reversal of the cross-link were investigated analyzing the N-terminal tail of histone H4 in mass spectrometry experiments by A. Villar-Garea (Dillinger et al., 2014). The results revealed that formaldehyde cross-linking and 1h heat reversal of cross-links represent the best conditions for histone PTM analyses.

2.1.4 Single-cell analyses of nucleolar morphology and nucleolus-associated tandem repeats in proliferating and senescent IMR90 cells

2.1.4.1 Changes in nucleolar morphology during replicative senescence

In order to evaluate senescent-associated changes in nucleolar morphology and number, proliferating and senescent IMR90 cells were fixed with formaldehyde and stained for B23 by immunofluorescence. B23 is a marker for the granular component of the nucleolus and labels the whole nucleolus, which makes it very suitable for this type of analyses. Figure 2.10 illustrates a representative young, proliferating (left) and a senescent (right) IMR90 cell nucleus, where the proliferating cell exhibits three nucleoli and the senescent cell a single, large nucleolus. This observation was quantitatively assessed in the following experiments.

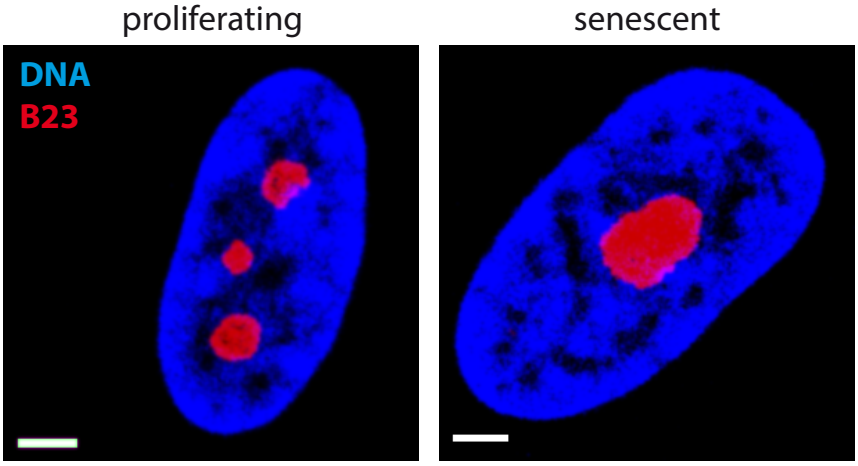

Figure 2.10 – Mid-sections of representative confocal microscope images of proliferating and senescent IMR90 cell nuclei.
Proliferating and senescent IMR90 cells were fixed with formaldehyde and stained with an antibody labeling the granular component of the nucleolus (B23) and DNA was counterstained with DAPI. Proliferating cells are characterized by a median of three nucleoli whereas senescent cells are characterized usually by complete fusion of nucleoli which results in one nucleolus (right). Nucleoli of proliferating cells are small, but fusing in senescence leads to an enlargement of nucleoli. Z-projections of mid-sections of confocal microscopy images are shown, DNA = blue, nucleolus = red, Scale bar: 1.6 µm.

Immunofluorescence experiments in proliferating and senescent IMR90 cells for four biological replicate experiments were performed and cells were stained for B23 and DAPI. The number of nucleoli per nucleus was counted manually for at least 30 cells of each experiment. Proliferating IMR90 cells contain 3.04 ± 1.23 nucleoli per nucleus in average whereas, when cells enter senescence, nucleoli fuse such that senescent cells contain 1.71 ± 1.1 nucleoli per nucleus (Figure 2.11). The median number of nucleoli is 3 and 1 in proliferating and senescent IMR90 cells, respectively.

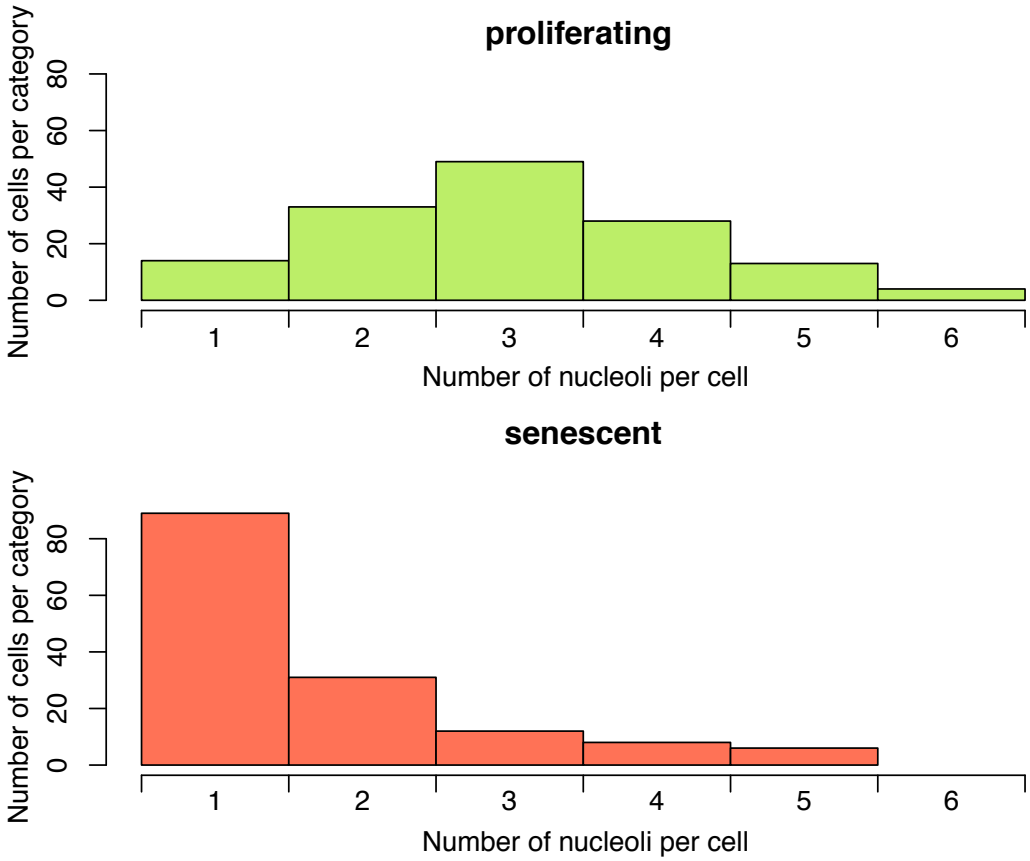

Figure 2.11 – The number of nucleoli decreases during replicative senescence in IMR90 cells.
The number of nucleoli per individual cell was counted and plotted as histogram. Proliferating cells (upper panel, n = 141) contain 3.04 ± 1.23 nucleoli, senescent cells (lower panel, n = 145) contain 1.71 ± 1.1 nucleoli per nucleus.

In addition to evaluating the number of nucleoli, the volume of nucleoli was analyzed. First, the volume of each individual nucleolus was measured. Young, proliferating IMR90 cells have small nucleoli (median = 10 µm^3), whereas nucleoli in senescent IMR90 cells are significantly larger (median = 63 µm^3, t-test: p-value = 5.072 x 10^{-14}, Figure 2.12).

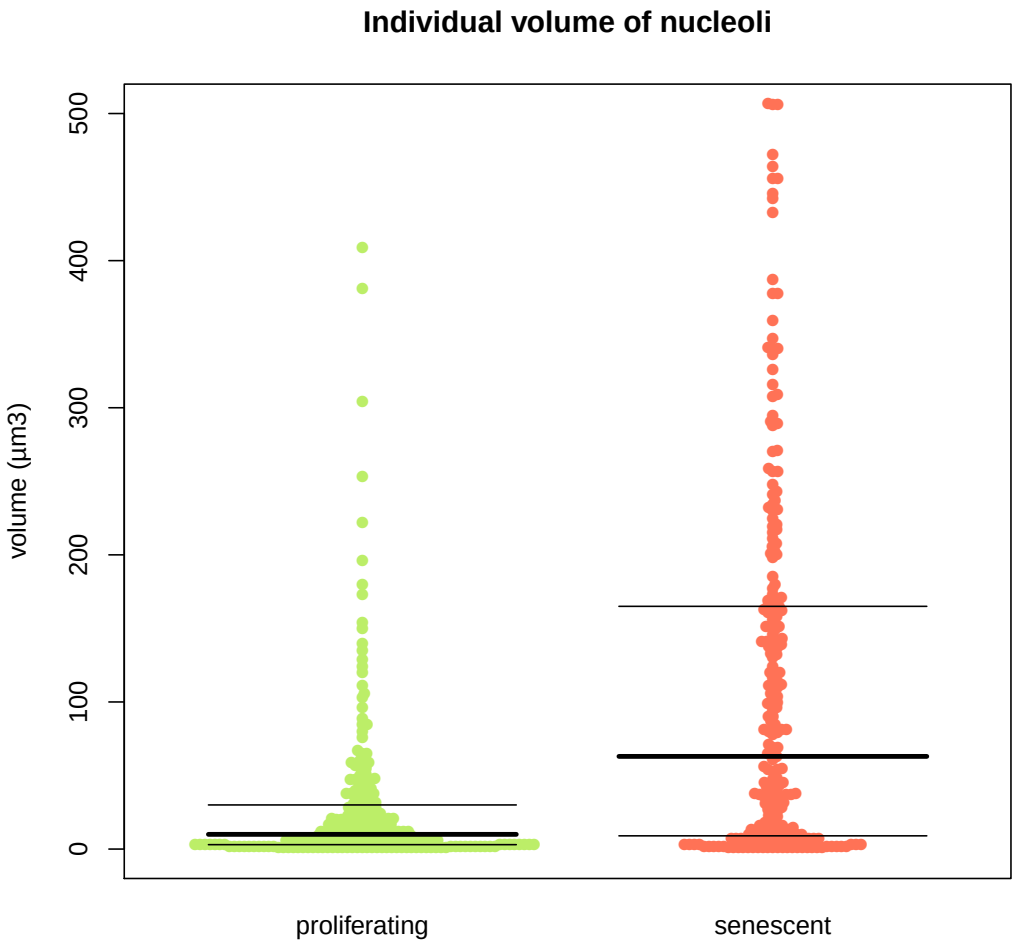

Figure 2.12 – The individual volume of nucleoli increases during replicative senescence in IMR90 cells.
The individual volume of nucleoli was measured after immunostaining of proliferating and senescent IMR90 cells for DAPI and B23 and illustrated as single data point. A boxplot indicates the median (solid line), and the upper and lower quartile (thin lines). Left: proliferating cells (median = 10 µm^3, n = 141), right: senescent cells (median = 63 µm^3, n = 145, t-test: p-value = 5.072 x 10^{-14})

Second, the individual volumes of nucleoli per one nucleus were summed up to give a total nucleolar volume per cell. A typical proliferating cell has nucleoli, which occupy 62 µm^3 (median volume), whereas nucleoli in senescent IMR90 cells occupy a significantly increased volume (median = 161 µm^3, t-test: p-value $<$ 2.2 x 10^{-16}, Figure 2.13).

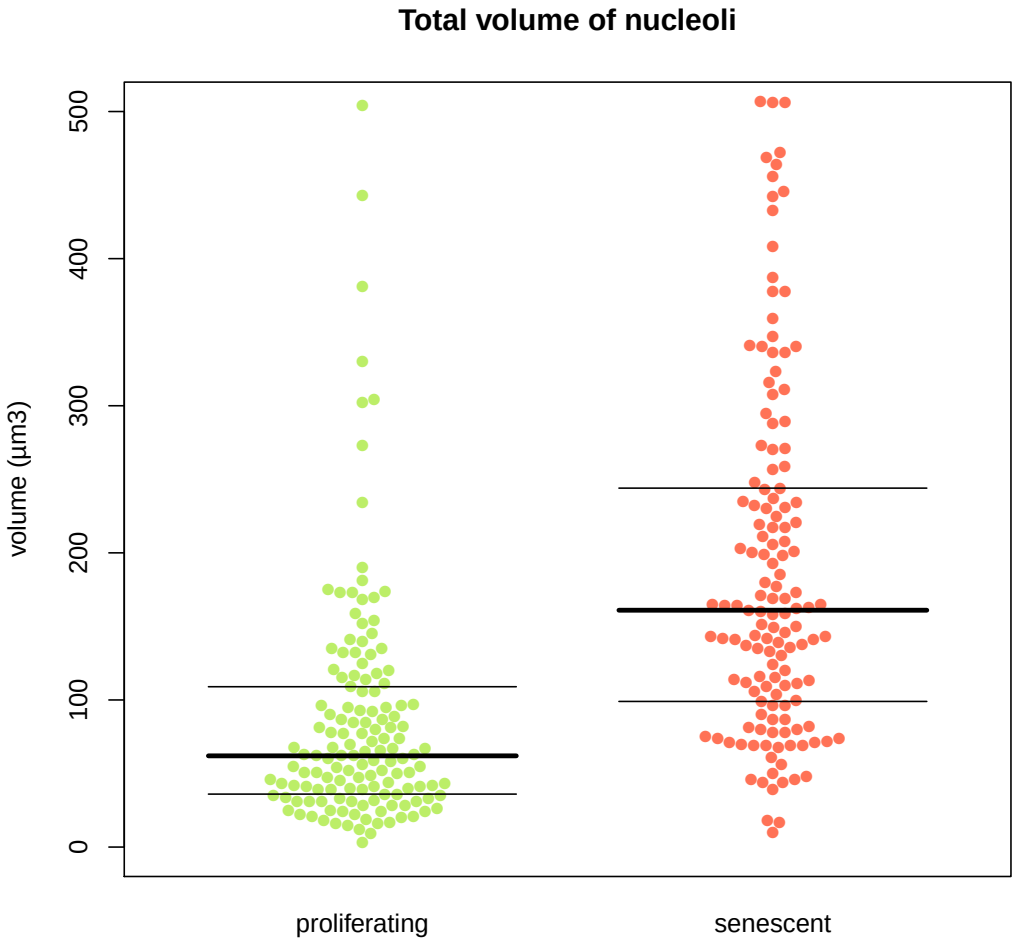

Figure 2.13 – The total volume of nucleoli increases during replicative senescence in IMR90 cells.
Nucleolar volumes per cell, were measured after immunostaining proliferating and senescent IMR90 cells for B23. Data points represent individual cells. A boxplot indicates the median (solid line), and the upper and lower quartile (thin lines). Left: proliferating cells (median = 62 µm^3, n = 141), right: senescent cells (median = 161 µm^3, n = 145 t-test: p-value < 2.2 x 10^{-16})

To investigate, whether the increased size of nucleoli in the nucleolus of senescent IMR90 cells is not just due to an enlargement of nuclei, the relative space which is occupied by nucleoli in proliferating and senescent IMR90 cells was calculated. Therefore the nuclear volume, determined by DAPI-staining, was measured and the relative volume that is occupied by nucleoli was calculated by dividing the total nucleolar volume per cell by the nuclear volume. In proliferating IMR90 cells nucleoli occupy 2.8 % of the respective nuclei, whereas the relative volume that is occupied by nucleoli significantly increases to 6.6 % when cells enter senescence (t-test: p-value < 2.2 x 10^{-16}, Figure 2.14).

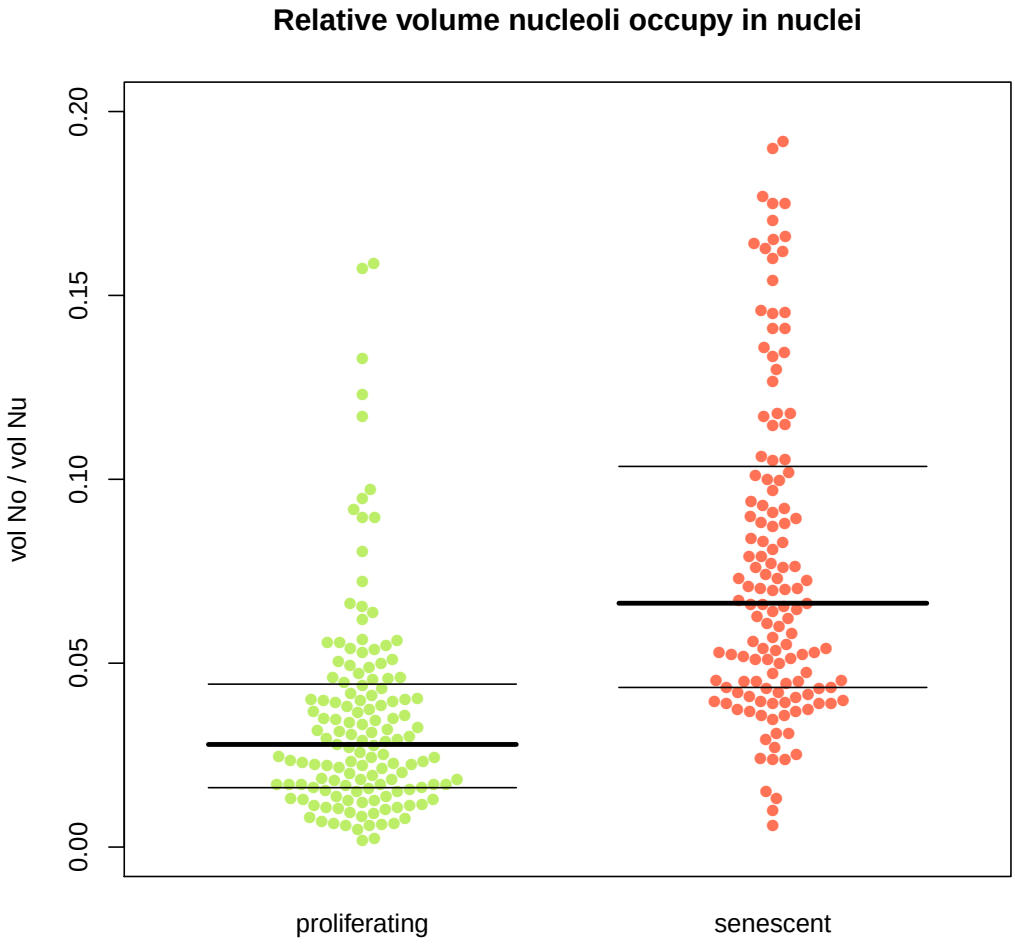

Figure 2.14 – The nuclear space occupied by nucleoli increases during replicative senescence in IMR90 cells.
The relative space that nucleoli occupy in the nucleus was calculated for proliferating and senescent IMR90 cells. Results are illustrated as single data points and a boxplot indicates the median (solid line), and the upper and lower quartile (thin lines). Left: proliferating cells (median = 2.8 %, n = 141), right: senescent cells (median = 6.6 %, n = 145, t-test: p-value $< 2.2 \times 10^{-16}$)

2.1.4.2 Qualitative analyses of the nuclear distribution of histone PTMs during replicative senescence by immunofluorescence

In order to evaluate, whether the senescence-associated changes in nucleolar morphology, where nucleoli are fused and enlarged, also leads to changes in the localization of eu- or heterochromatin, the distribution of the different types of chromatin in the cell nucleus was evaluated. Nucleoli are surrounded by a shell of perinucleolar heterochromatin, which is enriched for pericentromeric repeats and is associated with repressive histone PTMs, such as H3K9 methylation (Németh et al., 2010). H3K9me3 is a marker for constitutive

heterochromatin, whereas H3K9me2 and H3k27me2 are associated with facultative heterochromatin (Barski et al., 2007; Rosenfeld et al., 2009). Furthermore, H3K9ac is found associated with transcription start sites of active genes and thus labels euchromatin (Wang et al., 2008). The distribution of the mentioned histone PTMs was evaluated by immunfluorescence staining of proliferating and senescent IMR90 cells.

Qualitative analyses of the nuclear distribution of H3K27me3 during replicative senescence by immunofluorescence

To investigate the distribution of a marker for facultative heterochromatin, proliferating and senescent IMR90 cells were stained with an antibody labeling the histone PTM H3K27me3. A prominent example for this type of heterochromatin is the inactive X chromosome (Xi), which appears after immunostaining as a strong H3K27me3 signal in the cell. Figure 2.15 illustrates also the large overlap between H3K27me3 and DAPI staining. Since the Xi unites large portions of the fluorescence signal on one distinct area and is localized either to the the nuclear periphery or the perinucleolar space its localization would interfere with the quantification of the distribution of the fluorescence signal. Instead, the association frequency of the Xi with these two areas was investigated (see below).

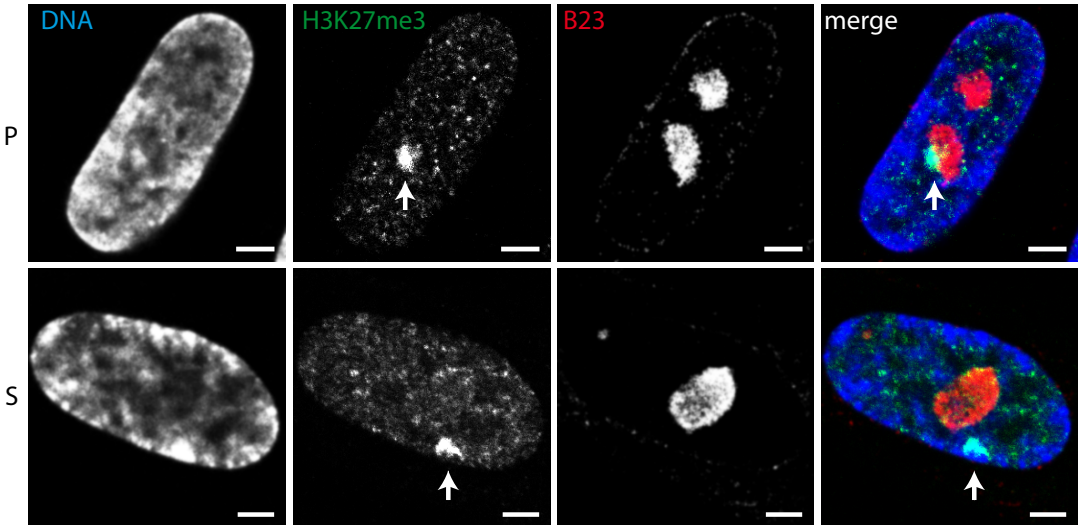

Figure 2.15 – Immunostaining for H3K27me3 in proliferating and senescent IMR90 cells.
Proliferating and senescent IMR90 cells were fixed with formaldehyde and stained with antibodies against H3K27me3 and the nucleolar marker B23. Mid light-optical sections are shown and Xi is marked with an arrow. Upper panel (P): proliferating IMR90 cells, lower panel (S): senescent IMR90 cells. DNA = blue, H3K27me3 = green, nucleolus = red. Scale bar: 1.6 µm.

Qualitative analyses of the nuclear distribution of H3K9me2 during replicative senescence by immunofluorescence

An additional marker for facultative heterochromatin is H3K9me2. Similar to H3K27me3 a region with dense immunostaining can be observed for H3K9me2 which represents the Xi and co-localizes largely with a DAPI-dense regions (Figure 2.16). As for H3K9me2 the location of the Xi would interfere with the quantification of the H3K9me2 staining, hence no such analysis was performed.

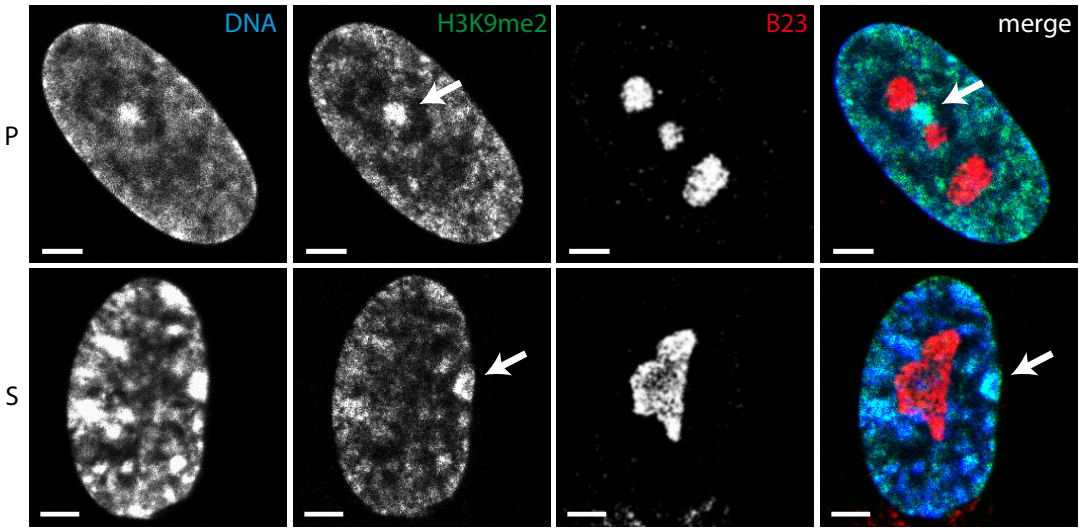

Figure 2.16 – Immunostaining of H3K9me2 in proliferating and senescent IMR90 cells.
Proliferating and senescent IMR90 cells were fixed with formaldehyde and stained with antibodies against H3K9me2 and the nucleolar marker B23. Prominent H3K9me2 signal marks the Xi (arrow). Mid light-optical sections are shown. Upper panel (P): proliferating IMR90 cells, lower panel (S): senescent IMR90 cells. DNA = blue, H3K9me2 = green, nucleolus = red. Scale bar: 1.6 µm.

The Xi chromosome associates more frequently with the nuclear lamina in senescent IMR90 cells than in proliferating ones

Besides qualitative assessment of H3K9me2 and H3K27me3, the intra-nuclear position of the densely stained area labeling the Xi was investigated in proliferating and senescent IMR90 cell nuclei. Therefore, the association of the Xi with either the nucleolus or the nuclear periphery was evaluated. The Xi was counted as being nucleolus-associated when no pixel was detected between the staining of the nucleolus and the staining for the respective histone PTM or they even overlapped. Peripheral association was assumed, when no DAPI stained pixel was present between the Xi and the DAPI-negative cytoplasm. In senescent IMR90 cells the Xi was found more frequently associated (72 %) to the nuclear periphery than in proliferating IMR90 cells (49 %, Figure 2.17).

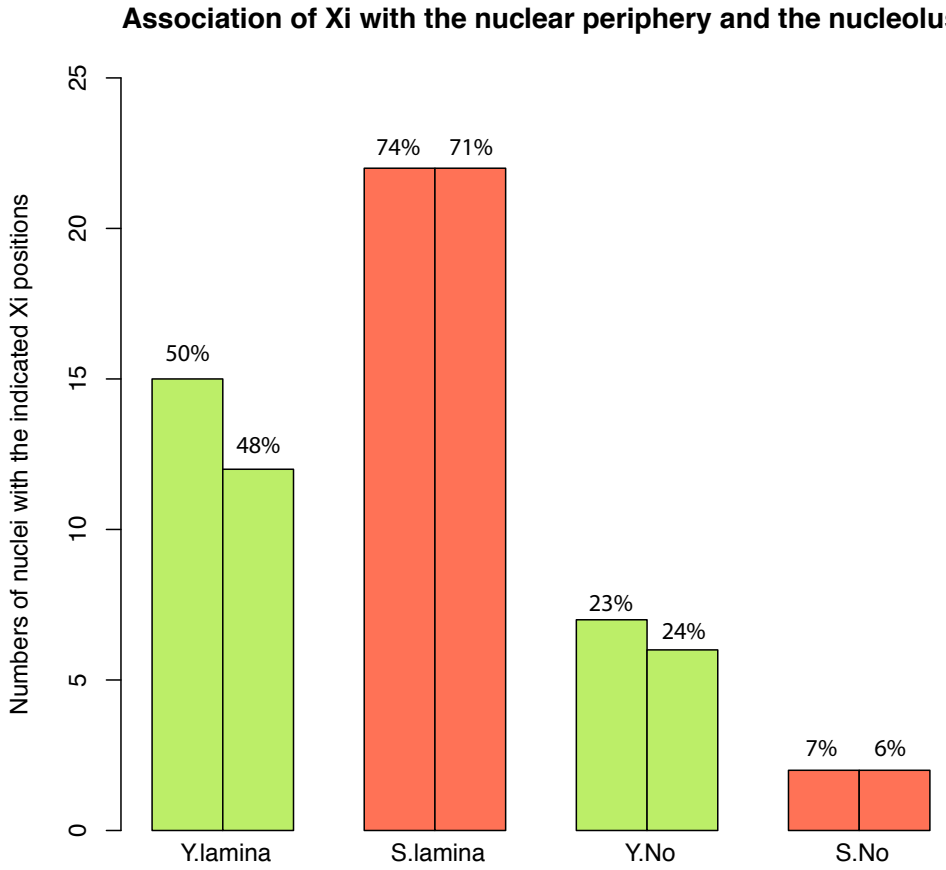

Figure 2.17 – Quantification of the association of Xi to nucleoli or the nuclear periphery in proliferating and senescent IMR90 cells.
The association of the Xi to nucleoli (No) or the nuclear periphery (lamina) was evaluated based on H3K9me2 and H3K27me3-staining of proliferating (green) and senescent (red) IMR90 cells. Hereby, the quantification based on H3K9me2 is represented by the left of the pairwise grouped bars and H3K27me3 by the right one. The Xi is associated more frequently to the nuclear periphery in senescent IMR90 cells. 55 proliferating and 61 senescent IMR90 cells were evaluated.

Qualitative analyses of the nuclear distribution of H3K9ac during replicative senescence by immunofluorescence

In contrast to H3K9me2 and H3K27me3, H3K9ac is found associated to transcription start sites of active genes (Wang et al., 2008). H3K9ac was not detectable in nucleoli and its signal was largely depleted at DAPI-dense regions in both proliferating and senescent IMR90 cells including the perinucleolar space and the nuclear periphery. Furthermore it was also not detectable at a single, prominent site of the nucleus in contrast to he Xi staining of H3K27me3 and H3K9me2 (Figure 2.18).

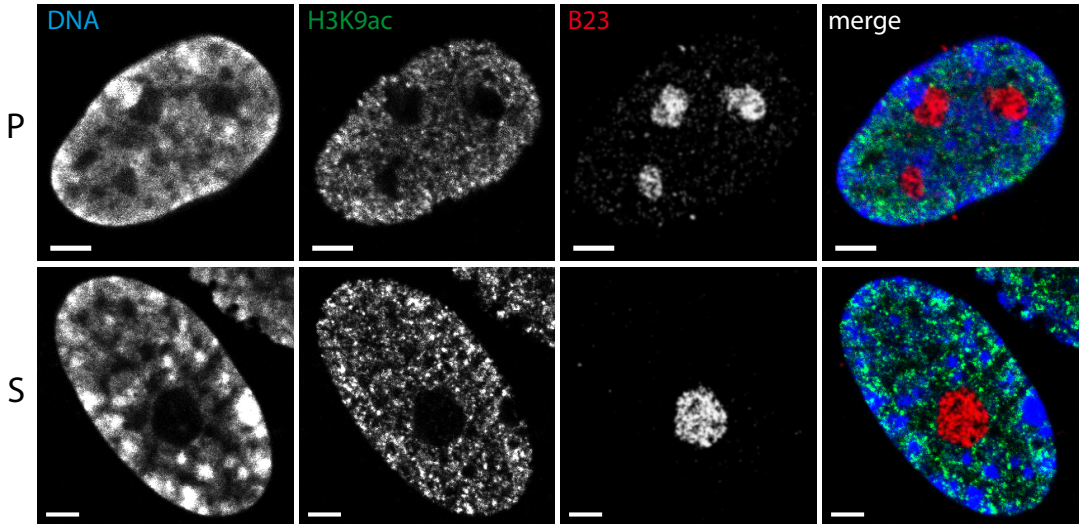

Figure 2.18 – Immunostaining for H3K9ac in proliferating and senescent IMR90 cells.
Proliferating and senescent IMR90 cells were fixed with formaldehyde and stained with antibodies against H3K9ac and the nucleolar marker B23. Mid light-optical sections are shown. Upper panel (P): proliferating IMR90 cells, lower panel (S): senescent IMR90 cells. DNA = blue, H3K9ac = green, nucleolus = red. Scale bar: 1.6 µm.

2.1.4.3 Quantitative immunofluorescence analysis of H3K9me3 in replicative senescence

In order to evaluate senescence-associated changes in the nuclear distribution of heterochromatin during replicative senescence, IMR90 cells were fixed with formaldehyde and stained for H3K9me3, a marker for constitutive heterochromatin (Figure 2.19). Confocal microscopy images were recorded and mid light-optical sections were subsequently analyzed. To evaluate the distribution of heterochromatin in the cell nucleus this analysis focused on the two main areas where heterochromatin is predominantly localized in human cells, the perinucleolar space and at the nuclear periphery. The perinucleolar space was defined as the area that forms within 240 nm outside of the nucleolus, as marked by B23/nucleophosmin immunostaining. The nuclear periphery was defined as the area that forms within 240 nm from the edge of the DAPI staining.

First, the relative amount of immunofluorescence intensity in the respective areas compared to the amount of immunofluorescence intensity in the whole nucleus was calculated. Second, the coefficient of variation (C.V.), which gives an indication of the heterogeneity of the staining in the respective areas (Zhang et al., 2015), was calculated and compared. Last, the distribution of the strongest H3K9me3 stained areas was evaluated. Areas that exhibit a high density of heterochromatin, such as centromeric and pericentromeric regions, appear as strongly stained H3K9me3 regions. Hence, monitoring the brightest pixels will give an impression about the distribution of the most heterochromatic regions.

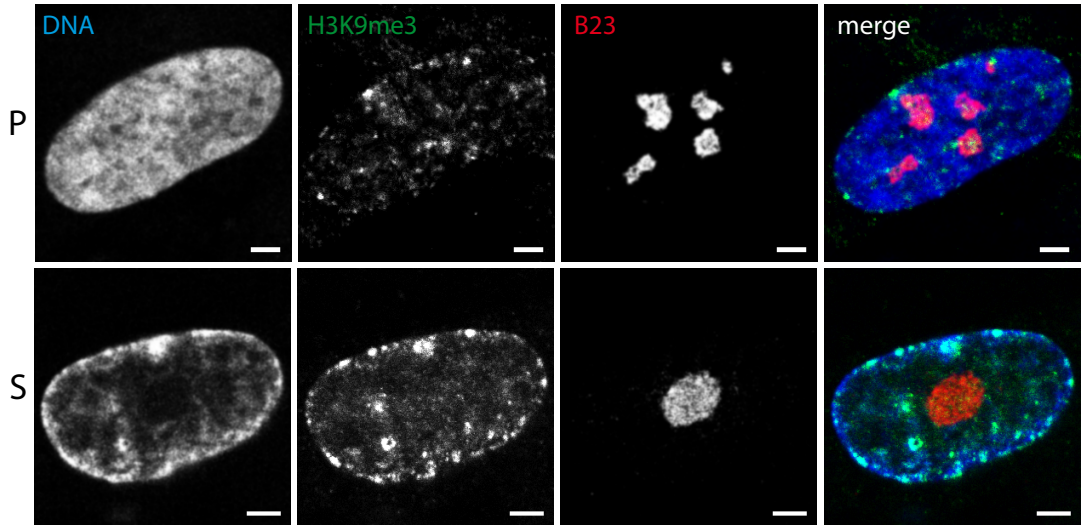

Figure 2.19 – Immunostaining for H3K9me3 in proliferating and senescent IMR90 cells.
Proliferating and senescent IMR90 cells were fixed with formaldehyde and stained with an antibody for H3K9me3. Mid light-optical sections are shown. Upper panel (P): proliferating IMR90 cells, lower panel (S): senescent IMR90 cells. DNA = blue, H3K9me3 = green, nucleolus = red.

The relative immunofluorescence signal of H3K9me3 decreases in the perinucleolar space in senescent IMR90 cells.

First, the relative immunofluorescence signal intensity in the perinucleolar space as well as at the nuclear periphery was measured. Therefore, the intensities of all pixels in the area of interest were summed up and the ratio was calculated compared to the total nuclear fluorescence intensity. There was a little, but significant difference between the relative fluorescence intensity in proliferating compared to senescent IMR90 cells (9.5 % vs 8.4 %, t-test: p-value = 0.0017) at the nuclear periphery. In contrast, relative immunofluorescence intensities decreased more remarkable from 5.2 % to 2.2 % at the perinucleolar space during cellular senescence (t-test: p-value $< 2.2 \times 10^{-16}$, Figure 2.20).

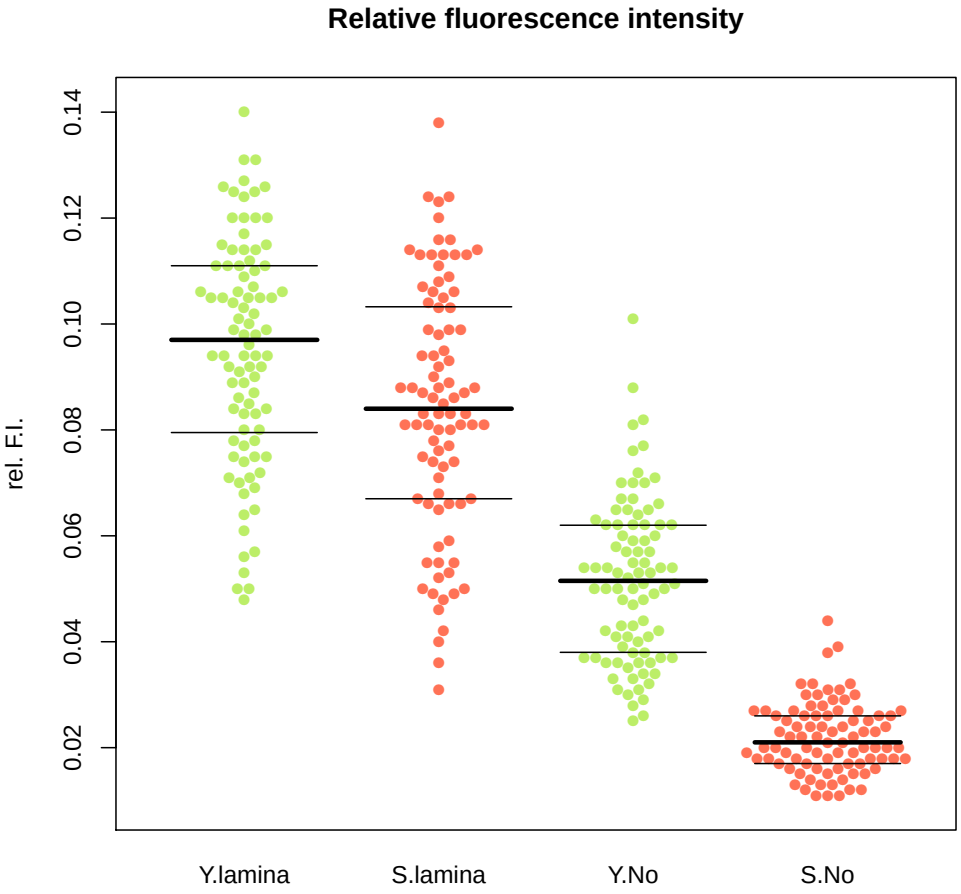

Figure 2.20 – Relative amounts of H3K9me3-labeled constitutive heterochromatin at the perinucleolar space and nuclear periphery of proliferating and senescent IMR90 cells.
Proliferating and senescent IMR90 cells were stained for H3K9me3 and the relative immunofluorescence intensities were measured at the nuclear periphery (lamina) and at the perinucleolar space (No). Values measured in proliferating cells ('Y') are shown in green, values measured in senescent cells ('S') are shown in red. Results are illustrated as single data points and a boxplot indicates the median (solid line), and the upper and lower quartile (thin lines). Median: Y.lamina = 0.095, S.lamina = 0.084, t-test: p-value = 0.0017; Y.No = 0.052, S.No = 0.022, t-test: p-value $< 2.2 \times 10^{-16}$. n = 88.

The heterogeneity of H3K9me3-staining increases significantly in senescent IMR90 cells at the nuclear periphery and globally in the nucleus in contrast to the perinucleolar space

Next, the heterogeneity of the staining in the whole nucleus, at the nuclear periphery and the perinucleolar space was evaluated. Hence, the mean and the standard devia-

tion of the fluorescence intensity were measured and the coefficient of variation ($C.V. = \frac{standard\ deviation}{mean}$) was calculated. The staining in the whole nucleus was significantly more heterogeneous in senescent than in proliferating IMR90 cells (0.677 vs 0.573, t-test: p-value = 2.6 x 10^{-8}). The mean C.V. at the nuclear periphery in senescent cells was slightly higher than in proliferating cells (0.709 compared to 0.632, t-test: p-value = 0.0008). In contrast, at the perinucleolar space the C.V. values did not differ significantly in proliferating and senescent cells (0.555 compared to 0.576, t-test: p-value = 0.284, Figure 2.21).

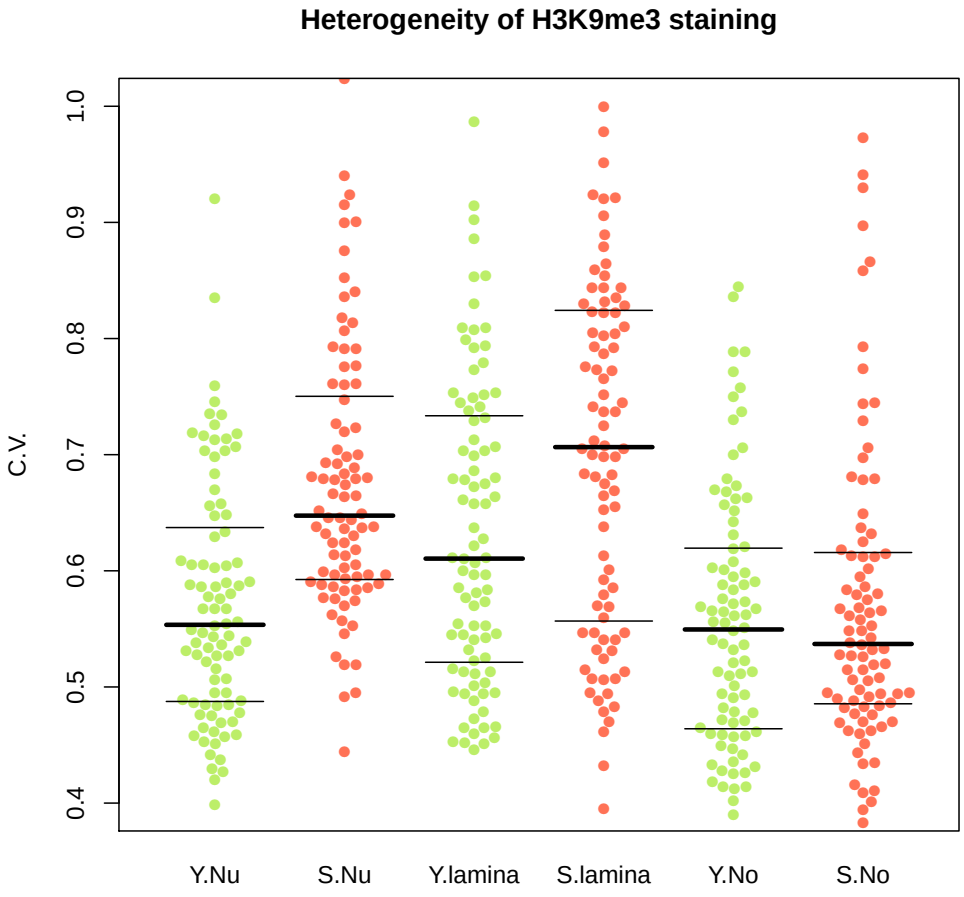

Figure 2.21 – Heterogeneity of heterochromatin in different areas of the nucleus of proliferating and senescent IMR90 cells.
Proliferating and senescent IMR90 cells were stained for H3K9me3 and the heterogeneity of staining was calculated as coefficient of variation (C.V.) for the total nucleus (Nu), the nuclear periphery (lamina) and the perinucleolar space (No). Values measured in proliferating cells ('Y') are shown in green, measured in senescent cells ('S') are shown in red. Results are illustrated as single data points and a boxplot indicates the median (solid line), and the upper and lower quartile (thin lines). Median: Y.Nu = 0.573, S.Nu = 0.677, t-test: p-value = 2.6 x 10^{-8}; Y.lamina = 0.632, S.lamina = 0.709, t-test: p-value = 0.0008; Y.No = 0.555, S.No = 0.576, t-test: p-value = 0.284. n = 88.

The abundance of the strongest H3K9me3 immunofluorescence signals decreases in the perinucleolar space in cellular aging

Next, the abundance of the most heterochromatic regions in the perinucleolar space and the nuclear periphery was evaluated. Therefore the image containing the H3K9me3-labeled heterochromatin was segmented by thresholding it with a value of 10 %. In the resulting image, the presence of heterochromatin was measured in the perinucleolar space and at the nuclear periphery. Here, the most prominent differences were visible. While the abundance of the brightest pixels, which represent the most heterochromatic regions, did not change significantly at the nuclear periphery (0.157 vs 0.137, t-test: p-value = 0.066), it strongly decreased at the perinucleolar space (0.056 vs 0.013, t-test: p-value = 2.09 x 10^{-9}, Figure 2.22).

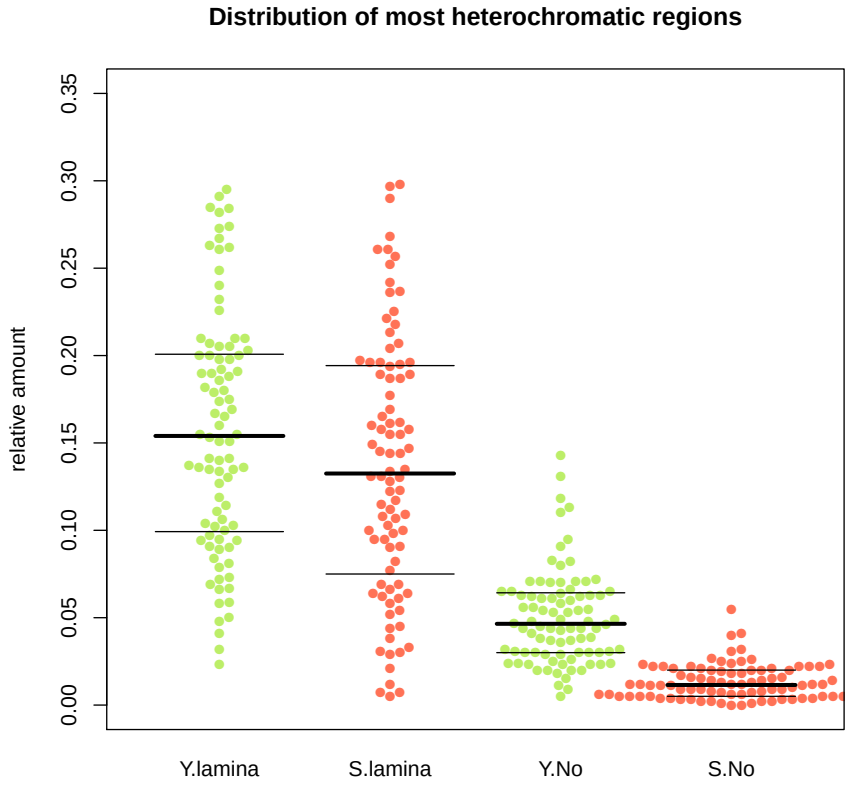

Figure 2.22 – Distribution of most heterochromatic regions in the nucleus of proliferating and senescent IMR90 cells.
Proliferating and senescent IMR90 cells were stained for H3K9me3 and the 10 % brightest pixels were selected. Then the distribution of these pixels was quantified at the nuclear periphery (lamina) and the perinucleolar space (No). Ratios were calculated compared to the whole nucleus. Values measured in proliferating cells ('Y') are shown in green, measured in senescent cells ('S') are shown in red. Results are illustrated as single data points and a boxplot indicates the median (solid line), and the upper and lower quartile (thin lines). Y.lamina = 0.157, S.lamina = 0.137, t-test: p-value = 0.066; Y.No = 0.056, S.No = 013, t-test: p-value = 2.09 x 10^{-9}. n = 88.

2.1.4.4 3D-FISH analysis of tandem repeat arrays in replicative senescence

In order to analyze the localization of repetitive regions of the genome which were shown to be major building blocks of NADs (Németh et al., 2010) and are not represented on CGH-microarrays, different probes labeling such sequences were selected and hybridized on fixed proliferating and senescent IMR90 cells in 3D FISH-experiments.

First, a probe labeling the rDNA was selected to monitor the location of the rDNA in proliferating and senescent cells and to test whether whole NORs get inactivated during cellular senescence, which would lead to their disassociation from nucleoli. Due to the large amount of rRNA that is produced from the coding region, a probe labeling the intergenic spacer was selected to avoid cross-hybridization signals. Second, a BAC labeling the distal junctions (DJs) of NORs was selected. This region was shown to localize to nucleoli and serve as an anchor for single NORs (Floutsakou et al., 2013). Next, a LNA-probe labeling satellite-2 repeats was selected. These repeats were shown to be a major component of nucleolus-associated domains. In addition, they are heavily decondensed in senescent cells (Swanson et al., 2013). Last, another LNA-probe for telomeric regions was selected, because subtelomeric regions were also found to associate frequently to nucleoli and telomere shortening is another feature of replicative senescence.

3D immuno-FISH analysis of rDNA in proliferating and senescent IMR90 cells

Two probes, named Hr4 and Hr6 labeling parts of the intergenic spacer of the rDNA (location illustrated in Figure 2.23), were labeled with either biotinylated dUTP or dUTP-Cy3.

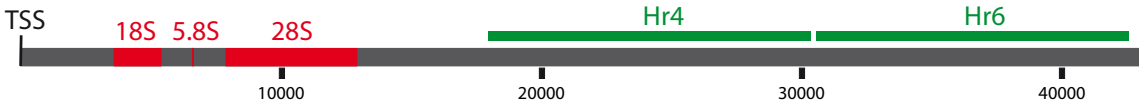

Figure 2.23 – Locations of rDNA BACs Hr4 and Hr6 on the rDNA array.
Illustration of the relative location of probes labeling parts of the intergenic spacer Hr4 and Hr6 (green) on the rDNA repeat unit. rRNA parts are indicated in green and positions relative to the transcription start site (TSS) are marked (black).

Both probes were tested first on metaphase chromosomes. Signals for Hr4 were well visible as bright signals (Figure 2.24 A,E). In contrast, Hr6-signals could not be distinguished from the background, when labeled with biotin (Figure 2.24 D) and did not improve enough when labeled with Cy3 (Figure 2.24 B,D). Hence, Hr4-Cy3 was used for further experiments.

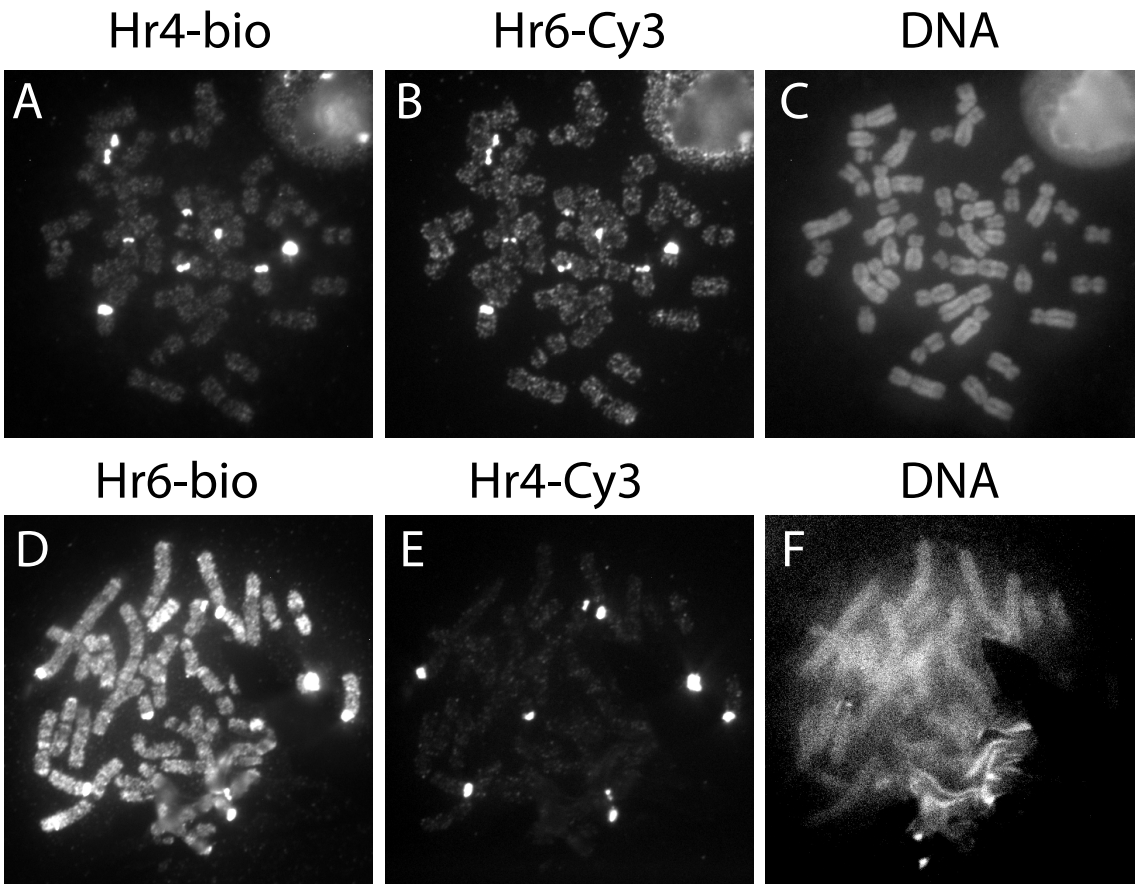

Figure 2.24 – Metaphase-FISH experiments with rDNA probes.
Hr4 (A, E) and Hr6 (B, D) were labeled in two different ways (biotin and Cy3, as indicated) and hybridized together on lymphocyte metaphase chromosomes. DNA staining is shown on the right side (C, F).

Figure 2.25 illustrates a strong rDNA staining inside the nucleoli of proliferating cells, whereas rDNA staining in senescent cells is weaker and some background staining is also visible outside of the nucleoli. Although the quality of staining was slightly weaker in senescent cells, the result clearly showed that the majority of the rDNA signal is intranucleolar in both proliferating and senescent cells. The lack of strong extranucleolar signals suggests that there is no entirely inactive NOR present in these cells.

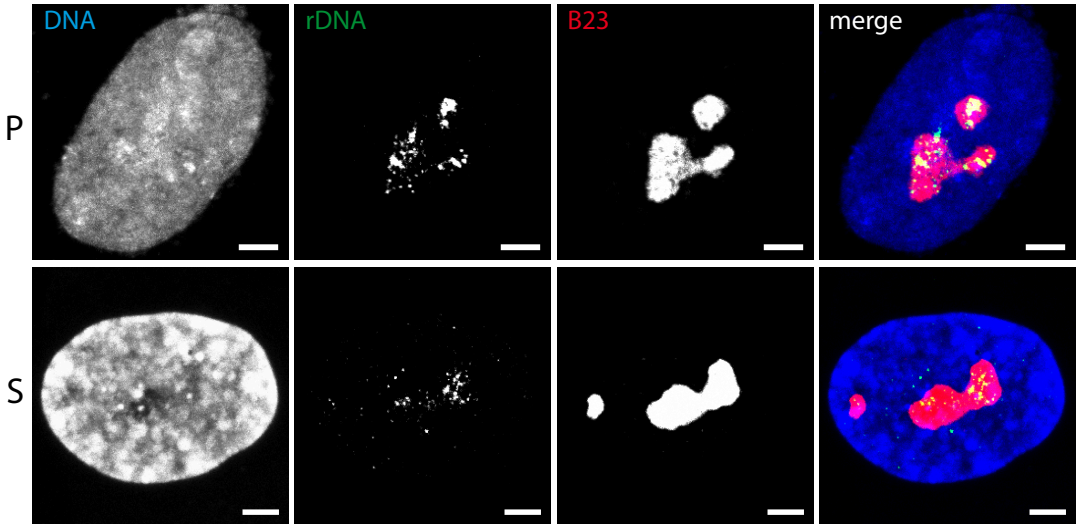

Figure 2.25 – 3D-FISH analysis of rDNA in proliferating and senescent IMR90 cells.
Proliferating and senescent IMR90 cells were fixed for FISH experiments and hybridized with a probe labeling the intergenic spacer of the rDNA. z-projections of confocal microscopy images are shown. Upper panel (P): proliferating cells, lower panel (S): senescent cells. DNA = blue, rDNA = green, nucleolus = red. Scale bar: 1.6 µm.

The rDNA repeats are located between the heterochromatic satellite repeat sequences at centromeres and telomeres. However, distal and proximal junctions are the direct flanking regions of the rDNA (see Introduction, Figure 1.8). The distal junction (DJ) was found to be localized to the periphery of nucleoli and has a complex genomic architecture and transcriptional activity, suggesting an involvement in nucleolar organization (Floutsakou et al., 2013). A BAC clone containing DJ sequences was biotinylated and hybridized on metaphase chromosomes. The hybridization signals localized primarily to the short arms of acrocentric chromosomes (Figure 2.26).

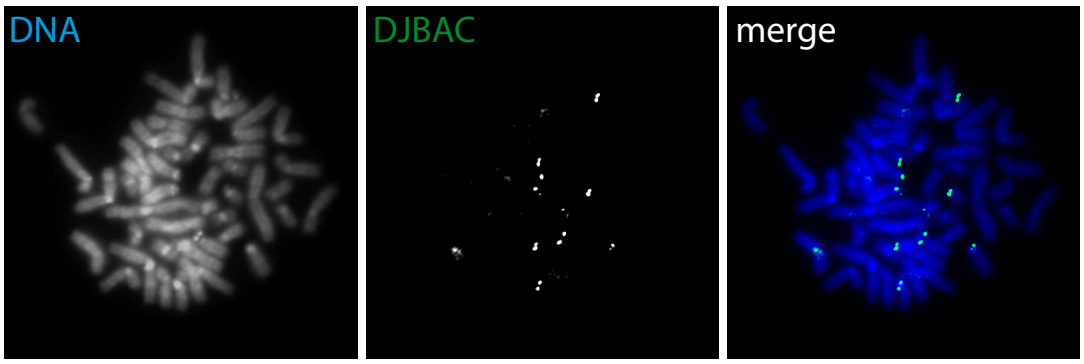

Figure 2.26 – Metaphase-FISH experiments of DJBAC DNA.
DJBAC DNA was labeled with biotinylated dUTP and hybridized on metaphase chromosomes. DNA = blue, DJBAC = green.

Subsequent 3D immuno-FISH experiments showed the co-localization of the most prominent DJ signals with nucleoli in proliferating and senescent IMR90 cells indicating that the distal junction remains nucleolus associated during cellular aging (Figure 2.27). Weaker, secondary signals were also visible, which could arise from genomic regions, which share segmentally duplicated fragments with the DJs of NORs.

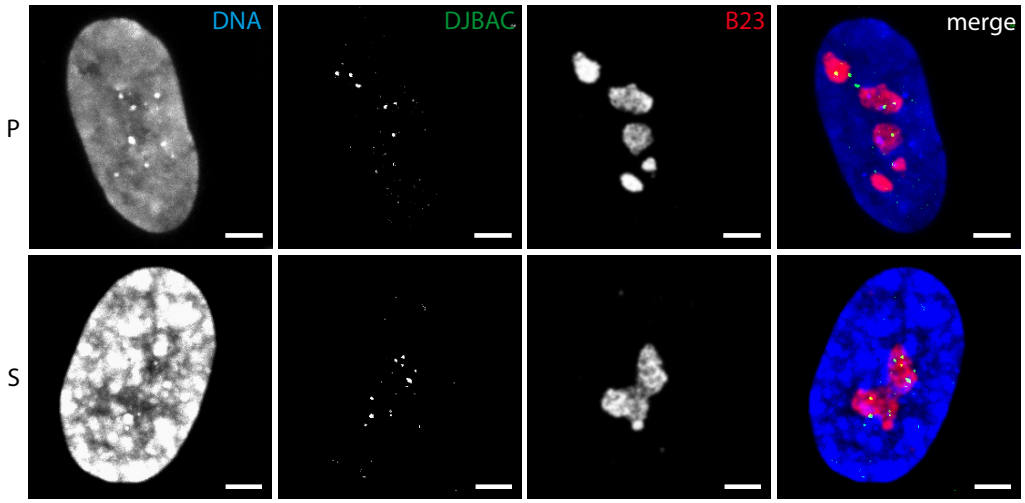

Figure 2.27 – 3D-FISH experiment of the distal junction of NORs in proliferating and senescent IMR90 cells.
IMR90 cells were fixed for FISH experiments and hybridized with a probe labeling the distal junction of the rDNA. z-projections of confocal microscopy images are shown. Upper panel (P): proliferating cells, lower panel (S): senescent cells. DNA = blue, DJBAC = green, nucleolus = red. Scale bar: 1.6 µm.

Satellite-2 repeats are decondensed in senescent IMR90 cells

Major pericentromeric satellite-2 clusters are found on chromosome 1, 9 and 16 and are frequently associated to nucleoli. In order to label these repeats, a commercially available, biotinylated LNA probe was used which was previously tested on metaphase chromosomes (Zillner et al., 2015). This probe labeled the 6 individual loci in proliferating IMR90 cells as bright spots, but also some smaller signals are visible in the proliferating cell nucleus, because satellite-2 repeats are one of the most abundant tandem repeats and occur on nearly every chromosome (Figure 2.28, upper panel). In contrast, senescent IMR90 cells showed a dispersed signal throughout the whole nucleus, indicating senescence associated distension of satellites (Figure 2.28, lower panel).

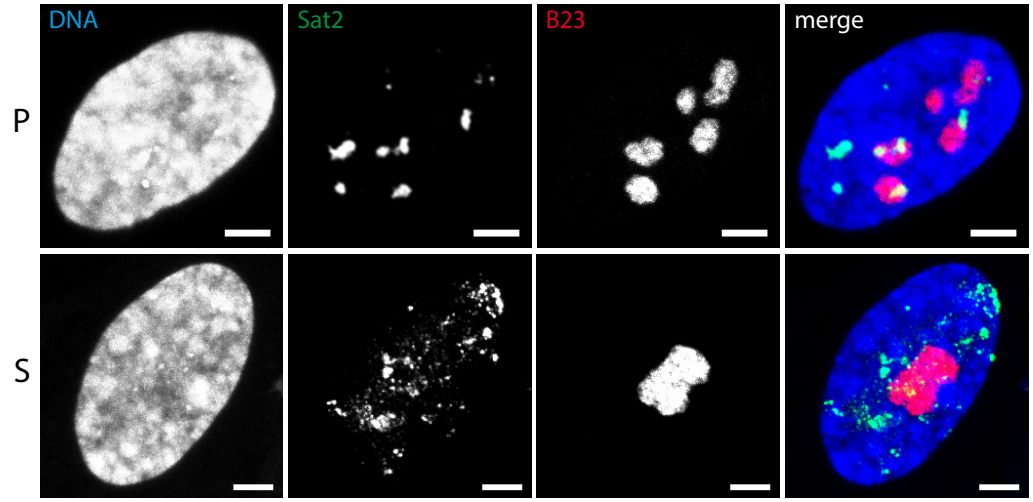

Figure 2.28 – 3D-FISH experiment with satellite-2 probe in proliferating and senescent IMR90 cells.
Proliferating and senescent IMR90 cells were fixed for FISH experiments and hybridized with a probe labeling satellite-2 repeats. z-projections of confocal microscopy images are shown. Upper panel (P): proliferating cells, lower panel (S): senescent cells. DNA = blue, satellite-2 = green, nucleolus = red, . Scale bar: 1.6 µm.

3D-FISH of telomeres in senescent IMR90 cells

In order to monitor alterations in telomere length and nucleolus-association during replicative senescence, a biotinylated LNA probe was used in 3D immuno-FISH experiments.

3D immuno-FISH experiments in proliferating and senescent IMR90 cells and image acquisition were done in parallel. The same image acquisition settings were used for both conditions enabling a direct comparison of the intensities of telomere signals. Telomeres in young, proliferating IMR90 cells were visible as bright spots (Figure 2.29, upper panel), whereas in senescent cells fewer and less bright spots were detected, indicating telomere shortening (Figure 2.29, lower panel). Furthermore, no obvious difference was observed with respect to nucleolus-association or nuclear distribution or clustering of telomeres.

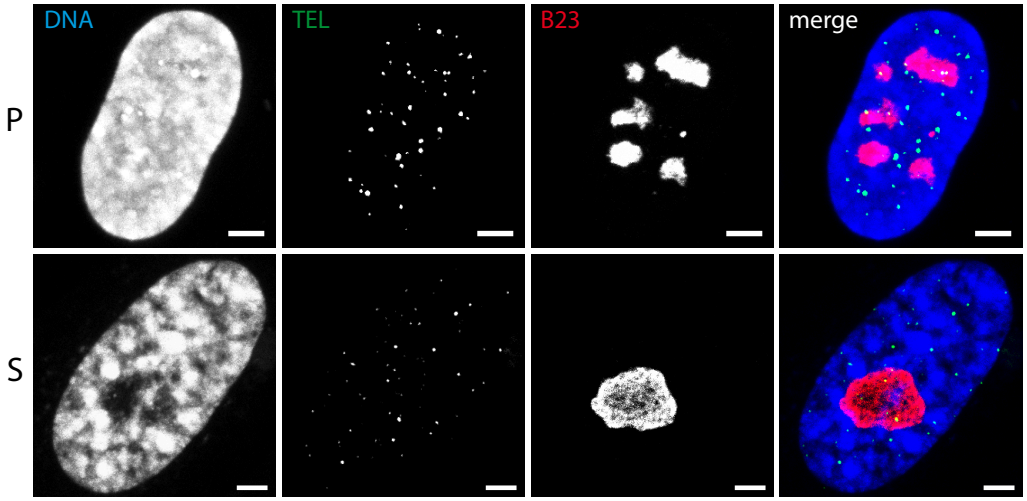

Figure 2.29 – 3D-FISH analysis of telomeres in proliferating and senescent IMR90 cells.
IMR90 cells were fixed for FISH experiments and hybridized with a probe labeling the telomeres. z-projections of confocal microscopy images are shown. Upper panel (P): proliferating cells, lower panel (S): senescent cells. DNA = blue, telomeres = green, nucleolus = red. Scale bar: 1.6 µm.

2.1.5 3D-FISH analysis of NADs in proliferating and senescent cells

In the course of this study nucleolus-associated DNA was isolated from proliferating and senescent IMR90 cells, subjected to CGH microarray analysis and NADs were identified subsequently (see Appendix 6.1). In order to investigate the nucleolus association of selected chromosomal regions using a different experimental approach, 3D immuno-FISH analyses were performed with selected BAC clones that harbor different genomic regions.

First, genomic regions that were already analyzed in studies in HeLa and proliferating IMR90 cells (Németh et al., 2010) were used to test their localization in cellular senescence. Genomic regions that exhibited high or low frequency of nucleolus-association (labeled with BACs RP11-90G23, -173M10, -44B13 and RP11-81M8, respectively) were investigated in this setting. Furthermore, the state of nucleolus association in the region of interest was illustrated as snapshot of normalized microarray data, which was visualized in the Integrated Genome Browser (IGB) (see Section 6.3).

Second, genomic regions were selected based on FISH-experiments performed by Sadaie et al. (2013). They investigated the association of genomic regions to the nuclear lamina in Ras-induced senescence (RIS). Results indicated that some genomic regions lose their association to the nuclear lamina. Moreover, the data suggested that some genomic regions change their localization from the nuclear periphery to the perinucleolar space in this type

of senescence (labeled with BACs RP11-784D7, -638N4). Hence, this two BACs were selected to test, whether the respective genomic regions show a re-localization to the perinucleolar space during replicative senescence.

Third, genomic regions were selected by evaluating snapshots of the normalized microarray data. Here, two regions that were not associated with nucleoli (labeled with BACs RP11-828F4 and -125O21) and one that exhibited a high association frequency to nucleoli (labeled with BAC RP11-914H1) were selected. Furthermore, a biotinylated LNA-probe for the satellite-2 repeats was included as an internal control to monitor the senescence status by the means of senescence-associated distension of satellites (SADS). Further information are provided in the Materials section 4.11.3 and the location of the selected BACs on the chromosomes is illustrated in Figure 2.30.

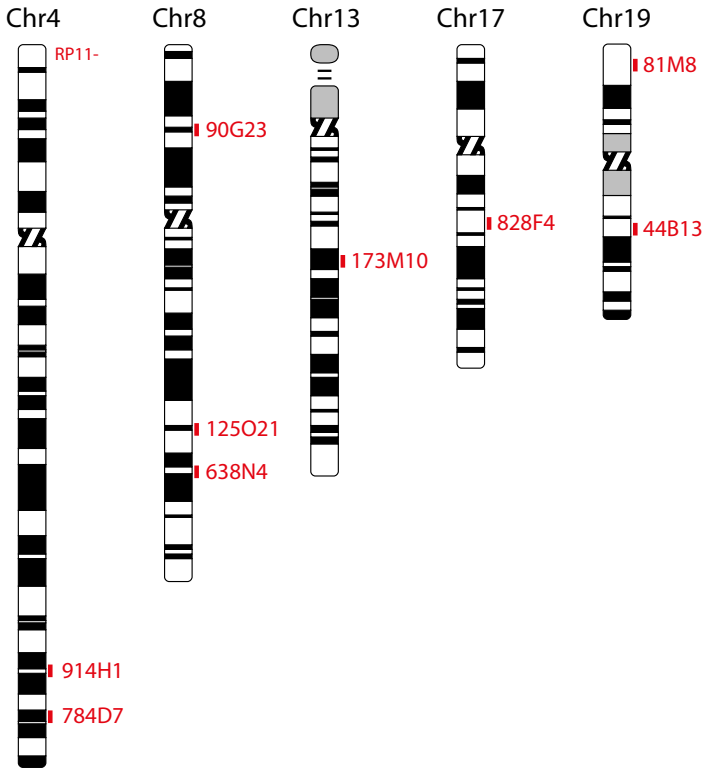

Figure 2.30 – Chromosomal location of BACs used in 3D-FISH experiments. The location of selected genomic regions are marked as red bars next to the ideograms of the respective chromosomes. All BACs are from the RP11 library, the numbers indicate their identification code within this library. Ideograms were taken from http://www.pathology.washington.edu/research/cytopages/idiograms/human/

BACs were labeled by nick-translation, either with biotin, Cy3 or Texas Red. To test the labeling efficiency the BACs were hybridized on metaphase chromosomes. For all BAC-clones strong signals were detected on two alleles without detectable cross-hybridization on other locations (Figure 2.31).

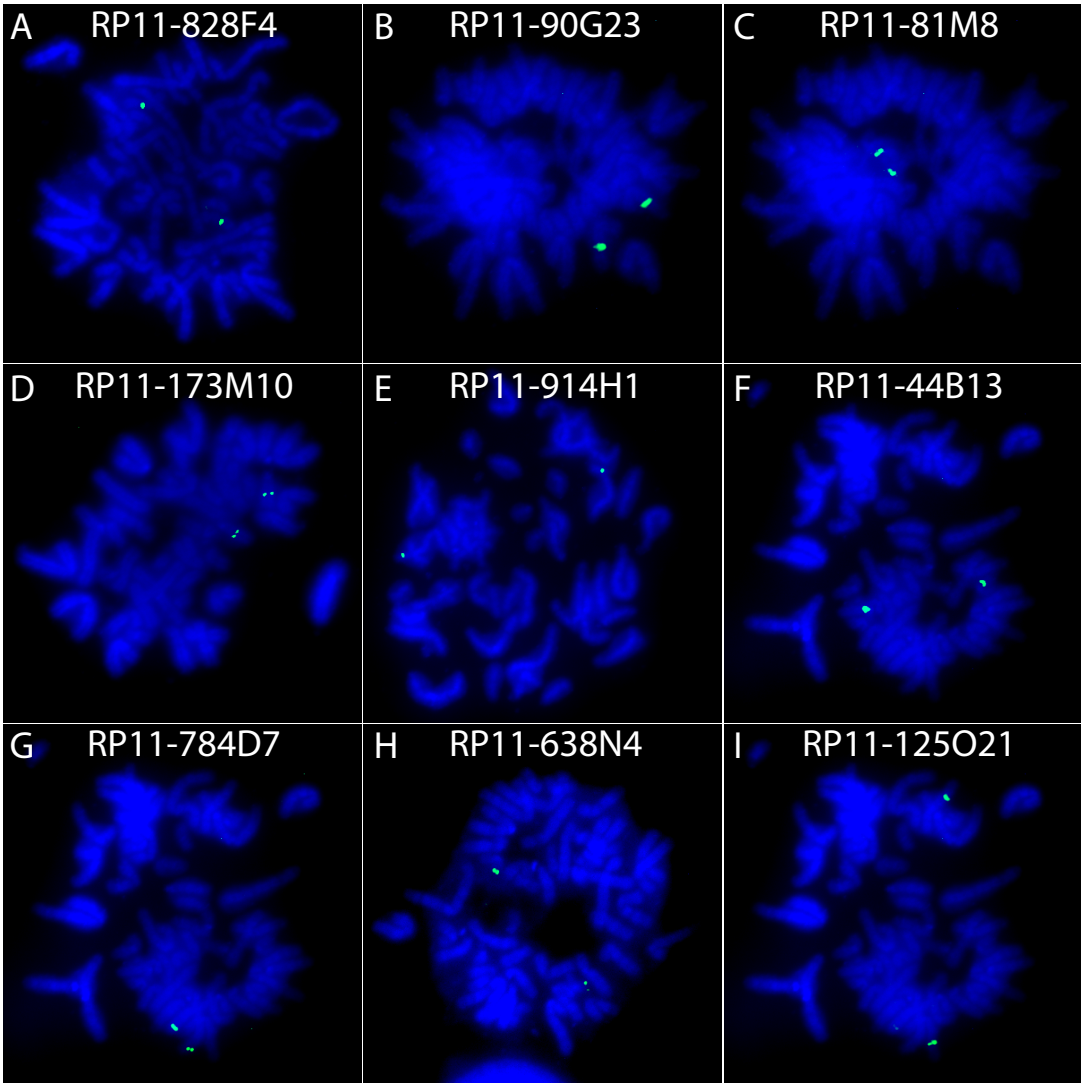

Figure 2.31 – FISH-analysis of selected BACs on metaphase chromosomes. Nine selected BAC clones were labeled with biotin, Cy3 or Texas-Red coupled nucleotides and hybridized on metaphase chromosomes. BACs are indicated in green and DNA in blue.

After the quality of the labeled BAC-clones was validated on metaphase-chromosomes, 3D immuno-FISH experiments were performed in formaldehyde-fixed proliferating and senescent IMR90 cells. A five-colour FISH-experiment was performed, where DNA was labeled with DAPI and the granular component of nucleoli was labeled with B23 and detected with a Cy5-coupled secondary antibody. In addition, 3 of the above described, probes were also hybridized and biotinylated DNA was detected with Alexa-Fluor-488-coupled streptavidin. Figure 2.32 illustrates such a five-colour FISH experiment, where two BACs were hybridized and the biotinylated satellite-2 LNA was included as senescence control. In this experiment one signal of RP11-828F4 associates with nucleoli in proliferating as well as in senescent IMR90. In contrast, no signal of RP11-173M10 was nucleolus-associated neither in proliferating nor in senescent IMR90 cells. Furthermore, a distension of satellite-2 repeats was observed, indicating SADS in senescent IMR90 cells.

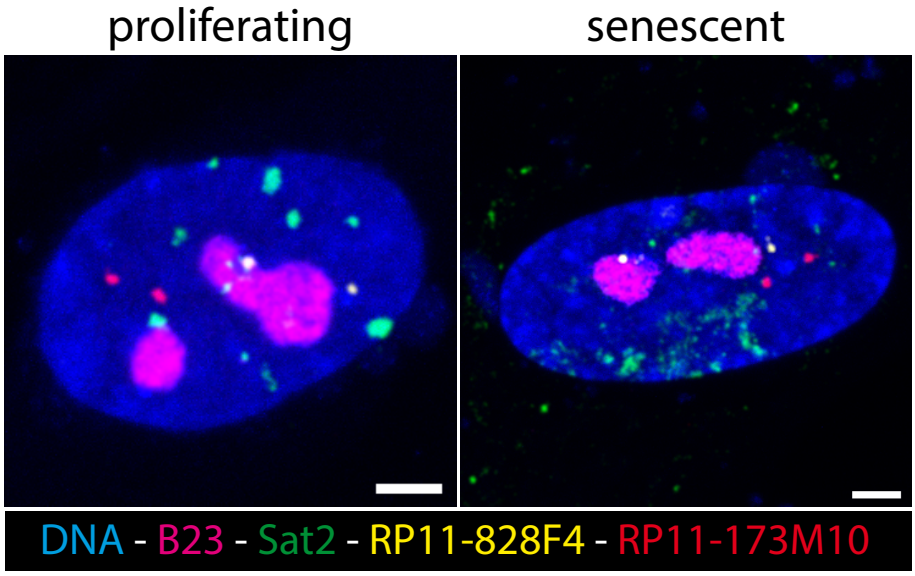

Figure 2.32 – Five colour 3D immuno-FISH analysis of selected genomic regions in proliferating and senescent IMR90 cells.
Representative image of a 5 colour FISH-experiment. DNA is labeled with DAPI, Nucleoli are stained with the nucleolus marker B23, 2 BACs were hybridized and a LNA-probe for satellite-2 was added as senescence control. z-projections of confocal microscopy images are shown. DNA = blue, nucleoli = magenta, Satellite-2 = green, RP11-828F4 = yellow, RP11-173M10 = red. Experiments were carried out in proliferating (left) and senescent (right) IMR90 cells. Scale bar: 1.6 µm.

For data analysis cells were imaged using a confocal laser scanning microscope and the whole nucleus was scanned. Then the localization of the selected regions in 50 proliferating and 50 senescent cells was evaluated. FISH-signals in single cells were considered as being associated to nucleoli, when there was no pixel between the staining of the respective hybridization probe and the staining of the nucleolus or they even overlapped. Furthermore, alleles were considered as being frequently associated to nucleoli, when more than 25 % of the alleles were associated to nucleoli, or not associated, when less than 15 % of them were associated to nucleoli.

Two out of the four probes that were already tested in the former HeLa study showed a high frequency of nucleolus-association. RP11-44B13 was shown to associate to nucleoli and this was also observed in experiments performed in the scope of this study, as 30 % of the alleles in proliferating and 28 % of alleles in senescent cells associated to nucleoli (Figure 2.33 A). This was a little surprising, in light of the microarray data, since this region shows a transition from unassociated to associated status and therefore a lower frequency of nucleolus association (15 % - 25 %) could have been expected (Figure 6.8). RP11-173M10 was shown to associate to nucleoli and this was also observed here, with 33 % nucleolus-association for proliferating and 24 % for senescent cells (Figure 2.33 E). An illustration of the normalized microarray data in the IGB showed the localization of this BAC in a large domain that associates to nucleoli, which is in good agreement with the results of the FISH experiments (Figure 6.6). The remaining two probes of the former

HeLa study exhibited a low frequency of nucleolus-association. For RP11-90G23 only 9 % of the signals in proliferating and 2 % of the signals in senescent IMR90 cells were found associated to nucleoli, which stands in contrast to results of the former experiments where this BAC exhibited a high frequency of nucleolus-association (Figure 2.33 I). Remarkably, the association frequency could not have been predicted based on the normalized microarray data (Figure 6.4) because there is no signal at the genomic region, where this BAC is located. The fourth genomic region labeled with the RP11-81M8 BAC clone was shown to exhibit a low association frequency in the former study and this was also observed in the presented work with 13 % association in proliferating and 12 % association in senescent IMR90 cells. This result is in perfect agreement with the normalized microarray data, as the IGB snapshots clearly show that the indicated region is not associated with nucleoli (Figure 6.5).

The next three genomic regions were selected for FISH analyses based on the normalized microarray data. The RP11-125O21-labeled genomic region was expected to exhibit no nucleolus association since it locates to a large genomic region with no nucleolus association (Figure 6.11). The 3D immuno-FISH analyses resulted in 13 % and 8 % association frequency for proliferating and senescent IMR90 cells, respectively (Figure 2.33 B). Results for the RP-828F4-labeled region indicated a low association frequency and this was also consistent with the expected status. Comparable to the previous BAC it resides in a large domain that is not associated with nucleoli as revealed by microarray analyses (Figure 6.3). 3D immuno-FISH experiments showed 11 % and 13 % association to nucleoli in proliferating and senescent IMR90 cells, respectively (Figure 2.33 D). The third genomic region, labeled with the BAC clone RP11-914H1 showed a low frequency of nucleolus association in 3D immuno-FISH experiments (Figure 2.33 H). However, it was expected to localize to nucleoli, since the results of microarray experiments indicated its association with nucleoli. In 3D immuno-FISH experiments, 9 % of the alleles in proliferating and 14 % in senescent IMR90 cells were associated to nucleoli. However, for this particular BAC only 27 and 29 IMR90 cells were analyzed and more experimental data would be required to assure this observation.

In the studies of the laboratory of M. Narita RP11-784D7- and RP11-638N4-labeled genomic regions showed an association to the nuclear periphery in proliferating IMR90 cells and lost this association in RIS (Sadaie et al., 2013). Based on the published microscopy images and localization statistics a potential re-localization of these regions to the nucleolus was assumed for RIS. However, no nucleolus-association could be observed for either of these genomic regions in proliferating or senescent IMR90 cells in 3D immuno-FISH experiments performed in this study (Figure 2.33 F,G; for exact values see Figure 2.34).

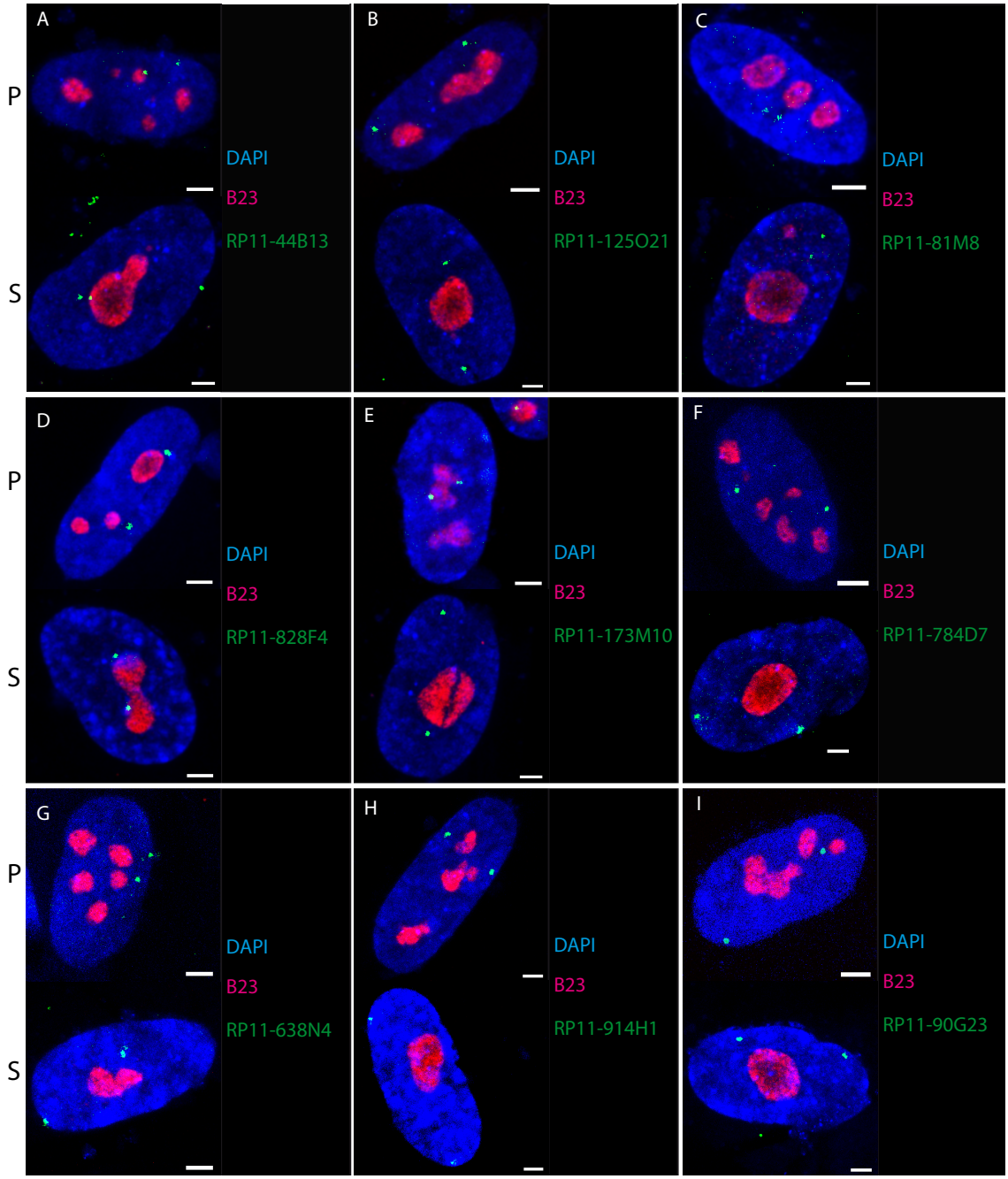

Figure 2.33 – 3D immuno-FISH analysis of selected genomic regions in proliferating and senescent IMR90 cells.
One representative image of 3D immuno-FISH experiments for each genomic region is illustrated for proliferating and senescent IMR90 cells. DNA was labeled with DAPI and nucleoli with B23. z-projections of confocal microscopy images are shown. DNA = blue, nucleolus = magenta, FISH-probes = green. Scale bar: 1.6 µm.

Figure 2.34 summarizes the results of all 3D-FISH experiments by showing the frequency of the nucleolus association of selected genomic regions.

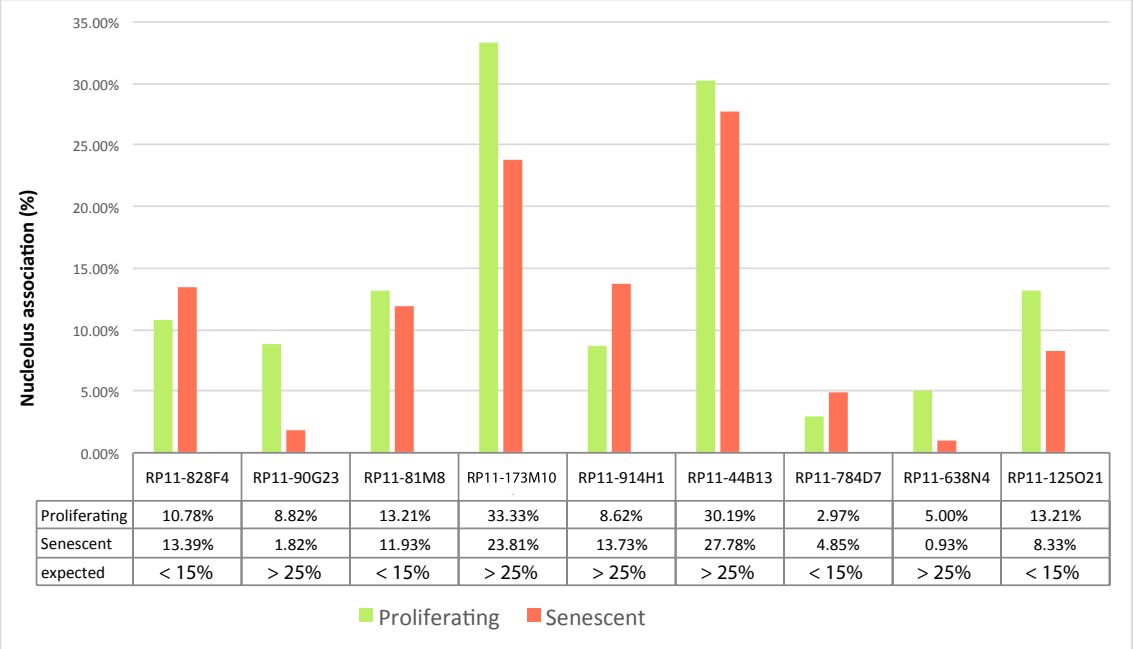

	RP11-828F4	RP11-90G23	RP11-81M8	RP11-173M10	RP11-914H1	RP11-44B13	RP11-784D7	RP11-638N4	RP11-125O21
Proliferating	10.78%	8.82%	13.21%	33.33%	8.62%	30.19%	2.97%	5.00%	13.21%
Senescent	13.39%	1.82%	11.93%	23.81%	13.73%	27.78%	4.85%	0.93%	8.33%
expected	< 15%	> 25%	< 15%	> 25%	> 25%	> 25%	< 15%	> 25%	< 15%

Figure 2.34 – Nucleolus association of selected chromosomal regions tested in FISH-experiments.
FISH experiments were performed for selected BAC-clones in proliferating and senescent IMR90 cells. Nuclei were imaged with a confocal microscope and nucleolus association was analyzed. Illustrated here are percent of nucleolus association in proliferating (red) or senescent (green) cells. Value < 15 % = no nucleolus association, > 25 % = high frequency of nucleolus association.

2.2 Changes in nucleolus-associated chromatin upon UBF knock-out in mouse embryonic fibroblasts (MEF)

Nucleolus-associated domains have only been studied in the human cells previously. In the course of this study a major goal was to initiate the analysis of nucleolus-associated chromatin in mouse. For nucleolus isolation mouse embryonic fibroblasts (MEFs) were used, which represent a comparable cell type to IMR90 human embryonic fibroblasts. Furthermore, to investigate the dynamics of nucleolus-associated domains in mouse cells after inactivation of Pol I, UBF knock-out MEFs were used a major goal was to initiate the analysis of nucleolus-associated chromatin in mouse. For nucleolus isolation mouse embryonic fibroblasts (MEFs) were used, which represent a comparable cell type to IMR90 human embryonic fibroblasts.

In vivo depletion of UBF leads to a downregulation of rRNA transcription through inactivation of Pol I and reorganization of nucleoli (Albert et al., 2013; Hamdane et al., 2014). In the MEF UBF knock-out system, exons 3-5 from the UBF wild-type gene were deleted by inserting flox-sites into intron 2 and 5 and excising the exons by the Tamoxifen inducible Cre-recombinase. In addition, these cell lines were immortalized using two different methods. The first cell lines, iMEF UBF$^{wt/wt}$/ER-Cre$^{+/+}$/SvT and iMEF UBF$^{fl/fl}$/ER-Cre$^{+/+}$/SvT, were immortalized by transforming primary MEF cells with the SV40 Tt antigenes (Hamdane et al., 2014) and other ones, MEF UBF$^{wt/wt}$/ER-Cre$^{+/+}$/p53$^{-/-}$ and MEF UBF$^{fl/fl}$/ER-Cre$^{+/+}$/p53$^{-/-}$, were immortalized by TP53 knock-out via genetic crossing (Hamdane et al., 2015).

In order to identify NADs in MEF cells, nucleolus-associated DNA of MEF and iMEF cells was isolated. To further monitor changes in NADs upon Pol I inactivation, nucleolus-associated DNA of MEF and iMEF cells was isolated 72 h after Tamoxifen treatment. Together, this nucleolus-associated DNA was subjected to microarray analysis. Furthermore, single cell analyses of nuclear architecture were performed, where the localization of the rDNA before and after knock-out compared to major satellite repeats was investigated.

2.2.1 Controls of the UBF knock-out system

To verify the genotype of MEF and iMEF cells genomic DNA was isolated from MEF UBF$^{wt/wt}$/ER-Cre$^{+/+}$/p53$^{-/-}$, MEF UBF$^{fl/fl}$/ER-Cre$^{+/+}$/p53$^{-/-}$, iMEF UBF$^{wt/wt}$/ER-Cre$^{+/+}$/SvT, iMEF UBF$^{fl/fl}$/ER-Cre$^{+/+}$/SvT cells and subjected to PCR analyses, in which the UBF, Cre-recombinase and TP53 gene sequences were investigated (Figure 2.35).

The results of the PCR analyses revealed that the four cell lines possess the supposed genotypes.

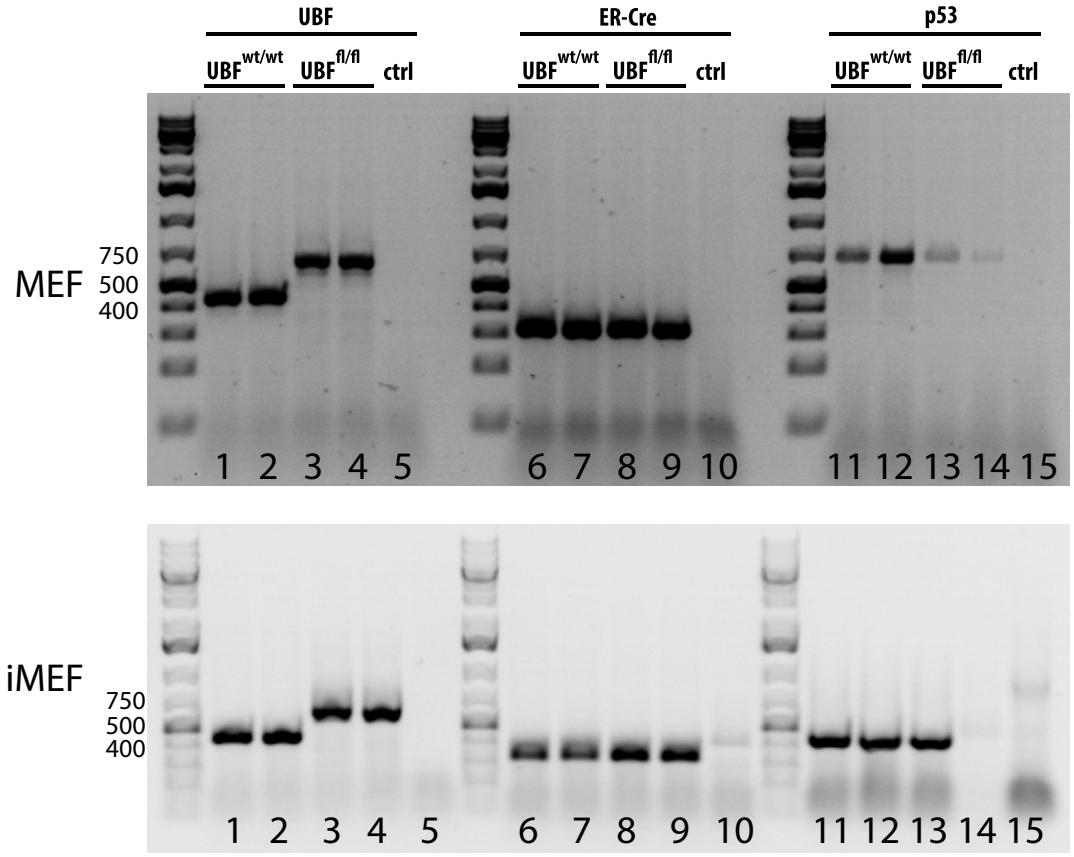

Figure 2.35 – Genotyping PCR for MEF and iMEF cells.
Genomic DNA of cultivated MEF and iMEF cells was isolated and subjected to PCR analyses. The status of the UBF, ER-Cre and p53-locus was monitored for $UBF^{wt/wt}$ and $UBF^{fl/fl}$ cells. PCR reactions were performed in duplicates and a no template control was included. Expected sizes of PCR-products: $UBF^{fl/fl}$ = 628 bp, $UBF^{wt/wt}$ = 428 bp, ER-$Cre^{+/+}$ = 320 bp, $p53^{-/-}$ = 650 bp, $p53^{+/+}$ = 450 bp. One technical replicate did not result a PCR product for iMEF cells (lane 14).

In order to control the depletion of UBF, protein extracts were prepared from MEF $UBF^{fl/fl}$/ER-$Cre^{+/+}$/$p53^{-/-}$ and MEF $UBF^{wt/wt}$ /ER-$Cre^{+/+}$/$p53^{-/-}$ cells 24 h, 48 h, 72 h and 96 h after Tamoxifen treatment. Those extracts were then subjected to western blot analysis in which the levels of UBF, tubulin, Pol I and fibrillarin were monitored. The depletion of UBF in $UBF^{fl/fl}$ cells is clearly visible, whereas levels in the control remained unchanged. In contrast, levels for Pol I or fibrillarin remained unchanged upon UBF depletion (Figure 2.36).

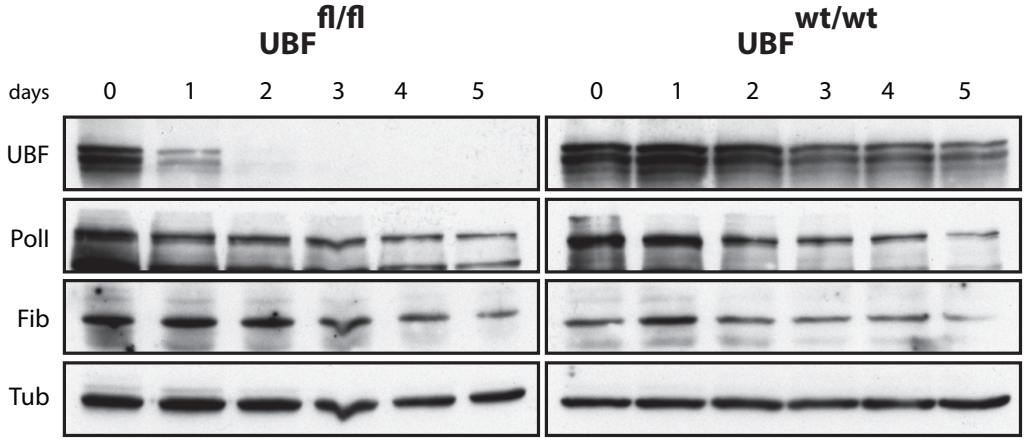

Figure 2.36 – Western blot analysis of UBF levels after Tamoxifen treatment. MEF UBF$^{fl/fl}$/ER-Cre$^{+/+}$/p53$^{-/-}$ and MEF UBF$^{wt/wt}$/ER-Cre$^{+/+}$/p53$^{-/-}$ cells were treated with 50 nM Tamoxifen for 4 h and protein extracts were prepared in 24 h intervals for 5 days. The extracts were subjected to western blot analysis to monitor depletion of UBF in UBF$^{fl/fl}$ cells. Results from cells with 'floxed' UBF alleles are shown on the left side and from wild-type control cells on the right side. Left panel shows that the depletion of UBF was complete after 2 days.

2.2.2 Isolation of nucleolus-associated DNA before and after induction of UBF knock-out

In order to collect data for comparative analyses of the mouse and human nucleolus-associated genome nucleoli were isolated from MEF cells. To further investigate the reorganization of nucleolus-associated chromosomal domains after UBF depletion, nucleoli were isolated 72 h after induction of genetic knock-out of UBF. This time point was selected, because UBF and rRNA synthesis were no longer detected, however the cells are viable and morphologically intact (Hamdane et al., 2014). Nucleoli were isolated using an adapted version of the cross-linking approach as described in 2.1.2 protocol (A) and in the Methods 5.1.3.2. Finally, immunofluorescence detection of fibrillarin and CENP-A was performed on the isolated particles to assess their identity using also a third approach. The quality of the isolated nucleoli, was monitored by the relative enrichment of fibrillarin in nucleolar fractions in western blot experiments, as well as by evaluating the size and shape of isolated nucleoli with DIC microscopy.

To monitor the enrichment of UBF and fibrillarin during the purification process, fractions were set aside at different stages of the purification and subjected to western blot analyses. The first fraction was taken from whole cells (whole cell extract = 'wce') and was used as a reference. The second fraction was taken after the first round of sonication and represents dirty nucleoli ('dNo') and the third fraction represents the final nucleolar fraction after the second round of sonication ('cNo'). Equal protein amounts were subjected to western blot analyses, in which the enrichment of fibrillarin, a marker for the DFC of nucleoli was monitored. In addition, levels of the nucleolar marker protein UBF were also checked,

which provided information also about the efficiency of its knock-out-mediated depletion. Furthermore, the amount of tubulin in the different fractions was monitored to serve as a control for the depletion of cytoplasmic proteins.

Figure 2.37 illustrates all western blot control experiments done for nucleolus isolations of the four different MEF cell lines at the two different time points. The results indicate an enrichment of the nucleolar protein fibrillarin compared to tubulin in nucleolar fractions ('dNo') and the depletion of UBF 72 h after its genetic knock-out.

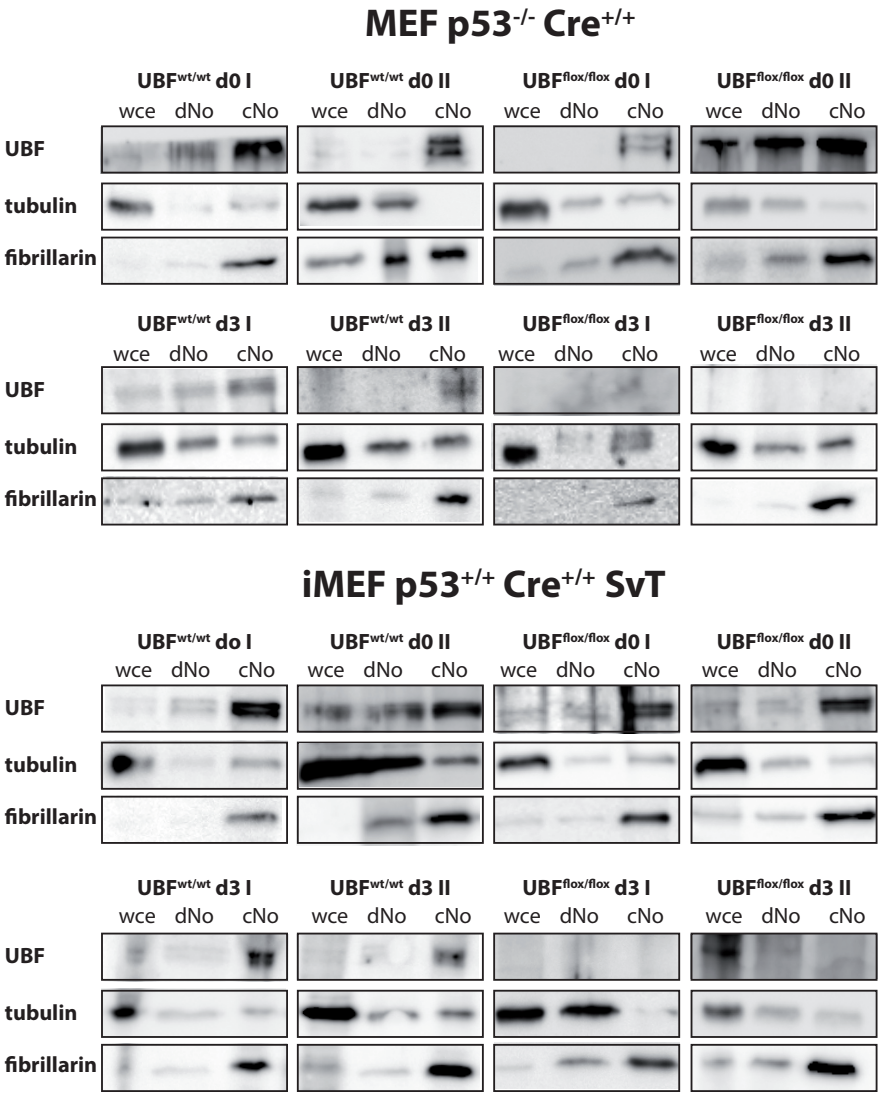

Figure 2.37 – Western blot control of UBF and fibrillarin in different fractions of nucleolus isolations from MEF and iMEF cells
Nucleoli were isolated from MEF ER-Cre$^{+/+}$/p53$^{-/-}$ and iMEF ER-Cre$^{+/+}$/SvT both for UBF$^{wt/wt}$ and UBF$^{flox/flox}$ before and after three days of UBF knock-out. Experiments were carried out in biological duplicates, which are labelled with 'I' and 'II'. Fractions of nucleolus isolations were analyzed with respect to the enrichment of UBF and fibrillarin compared to tubulin in the final fraction. wce = whole cell extract, dNo = dirty nucleoli, cNo = clean nucleoli.

In order to evaluate purified nucleoli in respect to their size and nuclear remnants, aliquots for DIC microscopy were collected during the purification procedure. Aliquots were taken from fixed cells, and from purified nucleoli prior to DNA precipitation. On the one hand, nucleoli were evaluated instantly during the purification process, after the individual sonication steps, to have an immediate quality control, on the other hand images were documented after the purification process from nucleoli that were stored at 4 $°C$.

Figure 2.38 depicts fixed cells from the MEF ER-Cre$^{+/+}$/p53$^{-/-}$ cell line. Size and shape of iMEF ER-Cre$^{+/+}$/SvT cells were comparable to them (not shown). Isolated nucleoli are visible as refractive bodies and exhibit comparable size and shape to the nucleoli in fixed MEF and iMEF cells before isolation.

On several images some areas with aggregated particles and also smaller particles were visible (see for instance Figure 2.38 second panel, right image). This is due to the fact that nucleoli were stored at 4 $°C$ until the documentation and if the storage time was longer than a few hours it often led to aggregation and also partial disintegration of nucleoli in the sucrose-free Tris buffer, nevertheless the good quality of the isolated nucleoli was already observed during the purification process.

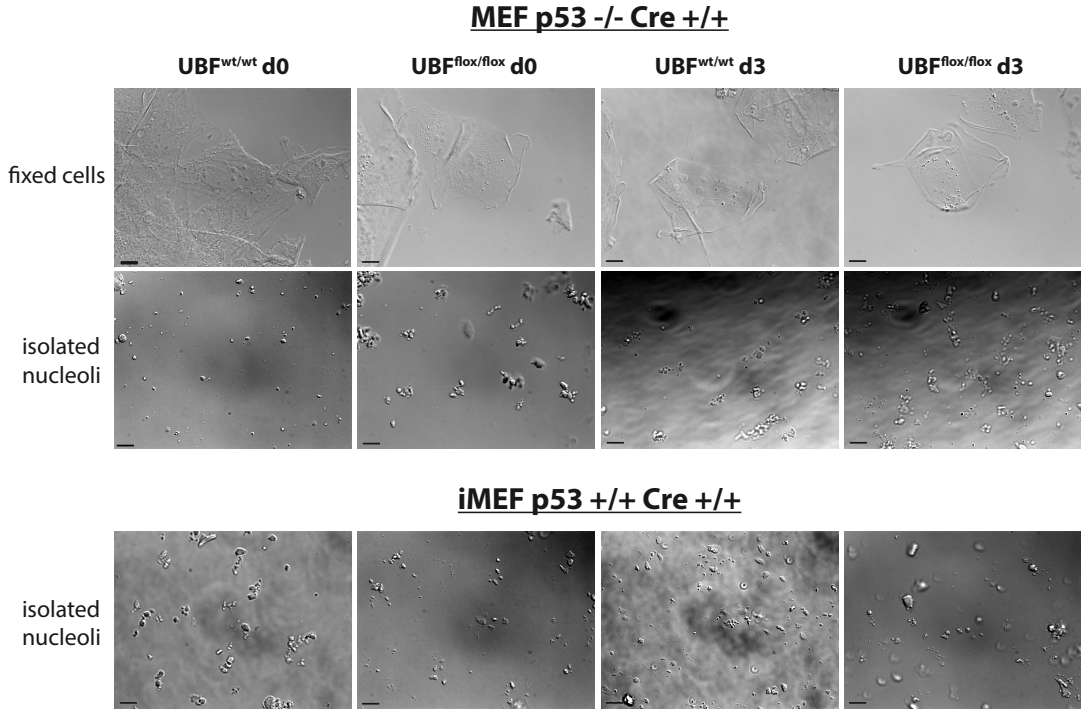

Figure 2.38 – Monitoring size and shape of isolated nucleoli with DIC microscopy.
Fixed cells and isolated nucleoli were observed under a light microscope. Purified nucleoli (lower two panels) exhibit same size and shape as nucleoli in fixed cells (upper panel). Representative images of one biological replicate are shown. Scale bar: 10 µm.

Large rearrangements of the nuclear architecture occur after depletion of UBF and nucleolar proteins, such as fibrillarin or Pol I subunits separate from rDNA and often accumulate in one proteinaceous body (Hamdane et al., 2014). To get more insight into the identity of the isolated particles derived from cells before and after tamoxifen treatment, immunofluorescence experiments were performed. The isolated fraction was immobilized on microscopy slides and nucleoli were stained for the centromeric protein CENP-A, to mark potential chromocenters, and for the nucleolus marker protein fibrillarin, furthermore DNA was counter-stained with DAPI. Comparable to the light microscopic analysis, nucleoli were stored over-night or occasionally longer at 4 $°C$ prior to immunostaining. This led again frequently to an aggregation and also partial disintegration of nucleoli. As shown on Figures 2.39 and 2.40, most of the isolated particles were positive for fibrillarin, indicating their nucleolar origin. Though the intensity of the staining was not constant (see iMEF UBF$^{flox/flox}$ d0 and MEF UBF$^{wt/wt}$ d3 in respective Figures), the co-localization of fibrillarin-staining with DAPI positive particles could be observed in nearly all cases. Furthermore, also a comparison with western blot analysis confirmed the enrichment of nucleolar proteins. After CENP-A immunostaining, centromeres appeared as small brightly stained spots with surrounding background signals (best visible on gray-scale images of Figures 2.39 and 2.40). Centromeres were most frequently associated with fibrillarin positive particles and just a few particles showed only DAPI and CENP-A staining.

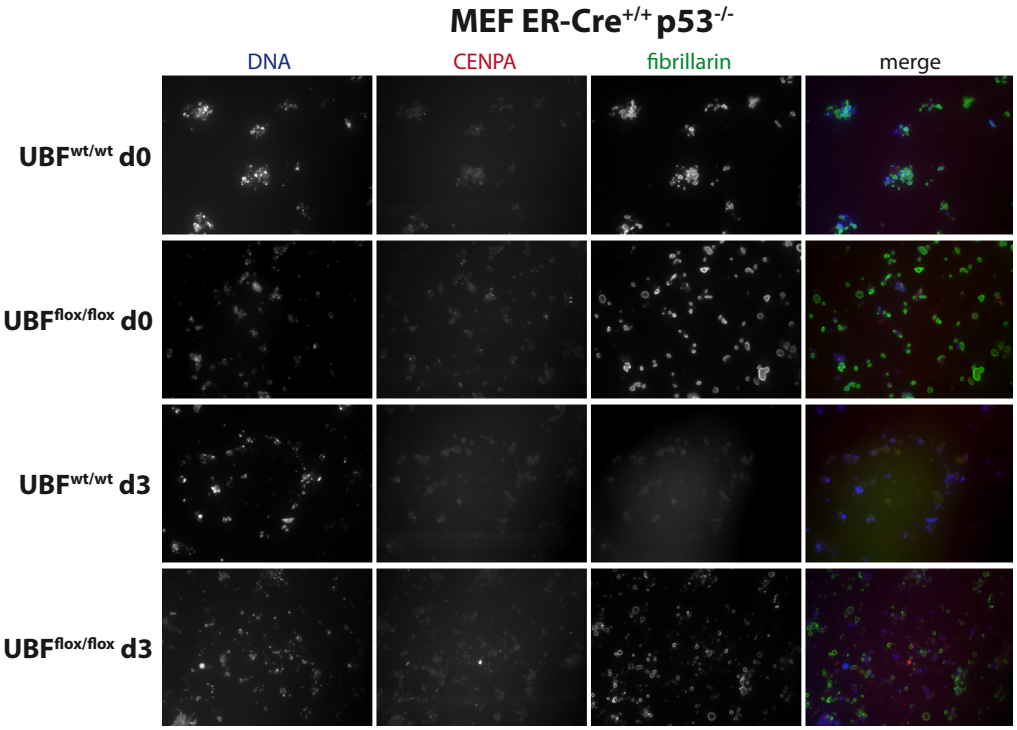

Figure 2.39 – Immunofluorescence staining of fibrillarin and CENP-A on isolated nucleolar fractions of MEF cells.
Isolated nucleoli were stained for CENP-A and fibrillarin and the DNA was counter-stained with DAPI. DNA = blue, CENP-A = red, fibrillarin = green.

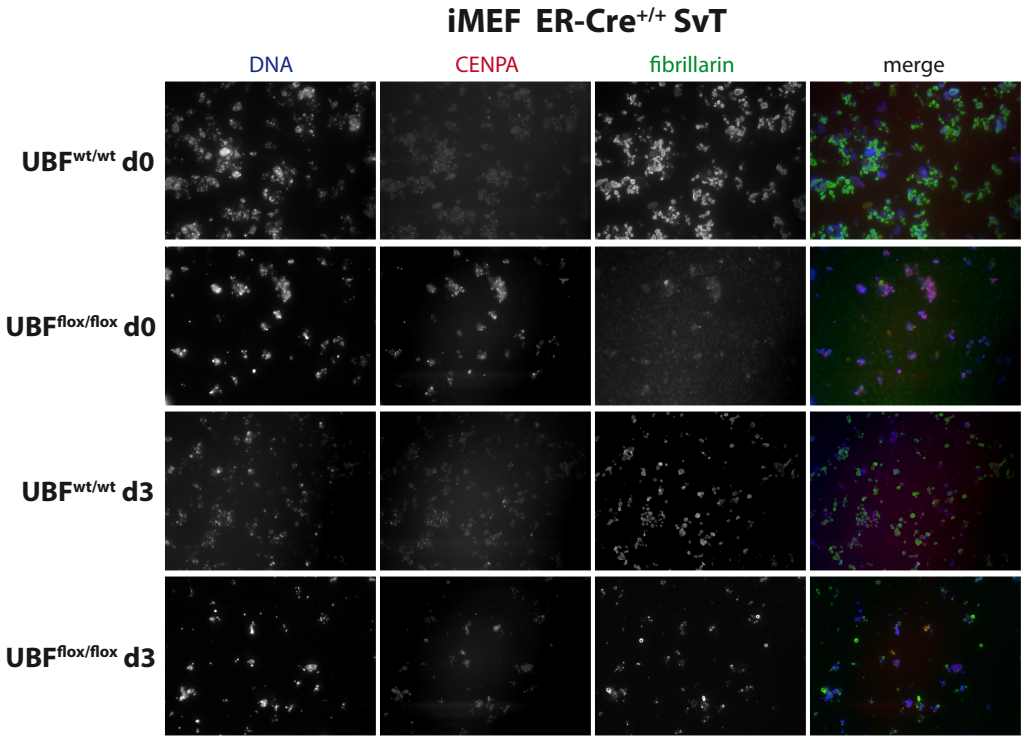

Figure 2.40 – Immunofluorescence staining of fibrillarin and CENP-A on isolated nucleolar fractions of iMEF cells.
Isolated nucleoli were stained for CENP-A and fibrillarin and the DNA was counter-stained with DAPI. DNA = blue, CENP-A = red, fibrillarin = green.

The DNA was isolated from nucleoli that passed these quality controls abd was subjected to Agilent SurePrint G3 high-resolution CGH microarray analyses. Primary data were collected for subsequent bioinformatical studies.

2.2.3 Analysis of rDNA and major satellite reorganization upon UBF depletion by 3D immuno-FISH in MEF cells

In order to evaluate changes in chromatin organization and nucleolar morphology associated with depletion of UBF, 3D immuno-FISH experiments were performed. Since rDNA and satellite repeats represent integral components of the nucleolar genome their localization patterns were investigated before and after UBF knock-out. For the monitoring of changes in nuclear organization of pericentric regions a probe for the major satellites was used. Major satellites are heterochromatic regions and located at pericentric regions and are therefore suitable for examining global organization of constitutive heterochromatin in the murine nucleus.

After UBF knock-out the transcription of the rDNA is shut down and the nuclear architecture is reorganized. A central part of the UBF-dependent nuclear reorganization process is that rDNA is no longer associated to nucleoli. This is marked by the separation of NORs from fibrillarin, Pol I and TIF1A (Hamdane et al., 2014). To monitor rDNA compaction and localization a 3D-FISH approach was used. Two probes, M6/2-2 and M6/31-2, marking parts of the intergenic spacer of the rDNA repeat were selected (Figure 2.41) and labeled with biotinylated nucleotides.

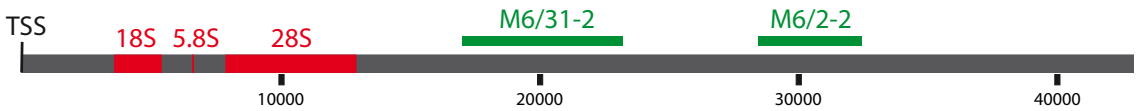

Figure 2.41 – Locations of rDNA fragments of M6/31-2 and M6/2-2 plasmids on the rDNA repeat unit.
Illustration of the location of probes labeling parts of the intergenic spacer (green) on the rDNA repeat unit. Coding regions for mature rRNA species are indicated (red) and positions relative to the transcription start site (TSS) are marked (black).

Both probes were tested on mouse metaphase chromosomes and rDNA signals were clearly visible with a lower background for M6/2-2 (Figure 2.42). Hence, M6/2-2 was used in 3D-FISH experiments.

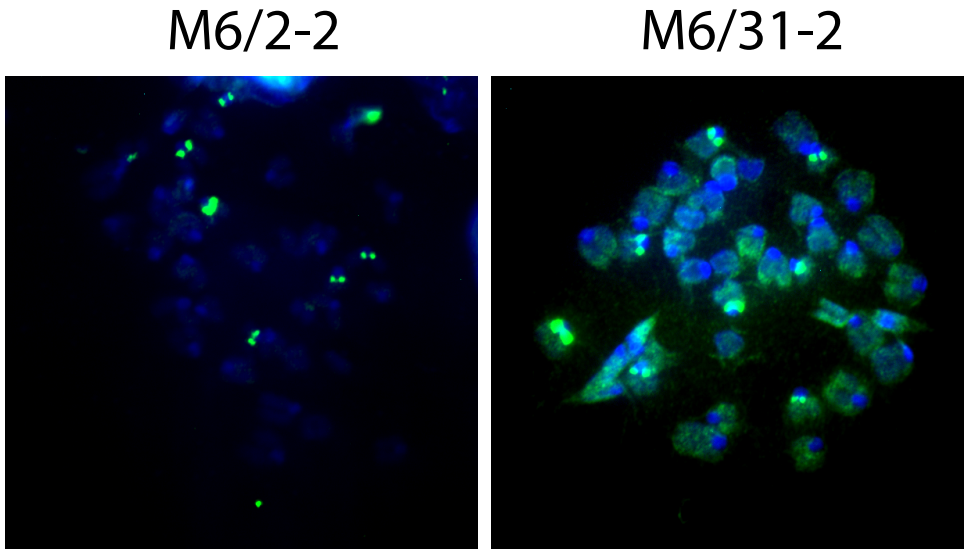

Figure 2.42 – Test of labeled rDNA probes M6/31-2 and M6/2-2 on metaphase chromosomes.
M6/31-2 (right panel) and M6/2-2 (left panel) were labeled with biotin and detected with StrA-A488 on metaphase chromosomes. Hybridization signals are illustrated in green and DNA in blue.

Furthermore, a probe, labeling the major satellites at the centromeres was selected to mark the centromeric regions of the chromosomes (Figure 2.43).

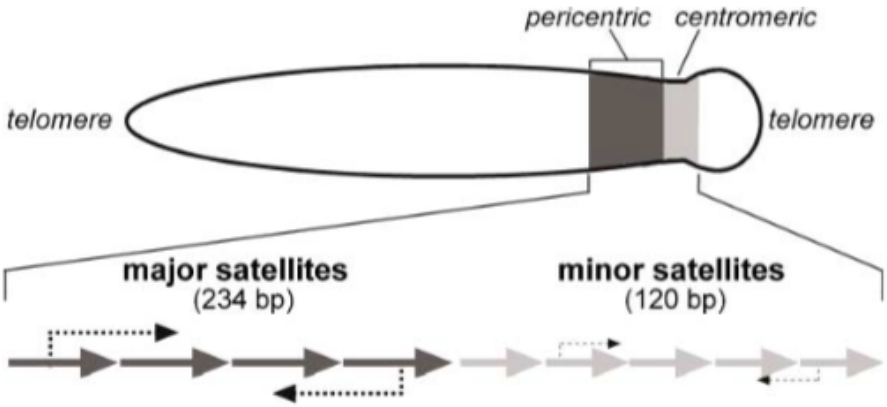

Figure 2.43 – Location of major and minor satellite repeats on mouse chromosomes.
Illustration of the location of major satellites on a mouse chromosome. Adapted from Lehnertz et al. (2003).

This probe was then labeled with digoxygenin coupled nucleotides and tested on mouse metaphase chromosomes.

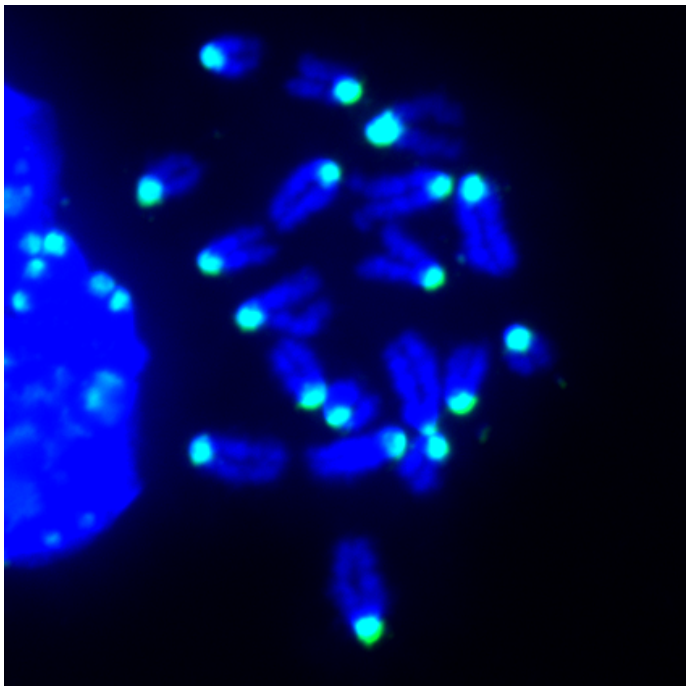

Figure 2.44 – FISH of labeled major-satellite probe on metaphase chromosomes.
Major satellite probe was hybridized on mouse metaphase chromosomes. Individual signals on each chromosome are visible on centromeres (green) with a low background.

Figure 2.44 illustrates the hybridization of the probe labeling the major satellites on mouse metaphase chromosomes. Signals are clearly visible on the ends of each chromosomes, where pericentric major satellite repeat clusters are located.

In the following, 3D immuno-FISH experiments were carried out using the rDNA and major satellite probes. Therefore, MEF ER-Cre$^{+/+}$/p53$^{-/-}$ UBF$^{wt/wt}$ and UBF$^{fl/fl}$ cells were fixed before and 72 h after Tamoxifen treatment. Then, cells were hybridized simultaneously with the rDNA and major satellite probe, stained with fibrillarin and the DNA was counter-stained with DAPI. (Figure 2.45).

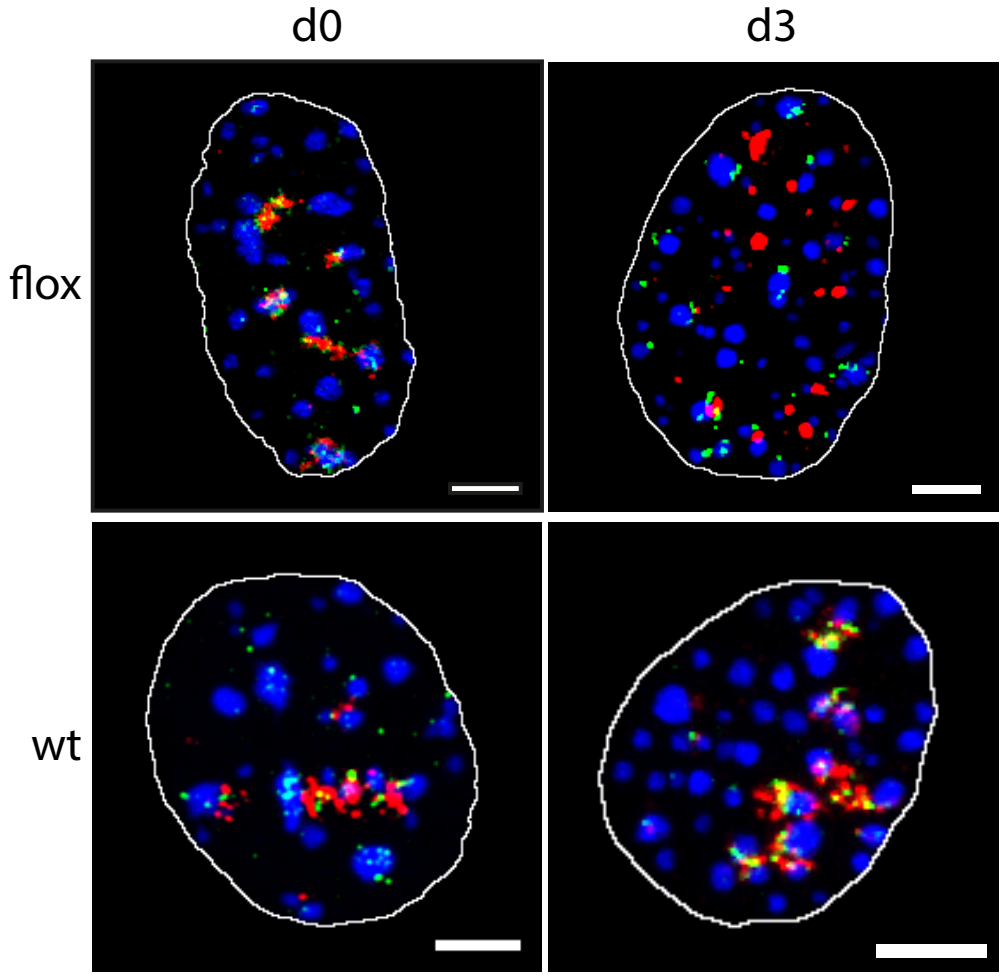

Figure 2.45 – 3D-FISH of rDNA and major satellites before and after UBF knock-out.
MEF UBF$^{fl/fl}$/ER-Cre$^{+/+}$/p53$^{-/-}$ and MEF UBF$^{wt/wt}$/ER-Cre$^{+/+}$/p53$^{-/-}$ cells were fixed for FISH-experiments before and after UBF knock-out. After UBF knock-out the rDNA forms small, condensed foci which associate to major satellite repeats and is no longer associated to nucleoli, marked by fibrillarin staining (B). In contrast, in the wild-type and in cells before knock-out the rDNA is associated to nucleoli (A, C, D). z-projections of confocal microscopy images are shown. Nucleus is marked by outlines, nucleolus = red, rDNA = green, major satellites = blue. d0 = without Tamoxifen, d3 = 72 h after induction of UBF knock-out. Scale bar: 1.6 µm.

After 72 h of UBF knock-out, rDNA condenses and forms distinct foci that are no longer associated with fibrillarin, a marker for nucleoli. They appear as compact foci associated with areas of constitutive heterochromatin stained with the major satellite probe (Figure 2.45 B), indicating that individual rDNA repeats condense to the centromeric regions of the respective chromosome and get inactivated. In control cells the rDNA signal is associated to fibrillarin signals and shows a more disperse distribution (Figure 2.45 A,C,D).

3 Discussion

3.1 Nucleolus-associated chromosomal domains in proliferating and senescent IMR90 cells

The nucleolus is the most prominent nuclear substructure which forms around actively transcribed NORs and can be observed through the light microscope in interphase. A shell of perinucleolar heterochromatin forms around nucleoli, which was shown to harbor among others centromeric regions (Ochs and Press, 1992) or the 5S rRNA gene (Matera et al., 1995). Later the genome of nucleolus-associated chromatin was analyzed and NADs were identified in HeLa and HT1080 cells (Németh et al., 2010; van Koningsbruggen et al., 2010).

Within the scope of this study, nucleolus-associated DNA was isolated from proliferating IMR90 cells using the same cross-linking approach as in former studies in our group (Németh et al., 2010) and hybridized on two-colour CGH microarrays. A microarray approach was favored over a sequencing approach here, since the former study revealed that 80 % of the NADs can be identified using this technique. Furthermore, repetitive DNA elements that are not represented on the microarrays were analyzed and characterized in 3D immuno-FISH experiments. NADs, that were identified in HeLa cells in the former study were then compared to NADs that were identified in non-transformed, diploid, proliferating human IMR90 fibroblasts based on the isolation of nucleolus-associated DNA in the scope of this study. Furthermore, to get new insight into the dynamics of nucleolus-associated chromatin during replicative senescence, nucleolus-associated DNA was isolated from replicative senescent IMR90 cells and also hybridized on CGH microarrays. Raw data were preprocessed by the manufacturer and were then evaluated in the IGB. Bioinformatical analyses were subsequently performed by T. Straub (LMU Munich, for a summary see Section 6.1).

Visual inspection of the normalized microarray data in the IGB revealed, that the overall genomic pattern of nucleolus-association remains when comparing the data of a previous (Németh et al., 2010) and this study. However a remarkable difference can be observed between the characteristics of hybridization signal intensities. In the initial work (Németh et al., 2010) tha analysis of HeLa nucleolus-associated DNA on microarrays resulted in hybridization signals with gradual intensities, which enabled NAD calling using a thresholding approach. The newly acquired data from IMR90 and K562 cells are different with respect to signal intensity variations, as they show saturation at most nucleolus-associated

chromosomal regions. Gradually emerging peaks do not show up, rather large domains of nucleolus-association can be detected, mostly with sharp borders and similar signal intensities throughout the domains (see Figure 6.2). Hence, NADs were identified using a two-state (enriched vs. depleted domains) Hidden Markov Model (HMM) instead of a thresholding approach. The observed differences were likely not due to a different quality of the material, since quality control experiments (see Section 2.1.1.2) showed comparable results. More likely the discrepancies arise from the use of two different versions of the same array-type. Nucleolus-associated DNA from HeLa cells was hybridized on HG18 CGH 385K Whole Genome Tiling v1.0 arrays with a probe spacing of 6270 bp, whereas nucleolus-associated DNA in the presented work was hybridized on high-resolution two-colour Human CGH 4.2M Whole Genome Tiling Arrays with a median probe spacing of 284 bp. The latter arrays contain greater than 10 times more different oligonucleotides than the old microarrays (4.2M vs. 385K) spotted on the same surface area. A possible explanation for the observed pattern might be, that they are saturated more rapid than the older version of the array.

Illustration of the normalized microarray data in the IGB showed very similar patterns of nucleolus-associated domains in proliferating and senescent IMR90 cells (see Figure 2.6). This result suggests that NADs are not subjected to large reorganizations during replicative senescence. In general, chromosomal loci were found to have a low mobility in interphase (Robinett et al., 1996; Chuang and Belmont, 2007) with an average apparent diffusion coefficient of 1–2 x 10^{-4} mm^2 s^{-2} (Görisch et al., 2005). Furthermore, a reorganization of chromosome territories and nuclear architecture takes place after mitosis in early interphase where the spatial organization of the nucleus is set. These observations and the fact that senescent cells do not go through mitosis any more and are in G0 might be an explanation for the low amount of differences with respect to nucleolus-association found in these experiments. However, a few genomic loci with altered gene expression during cellular aging show differences regarding their association to nucleoli. At the global level one might speculate that the longer the last mitosis dates back, the larger the differences in localization of specific genomic regions might be.

Bridger et al. (2000) demonstrated in FISH analysis of radial positioning in human diploid fibroblasts, that HSA18 changes its localization in replicative senescence from the nuclear periphery to the nuclear center. However, this difference in radial localization did not have any effect on nucleolus-association as analyzed in microarray experiments that were done in the scope of this study. This discrepancy is not surprising, since the localization of nucleoli in the nucleus is not fixed and do not have to be localized in the center of the nucleus. Reorganization of nuclear architecture was also observed in oncogene induced senescence, where the formation of SAHF was described (Narita et al., 2003). These foci exhibit a layered structure of heterochromatin marks such as trimethylated H3K9, H3K27 and H3K36 and were found to be associated with gene silencing of E2F target genes that influence the progression through the cell cycle (Corpet and Stucki, 2014). Furthermore, individual

SAHFs were shown to originate from individual chromosome territories (Funayama et al., 2006). It has been revealed recently, however, that the formation of SAHF is cell- and senescence-type specific. Whereas formation of SAHF was observed in H-Ras oncogene induced senescence in all tested cell types, the appearance and frequency of SAHF was variable in replicative senescence (Kosar et al., 2014). Indeed, this type of chromatin reorganization was rare in replicative senescent IMR90 cells under the experimental conditions used in this study.

In summary, data presented here suggest, that NADs are stable units of chromosome organization that display similar genomic patterns in the HeLa, K562 and IMR90 human cell lines and do not show global rearrangements during replicative senescence.

3.2 Comparison of experimental procedures for the analysis of nucleolus-associated chromatin

Along with analyses of the dynamics of NADs in replicative senescence, the influence of different purification methods on the identification of NADs and the analysis of histone PTMs was evaluated. The way how nucleoli are purified from human cells did not change much during the past decades, since all protocols are based on fractionation and sequential centrifugation. Procedures were established in the 1950s and 60s (Vincent, 1952; Monty et al., 1956; Busch et al., 1963) and were adapted in the 70s (Bhorjee and Pederson, 1973) and early 2000s (Sullivan et al., 2001; Andersen et al., 2002). The main differences lie in the use of formaldehyde to cross-link cells, the concentration of Mg^{2+} and the intensity of sonications (see Section 2.1.2). One could speculate that these differences might lead to a variation in NADs that are identified after isolating nucleolus-associated DNA from the same cell line or to differences in the detection of histone PTMs in mass spectrometry.

Visualization of the normalized microarray data in the IGB (see Figure 2.8) suggested that NADs can be identified very robustly and the obtained nucleolus-associated domains are very consistent. However, a profound bioinformatical analysis has to be performed to further strengthen this assumption. Surprisingly, this visualization indicated, that the difference of biological replicates can be larger than the differences that are observed between the three different purification protocols. This robustness of different protocols to isolate nucleoli was already observed in former studies, which identified the DNA content of nucleolus-associated chromatin (Németh et al., 2010; van Koningsbruggen et al., 2010). Németh et al. (2010) isolated nucleolus-associated DNA from HeLa cells using a cross-linking approach (Protocol (A) in 2.1.2). NADs were then identified on the one hand using a thresholding approach from array CGH experiments and on the other hand by 454-sequencing. In contrast, van Koningsbruggen et al. (2010) isolated nucleolus-associated DNA from HT1080 cells using a native approach (Protocol (B) in 2.1.2). NADs were

then identified after Illumina sequencing using a comparative sequencing approach. Remarkably, despite the fundamentally different approaches both laboratories found similar genomic regions enriched in the purified nucleolar DNA, including chromatin regions containing olfactory receptor genes, zinc finger genes, immunoglobulin gene families, and 5S RNA genes. However, some differences also arised, as only Németh et al. (2010) found tRNA genes frequently associated to nucleoli. One major point investigated by van Koningsbruggen et al. (2010) was, that NADs can relocalize to the nuclear lamina after cells went through mitosis. A complementary observation was recently also made by Kind et al. (2013) for LADs. There, results illustrated that LADs localize stochastically to the nuclear lamina or the perinucleolar space in daughter cells after cell division.

Besides analyzing the DNA content of nucleoli, nucleolus-associated chromatin was characterized with respect to histone PTMs. The distribution of histone PTMs in the nucleus can be evaluated using antibody-based techniques, or mass spectrometry. Antibody-based techniques require the use of high-specific antibodies against the modification of interest. In contrast, mass spectrometry offers the possibility for quantitative analyses and is able to target different modifications at the same time. When cells are cross-linked the mobility of proteins in the cell changes and the activity of enzymes is restricted by the cross-linking agent. Hence, the activity of chromatin modifying enzymes is limited. Sodium-butyrate, an inhibitor of histone deacetylases, was added to native preparations to inhibit their enzymatic activity. Here, nucleoli were isolated using a cross-linking and a native approach, with and without the addition of sodium butyrate, and an approach for analyzing the N-terminal tail of histone H4 with respect to its acetylation was developed using a mass spectrometry approach by A. Villar-Garea (Dillinger et al., 2014). Comparison of different experimental settings enabled the definition of the optimal conditions for future mass spectrometry analyses of histone PTMs in nucleolus-associated chromatin. These include formaldehyde cross-linking with a short heat reversal, but no requirement of sodium butyrate.

3.3 Single-cell analyses of nucleolar morphology and nucleolus-associated tandem repeats

Population-based analyses of nucleolus-associated chromatin revealed the presence of specific gene families and the enrichment of satellite repeats in the perinucleolar space. This satellite repeats are associated with marks of repressive chromatin, which is also supported by the finding that the nucleolus-associated chromatin is enriched for repressive histone PTMs. Furthermore, it was observed in former studies that genes located in the nucleolar periphery are expressed at low levels. These findings prompted us to investigate the distribution of heterochromatin in single cell experiments, furthermore to investigate the location of different nucleolus-associated tandem repeats in proliferating and senes-

cent IMR90 cells in quantitative immunofluorescence and 3D immuno-FISH experiments, respectively.

3.3.1 Global nucleolar morphology dynamics during replicative senescence

The morphological changes of nucleoli during replicative senescence in human fibroblasts cultivated *in vitro* were investigated in the past using different methods. WI-38 cells were analyzed concerning their dry mass, their area and the number of nucleoli in cells with low and high passage numbers. The results revealed an increase in nucleolar area and nucleolar dry mass. Furthermore, the amount of cells containing one large nucleolus increased from 17 % in early-passage cells to 66 % in late-passage cells (Bemiller and Lee, 1978; Bemiller and Miller, 1979). Further analysis revealed that late-passage IMR90 cells have larger nucleoli as determined by morphometric analysis. However, the increase in nucleolar area was proportional to the overall increase in nuclear area and consequently this increase in nucleolar dry mass was not significant (Pool et al., 1982). Due to the limitations of the methods at that time, only the area of nuclei and nucleoli was analyzed and this deficit was overcome by analyzing the volume and the number of nucleoli by immunofluorescence staining of proliferating and senescent IMR90 cells and measuring the volume with the '3D Objects counter' plugin of FIJI (see Methods Section 5.4.4) in this study.

In agreement with experiments performed by Bemiller in WI-38 fibroblasts, results presented in Section 2.1.4.1 demonstrate that the number of nucleoli decreases from a median of 3 in proliferating cells to a median of 1 nucleolus in senescent IMR90 cells and the amount of nuclei having one nucleolus increased from 10 % in proliferating to 61 % in senescent IMR90 cells. Furthermore, results also indicate that nucleoli are about 2.5-fold larger in senescent IMR90 cells compared to cells with low passage numbers. Values, that were obtained in this study were in the same range as published data in the BioNumbers database (Diameter 0.5-5 µm, Bionumbers ID: 107498; Milo et al. (2009)). In contrast, the volume of ill-identified objects in esophageal epithelial cells after smearing, hematoxylin staining and dehydration was measured and was in the range of 5 µm (Bionumbers ID: 106593; Nandakumar et al. (2010)) However, methods that were used to measure the different parameters differed greatly from the methods used in the presented work. Data presented here were obtained by measuring the volume of nucleoli in IMR90 cells with immunostaining of the granular component using an antibody labeling B23/nucleophosmin, which markss the whole nucleolus. Discrepancies in the values might stem from labeling different parts of the nucleolus or using different techniques to measure the different parameters. In contrast to Pool et al. (1982), who stated that the increase in nucleoli was due to an overall increase of nuclear area and dry mass, the relative volume that is occupied by nucleoli in senescent cells increases from 2.8 % to 6.6 % by about three fold.

Comparable to the change in replicative senescence, nucleoli also show a change in their numbers in different phases of the cell cycle. After mitosis, individual nucleoli forming around each single NOR can be observed, whereas only one nucleolus is visible at the end of G1 Phase (Anastassova-Kristeva, 1977). This reduction in numbers is caused by nucleolar fusion, which was observed already 50 years ago (Amenta, 1961). Since senescent cells exit the cell cycle and do not enter M Phase again, this cell cycle depending fusion of nucleoli might be the reason for the decrease of nucleolar numbers in cellular senescence. Remarkably, a physical model explaining the fusion of nucleoli was recently proposed, describing a liquid-drop like behavior for nucleoli in *Xenopus laevis*, which leads to fusion of nucleoli (Brangwynne et al., 2011). However it should be noted that nucleoli of *Xenopus* oocytes are not equivalent with nucleoli of cultured human cells, as they are more numerous and not formed around NORs (Gall et al., 1995; Farley et al., 2015).

3.3.2 Nuclear distribution of histone PTMs in proliferating and senescent cells

During replicative senescence nuclear architecture is subjected to large reorganizations, such as merging of nucleoli, SADS or re-localization of whole chromosomes (Swanson et al., 2013; Bridger et al., 2000). Furthermore, lamin B1, a major component of the nuclear lamina was shown to be downregulated in replicative senescence, which leads to large reorganizations of the nuclear architecture at the nuclear periphery (Shah et al., 2013; Camps et al., 2014). In order to investigate whether nuclear reorganizations lead to a different localization of facultative and constitutive heterochromatin and euchromatin, immunofluorescence experiments in proliferating and senescent IMR90 cells were performed. Two markers for facultative heterochromatin, H3K9me2 and K3K27me3, were tested. A major example for this type of heterochromatin is the Xi, which was found as bright stained area in proliferating as well as senescent IMR90 cells (Boggs et al., 2001; Heard et al., 2001). The Xi was found to localize to both heterochromatic compartments in mammalian cells (Bourgeois et al., 1985), however it localizes to the nucleolus during S Phase to maintain its silenced status (Zhang et al., 2007). A quantification of the localization of the Xi demonstrated, that it is localized more frequently to the nuclear periphery in senescent than in proliferating IMR90 cells and it is very rarely found in between. In addition, a marker for active parts of the genome, H3K9ac, was investigated. This histone PTM was not detectable witin nucleoli, despite the presence of the highly active rRNA genes likely due to the dilution of the signal on decondensed rDNA chromatin. Furthermore, an exclusion from the DAPI-dense Xi was observed. However, no apparent difference was visible in senescent compared to proliferating cells.

Besides the qualitative analysis of the distribution of facultative heterochromatin and euchromatin in proliferating and senescent IMR90 cells, the distribution of constitutive heterochromatin, by H3K9me3 labeling, was performed. Main nuclear sites of this type of

heterochromatin in proliferating cells are the nuclear periphery as well as the perinucleolar space (Bickmore, 2013).

The overall variations in replicative senescence concerning active and repressive chromatin marks were investigated in recent years by analyzing levels of H3K4me3 and H3K27me3, respectively (Cruickshanks et al., 2013), but a spatial analysis of the distribution of constitutive heterochromatin by H3K9me3 quantification in proliferating and senescent IMR90 cells was not performed. For this kind of experiment the quality of the used antibody is crucial. Large-scale control experiments summarized in two different studies provided information about the quality of a wide range of different antibodies labeling histone PTMs (Egelhofer et al., 2010; Rothbart et al., 2015). These results are publicly accessible on the respective web-sites (Antibody Validation Database: http://compbio.med.harvard.edu/antibodies/; The Histone Antibody Specificity Database. http://www.histoneantibodies.com). Surprisingly, the results for the same antibody can differ dramatically between suppliers and even between different batches of the same supplier. Moreover, the quality of different antibodies against a specific histone PTM varies even more. Here, a highly specific monoclonal antibody was used that recognizes H3K9me3 (Hayashi-Takanaka et al., 2011) and the experiments were repeated with a second antibody from abcam, which was rated with good quality in the Antibody Validation Database.

During cellular senescence the nucleus is subjected to major reorganizations and the distribution of constitutive heterochromatin is possibly also changed. Hence, a rearrangement of H3K9me3 was postulated during this physiological process. Consequently the nuclear distribution of H3K9me3 was monitored with specific attention to the perinucleolar space and the nuclear periphery. In this study the perinucleolar space was defined as the area that forms within 240 nm outside the B23-stained nucleolus, the nuclear periphery was defined as the area that forms within 240 nm from the edge of the DAPI-stained nucleus.

In order to characterize the presence of heterochromatin in the two defined areas, three parameters were tested. First, the relative fluorescence dropped from 5.2 % to 2.2 % at the perinucleolar space during replicative senescence, whereas at the nuclear periphery it remained unchanged at about 10 %. Second, the coefficient of fluorescence signal variation was measured as described (see Section 5.4.3.2, Zhang et al. (2015)). Interestingly, the overall heterogeneity in senescent compared to proliferating IMR90 cells increases, indicating a more clear separation of eu- and heterochromatic regions. Moreover, a slight increase was observed also at the nuclear periphery, whereas no change was observed at the perinucleolar space. Third, the distribution of the highest intensity signals was calculated. This analysis provided information about regions which feature a high content for H3K9me3 such as centromeric and pericentromeric regions, which play an important role in genome organization. Strikingly, the abundance of the most heterochromatic regions at the perinucleolar space decreased to about $\frac{1}{4}$ in senescent cells compared to proliferating ones, however no significant change was visible at the nuclear periphery. Reorganization of

heterochromatin in OIS differs from reorganizations observed in replicative senescence, as OIS-cells develop SAHFs. There heterochromatic domains get detached from the nuclear lamina and form SAHFs that exhibit a layered structure of different repressive histone PTMs (see Section 3.1 and Chandra et al. (2015)).

Together with the analyses concerning nucleolar numbers, these results illustrate major reorganizations of the nucleus during cellular aging. Nucleoli fuse and get enlarged, whereas perinucleolar heterochromatin is reduced and the H3K9me3-labeled chromatin becomes more homogeneous in this area. In contrast, the H3K9me3, that is constitutive heterochromatin, signal distribution gets more heterogeneous in other nuclear regions.

3.3.3 Large-scale spatial rearrangements of tandem repeat arrays in replicative senescence

Major building blocks of nucleolus-associated domains among others are the rDNA tandem repeats, satellite-2 repeats and sub-telomeric regions. In order to monitor changes in their localization during replicative senescence, 3D immuno-FISH experiments using probes labeling parts of these repeats were performed in proliferating and senescent IMR90 cells. Not surprisingly, the localization of the rDNA with respect to the nucleolus did not change, because replicative stress does not lead to a shut down of rRNA transcription but only to a delay in processing of rRNA (Nishimura et al., 2015). This was illustrated by the stable association of rDNA and DJ signals to nucleoli in proliferating as well as senescent IMR90 cells. Moreover, telomeres play an important role during replicative senescence, as their shortening induces DDR and leads to a p53-induced arrest in proliferation. Analyzing their fluorescence-intensity in 3D immuno-FISH experiments confirmed telomere attrition, however no obvious difference in localization or clustering of telomeres was observed. Most remarkable differences were shown for satellite repeat clusters, as they decondense during cellular aging which was observed to be an universal and early marker for cellular senescence (Swanson et al., 2013). This phenomenon was reproduced by labeling satellite-2 repeat regions in replicative senescent IMR90 cells, providing an additional internal control for the senescence status.

In summary, immunofluorescence and 3D immuno-FISH experiments presented here indicate rearrangements in the nucleus of IMR90 cells during cellular aging, which largely agree with and extend former observations. Nucleoli fuse and are enlarged during replicative senescence. Furthermore, satellite repeat clusters decondense, which is shown exemplified by the distension of satellite-2 repeats. Satellite repeats are marked by H3K9me3, hence, their decondensation could be the primary cause of the decrease of H3K9me3 signal specifically at the nucleolus. Table 3.1 summarizes published data and results that were obtained during the course of this study concerning cellular senescence. In addition the differences of oncogene induced senescence and replicative senescence are displayed.

proliferating	RS	OIS
proliferation	no proliferation* (Hayflick, 1965)	no proliferation (Serrano et al., 1997)
normal morphology	flattening of cells	
few small nucleoli*	1 large nucleolus*	increased size of nucleoli (Nishimura et al., 2015)
long telomeres	telomere shortening/DDR (Harley et al., 1990)	varying length
	cell-type-dependent SAHF (Kosar et al., 2014)	formation of SAHF (Narita et al., 2003)
condensed satellites*	SADS* (Swanson et al., 2013)	SADS (Swanson et al., 2013)
	SASP (Coppé et al., 2008)	SASP (Coppé et al., 2008)
β-gal negative*	β-gal positive* (Dimri et al., 1995)	β-gal positive (Dimri et al., 1995)
heterochromatin is mainly located at perinunclear space or nuclear periphery (Bickmore, 2013)	relative amount of heterochromatin in perinucleolar space decreases*	formation of SAHF (Narita et al., 2003)
	decrease of H3K9me3 levels in aged cells (O'Sullivan et al., 2010)	
	depletion of lamin B1 (Shah et al., 2013)	
	downregulation of DNMT1 and upregulation of DNMT3B (Cruickshanks et al., 2013)	

Table 3.1 – Alterations in human cells during cellular senescence.
RS = replicative senescence, OIS = Oncogene induced senescence, asterisk marks results of this study

3.3.4 NAD dynamics in replicative senescence

NADs were identified in proliferating and senescent IMR90 cells after hybridizing nucleolar DNA on two-colour Human CGH 4.2M Whole Genome Tiling Arrays. In order to verify the identified NADs in single cells with an independent method various genomic regions were selected and tested in 3D immuno-FISH experiments (see Table 3.2).

		association frequencies [%]		
		HeLa/IMR90	IMR90	
BAC-ID	Position	or expected	Y	S
RP11-828F4	17q21.31	< 15 %	10.8	13.4
RP11-90G23	8q21.2	23.3/31.7	8.8	1.8
RP11-81M8	19p13.3	6.1/8.5	13.2	11.9
RP11-173M10	13q21.1	27.1/28.7	33.3	23.8
RP11-914H1	4q32.3	> 25 %	8.6	13.7
RP11-44B13	19q13.12	36.5/42.5	30.2	27.8
RP11-784D7	4q34.1	-	3.0	4.9
RP11-638N4	8q23.2	-	5.0	0.9
RP11-125O21	8q22.2	< 15 %	13.2	8.3

Table 3.2 – Overview of 3D immuno-FISH results from a previous (Németh et al., 2010) and this study.
Genomic positions of selected BACs are listed. The nucleolus-association frequencies of alleles in HeLa and proliferating IMR90 cells as measured by 3D immuno-FISH (Németh et al., 2010) or the expected values based on microarray CGH results are indicated in the left column. RP11-784D7 and RP11-638N4 were shown to mark LADs that move away from the periphery during oncogene induced senescence (Sadaie et al., 2013). The right column summarizes association frequencies for proliferating and senescent IMR90 cells, that were determined in this study.

The selection of the first group of genomic regions for 3D immuno-FISH experiments was based on the the analysis of NADs in HeLa cells in a former study (Németh et al., 2010), which included also 3D immuno-FISH experiments in IMR90 cells. The BACs representing these genomic regions are: RP11-90G23, which harbors the REX1L gene and resulted in an association frequency of 23.3 % and 31.7 % in HeLa and proliferating IMR90 cells, respectively; RP11-173M10, which included the 7SKRNA gene and exhibited an association-frequencies of 27.1 % and 28.7 % and RP11-44B13, which included various zinc finger genes and showed a strong nucleolus-association with 36.5 % and 42.5% asso-

ciation frequencies. Moreover, a BAC (RP11-81M8) hybridizing to a control region, which exhibited low frequencies of nucleolus-association in the former study (6.1 % for Hela and 8.5 % for proliferating IMR90 cells) was selected. Despite the high frequency of nucleolus-association that was observed in 3D FISH-experiments in HeLa and proliferating IMR90 cells in the former study, RP11-90G23 exhibits a low frequency of nucleolus-association in 3D FISH-experiments in this study, with 9 % and 2 % association frequency in proliferating and senescent IMR90 cells, respectively. Evaluation of the normalized microarray data in the IGB (see Figure 6.4) revealed missing signals in the genomic region where the BAC localizes. Although the up- and downstream flanking regions of this gap exhibit nucleolus-association, no statements can be made concerning the status of nucleolus-association of this genomic regions in microarray analysis. Hence, an evaluation of the status of nucleolus-association of this genomic regions is problematic. In agreement with the former study, results here indicate that RP11-173M10 exhibits a high frequency of nucleolus-association in microarray experiments as this BAC is located in an area that is stably associated to nucleoli as visualized in the IGB (see Figure 6.6). Further, 3D-FISH experiments also revealed this high frequency of nucleolus association with 33 % and 24 % association frequencies in proliferating and senescent IMR90 cells, respectively. Despite its localization at a transition from a region with low frequency of nucleolus-association to a region which was identified as NAD, 3D FISH experiments results for RP11-44B13 indicate a high frequency of nucleolus association with 30 % and 28 % nucleolus association frequency in proliferating and senescent IMR90 cells, respectively. However, lower hybridization signal intensities of this region in the microarray data indicate, that the association-frequency to nucleoli of this NAD might be weak. Moreover, RP11-81M8 was selected as a control region, which included the REX1 gene and exhibited a low frequency of nucleolus-association in the former study with 6.1 % association frequency in HeLa and 8.5 % in proliferating IMR90 cells. In contrast to all other BACs, which span about 200 kb this BAC spans almost 2 Mb and is located at the sub-telomeric region of chromosome 19. In agreement with the former 3D immuno-FISH results, illustration of the normalized microarray data shows, that this BAC localizes to a region which exhibits a very low frequency of nucleolus-association in a region of about 6 Mb (see Figure 6.5). In addition, the results of FISH experiments also indicate a low association-frequency with 13 % and 12 % nucleolus association frequency in proliferating and senescent IMR90 cells, respectively.

Further genomic regions were selected based on experiments done by Sadaie et al. (2013). There, the association of genomic regions to the nuclear lamina in RIS was investigated. It was observed that specific genomic regions lose their association to the nuclear lamina. Moreover, the data suggested that some genomic regions change their localization from the nuclear periphery to the perinucleolar space in this type of senescence. Hence, two BACs were tested with respect to their nucleolus-association in replicative senescence. In RIS both BACs, RP11-784D7 and RP11-638N4, show a decrease in localization to the nuclear periphery from about 70 % to about 30 % (Sadaie et al., 2013). Furthermore, mi-

croscopy images shown in this study suggest a nucleolus-association of the genomic region labeled by the BAC RP11-784D7 in RIS, therefore this BAC and in addition RP11-638N4 were selected to test their localization in replicative senescence. Visualization of LAD (Sadaie et al., 2013) and NAD maps in the IGB illustrated the association to the nuclear periphery in proliferating IMR90 cells and a high frequency of nucleolus-association in proliferating and senescent IMR90 cells (see Figures 6.9, 6.10). However, the results of 3D FISH-experiments indicate a very low frequency of nucleolus-association, with association frequencies below 5 % for both genomic regions in proliferating and senescent IMR90 cells. The different types of nuclear rearrangements in RIS and replicative senescence (see Section 3.1) might explain the variation in the localization of the tested genomic regions between this and the other study (Sadaie et al., 2013).

Last, genomic regions were selected by visualization of the normalized microarray data in the IGB. RP11-828F4 spans a genomic region, where the UBF gene is located and that exhibits a very low frequency of nucleolus-association (Figure 6.3). This was in agreement with data obtained in 3D immuno-FISH experiments with 10 % and 13 % association frequency in proliferating and senescent IMR90 cells, respectively. In addition, RP11-125O21 was also located in a genomic region, which exhibits a low frequency of nucleolus-association (Figure 6.11). This status of low association frequency was reproduced in 3D immuno-FISH experiments, where this genomic region showed 13 % and 8 % association-frequency in proliferating and senescent IMR90 cells, respectively. In contrast, RP11-914H1 localizes to a region that exhibited nucleolus association in the normalized microarray data in proliferating and senescent IMR90 cells (Figure 6.7). However, 3D immuno-FISH experiments showed a low frequency of nucleolus-association, with 8 % and 14 % of the alleles associated to nucleoli in proliferating and senescent IMR90 cells, respectively.

Experiments presented here were carried out in 50 cells for each physiological condition except for RP11-914H1, where 27 and 29 IMR90 cells were analyzed for proliferating and senescent IMR90 cells, respectively. To further validate and strengthen the statements, additional analyses should be performed at additional genomic loci and by collecting more data from the localization of each chromosome region. It is worth mentioning that high-throughput data and cytological assays do not always give comparable results (Williamson et al., 2014). High-throughput methods depend on parameters like the cross-linking reagent and give usually an average over the complete cell population, while providing a high resolution. In contrast, 3D FISH analysis is a low throughput method giving information about the status in a single cell, however it requires analysis of a vast amount of cells to get reliable results at a lower resolution. The use of single-cell genomics will presumably reduce the gap between high-throughput genomics and FISH analyses of nuclear architecture, however it can certainly not replace FISH analyses, which are to date the most valuable validation assays for genomics studies of nuclear architecture.

3.4 Changes in nucleolus-associated chromatin upon UBF knock-out in MEF cells

The analysis of NADs was initially performed in human cancer cell lines (Németh et al., 2010; van Koningsbruggen et al., 2010) and it was extended to their senescence-dependent dynamics in normal human diploid cells in this study. However, no analysis has been performed before in other species. Therefore the analysis of mouse NADs was initiated here to provide the basis for future comparative analyses. Furthermore, the dynamics of NADs after inactivation of Pol I, which was achieved by genetic depletion of UBF in a mouse model system, should be characterized. When UBF is knocked-out this leads to large rearrangements of the nuclear architecture and the disruption of nucleoli. Nucleolar proteins, such as fibrillarin or Pol I cluster in one proteinaceous body which does no longer harbor the rDNA (Hamdane et al., 2014). This reorganization prompted us to analyze nucleolus-associated chromatin in mouse cells before and after knock-out of UBF.

In order to identify NADs in MEF cells and to characterize their dynamics after inactivation of Pol I, nucleolus-associated DNA was isolated from mutant and wild-type MEF and iMEF cells before and 72 h after UBF knock-out. Nucleoli were isolated 72 h after UBF knock-out, since rRNA transcription was no longer detected and MEF cells were still viable and did not show gross morphological alterations. The size an shape of isolated nucleoli was evaluated with light microscopy during the isolation procedure, to evaluate the quality of the isolated particles. Nucleoli were visible as refractive bodies that exhibited comparable size an shape as nucleoli in MEF cells before isolation. Moreover, the nucleolar origin of isolated particles was validated in immunofluorescence experiments in which nearly all particles stained positive for the nucleolus marker fibrillarin. The isolated nucleolar DNA was then hybridized on CGH arrays against genomic DNA and the raw data are currently analyzed.

Satellite repeats and centromeric heterochromatin are major building blocks of NADs in human diploid fibroblasts. In MEF cells centromeric regions are very well visible in DAPI-stained nuclei as DAPI-dense regions, known as chromocenters, that form a large portion of the murine constitutive heterochromatin. Satellite repeat regions cluster at the centromeres in mouse cells: minor satellite repeats build the centromeres and major satellite repeats are localized in the pericentric regions (see Figure 2.43). The rDNA is localized on the NOR-bearing chromosomes 12, 15, 16, 17, 18 and 19 adjacent to the centromeres on the linear DNA sequence. Hence, the localization of the rDNA with respect to the major satellite repeats was investigated in 3D immuno-FISH experiments in MEF cells before and after UBF knock-out. The results supported the previously observed separation of the rDNA from the nucleolar marker protein fibrillarin. Furthermore, rDNA appears as condensed foci, which co-localized with regions of the constitutive heterochromatin formed by major

satellite repeat units, illustrating their inactivation. In summary these analyses provide the basis for further investigations of NADs and their dynamics in mouse cells.

4 Materials

Unless otherwise stated, all common chemicals and materials were purchased from Bio-Rad, GE-Healthcare, Merck, Invitrogen, Fermentas, New England Biolabs (NEB), Promega, Roche, Roth, Serva, Stratagene/Agilent, Sigma-Aldrich and Qiagen.

4.1 Instruments

Instrument	Supplier
-80 $°C$ freezer	Sanyo
37 $°C$ incubator	Heraeus Instruments
37 $°C$ plate incubator	Memmert
agarose gel chamber	Werkstatt Universität Regensburg
Autoclave LTA 25B2	Zirbus
Axiovert 200M inverted fluorescence microscope equipped with a greyscale CCD camera	Zeiss
Axiovert 35 inverted fluorescent microscope equipped with a ColourView imaging system	Zeiss
Bioruptor®	Diagenode
Centrifuge 5415R	Eppendorf
Centrifuge Centrikon T-324	Kontron Instruments
Centrifuge 3-16 K	Sigma
Centrifuge 1-14 (non-cooled)	Sigma
Centrifuge 4-15 (ZK)	Sigma
Drying cabinet	Memmert
GelMax UV imaging system	Intas
Laminar flow hood	antair BSK
Ice machine	Ziegren
Incubator SafeCell UV	Sanyo
Cooled incubator	LMS
Magnetic stirrer MR Hei-Mix L	Heidolph
Magnetic stirrer MR 3001	Heidolph
Microwave	Sharp

Instrument	Supplier
Microwave	MDA
Veriti 60 well cycler	Applied Biosystems
NanoDrop UV Spectrometer ND-1000	PeqLab
Overhead shaker	Biosan
Purelab Ultra	ELGA
pH electrode	Knick
pH meter	Knick
Photometer	Amersham Biosciences
Pipetman pipets	Gilson
Pipethelper Pipetboy comfort	Integra Biosciences
Power supply - EPS301	GE Healthcare
Protein gel chambers	Invitrogen
Qubit 2.0 Fluorometer	Invitrogen
Rotor-Gene RG3000 system	CORBETT Research
RotorShake genie	Scientific Instruments
SafeImager	Invitrogen
Sonifier 250	Branson
TCS SP8 MP confocal microscope	Leica
Thermomixer comfort	Eppendorf
Trans-Blot® SD Semi-Dry Transfer Cell	BioRad

4.2 Software and online tools

Software	Supplier
Axiovision	Zeiss
ImageJ v1.49s	NIH, open-source http://imagej.nih.gov/ij/
R-Studio	open-source http://www.rstudio.com/
IGB	NIH, open-source http://bioviz.org/igb/
UCSC gene browser	http://genome.uscs.edu
Rotorgene 6000	CORBETT research

4.3 Consumables and Chemicals

Description	Supplier
Immobilon-P Membrane	Millipore
Parafilm "M" Laboratory Film	Pechiney
Pasteur pipets glass 230 mm	Hirschmann
Petri dishes	Greiner
Pipet tips	Sarstedt
poly-L-Lysine coaeted microscopic slides	Sigma
Reaction tubes 1.5 ml/2 ml	Roth
Stuffed pipet tips	Biosphere
Test tube with screw cap 15 ml	Sarstedt
Test tube with screw cap 50 ml	Sarstedt
Whatman paper	Macherey-Nagel
Ammoniumpersulfate (APS)	Fluka
Ampicillin (Na-salt)	Roth
β-mercaptoethanol	Sigma
Bluo-Gal	Invitrogen
Bradford Reagent	BioRad
Bromphenolblue	Serva
BSA (albumin fraction V)	NEB
N-cyclohexyl-3-aminopropanesulfonic acid (CAPS)	Sigma
Coomassie Brilliant Blue G-250	Biorad
Complete Protease Inhibitor Cocktail Tablets (PI) EDTA free	Roche
Cot-1 DNA	Invitrogen
Dimethylsulfoxide	Merck
dNTPs	Invitrogen
Fetal Calf Serum (FCS)	PAA + Sigma
Formamide	Sigma
para-Formaldehyde	Merck
Formaldehyde 37 %, stabilized with 10 % MeOH	Merck
Glycerol 87 %	Merck
HEPES	GIBCO
Isopropanol p.a.	Merck
Kanamycin	Roth
Magnesium chloride	Merck

Description	Supplier
Milk powder	Sucofin
Orange-G	Sigma
Ponceau S	Sigma
Rotiphorese® Gel 30	Roth
rubber cement (Fixogum)	Marabu
Salmon Sperm DNA	Invitrogen
Sodium dodecyl phosphate	Merck
SYBR Safe	Invitrogen
(Z)-4-Hydroxytamoxifen	Sigma
Tris-(2-carboxyethyl)-phosphin (TCEP)	Sigma
N,N,N',N'-Tetramethylethylendiamine (TEMED)	Roth
Triton-X 100	Roth
TE-buffer	Invitrogen
Trypsin-EDTA	Invitrogen
Tween® 20	Roth
dUTP-Cy3	kind gift by Cremer Lab
dUTP-Texas Red	kind gift by Cremer Lab
dUTP-biotin	Jena Bioscience
Vectashield	Vector Laboratories Inc.

4.4 Buffers, Solutions and Media

Buffer	Ingredients
Western-Blot (WB) Anode buffer 1	300 mM Tris, 15 % methanol (v/v)
WB Anode buffer 2	25 mM Tris, 15 % methanol (v/v)
WB Cathode buffer	70 mM CAPS pH 10.5, 15 % methanol (v/v)
DNA sample buffer	50 % glycerol (v/v), 50 mM Tris/HCl pH 7.6, 10 mM EDTA, 0.05 % Orange G (w/v)
LB medium	1 % Bacto™ Tryptone (w/v), 0.5 % Bacto™ Yeast Extract (w/v), 1 % NaCl (w/v), add 2 % agar (w/v) for agar plates
DNA lysis buffer	50 mM Tris pH 8.0, 100 mM EDTA, 100 mM NaCl, 1 % SDS (w/v)

Buffer	Ingredients
Phosphate buffered Saline (PBS)	137 mM NaCl, 2.7 mM KCl, 1 mM Na_2HPO_4, 2 mM KH_2HPO_4 pH 7.4
PBS-T buffer	PBS with 0.1 % Tween 20 (v/v)
PBS-T milk buffer	PBS-T with 5 % milk powder (w/v)
SDS-protein sample buffer (6x)	300 mM Tris-HCl pH 6.8, 10 % SDS (w/v), 50 % glycerol (v/v), 5 % β-Mercaptoethanol (v/v), 0.2 % bromphenol blue (w/v)
SDS-Page stacking buffer (4x)	0.5 M Tris-HCl, 0.4 % SDS (w/v), pH 6.8 with HCl
SDS-Page separating buffer (4x)	1.5 M Tris-HCl, 0.4 % SDS (w/v), pH 8.8 with HCl
SDS running buffer	3.5 mM SDS, 25 mM Tris, 190 mM glycine
TBE buffer	90 mM Tris/HCl, 90 mM boric acid, 2 mM EDTA, pH 8.0
10x NT-buffer	0.5 M Tris-HCl pH 7.5, 50 mM $MgCl_2$, 0.05 % BSA (w/v)
STOP MIX for NT	0.1 % bromphenolblue (w/v), 0.5 % dextranblue (w/v), NaCl 0.1 M, EDTA pH 8 20 mM, Tris HCl pH 7.5 20 mM
Master Mix for NT	2 x SSC, 20 % dextran sulfate (w/v)
High Magnesium (HMg)	10 mM Hepes pH 7.4, 0.88 M sucrose, 12 mM $MgCl_2$, 1 mM TCEP, PI
Low Magnesium (LMg)	10 mM Hepes pH 7.4, 0.88 M sucrose, 1 mM $MgCl_2$, 1 mM TCEP, PI
TE buffer	10 mM Tris pH 7.5, 1 mM EDTA
20x SSC	3 M NaCl, 300 mM $Na_3C_6H_5O_7$ pH 7.0
Buffer A	10 mM Hepes pH 7.9, 10 mM KCl, 1.5 mM $MgCl_2$, 0.5 mM TCEP
Nucleolus isolation Solution S1	0.25 mM Sucrose, 10 mM $MgCl_2$
Nucleolus isolation Solution S2	0.35 mM Sucrose, 0.5 mM $MgCl_2$
Nucleolus isolation Solution S3	0.88 mM Sucrose, 0.5 mM $MgCl_2$
Reticulocyte standard buffer (RSB)	10 mM NaCl, 1.5 mM $MgCl_2$, 10 mM Tris-HCl pH 7.0

Buffer	Ingredients
30 % sucrose	30 % sucrose (w/v), 10 mM NaCl, 2.5 mM Tris-HCl pH 7.2

4.5 Enzymes

Enzymes	Supplier
DNase I grade II	Roth
DNA Polymerase I	Fermentas
Proteinase K	Sigma
RNase A	Sigma
Taq DNA polymerase	Langst lab
HotStarTaq	Qiagen
Trypsin/EDTA	PAA and Gibco

4.6 Kits

Kit	Supplier
BM Chemilumineszenz Blotting Substrate (POD)	Roche
RNA isolation kit	Macherey and Nagel
Senescence detection kit	BioVision
Qbit dsDNA BR Kit	Invitrogen
Qbit dsDNA HS Kit	Invitrogen
Qbit RNA Kit	Invitrogen
Qiagen Mini Prep Kit	Qiagen
Super Signal WEST Dura WB Kit	Pierce
illustra GenomiPhi V2 DNA Amplification Kit	GE Healthcare Life Sciences

4.7 Standard DNA and protein weight markers

Weight marker	Supplier
2-log ladder	NEB
50bp ladder	NEB
Gene ruler 1kb plus DNA ladder	Fermentas
Prestained Protein ladder plus	Fermentas

4.8 Antibodies

Abbreviations: IF - Immunofluorescence, WB - Western Blot, M - mouse, Rb - Rabbit, G - goat, DL - Dye Light, StrA - Streptavidin, Dig - Digoxigenin, Rho - Rhodamine.

4.8.1 Primary antibodies

Antibody	Supplier	species	Dilution
anti-UBF	Santa Cruz sc-9131	rabbit, polyclonal	IF, use at 1:50 WB, use at 1:1000
anti-B23	Santa Cruz sc-56622	mouse, monoclonal	IF, use at 1:150 WB, use at 1:1000
anti-B23	Santa Cruz sc6013R	rabbit, monoclonal	IF, use at 1:100 WB, use at 1:1000
anti-RPA194	Santa Cruz sc-48385	mouse, monoclonal	IF, use at 1:250
anti-RPA194	Santa Cruz sc-28714	rabbit, polyclonal	IF, use at 1:100
anti-Ki-67	Santa Cruz sc-15402	rabbit, polyclonal	IF, use at 1:100
anti-Fibrillarin	Santa Cruz sc-56676	mouse, monoclonal	IF, use at 1:100 WB, use at 1:1000
anti-Fibrillarin	Novus, NB300-269	mouse, monoclonal	IF, use at 1:100
anti-H3K9me1	Kimura lab (Hayashi-Takanaka et al., 2011)	mouse, monoclonal	IF, use at 1:100
anti-H3K9me3	Kimura lab (Hayashi-Takanaka et al., 2011)	mouse, monoclonal	IF, use at 1:100
anti-H3K9me2	Kimura lab (Hayashi-Takanaka et al., 2011)	mouse, monoclonal	IF, use at 1:100
anti-H3K9ac	Kimura lab (Hayashi-Takanaka et al., 2011)	mouse, monoclonal	IF, use at 1:500
anti-H3K9me3	abcam ab8898	rabbit, polyclonal	IF, use at 1:100
anti-H3K27me3	Active Motif 61017	mouse, monoclonal	IF, use at 1:100
anti-LaminB1	Santa Cruz sc-6216	goat, polyclonal	IF, use at 1:250 WB, use at 1:500
anti-Tubulin DM1A	abcam ab7291	mouse, monoclonal	IF, use at 1:200 WB, use at 1:1000
anti-Lamin A/C	Santa Cruz sc-20681	rabbit, polyclonal	WB, use at 1:500

4.8.2 Secondary antibodies

Antibody	Supplier	Species	Dilution
anti-M-Cy3	Jackson IR	goat	IF, use at 1:500
anti-M-Cy5	Jackson IR	goat	IF, use at 1:500
anti-M-DL488	Jackson IR	donkey	IF, use at 1:500
anti-M-A488	Molecular Probes	goat	IF, use at 1:500
anti-M-A350	Life Technologies	goat	IF, use at 1:250
anti-Rb-DL488	Jackson IR	donkey	IF, use at 1:200
anti-Rb-Cy3	Jackson IR	goat	IF, use at 1:200
anti-Rb-A594	Molecular Probes	goat	IF, use at 1:500
anti-G-DL594	Jackson IR	goat	IF, use at 1:500
StrA-A488	Invitrogen	-	IF, use at 1:250
anti-Dig-Rho	Roche	sheep	IF, use at 1:100

4.9 Bacterial strains

XL-1 Blue	
general	F-episome, general DNA plasmid propagation, blue/white screening
resistance	tetracycline
genotype	recA1 endA1 gyrA96 thi-1 hsdR17 supE44 relA1 lac F'proAB laclqZDM15 Tn10

4.10 Mammalian cell lines

IMR90-79	
cell type	human fetal lung fibroblast
maintenance	37 °C, 5 % CO_2, DMEM-GlutaMAX, low Glucose (1 g/L), 10 % FCS
supplier	Coriell Cell Repositories
cells were obtained at a PDL of 12, characterized by Nichols et al. (1977)	
HeLa	
cell type	human cervix carcinoma
maintenance	37 °C, 5 % CO_2, DMEM-GlutaMAX, low Glucose (1 g/L), 10 % FCS
cells were obtained second hand at a low passage number	
K562	
cell type	human blood cells (chronic myelogenous leukemia)
maintenance	37 °C, 5 % CO_2, RPMI 1640 + 2 mM Glutamine, 10 % FCS
cells were obtained second hand at a low passage number	
MEF UBF$^{wt/wt}$/ER-Cre$^{+/+}$/p53$^{-/-}$ + MEF UBF$^{fl/fl}$/ER-Cre$^{+/+}$/p53$^{-/-}$	
cell type	mouse embryonic fibroblast
maintenance	37 °C, 5 % CO_2, DMEM-GlutaMAX, high Glucose (4 g/L), 10 % FCS
MEF-cells were kindly provided by Professor Tom Moss (CRCHU de Québec) characterized in (Hamdane et al., 2015)	
iMEF UBF$^{wt/wt}$/ER-Cre$^{+/+}$/SvT + iMEF UBF$^{fl/fl}$/ER-Cre$^{+/+}$/SvT	
cell type	mouse embryonic fibroblast
maintenance	37 °C, 5 % CO_2, DMEM-GlutaMAX, high Glucose (4 g/L), 10 % FCS
MEF-cells were kindly provided by Professor Tom Moss (CRCHU de Québec) characterized in (Hamdane et al., 2014)	

4.11 Oligonucleotides

4.11.1 Genotyping primer

Name		sequence (5'-3')
UBF	A	TGATCCCTCCCTTTCTGATG
UBF	B	CACGGGAAAACAAGGTCACT
UBF	C	TGGGGATAGGCCTTAGAGAGA
ERCre	R1295	GCGAAGAGTTTGTCCTCAACC
ERCre	R523	GGAGCGGGAGAAATGGATATG
ERCre	R26F2	AAAGTCGCTCTGAGTTGTTAT
p53	A	ACAGCGTGGTGGTACCTTAT
p53	B	TATACTCAGAGCCGGCCT
p53	C	CTATCAGGACATAGCGTTGG

4.11.2 qPCR primer

Name		sequence (5'-3')
Hs5	fwd	CCTGCTGTTCTCTCGCGC
(5S rRNA)	rev	GGTCAGAGACCCGGACCC
	TaqMan probe	6FAM-AGCGTCCCGACTCCCGGTGC-TAMRA
HBac	fwd	TGCCGACAGGATGCAGAAG
(b-actin)	rev	GCCGATCCACACGGAGTACTT
	TaqMan probe	6FAM-TCAAGATCATTGCTCCTCCTGAGC-TAMRA
HF9776	fwd	GCCACTTTTGGTAAGCAGAACTG
(28S rRNA)	rev	CATCGGGCGCCTTAACC
	TaqMan probe	6FAM-CTGCGGGATGAACCGAACGCC-TAMRA

4.11.3 BAC clones

BAC cloes were obtained from BACPAC resources (http://bacpac.chori.org/libraries.php).

BAC-ID	Position	internal code	features
RP11-828F4	17q21.31	**AN-16**	UBF
RP11-90G23	8q21.2	**AN-19**	REX1L
RP11-81M8	19p13.3	**AN-23**	REX1 gene
RP11-173M10	13q21.1	**AN-24**	7SKRNA
RP11-914H1	4q32.3	**AN-39**	ctrl FRG1A,2A
RP11-44B13	19q13.12	**AN-51**	various ZNF genes
RP11-784D7	4q34.1	**AN-56**	(Sadaie et al., 2013)
RP11-638N4	8q23.2	**AN-57**	(Sadaie et al., 2013)
RP11-125O21	8q22.2	**AN-58**	-
distal junction (DJ)	BAC labeling the distal region of the rDNA repeat for further information see (Floutsakou et al., 2013)		

4.11.4 Biotinylated oligonucleotides

Telomere	LNA™ FISH Probe labeling telomere region (EXIQON)
Satellite-2	LNA™ FISH Probe labeling satellite-2 repeats (EXIQON)
LNA-2	ATtCcAtTcaGaTtCcAtTcGaTc*
	*Capital letters indicating LNA-nucleotides
alpha-satellite	LNA™ FISH Probe labeling α-satellite repeats (EXIQON)

4.12 Plasmids

human sequences	
Clone	position rel. to Gene Bank Acc# U13369
Hsr4	18.1 - 30.5 of intergenic spacer
Hsr6	30.5 - 42.5 of intergenic spacer
	for further information see (Mais et al., 2005)

murine sequences	
Clone	position in BK000964
M6/2-2	5646 - 12252
M6/31-2	20138 - 26351
	for further information see (Grozdanov et al., 2003)

5 Methods

5.1 DNA methods

5.1.1 Isolation of genomic DNA from human cells

In order to isolate genomic DNA cells were grown on 6-well plates. After aspirating the medium lysis buffer was added and incubated for 2 min (at least 300 µL per 6-well). The suspension was transferred into a sterile cup and 10 µL of a 10 $\frac{mg}{mL}$ RNase A solution was added per milliliter lysate. After the sample was incubated for a minimum of 2 hours at 37 $°C$, 25 µL of a 10 $\frac{mg}{mL}$ proteinase K solution per milliliter lysate was added and incubated over night at 50 $°C$.

The next day, the lysate was mixed with 0.5 volumes of 7.5 M ammonium acetate solution and 2 volumes of absolute ethanol were added to the DNA solution together with 2 µL 20 $\frac{mg}{mL}$ glycogen. The mixture was spun down in a tabletop centrifuge for 10 min at 16,100 g. The supernatant was carefully removed and the pellet washed with 1 mL 70 % ethanol and centrifuged at room temperature for 5 min. The pellet was then air-dried for about 10 min. It was then resuspended in the required volume of water.

5.1.2 Isolation of plasmid DNA from bacteria

Small scale DNA preparations were performed with 3 mL of an overnight bacteria culture using the Qiagen Mini prep used according to the manufacturer's instructions.

5.1.3 Isolation of nucleolar DNA and array CGH experiments

5.1.3.1 Isolation of nucleolar DNA after formaldehyde cross-linking from human cells

Isolation of nucleoli was performed as described earlier (Sullivan et al., 2001). In short: cells were grown on 15 cm plates and formaldehyde (37 %, stabilized with 10 % MeOH) was added to a final concentration of 1 % to fix $1x10^8$ cells (about 10 plates with approximately 70-80 % cell density) for 10 min at room temperature on a shaking platform. To stop fixation and to bind residual formaldehyde 800 µL of 3.25 M glycine per plate was added and incubated for 5 min on a shaking platform. After washing cells 2 times with ice cold 1xPBS they were scraped off and pooled in 100 mL 1xPBS and spun down at 750 g

for 5 min at 4 $°C$. Supernatant was discarded and cells were resuspended in 1 mL HMg buffer. 5 µL sample was taken for SDS-PAGE, furthermore an aliquot was taken for light microscopic analysis. Cells were sonicated on ice for 3x10 sec with fine tip (Branson sonifier; 65 % output, 70 % duty cycle) in a 15 mL tube. After centrifugation (15000 g, 30 s), a 5 µL aliquot was taken for SDS-PAGE. Supernatant was set aside for DNA precipitation and the pellet was then resuspended in 1 mL LMg buffer and release of nucleoli was monitored under the light microscope. Nucleoli were sonicated on ice for 2x10 sec (Branson sonifier; 65 % output, 70 % duty cycle) and centrifuged (15000 g, 2 min). Supernatant was set aside for DNA precipitation and the pellet was then resuspended in 200 µL 20 mM Tris pH 8.1 and the cleaning of nucleoli was monitored microscopically. Additionally an aliquot (10 µL) was taken for SDS-PAGE. After adding 3 µL of RNAse A (10 $\frac{mg}{mL}$) nucleoli were incubated for 1 h at 37 $°C$. Then 5 µL Proteinase K were added and proteins were digested at 37 $°C$ for 8 h and the cross-link was reversed at 65 $°C$ for 8 h. DNA was precipitated as described above (see Section 5.1.1) and finally dissolved in 27 µL TE buffer. For quality control analysis 1 µL of DNA was separated on a 1 % agarose gel and concentrations were measured.

5.1.3.2 Isolation of nucleolar DNA after formaldehyde cross-link from MEF cells

Isolation of nucleoli from MEF cells was performed as described for IMR90 cells above with the following changes in the experimental procedure.

Instead of performing the sonication of the cells with the Branson sonifier cells were sonified with the Bioruptor® (Diagenode) device. For the first sonication the resuspended pellet was split into aliquots of 300 µl in standard 1.5 mL reaction cups, and they were sonicated on ice-cold water 30 sec on 30 sec off for 3 × 5 min with high mode. Then the pellet was centrifuged and resuspended in HMg as described above. For the second sonication the resuspended pellet was again split in 300 µl aliquots and sonicated for 3 × 5 min, 30 sec on 30 sec off. This time the nucleoli were checked after each 5 min sonication step and sonication was stopped if the quality of the isolated nucleoli was already good and no nuclear remnants were visible. After the second sonication protein digestion, RNA digestion and DNA precipitation was performed as described for IMR90 cells.

5.1.3.3 Isolation of nucleolar DNA without formaldehyde cross-linking from human cells

Nucleolus isolation with one step of centrifugation after nucleus preparation

Isolation of nucleoli was performed based on a procedure described earlier (Bhorjee and Pederson, 1973). In short, 1x10^8 K562 cells were washed 3 times with ice-cold PBS and centrifuged (300 g, 4 min, 4 $°C$). Cells were broke to release nuclei using a pre-chilled dounce homogenizer (10 strokes with a tight pestle) and centrifuged (1000 g, 3 min, 4 $°C$). Nuclear pellet was washed twice in 5 ml RSB. The pellet was was resuspended in 3 ml RSB and sonicated using Branson sonifier 250 on ice (5 $\times$ 10 sec, output 2, constant, 1 min pauses). The sonicated sample was then layered over 3 ml 30 % sucrose and centrifuged (4500 g, 15 min, 4 $°C$). The pelleted nucleoli were resuspended in 1 ml RSB and DNA isolation (including protein and RNA digestion) was performed as described above.

Nucleolus isolation with two steps of centrifugation after nucleus preparation

Isolation of nucleoli was performed as described in Andersen et al. (2002) which is based on a protocol described earlier (Muramatsu et al., 1963). In short, 1x10^8 cells were washed 3 times with ice-cold PBS and centrifuged (300 g, 4 min, 4 $°C$). After resuspending the cells in 5 mL of Buffer A they were kept on ice for 5 min. Cells were broken up to release nuclei using a pre-chilled dounce homogenizer (10 strokes with a tight pestle). Then cells were centrifuged (228 g, 5 min, 4 $°C$) and the pellet was resuspended in 3 mL S1 and layered over 3 mL S2 in a 15 mL tube. After centrifugating (1430 g, 5 min, 4 $°C$) the pellet was resuspended in 3 mL S2 and sonicated using the Bioruptor (6-9 x 10 sec, 30 sec on ice in between). The release of nucleoli was checked under the light microscope and the sonicated sample was layered over 3 mL S3 in a 15 mL tube and centrifuged (2800 g, 10 min, 4 $°C$). Nucleoli were washed once in 500 µL S2 and resuspended in 1 mL S2. Then proteins and RNA were digested and DNA was precipitated as described above.

5.1.3.4 Microarray experiments

2 µg of isolated nucleolar DNA of two biological replicates from proliferating and senescent IMR90 cells as well as nucleolus-associated DNA purified with different approaches from K562 cells were submitted to Source Biosciences (Berlin) and analyzed on high-resolution two-colour Human CGH 4.2M Whole Genome Tiling Arrays with a median probe spacing of 284 bp. At Source Biosciences (Berlin) the nucleolus-associated DNA was labeled with Cy3 and the genomic control DNA with Cy5 and hybridized together on one array. Signal intensity data were extracted from the scanned images of each array and a spatial correction was applied to reduce signal variation. Then signals were normalized using the

qspline normalization method (Workman et al., 2002). Finally, a window-averaging step with a window size of 2800 bp was included. The term 'normalized microarray data' refers to this data processing throughout the text.

Isolated nucleolar DNA from MEF cells was submitted for analysis on Agilent SurePrint G3 microarrays with a median probe spacing of 1.5 kb for coding regions and 2.5 kb for non-coding regions. No normalization was performed by the service provider and primary microarray data are currently analyzed.

5.1.4 DNA agarose gel electrophoresis

DNA was analyzed by electrophoresis on 1 % agarose gels unless otherwise stated. 0.5 g agarose was mixed with 50 mL 1xTBE buffer and heated until the agarose was completely dissolved. Before the mixture was poured in a gel chamber, SYBR Safe was added as a staining reagent. When the gel was solidified samples were mixed with 10xDNA loading buffer, and the gel was run after sample loading in 1xTBE buffer at 100 V for the appropriate time to separate the different DNA fragments. To visualize the DNA, the Invitrogen SafeImager system was used.

5.1.5 Measurement of DNA concentration

DNA concentrations were determined via absorbance measurement at 260 nm using NanoDrop ND1000. The purity of the DNA sample was checked by determining A260/A280 and A260/A230 absorbance ratios in addition to the agarose gel electrophoresis.

5.1.6 PCR genotyping of MEF cells

To check the genetic status of the different MEF knockout cells different genotyping PCRs were performed for the cell lines with $p53^{-/-}$ / $p53^{+/+}$, $UBF^{wt/wt}$ / $UBF^{fl/fl}$ and $ER\text{-}Cre^{+/+}$ genetic background.

	[µL]
H_2O	19
Taq Buffer 10x	2.5
dNTP 10 mM	1.25
Primer 1 100 $\frac{pmol}{\mu L}$	0.25
Primer 2 100 $\frac{pmol}{\mu L}$	0.25
Primer 3 100 $\frac{pmol}{\mu L}$	0.25
Taq Polymerase	0.5
DNA (25 ng)	0.5

Cycling conditions were slightly different for p53 and UBF/Cre. p53 primers needed 58 °C annealing temperature whereas UBF and Cre needed 54 °C. For p53 fragment amplification 29 cycles were needed, for UBF and Cre DNA fragments 35.

Initial denaturation	95 °C	10 min	1x
Denaturation	95 °C	1 min	
Annealing	58/54 °C	1 min	29/35x
Extension	72 °C	90 sec	
Final Extension	72 °C	5 min	1x

PCR product sizes were as follows:

p53	
WT	450 bp
delta	650 bp
UBF	
flox/flox	628 bp
wt/wt	428 bp
Cre	
Cre/Cre	320 bp
wt/wt	650 bp

5.1.7 Quantitative PCR (qPCR)

Real-time PCR was used to measure the amount of a specific DNA fragment in a quantitative manner. Each reaction was performed in technical triplicates. The quantity of DNA was detected after each PCR cycle by measuring the fluorescence of 6-fluorescein amidite (6-FAM) which is released from the TaqMan-probe and is no longer quenched.

qPCR reactions were performed in 0.2 mL PCR tubes with a reaction volume of 20 µL.

PCR reaction:

	[µL/reaction]
MasterMix	9.67
HotStar Taq Qiagen 5 $\frac{U}{mL}$	0.08
fwd Primer [4 mM]	1.5
rev Primer [4 mM]	1.5
FAM labeled Primer [2 mM]	2
water	1.25
DNA	4

MasterMix:

	[µL/reaction]
25 mM $MgCl_2$	0.8
10x PCR buffer (Qiagen)	2
10 mM dNTPs	0.4
water	6.47

qPCR was performed using the Rotor-Gene RG3000 system from CORBETT Research, 6-FAM was excited at 480 nm, fluorescence was recorded at 510 nm. After all reactions were prepared, PCR-reaction was performed following this program.

Initial denaturation	$95°C$	15min	1x
Denaturation	$95°C$	10 sec	40x
Extension	$60°C$	60 sec	

Calculating the enrichment of nucleolar DNA compared to gDNA was performed as follows: c_t values for one amplified region from nucleolar DNA and gDNA were determined using the Rotorgene 6000 software. Then the enrichment was calculated using the Δ c_t value: $2^{c_{t_{NoDNA}} - c_{t_{gDNA}}}$. This was then normalized to the initial template concentrations that were present in the reactions, to get the final fold-enrichment: $\frac{enrichment}{\frac{c(NoDNA)}{c(gDNA)}}$.

5.2 Protein methods

5.2.1 SDS polyacrylamide gel electrophoresis

Proteins were separated according to their molecular weight by SDS-PAGE.

Invitrogen MiniCell cassettes were used for SDS-PA gels of different percentages. The solutions were prepared according to the following pipetting scheme for one gel (Sep: Separating gel, Stack: Stacking gel).

Gel type	**Sep 7.5%**	**Sep 10%**	**Sep 17%**	**Stack 5%**
water (mL)	2.96	2.46	1.06	0.87
30% acrylamide (mL)	1.5	2.00	3.4	0.25
4x lower buffer (mL)	1.5	1.5	1.50	/
4x upper buffer (mL)	/	/	/	0.38
20% APS w/v (mL)	0.03	0.03	0.03	0.0075
TEMED (mL)	0.006	0.006	0.006	0.0015

APS and TEMED were added at last to start polymerization. The solution for the separating gel was subsequently poured into the gel chamber and overlaid with isopropanol. After polymerization, the isopropanol was removed, the stacking solution prepared and immediately cast onto the separating gel. Then, combs were inserted and the gel got polymerized. Finally, gels were wrapped in wet tissue paper and plastic foil for storage at 4 $°C$.

Protein samples were mixed with the appropriate amount of 6x Laemmli buffer and boiled for 10 min at 95 $°C$. The samples were pipetted into the slots of the gel. Electrophoresis was carried out at constant current of 35 mA for the required time at room temperature. The gel chamber was then disassembled and Coomassie staining or Western Blot analysis were performed as described in the following.

5.2.2 Western blot

In a western blot, proteins are transferred by electrophoresis, capillary action or diffusion to a carrier membrane where they get immobilized and detected. Here semi-dry electroblotting was used and the proteins were visualized by immunodetection.

5.2.2.1 Semi-dry blotting

Negatively charged SDS-protein complexes were transferred from an SDS-PA gel onto a PVDF membrane by electrophoresis. SDS-PAGE was done as described above and after

this, the gel was cut to a size of 8x5 cm. Three 0.34 mm thick Whatman blotting papers and the PVDF membrane were also cut to the same size. Then they were soaked in the following buffers for 5 min and assembled in a BioRad semi-dry blotting apparatus in the following order from anode to cathode:

2 Whatman paper	WB Anode buffer 1
2 Whatman paper	WB Anode buffer 2
PVDF membrane	100% methanol
2 Whatman paper	WB Cathode buffer

The blot was assembled without air-bubbles between the different layers. Transfer was carried out at room temperature at 100 mA (2.5 $\frac{mA}{cm^2}$) at constant voltage for 60 min.

5.2.2.2 Ponceau S staining

To see whether the transfer to the membrane worked a Ponceau S staining was performed. This method stains proteins reversibly and does not interfere with subsequent immunodetections. The membrane was first rinsed in H_2O_{dd} and incubated in methanol for 10 min. Afterwards it was incubated in the Ponceau S staining solution (0.1 % Ponceau S (w/v) in 5.0 % acetic acid (w/v)). Then the membrane was rinsed in H_2O_{dd} and the staining got visible. Staining was removed by continued washing steps. After Ponceau S staining, the membrane was blocked in 1xPBS-T containing 5 % milk powder and immunodetection was carried out.

5.2.2.3 Immunodetection

The immobilized proteins were visualised by immunodetection. First, a primary antibody that is directed against the protein of interest is used, which is recognized by a secondary, enzyme-coupled antibody that recognizes the Fc part of the primary antibody. The coupled enzyme, a horse-radish peroxidase, is therefore bound to the target protein and makes it visible by catalyzing a light-reaction which can be detected.

The membrane from the semidry transfer was blocked in 1xPBS-T containing 5 % milk powder (w/v) for one hour. After that, the primary antibody diluted in blocking solution was incubated with the membrane overnight at 4 $^{\circ}C$ under constant shaking. The membrane was washed with 1xPBS-T three times for 15 min with mild shaking at room temperature. Afterwards, the membrane was incubated with the secondary antibody diluted in 1xPBS-T dry milk for 45 min and washed again three times for 15 min at room temperature.

After washing, the membrane was developed by using a Chemiluminescence kit. The substrates were removed by wiping with a paper towel and the chemiluminescence was detected at different exposure times with the Fuji LAS3000 Fluorescence Image Reader.

5.3 Mammalian cell culture

5.3.1 Maintenance

All work with mammalian tissue culture was performed under a sterile hood with laminar flow, solutions were purchased sterile or sterilized by autoclaving. Working space, gloves and all devices were cleaned with 70 % ethanol before use.

Mammalian cells were propagated in their recommended medium (see 4.10). Before the media were used, they were warmed to room temperature, but stored at 4 $°C$. Cells were split at an estimated confluency of 80-90 %. For splitting, medium was aspirated with a sterile pasteur pipette and the required amount of Trypsin/EDTA solution was added to the cells (5 mL for a 15 cm pate). The cells were incubated at 37 $°C$ until cells were detached which was about 5 min in most cases. Then, fresh medium was added to stop the reaction and cells were split depending on their growth properties and the diameter of the plate to different ratios. For IMR90 this was usually 1:2 every two days and 1:10 every two days for MEF, K562 and HeLa cells. Cells were incubated in a humidified incubator at 37 $°C$ and 5 % CO_2.

5.3.2 Freezing and thawing of cells

Mammalian cell cultures can be cryopreserved and stored for long time at -80 $°C$ or in liquid nitrogen. For cryopreservation, a cell culture was expanded to several 10 cm-plates. At approximately 70 % confluency, cells were detached by adding Trypsin/EDTA, the reaction was stopped by adding medium and the cells were spun down at 500xg for 5 min. The supernatant was removed and the cells were washed once with cell culture medium. The cell pellet was carefully resuspended in FCS containing 5 % DMSO (v/v) to reach a final cell density of 10^6 to 10^7 cells/mL. The suspension was as fast as possible split in aliquots of 1 mL in sterile cryotubes which were inserted into polystyrene holders and incubated overnight at -20 $°C$. The tubes were then stored at -80 $°C$ or in liquid nitrogen.

When the cryo-cultures were needed again, they were removed from the -80 $°C$ freezer, thawed quickly at 37 $°C$ and poured into a 10 cm plate containing 13 mL of the required medium. The cells were incubated at 37 $°C$ and the medium was changed the next day to remove remaining DMSO. If the cell line was sensitive to DMSO, cells were washed with medium prior to plating.

5.3.3 Determining the cell number

In order to determine growth rates, cell number had to be determined. Therefore medium was removed and the required amount of Trypsin/EDTA solution was added to the cells. After incubation at 37 $°C$ until cells were detached, fresh medium was added to stop the reaction. Then cells were spun down at 300 g and resuspended in an appropriate amount of DMEM. Then 10 µL cell suspension were applied to the Neubauer counting chamber. After counting the cells in the two marked areas the average was calculated. This average was then multiplied with 10^4 to get the actual cell number per milliliter.

5.3.4 Preparation of quiescent cell populations

To get quiescent cells for nucleolus isolations, cells were grown on 15 cm sterile petri dishes in standard medium supplemented with 0.1 % FCS for 5 days prior to nucleolus isolation.

5.3.5 Preparation of senescent cell populations

In order to get senescent IMR90 cells for nucleolus isolations and single cell experiments cells were grown until a blue staining of nearly all cells in the cell population was visible in senescence-associated β-galactosidase test and cells stopped to grow, which was determined by counting the cells. Then they were kept in culture for additional 2 weeks with constant supply of fresh standard medium to prevent starvation.

5.3.6 Senescence test

To stain and identify senescent cells the *BioVision senescence detection kit* (after (Dimri et al., 1995))was used. Cells were grown on coverslips in 6 well plates and fixated with para-formaldehyde for 10-15 min. After washing cells twice with 1 mL of 1xPBS, 0.5 mL of the Staining solution were added and incubated overnight at 37 $°C$. For each well the staining solution mix was prepared as shown in the following.

940 µL	Staining solution
10 µL	Staining supplement
50 µL	20 $\frac{mg}{mL}$ X-gal in DMF

After staining cells were observed under a microscope (Axiovert 35 Inverted Fluorescent Microscope, equipped with a colour camera) to identify senescent status and take pictures.

5.3.7 Knock-out of UBF in MEFs

MEF cells were grown under standard conditions. To activate ER-Cre, 4-hydroxytamoxifen (4-HT) was added to a final concentration of 50 nM and after 4 hr incubation the medium was replaced with fresh medium without 4-HT and cells were used for experiments after 24 h, 48 h or 72 h.

5.4 Immunfluorescence

Cells were grown on sterile glass coverslips in 6-well plates to a confluency of 70 %. For washing steps coverslips were placed into a new 6-well plate and a volume of 2 mL was added per well from the different solutions.

5.4.1 Fixation and immunostaining of mammalian cells

For immunostaining cells were grown on coverslips in a 6-well plate. For fixation they were rinsed in 2-3 changes of 1xPBS and then incubated with 2 % para formaldehyde in PBS (freshly made, pH 7.0) for 10-15 min. After washing cells with 0.01 % Triton X-100 3 $\times$ 3 min at RT they were permeabilised with 0.5 % Triton X-100 in PBS for 5 min at RT. Cells were then washed with 1xPBS-T for 3 $\times$ 3 min at 37 $°C$ and incubated with the primary antibody in 4 % BSA PBS-T at the appropriate dilution for at least 45 min at 37 $°C$. After washing for 3 $\times$ 3 min at 37 $°C$ on a shaking platform with 1xPBS-T at 37 $°C$ the secondary antibody was applied in 4 % BSA PBS-T at the appropriate dilution for 30 min at 37 $°C$. Then coverslips were washed with 1xPBS-T for 2 $\times 5$ min at 37 $°C$ and DNA was counterstained with 50 $\frac{ng}{mL}$ DAPI in 1xPBS-T for 5 min at 37 $°C$. Afterwards cells were washed with PBS-T and mounted in Vectashield.

5.4.2 Immunostaining of nucleoli after isolation

In order to stain nucleoli after isolation with DAPI and Fibrillarin to control their purity, they were first dried on Poly-L-Lysine-coated microscopic slides for 5 min at 37 $°C$. Then they were fixed onto the slides with 2 % para formaldehyde. Nucleoli were washed for 3 $\times$ 3 min at 37 $°C$ in a coplin jar and were then incubated with the primary antibody in 4 % BSA PBS-T at the appropriate dilution for at least 45 min at 37 $°C$. After washing for 3 $\times$ 3 min at 37 $°C$ in a coplin jar with 1xPBS-T at 37 $°C$ the second antibody was applied in 4 %BSA PBS-T at the appropriate dilution for 30 min at 37 $°C$. Then microscopy slides were washed with 1xPBS-T for 2 $\times 5$ min at 37 $°C$ and DNA was counterstained with 50 $\frac{ng}{mL}$ DAPI in 1xPBS-T for 5 min at 37 $°C$. Afterwards nucleoli were washed with PBS-T and mounted in Vectashield.

5.4.3 Quantitative immunofluorescence

This protocol provides a detailed step-by-step description as how to quantitatively analyze different areas of the nucleus using confocal laser scanning microscope (CLSM) images of immunofluorescence stained nuclei in a semi-automated manner. The commands of a script, which was written for ImageJ, are integrated in this description. ImageJ commands are written in brackets and italic text commands in the self-written script are depicted in bold text. The plugins 'Action Bar' and 'Bio-Formats' should be installed.

5.4.3.1 Determination of relative immunofluorescence intensities in the ROIs

The selected optical section of the CLSM image file was opened as separate grey channels. The channel with the DAPI signal was duplicated and named 'DAPI_mask' [*Shift + D*]. The customized Action Bar (quant_IF) was used from this step on. Get the **binary mask** [*Process > Binary > Make Binary*]. Holes that appear due to unequal staining were filled up [*Process > Binary > Fill holes*]. Bumps and dints were removed [*Process > Filters > Gaussian Blur 3D... (x = 2, y = 2, z = 2)*]. The image was thresholded with a value of 128 [*Shift + cmd + T, Apply*] and unwanted background and partial nuclei deleted manually.

The channel containing the staining to be quantified was duplicated and named 'histone_channel' [*Shift + D*]. To get the binary mask for nucleoli the channel with the nucleolus staining (in our case B23) was selected and an appropriate mid-section chosen and duplicated [*Shift + D*]. Then the resulting image was named 'No_mask'.

A **Gaussian filtering** was performed [*Process > Filters > Gaussian Blur 3D... (x=2, y=2, z=2)*] and the threshold set manually to separate the nucleoli from the background and to get the outlines of the nucleoli [*Shift + cmd + T, Apply*].

Bumps and dints were removed [*Process > Filters > Gaussian Blur 3D... (x=2, y=2, z=2)*] and the image thresholded with a value of 128 [*Shift + cmd + T, Apply*]. Unwanted background and nucleoli from all but the selected cell were deleted manually.

All measurements were made: In the following steps several additional masks for the perinucleolar space and the nuclear border were created, which were then applied to the previously generated mid-section images and finally fluorescence intensities were measured. First the total nuclear fluorescence intensity was measured to get a reference for relative quantification. 'DAPI_mask' was applied to the histone_channel [*Process > Image Calculator > AND*] and the total fluorescence intensity [*cmd + M*] was measured. To create a 240 nm mask for the nuclear periphery 'DAPI_mask' was selected, duplicated and named 'DAPI_mask_240'. 3 pixels (= 240.75 nm) [*Process > Binary > Options... ; Iterations=3 ; EDM output: Overwrite; Do: erode*] were eroded and the smaller mask was

subtracted from the larger one [*Process* > *Image Calculator* > *Subtract*]. This mask (Result of DAPI_mask) was then applied to the histone_channel [*Process* > *Image Calculator* > *AND*] (Figure 5.1) and the total fluorescence intensity of this area [*cmd* + *M*] was measured. To mask a 240 nm rim around nucleoli the 'No_mask' was duplicated and renamed 'No_mask_240'. Then it was dilated by 3 pixels [*Process* > *Binary* > *Options... ; Iterations=3 ; EDM output: Overwrite; Do: dilate*] and the smaller mask subtracted from the larger one [*Process* > *Image Calculator* > *Subtract*]. This mask (Result of No_mask_240) was then applied to the histone_channel [*Process* > *Image Calculator* > *AND*] (Figure 5.1). The total fluorescence intensity of this area was measured [*cmd* + *M*] and all values transferred to Excel to calculate relative fluorescence intensities.

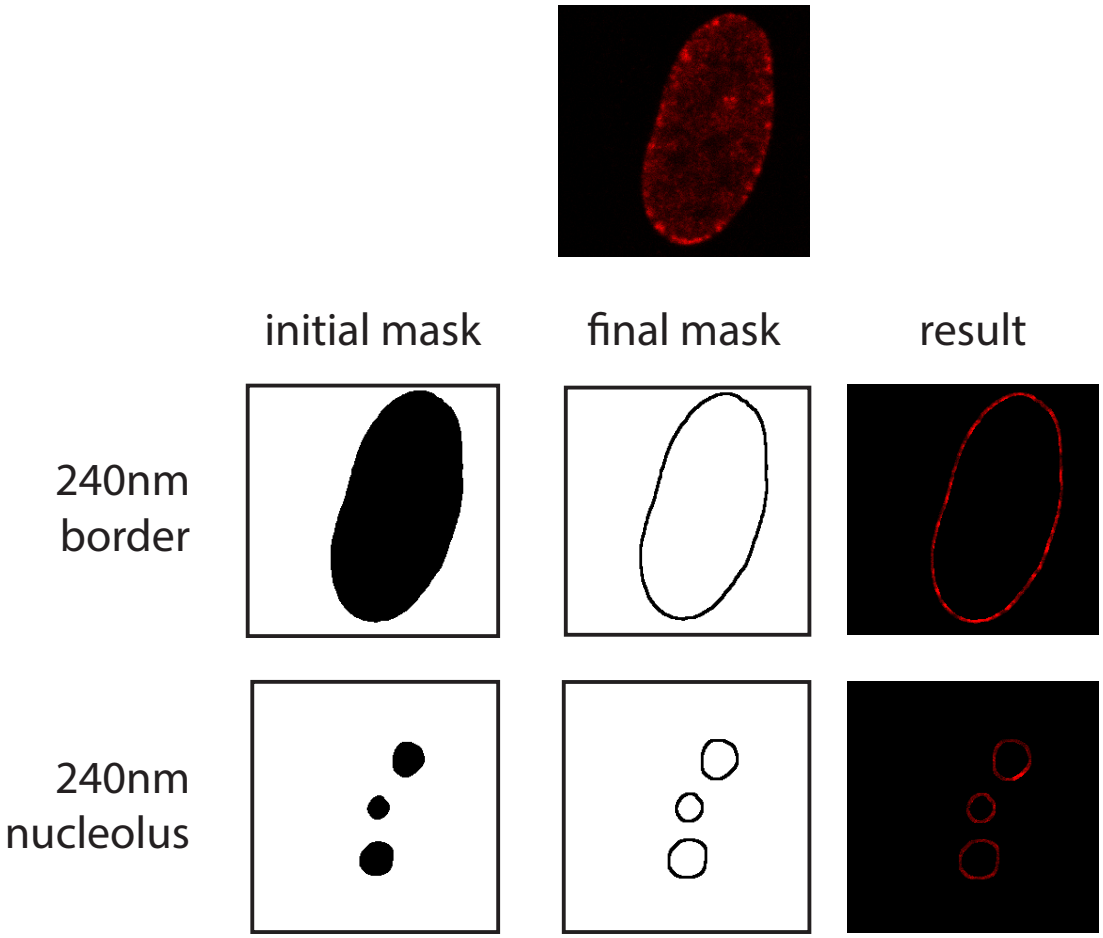

Figure 5.1 – Definition of the perinucleolar space and the nuclear periphery to measure fluorescence intensity values
Initial masks after thresholding (left), final masks with a width of 240 nm-3 px (center) and the result of masks applied to the histone channel (top) are shown (right).

5.4.3.2 Determination of the heterogeneity of staining in the ROIs

The heterogeneity (pixel-to-pixel variation) of given staining intensities in the ROIs is calculated by dividing standard deviation of fluorescence intensity values with the mean fluorescent intensity value. The resulting value is called coefficient of variation (CV) (Zhang et al., 2015).

The DAPI_mask, DAPI_mask_240, No_mask, No_mask_240, histone_channel images that were created in 5.4.3.1 were reused. The heterogeneity of the staining in the entire nucleus (**Nu CV**) was measurend and the histogram of the nucleus inspected to evaluate the total staining of the nucleus in respect to over-, underexposure, width of the histogram and normal distribution. DAPI_mask was selected and nuclear outlines were added to the ROI Manager [*Analyze* > *Analyze particles...*]. The created ROI and the histone_channel were selected sequentially in the ROI Manager, so that the outline of the nucleus appeared in the histone_channel window. This was selected, measured [*cmd + M*] and values for standard deviation and mean were transfered to an Excel sheet for further calculations. Additionally a histogram [*Analyze* > *Histogram...*] was created.

Then the heterogeneity of the staining at the nuclear periphery (**rim CV**) was calculated. To get the CV from the border of the nucleus DAPI_mask_240 was selected and the smaller nuclear mask was added to the ROI Manager [*Analyze* > *Analyze particles...*], which already contained the DAPI_mask. The histone_channel, the two ROIs (DAPI_mask and DAPI_mask_240) were selected and the command [*More* > *XOR*] was run from the ROI Manager menu. This specified the nuclear border, i.e. the area that is included in the bigger ROI but not in the smaller one. Standard deviation and mean values were measured [*cmd + M*] and transferd to an Excel sheet and nuclear border ROI were deleted from the ROI Manager.

The heterogeneity of the staining in the perinucleolar space (**no CV**) was calculated. To get the CV from the perinucleolar space, the two nucleolar masks (No_mask, No_mask_240) were added to the ROI Manager [*Analyze* > *Analyze particles...*]. Since the number of nucleoli varies, the ROIs were selected manually and added to the histone_channel image using the [*More* > *XOR*] command from the ROI Manager menu. Standard deviation and mean values were measured [*cmd + M*] and transfered to an Excel sheet and nuclear border ROI were deleted from the ROI Manager.

5.4.3.3 Determination of the subnuclear distribution of the 10% brightest pixels

To get an overview about the distribution of heterochromatin in the nucleus, the distribution of the brightest pixels of the H3K9me3 immunofluorescence staining was evaluated. The analysis of the brightest pixels delivers information about the spatial arrangement of the densest heterochromatic regions of chromosomes in the nucleus.

To get an image with only the 10 % brightest pixels of the nucleus (**Crop nucleus**) apply first the DAPI_mask to the histone_channel [*Process* > *Image Calculator* > *AND*]. The image was thresholded manually to 10 % [*Shift + cmd + T, Apply*] (The histogram has 255 bins where pixels are assigned. Due to this fact one cannot threshold the image exactly at 10 %. Therefore the value just above 10 % was chosen.).

To get the pixels which are located at the nuclear periphery (**add rim**) add DAPI_mask and DAPI_mask_240 to the ROI Manager [*Analyze* > *Analyze particles...*]. The top 10 % pixel image (histone_channel) was selected then the ROIs were selected manually in the ROI Manager and added to the histone_channel using the command [*More* > *XOR*] (Figure 5.2).

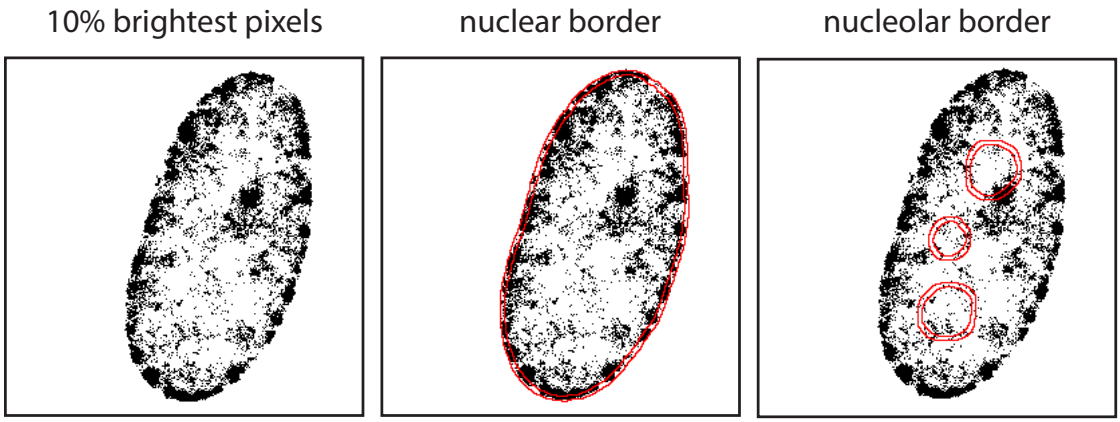

Figure 5.2 – Distribution of the 10 % brightest pixels.
The brightest pixels (top 10 %) of H3K9me3 staining are shown on the left, and the ROIs are outlined in the middle (nuclear periphery) and on the right side (perinucleolar space).

The number of pixels [*cmd + M*] was measured and transfered to an Excel sheet and the nuclear border ROI deleted from the ROI Manager.

For counting the pixels in the perinucleolar space (**add no**) No_mask and No_mask_240 were added to the ROI Manager [*Analyze* > *Analyze particles...*]. Due to the variable numbers of nucleoli, the ROIs had to be selected manually and added to the histone_channel image using the [*More* > *XOR*] command from the ROI Manager menu (Figure 5.2). The number of pixels [cmd + M] was measured and transfered to an Excel sheet. The nucleolar border ROI were deleted from the ROI Manager.

All windows were closed (**close all windows**) and the canvas was clean for the analysis of the next nucleus.

5.4.4 Determining number and volume of nucleoli

After immunostaining of nucleoli with an anti B23 antibody labeling the granular component of nucleoli, z-stack images were acquired with the Zeiss Axiovert200 Microscope using a 63x objective with immersion oil, scanning through the whole nucleus with a z-step size of 500 nm. Voxel sizes were obtained by a calibration of the objective and values were saved and transferred to FIJI and the volume in µm was calculated by measuring the number of object voxels. The following analyses were performed using the open source software FIJI. The channel containing the Nucleolus signal was opened as gray channel image, then the image was thresholded, nucleoli were counted manually and the volume of nucleoli per cell was measured using the '3D Objects Counter' plug-in of FIJI.

[*Analyze > 3D OC Options*] was opened and 'Volume' and 'Nb of Obj. voxels' selected to configure measurements. Then the image containing nucleolar staining was selected and [*Analyze > 3D Objects counter*] was run. A threshold was set manually to separate the nucleoli and 'Objects' was selected under 'Maps to show' as well as 'Statistics and Summary' from the 'Results tables to show'. Volume of nucleoli was measured in μm^3. Then nucleoli were counted and assigned to cells manually. the amount of nucleoli per cell was illustrated in a histogram (R-command *histogram*). The same measurements were also performed for the DAPI channel, to get the total nuclear volume. Values for nucleoli and nuclei were then transferred to an Excel-sheet and the average nucleolar volume, total nucleolar volume per cell and the ratio of nucleoli/nuclei was calculated and a Boxplot (R-command *boxplot*) containing the individual values (R-command *beeswarm*) was made. A boxplot illustrates values of a population of data. First, the median is displayed in the middle as solid line. Second, the upper and lower quartile are marked as light lines, marking the range of 50 % of the data. The whiskers show the maximum and the minimum of the data, as long as they do not deviate more than 1.5 times the interquartile distance from the median. Points that deviate more than that from the median are displayed as single data-points.

5.5 FISH-techniques

5.5.1 Preparation of hybridization probes

5.5.1.1 Amplification of DNA

BACs were ordered at BACPAC Resources and received as bacterial stocks in solid LB-Agar. First they were grown on LB-Amp plates and amplified in 3 mL LB-medium and DNA isolated. After this 1-10 ng of DNA was amplified using the illustra GenomiPhi V2 DNA Amplification Kit. In short 1 µl of template DNA was mixed with 9 µl of sample buffer and denaturated for 3 min at 95 $°C$. Then 9 µl of reaction buffer and 1 µl of Phi

Polymerase were added and incubated for 2 h at 30 °C, afterwards the Polymerase was inactivated for 10 min at 65 °C. In the end the yield was about 6-10 µg with a product size of 2-12 kb.

5.5.1.2 Nick-translation

For hybridization amplified BAC DNA has to be labeled, therefore the following reaction mixture was prepared and incubated for 2 h at RT. After the reaction an aliquot was taken and analyzed on a 1 % agarose gel. Probe length should be between 250 and 1000 bp.

	[µL]
DNA (1 µg)	x
NT buffer	5
0.1M ME	5
dNTP mix	5
labeled dUTP	1
H_2O	32-x
DNAse (1:250)	1
DNA Pol I	1

Reaction mix was put on ice and an equal amount of STOP mix was added to the NT reaction.

5.5.1.3 Hybridisation mix preparation

	[µL]
NT-Mix	100
Cot-1 DNA (human)	10
Salmon Sperm DNA	1
H_2O	89

Reaction mix was prepared as shown above and DNA was precipitated as described. For probes that target repetitive sequences the amount of Cot-1 DNA was increased up to 30 µL in order to reduce background signals. After air-drying the pellet 3 µL of 100 % formamide was pipetted directly on top of the pellet and incubated at 50 °C for 15 min. DNA was vortexed well and and incubated further at 50 °C for 15 min. If pellet was

dissolved 3 µL of pre-warmed Master Mix (2xSSC, 20 % dextran sulfate (w/v)) were added and incubated at 50 °C for 15 min.

5.5.2 Fixation of cells for 3D-FISH

Cells were rinsed two times in PBS at 37 °C. After fixation in 4 % para formaldehyde for 10 min cells were washed for 3×3 min in PBS with 0.01 % Triton X-100 in PBS at room temperature. To permeabilize the cells they were incubated for 5 min at room temperature with 0.5 % Triton X-100 in PBS. To preserve the three-dimensional structure of cells they were put on 20 % glycerol for at least one hour, then frozen in liquid nitrogen, thawed gradually at room temperature and soaked in 20 % glycerol. The freezing-thawing step was repeated 4-6 times. After washing cells for 3×10 min in PBS with 0.01 % Trition X-100 in PBS cells were incubated in 0.1 M HCl for 5 min. Cells were rinsed in $2 \times SSC$ and incubated in 50 % Formamide in 2× SSC for at least 30 min or over night. A probe was put directly on a coverslip, sealed with rubber cement and then the coverslip was put on a hot block for 2-3 min at 75 °C to denaturate the DNA. Hybridization was carried out at 37 °C for at least over night, or longer.

5.5.3 Immunostaining

Slides were washed after FISH with $2 \times SSC$ for 3×10 min at 37 °C, for 5 min at 60 °C with $0.1 \times SSC$, for 5 min at 37 °C with $4 \times SSC$ + 0.1 % Tween and for 3×3 min at 37 °C with PBS 0.1% $Tween$. They were incubated with the first antibody in 4% BSA PBS-T for at least 45 min at 37°C. Cells were washed with PBS 0.1% $Tween$ for 3×3 min at 37°C and the second antibody was applied in 4% BSA PBS-T for 30 min at 37 °C. After washing cells for 2×5 min at 37 °C DNA was counterstained with 50 $\frac{ng}{mL}$ DAPI. Cells were washed once with PBS 0.1% $Tween$ and mounted in Vectashield on a microscope slide and sealed with nail polish for long-time storage.

5.5.4 Image acquisition settings

For image acquisition a Leica SP8 confocal microscope was used. Settings were selected according to the rules described in Ronneberger et al. (2008). Image acquisition settings:

Format	512 x 512
Speed	600 Hz
Zoom Factor	4.5
Image Size	41.01 x 41.01 µm
Pixel Size	**80.25 x 80.25 nm**
Line Average	2
Z-step size	200 nm

In order to identify single genomic loci in 5-colour-FISH experiments, filter settings were set-up to ensure a clear colour separation.

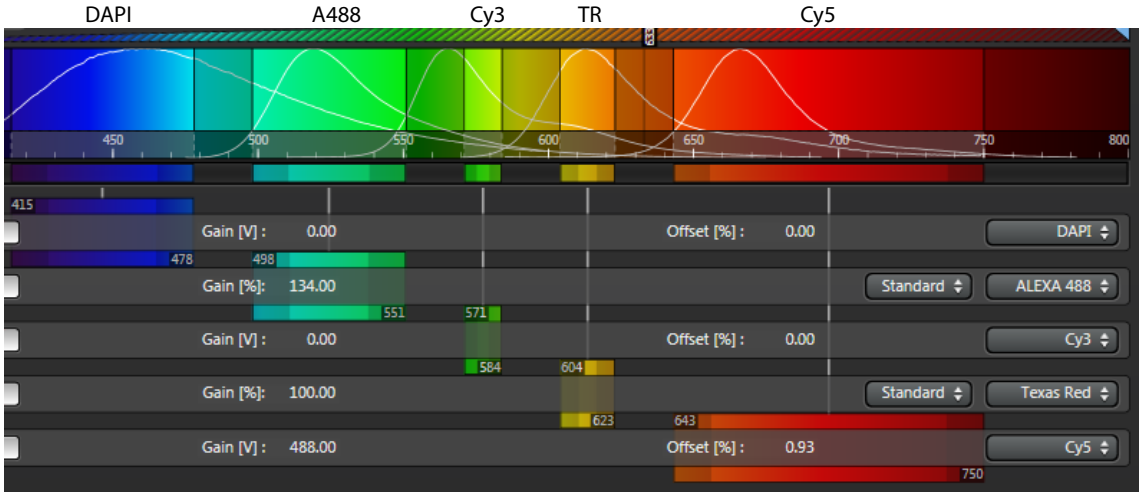

Figure 5.3 – Filter settings for 5-colour-FISH in the Leica SP8 interface.
FISH experiments were carried out using 5 colours as indicated. Filter settings were set-up such, that FISH signals of the respective channels could be identified unambiguously. A screenshot from the Leica SP8 user interface with used settings for different filters is shown.

6 Appendix

6.1 Identification of NADs

Nucleolus-associated domains were initially identified in our lab as well as the laboratory of A. Lamond (Németh et al., 2010; van Koningsbruggen et al., 2010). Németh et al. (2010) isolated nucleolus-associated DNA from HeLa human cervix carcinoma cells and it was hybridized against genomic DNA on HG18 CGH 385K Whole Genome Tiling v1.0 arrays with a probe spacing of 6270 bp. NADs were then called using a thresholding approach. Regions were considered as being NADs if their mean value was greater than the 85 percentile of the sample distribution at 0.1 Mb running window size. Using this approach 97 chromosomal regions were identified, which span about 4 % of the human genome (see Figure 6.1). NADs contained gene families that are organized in large clusters and are expressed in a tissue-specific manner like zinc finger, defensin, T-cell receptor and olfactory receptor genes. Furthermore, satellite repeats such as alpha, satellite-2, $(CATTC)_n/(GAATG)_n$, beta and others were also enriched in NADs. Analyses of chromatin features revealed the repressive nature of nucleolus-associated chromatin with the enrichment of trimethylated H3K9, H3K27 and H4K20.

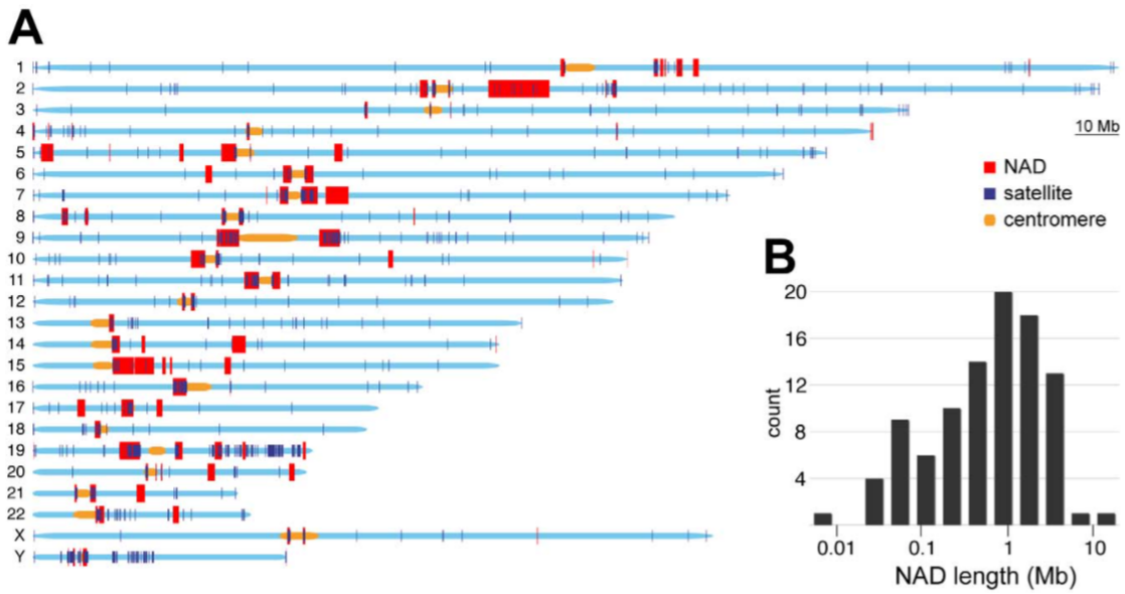

Figure 6.1 – HeLa NADs.
(A) Karyogram with marked NADs, satellite repeats and centromeres. (B) Histogram of NAD domain-sizes. Adapted from (Németh et al., 2010).

In the presented work, NADs were identified in proliferating IMR90 human diploid fibroblasts and compared to NADs that were identified in HeLa cells. Furthermore, the dynamics of NADs in cellular senescence was initially characterized. Nucleolus-associated DNA was isolated from proliferating and senescent IMR90 cells and hybridized on two-colour Human CGH 4.2M Whole Genome Tiling Arrays with a median probe spacing of 284 bp. These arrays featured a higher resolution with a closer probe spacing. Visualization of the microarray data of HeLa and proliferating IMR90 revealed their different nature. NADs were identified using a thresholding approach in the first study (Németh et al., 2010). Called later 'top NADs' as they represent those NADs with the highest association-frequency. Microarray hybridizations of nucleolus-associated DNA of IMR90 cells in this study showed mostly saturated signals at nucleolus-associated regions and thus NADs are visible as blocks with mostly comparable hybridization signal intensities and sharp borders (see Figure 6.2). Hence, NAD calling using thresholding and a moving window of 100 kb did not result in usable results and NADs were identified using a two-state Hidden Markov Model by T. Straub (LMU Munich). The resulting NADs were called 'all NADs', since this saturation did not result in any differentiation of association frequencies. Nevertheless, chromatin features that reside in genomic regions that were shown to associate with nucleoli exhibit the same characteristics of repressive chromatin like in the HeLa study.

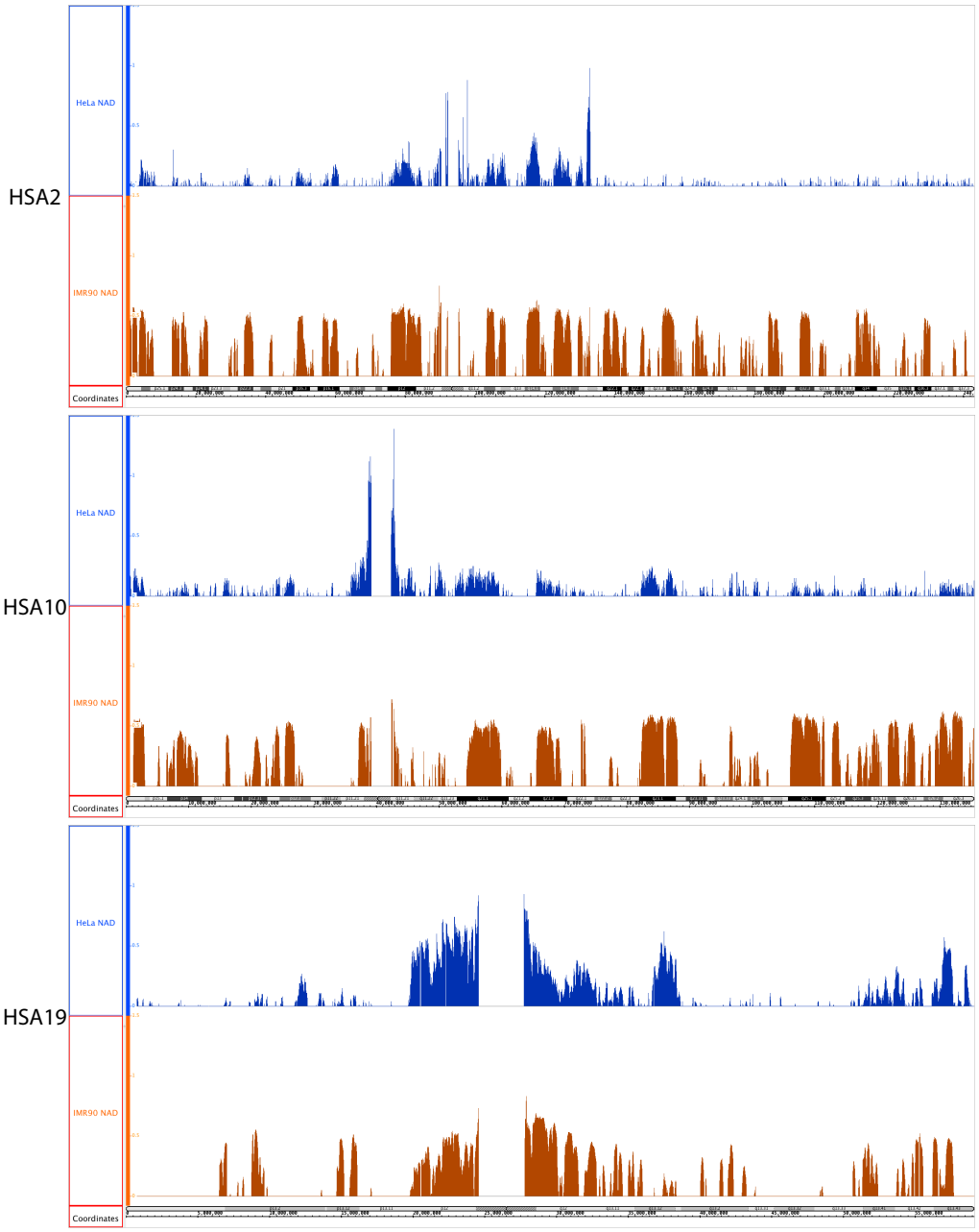

Figure 6.2 – Comparison of CGH data of HeLa and IMR90 cells.
Normalized hybridization data of nucleolus-associated DNA on CGH microarrays are shown for chromosomes 2, 10 and 19 of HeLa and proliferating IMR90 cells. Data tracks of HeLa cells exhibit a more gradual pattern of signal intensities, whereas data tracks of proliferating IMR90 cells show large domains with mostly sharp borders and less variation in hybridization signal intensities. Positive values represent nucleolus-association. HeLa = blue, IMR90 = brown.

6.2 Quantitative immunofluorescence

The following script was used to quantify immunofluorescence signals as described in the Methods (Section 5.4.3).

```
// Action Bar description file :quant_IF
run("Action Bar","/plugins/ActionBar/quant_IF_everything.txt");
exit();


<line>
<button>
label=Get binary mask
arg=<macro>
selectWindow("DAPI_mask");
setOption("BlackBackground", false);
run("Make Binary");
run("Fill Holes");
run("Gaussian Blur 3D...", "x=2 y=2 z=2");
//run("Threshold...");
//setThreshold(128, 255);
setOption("BlackBackground", false);
run("Convert to Mask");
</macro>

<button>
label=gaussian filtering
arg=<macro>
run("Gaussian Blur 3D...", "x=2 y=2 z=2");
run("Gaussian Blur 3D...", "x=2 y=2 z=2");
</macro>

<button>
label=bumps&dints
arg=<macro>
run("Gaussian Blur 3D...", "x=2 y=2 z=2");
//run("Threshold...");
run("Convert to Mask");
run("Fill Holes");
</macro>
</line>

<line>
<button>
label=make all measurements
arg=<macro>
```

```
selectWindow("histone_channel");
run("8-bit");
imageCalculator("AND create", "histone_channel", "DAPI_mask");
selectWindow("Result of histone_channel");
run("Measure");
selectWindow("Result of histone_channel");
close();
selectWindow("DAPI_mask");
run("Duplicate...", "title=DAPI_mask_240");
run("Options...", "iterations=3 count=1 pad edm=Overwrite do=Erode");
imageCalculator("Subtract create", "DAPI_mask","DAPI_mask_240");
imageCalculator("AND create", "histone_channel","Result of DAPI_mask");
run("Measure");
imageCalculator("AND create", "DAPI_channel","Result of DAPI_mask");
run("Measure");
selectWindow("Result of histone_channel");
close();
selectWindow("Result of DAPI_channel");
close();
selectWindow("Result of DAPI_mask");
close();
selectWindow("DAPI_mask");
run("Duplicate...", "title=DAPI_mask_480");
run("Options...", "iterations=6 count=1 pad edm=Overwrite do=Erode");
imageCalculator("Subtract create", "DAPI_mask","DAPI_mask_480");
imageCalculator("AND create", "histone_channel","Result of DAPI_mask");
run("Measure");
imageCalculator("AND create", "DAPI_channel","Result of DAPI_mask");
run("Measure");
selectWindow("Result of histone_channel");
close();
selectWindow("Result of DAPI_channel");
close();
selectWindow("Result of DAPI_mask");
close();
imageCalculator("AND create", "histone_channel","No_mask");
run("Measure");
imageCalculator("AND create", "DAPI_channel","No_mask");
run("Measure");
selectWindow("Result of DAPI_channel");
close();
selectWindow("Result of histone_channel");
close();
selectWindow("No_mask")
run("Duplicate...", "title=No_mask_240");
run("Options...", "iterations=3 count=1 pad edm=Overwrite do=Dilate");
```

```
imageCalculator("AND create", "histone_channel","No_mask_240");
selectWindow("Result of histone_channel")
run("Measure");
imageCalculator("AND create", "DAPI_channel","No_mask_240");
selectWindow("Result of DAPI_channel")
run("Measure");
selectWindow("Result of DAPI_channel");
close();
selectWindow("Result of histone_channel");
close();
selectWindow("No_mask_240");
close();
selectWindow("No_mask")
run("Duplicate...", "title=No_mask_480");
run("Options...", "iterations=6 count=1 pad edm=Overwrite do=Dilate");
imageCalculator("AND create", "histone_channel","No_mask_480");
run("Measure");
imageCalculator("AND create", "DAPI_channel","No_mask_480");
run("Measure");
selectWindow("Result of DAPI_channel");
close();
selectWindow("Result of histone_channel");
close();
selectWindow("No_mask_480");
close();
selectWindow("No_mask");
run("Duplicate...", "title=No_mask_240");
run("Options...", "iterations=3 count=1 pad edm=Overwrite do=Dilate");
imageCalculator("Subtract create", "No_mask_240","No_mask");
selectWindow("Result of No_mask_240");
imageCalculator("AND create", "histone_channel","Result of No_mask_240");
selectWindow("Result of histone_channel");
run("Measure");
imageCalculator("AND create", "DAPI_channel","Result of No_mask_240");
selectWindow("Result of DAPI_channel");
run("Measure");
selectWindow("Result of No_mask_240");
close();
selectWindow("Result of histone_channel");
close();
selectWindow("Result of DAPI_channel");
close();
selectWindow("No_mask");
run("Duplicate...", "title=No_mask_480");
run("Options...", "iterations=6 count=1 pad edm=Overwrite do=Dilate");
imageCalculator("Subtract create", "No_mask_480","No_mask");
```

```
selectWindow("Result of No_mask_480");
imageCalculator("AND create", "histone_channel","Result of No_mask_480");
selectWindow("Result of histone_channel");
run("Measure");
imageCalculator("AND create", "DAPI_channel","Result of No_mask_480");
selectWindow("Result of DAPI_channel");
run("Measure");
selectWindow("Result of No_mask_480");
close();
selectWindow("Result of histone_channel");
close();
selectWindow("Result of DAPI_channel");
close();
</macro>
</line>

<line>
<button>
label=Nu CV
arg=<macro>
selectWindow("DAPI_mask");
setOption("BlackBackground", false);
run("Make Binary");
run("Fill Holes");
run("Gaussian Blur 3D...", "x=2 y=2 z=2");
//run("Threshold...");
//setThreshold(128, 255);
setOption("BlackBackground", false);
run("Convert to Mask");
run("Analyze Particles...", "display exclude summarize add");
selectWindow("histone_channel");
roiManager("Select", 0);
run("Measure");
run("Histogram");
</macro>

<button>
label=rim CV 240
arg=<macro>
selectWindow("DAPI_mask_240");
run("Analyze Particles...", "display exclude summarize add");
selectWindow("histone_channel");
roiManager("Select", 0);
roiManager("Select", newArray(0,1));
roiManager("XOR");
run("Measure");
```

```
</macro>

<button>
label=rim CV 480
arg=<macro>
selectWindow("DAPI_mask_480");
run("Analyze Particles...", "display exclude summarize add");
selectWindow("histone_channel");
roiManager("Select", 0);
roiManager("Select", newArray(0,1));
roiManager("XOR");
run("Measure");
</macro>

<button>
label=no CV 240
arg=<macro>
selectWindow("No_mask");
run("Analyze Particles...", "display exclude summarize add");
selectWindow("No_mask_240");
run("Analyze Particles...", "display exclude summarize add");
</macro>

<button>
label=no CV 480
arg=<macro>
selectWindow("No_mask");
run("Analyze Particles...", "display exclude summarize add");
selectWindow("No_mask_480");
run("Analyze Particles...", "display exclude summarize add");
</macro>
</line>

<line>
<button>
label=crop nucleus
arg=<macro>
imageCalculator("AND create", "histone_channel", "DAPI_mask");
selectWindow("Result of histone_channel");
selectWindow("histone_channel");
close();
selectWindow("DAPI_mask");
run("Analyze Particles...", "display exclude summarize add");
roiManager("Select", 0);
selectWindow("Result of histone_channel");
roiManager("Select", 0);
```

```
</macro>

<button>
label=add 240 rim
arg=<macro>
selectWindow("DAPI_mask_240");
run("Analyze Particles...", "display exclude summarize add");
selectWindow("Result of histone_channel");
roiManager("Select", 0);
roiManager("Select", newArray(0,1));
roiManager("XOR");
selectWindow("Result of histone_channel");
run("Measure");
</macro>

<button>
label=add 480 rim
arg=<macro>
selectWindow("DAPI_mask_480");
run("Analyze Particles...", "display exclude summarize add");
selectWindow("Result of histone_channel");
roiManager("Select", 0);
roiManager("Select", newArray(0,1));
roiManager("XOR");
selectWindow("Result of histone_channel");
run("Measure");
</macro>

<button>
label=add no 240
arg=<macro>
selectWindow("No_mask");
run("Analyze Particles...", "display exclude summarize add");
selectWindow("No_mask_240");
run("Analyze Particles...", "display exclude summarize add");
</macro>

<button>
label=add no 480
arg=<macro>
selectWindow("No_mask");
run("Analyze Particles...", "display exclude summarize add");
selectWindow("No_mask_480");
run("Analyze Particles...", "display exclude summarize add");
</macro>
</line>
```

```
<line>
<button>
label=close all windows \o/
arg=<macro>
selectWindow("No_mask");
close();
selectWindow("No_mask_240");
close();
selectWindow("No_mask_480");
close();
selectWindow("DAPI_mask");
close();
selectWindow("DAPI_mask_240");
close();
selectWindow("DAPI_mask_480");
close();
selectWindow("Result of histone_channel");
close();
selectWindow("DAPI_channel");
close();
</macro>
</line>
```

6.3 NADs and LADs of the genomic regions analyzed in 3D immuno-FISH experiments

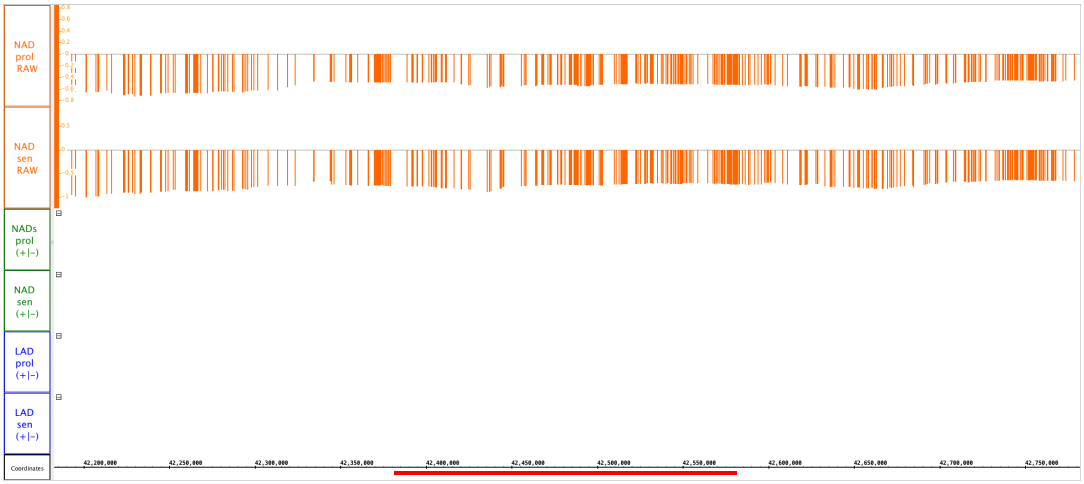

Figure 6.3 – IGB-snapshot of the genomic region corresponding to the BAC RP11-828F4.
Snapshot of a 600 kb region of HSA 17 containing the RP11-828F4 sequence which is indicated in red. Orange tracks: normalized microarray data (top:proliferating, bottom senescent). Positive values show enrichment in nucleolus-associated DNA, negative values a depletion. Green tracks: IMR90 all NADs identified by T. Straub (top: proliferating, bottom: senescent). Blue tracks: IMR90 LADs (Sadaie et al., 2013).

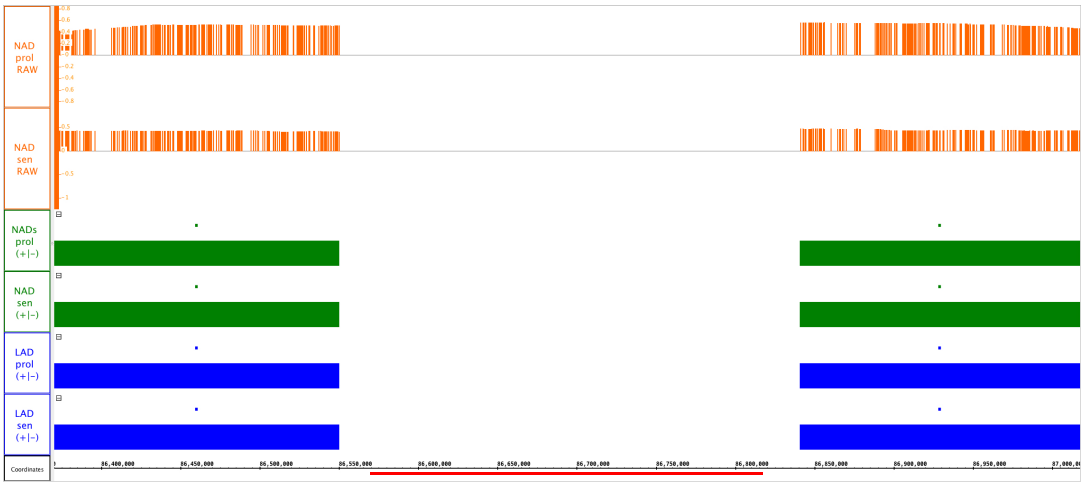

Figure 6.4 – IGB-snapshot of the genomic region corresponding to the BAC RP11-90G23.
Snapshot of a 600 kb region of HSA 8 containing RP11-828F4 which is indicated in red. Orange tracks: normalized microarray data (top:proliferating, bottom senescent). Positive values show enrichment in nucleolus-associated DNA, negative values a depletion. Green tracks: IMR90 all NADs identified by T. Straub (top: proliferating, bottom: senescent). Blue tracks: IMR90 LADs (Sadaie et al., 2013).

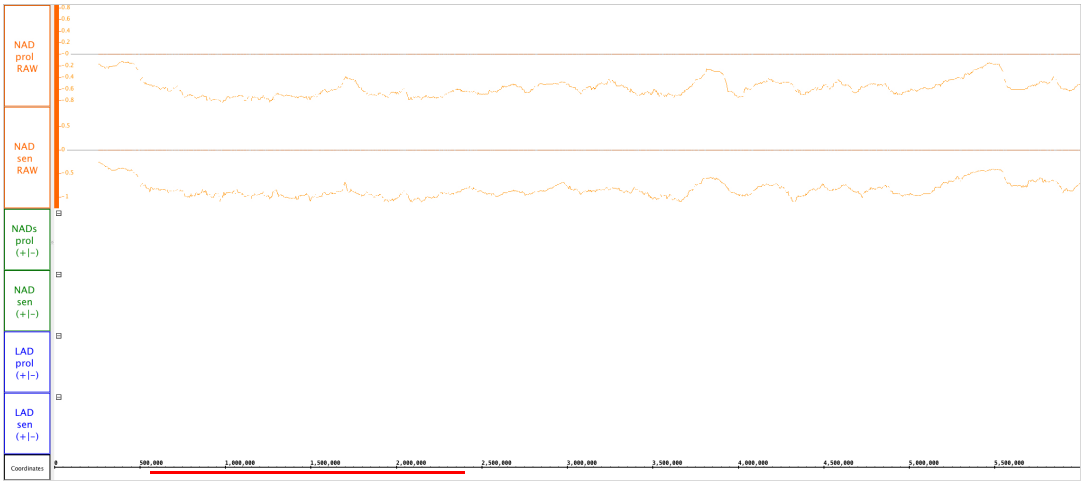

Figure 6.5 – IGB-snapshot of the genomic region corresponding to the BAC RP11-81M8.
Snapshot of a 6 Mb region of HSA 19 containing RP11-828F4 which is indicated in red. Orange tracks: normalized microarray data (top:proliferating, bottom senescent). Positive values show enrichment in nucleolus-associated DNA, negative values a depletion. Green tracks: IMR90 all NADs identified by T. Straub (top: proliferating, bottom: senescent). Blue tracks: IMR90 LADs (Sadaie et al., 2013).

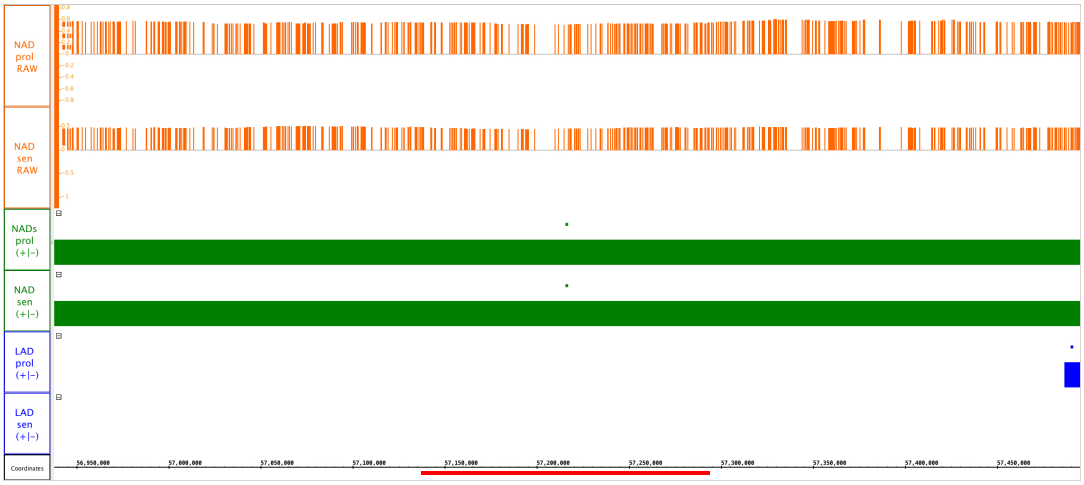

Figure 6.6 – IGB-snapshot of the genomic region corresponding to the BAC RP11-173M10.
Snapshot of a 600 kb region of HSA 13 containing RP11-828F4 which is indicated in red. Orange tracks: normalized microarray data (top:proliferating, bottom senescent). Positive values show enrichment in nucleolus-associated DNA, negative values a depletion. Green tracks: IMR90 all NADs identified by T. Straub (top: proliferating, bottom: senescent). Blue tracks: IMR90 LADs (Sadaie et al., 2013).

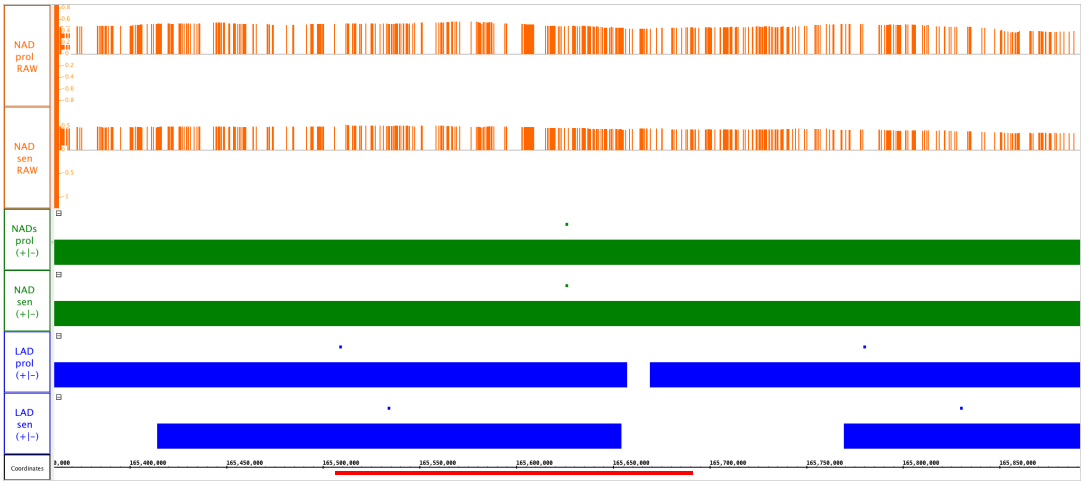

Figure 6.7 – IGB-snapshot of the genomic region corresponding to the BAC RP11-914H1.
Snapshot of a 600 kb region of HSA 4 containing RP11-828F4 which is indicated in red. Orange tracks: normalized microarray data (top:proliferating, bottom senescent). Positive values show enrichment in nucleolus-associated DNA, negative values a depletion. Green tracks: IMR90 all NADs identified by T. Straub (top: proliferating, bottom: senescent). Blue tracks: IMR90 LADs (Sadaie et al., 2013).

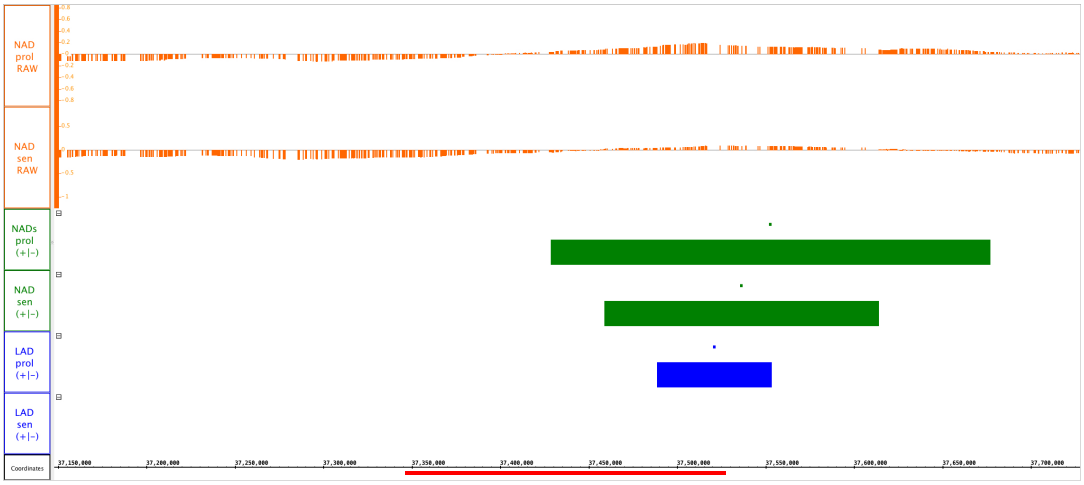

Figure 6.8 – IGB-snapshot of the genomic region corresponding to the BAC RP11-44B13.
Snapshot of a 600 kb region of HSA 19 containing RP11-828F4 which is indicated in red. Orange tracks: normalized microarray data (top:proliferating, bottom senescent). Positive values show enrichment in nucleolus-associated DNA, negative values a depletion. Green tracks: IMR90 all NADs identified by T. Straub (top: proliferating, bottom: senescent). Blue tracks: IMR90 LADs (Sadaie et al., 2013).

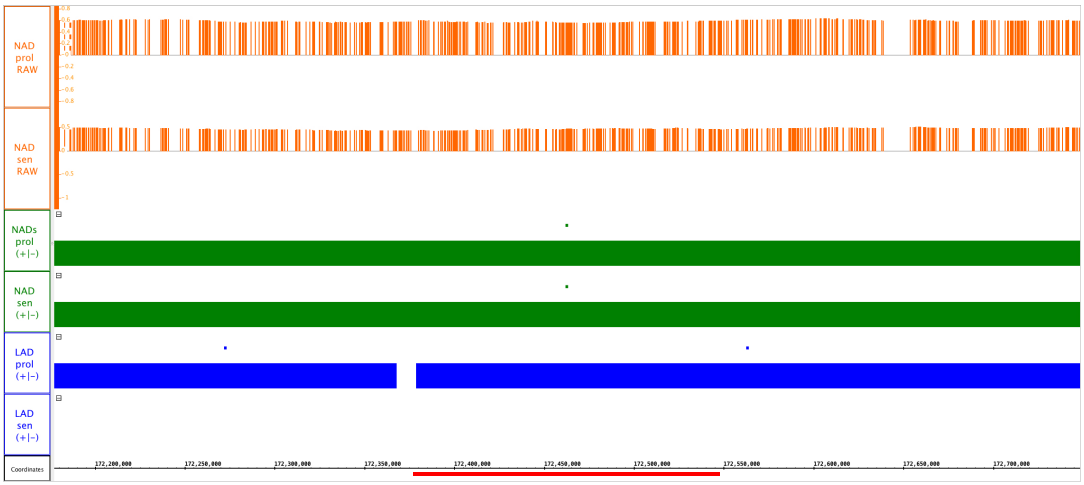

Figure 6.9 – IGB-snapshot of the genomic region corresponding to the BAC RP11-784D7.
Snapshot of a 600 kb region of HSA 4 containing RP11-828F4 which is indicated in red. Orange tracks: normalized microarray data (top:proliferating, bottom senescent). Positive values show enrichment in nucleolus-associated DNA, negative values a depletion. Green tracks: IMR90 all NADs identified by T. Straub (top: proliferating, bottom: senescent). Blue tracks: IMR90 LADs (Sadaie et al., 2013).

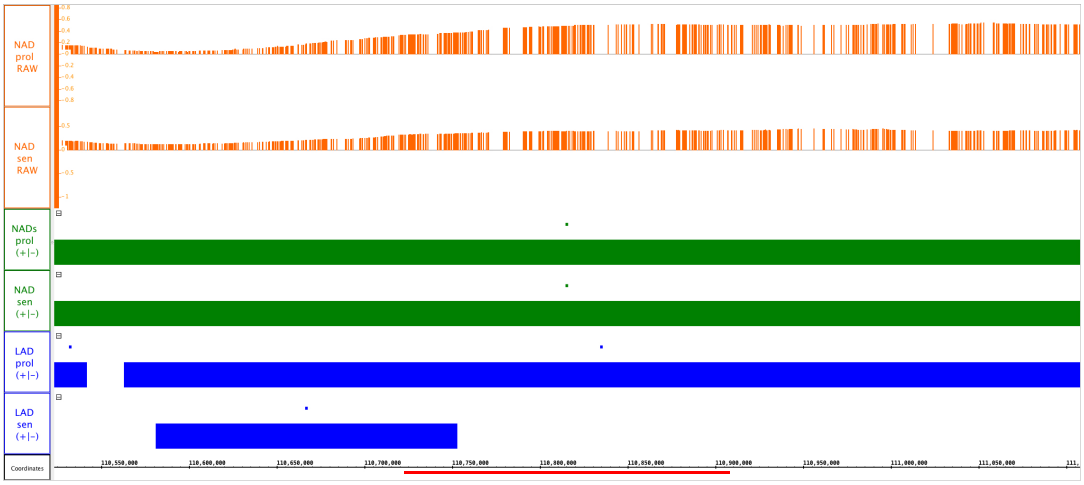

Figure 6.10 – IGB-snapshot of the genomic region corresponding to the BAC RP11-638N4.
Snapshot of a 600 kb region of HSA 8 containing RP11-828F4 which is indicated in red. Orange tracks: normalized microarray data (top:proliferating, bottom senescent). Positive values show enrichment in nucleolus-associated DNA, negative values a depletion. Green tracks: IMR90 all NADs identified by T. Straub (top: proliferating, bottom: senescent). Blue tracks: IMR90 LADs (Sadaie et al., 2013).

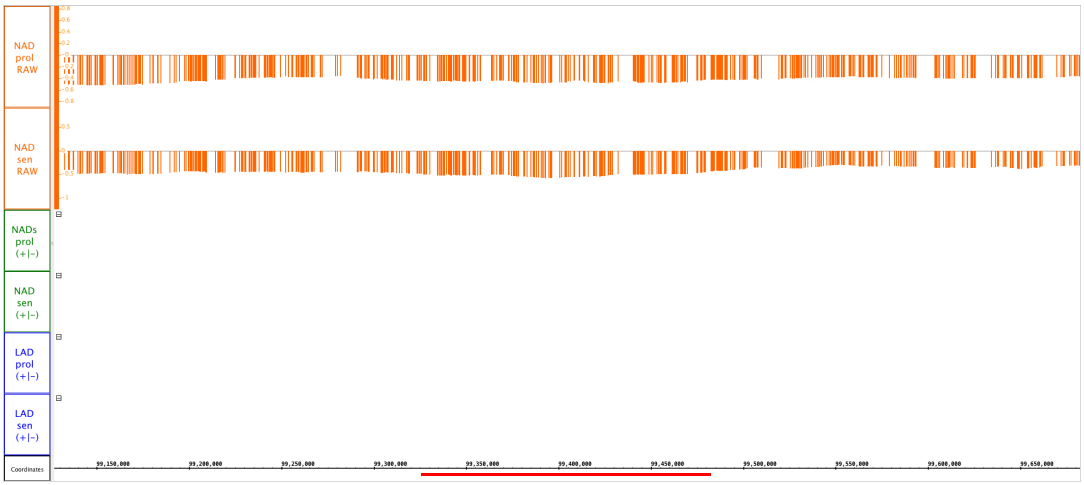

Figure 6.11 – IGB-snapshot of the genomic region corresponding to the BAC RP11-125O21.
Snapshot of a 600 kb region of HSA 8 containing RP11-828F4 which is indicated in red. Orange tracks: normalized microarray data (top:proliferating, bottom senescent). Positive values show enrichment in nucleolus-associated DNA, negative values a depletion. Green tracks: IMR90 all NADs identified by T. Straub (top: proliferating, bottom: senescent). Blue tracks: IMR90 LADs (Sadaie et al., 2013).

7 Acknowledgements

At the end I would like to take the opportunity to thank the people who made my PhD-thesis possible.

At first, my special thank you goes to my supervisor PD Dr. Attila Németh. Thank your for giving me the opportunity to continue with the NAD project, the fruitful scientific discussions as well as scientific and technical support. Moreover, I would like to thank Prof. Dr. Tom Moss for giving me the opportunity to spend three months his laboratory an the Bavaria-Québec International Research Cooperation Program for the traveling grant.

Furthermore, I would like to thank Prof. Dr. Herbert Tschochner and Prof. Dr. Gernot Längst for supporting me financially during my PhD work. Furthermore, I would like to thank Gernot for supporting all my activities in the 'Regensburg international Graduate School' (RiGeL).

In addition, I would like to thank my mentors PD Dr. Achim Griesenbeck and Prof. Dr. Tom Moss from the University Laval in Québec for the scientific discussions we had during the mentor meetings and for being always available for discussions. Furthermore, I would like to thank Prof. Dr. Tom Moss for agreeing to be a reviewer of my PhD thesis and travel to Germany to participate in my thesis defense.

I would like to thank the 'House of the Ribosome' for the welcoming atmosphere which made me stay on the Departement from the first practical course in 2010 until the end of my PhD, now in 2016. Thank you for being open and helpful whenever I needed help and had to ask somebody and also for the occasional 'Feierabendbier' or BBQ.

I also would like to thank the 'Graduate Research Academy of the SFB960' for supporting the progress of my project with financial support of a WHK-student of three months.

Moreover, I would like to thank Christina Fischer and Sebastian Fladerer, who helped me with cell extracts and western blot analyses.

Finally, I would like to thank my family for the constant support, be it financially or emotionally. Thank your for everything.

List of Tables

3.1 Alterations in human cells during cellular senescence. 75
3.2 Overview of 3D immuno-FISH results from a previous (Németh et al., 2010) and this study. 76

List of Figures

1.1 Visualization of chromosome territories. 1
1.2 Scheme depicting different interaction possibilities of chromosomal domains with nuclear subcompartments. 2
1.3 Nuclear bodies. 3
1.4 First illustration of the nucleolus. 4
1.5 Structural features of the human nucleolus on microscopy images. 5
1.6 The nucleolar '-omics'. 7
1.7 Classification of the different types of repetitive DNA found in the genomes of eukaryotes. 9
1.8 Location of the rDNA arrays on human acrocentric chromosomes. 10
1.9 Illustration of the rDNA repeat unit structure. 12
1.10 Illustration of sequence conservation of UBF variants. 12
1.11 Molecular mechanisms of cellular senescence. 15
1.12 Senescent and quiescent cells exit the cell cycle. 16
1.13 Association and dissociation of nucleoli during the cell cycle. 18

2.1 β-galactosidase staining indicates senescence status. 20
2.2 Lack of Ki-67 staining indicates stop of proliferation. 21
2.3 Western blot detection of UBF and tubulin to monitor levels in different fractions of nucleolus preparations. 22
2.4 Monitoring size and shape of isolated particles with DIC microscopy. 23
2.5 qPCR analysis of rDNA amounts in isolated nucleolar DNA compared to genomic DNA. 24
2.6 Illustration of normalized data of CGH-microarrays. 25
2.7 Western blot detection of UBF and tubulin in K562 cellular fractions. 27
2.8 Array CGH analysis of nucleolus-associated DNA prepared by using different nucleolus isolation methods. 28
2.9 Comparison of histones from different fractions of nucleolus preparations by Coomassie staining of SDS-polyacrylamide gels. 29
2.10 Mid-sections of representative confocal microscope images of proliferating and senescent IMR90 cell nuclei. 31
2.11 The number of nucleoli decreases during replicative senescence in IMR90 cells. 32
2.12 The individual volume of nucleoli increases during replicative senescence in IMR90 cells. 33

2.13 The total volume of nucleoli increases during replicative senescence in IMR90 cells. . . . 34
2.14 The nuclear space occupied by nucleoli increases during replicative senescence in IMR90 cells. . . . 35
2.15 Immunostaining for H3K27me3 in proliferating and senescent IMR90 cells. . 36
2.16 Immunostaining of H3K9me2 in proliferating and senescent IMR90 cells. . . 37
2.17 Quantification of the association of Xi to nucleoli or the nuclear periphery in proliferating and senescent IMR90 cells. . . . 38
2.18 Immunostaining for H3K9ac in proliferating and senescent IMR90 cells. . . 39
2.19 Immunostaining for H3K9me3 in proliferating and senescent IMR90 cells. . 40
2.20 Relative amounts of H3K9me3-labeled constitutive heterochromatin at the perinucleolar space and nuclear periphery of proliferating and senescent IMR90 cells. . . . 41
2.21 Heterogeneity of heterochromatin in different areas of the nucleus of proliferating and senescent IMR90 cells. . . . 42
2.22 Distribution of most heterochromatic regions in the nucleus of proliferating and senescent IMR90 cells. . . . 43
2.23 Locations of rDNA BACs Hr4 and Hr6 on the rDNA array. . . . 44
2.24 Metaphase-FISH experiments with rDNA probes. . . . 45
2.25 3D-FISH analysis of rDNA in proliferating and senescent IMR90 cells. . . . 46
2.26 Metaphase-FISH experiments of DJBAC DNA. . . . 46
2.27 3D-FISH experiment of the distal junction of NORs in proliferating and senescent IMR90 cells. . . . 47
2.28 3D-FISH experiment with satellite-2 probe in proliferating and senescent IMR90 cells. . . . 48
2.29 3D-FISH analysis of telomeres in proliferating and senescent IMR90 cells. . 49
2.30 Chromosomal location of BACs used in 3D-FISH experiments. . . . 50
2.31 FISH-analysis of selected BACs on metaphase chromosomes. . . . 51
2.32 Five colour 3D immuno-FISH analysis of selected genomic regions in proliferating and senescent IMR90 cells. . . . 52
2.33 3D immuno-FISH analysis of selected genomic regions in proliferating and senescent IMR90 cells. . . . 54
2.34 Nucleolus association of selected chromosomal regions tested in FISH-experiments. 55
2.35 Genotyping PCR for MEF and iMEF cells. . . . 57
2.36 Western blot analysis of UBF levels after Tamoxifen treatment. . . . 58
2.37 Western blot control of UBF and fibrillarin in different fractions of nucleolus isolations from MEF and iMEF cells . . . 59
2.38 Monitoring size and shape of isolated nucleoli with DIC microscopy. . . . 60
2.39 Immunofluorescence staining of fibrillarin and CENP-A on isolated nucleolar fractions of MEF cells. . . . 61

2.40 Immunofluorescence staining of fibrillarin and CENP-A on isolated nucleolar fractions of iMEF cells. 62
2.41 Locations of rDNA fragments of M6/31-2 and M6/2-2 plasmids on the rDNA repeat unit. 63
2.42 Test of labeled rDNA probes M6/31-2 and M6/2-2 on metaphase chromosomes. 63
2.43 Location of major and minor satellite repeats on mouse chromosomes. . . . 64
2.44 FISH of labeled major-satellite probe on metaphase chromosomes. 64
2.45 3D-FISH of rDNA and major satellites before and after UBF knock-out. . . 65

5.1 Definition of the perinucleolar space and the nuclear periphery to measure fluorescence intensity values 105
5.2 Distribution of the 10 % brightest pixels. 107
5.3 Filter settings for 5-colour-FISH in the Leica SP8 interface. 111

6.1 HeLa NADs. 112
6.2 Comparison of CGH data of HeLa and IMR90 cells. 114
6.3 IGB-snapshot of the genomic region corresponding to the BAC RP11-828F4.122
6.4 IGB-snapshot of the genomic region corresponding to the BAC RP11-90G23.122
6.5 IGB-snapshot of the genomic region corresponding to the BAC RP11-81M8. 123
6.6 IGB-snapshot of the genomic region corresponding to the BAC RP11-173M10.123
6.7 IGB-snapshot of the genomic region corresponding to the BAC RP11-914H1.124
6.8 IGB-snapshot of the genomic region corresponding to the BAC RP11-44B13.124
6.9 IGB-snapshot of the genomic region corresponding to the BAC RP11-784D7.125
6.10 IGB-snapshot of the genomic region corresponding to the BAC RP11-638N4.125
6.11 IGB-snapshot of the genomic region corresponding to the BAC RP11-125O21.126

Bibliography

Albert, B., Colleran, C., Leger-Silvestre, I., Berger, A. B., Dez, C., Normand, C., Perez-Fernandez, J., McStay, B., and Gadal, O. (2013). Structure-function analysis of Hmo1 unveils an ancestral organization of HMG-Box factors involved in ribosomal DNA transcription from yeast to human. *Nucleic Acids Research*, 41(22):10135–10149. 2.2

Alexandrov, I. A., Medvedev, L. I., Mashkova, T. D., Kisselev, L. L., Romanova, L. Y., and Yurov, Y. B. (1993). Definition of a new alpha satellite suprachromosomal family characterized by monomeric organization. *Nucleic Acids Research*, 21(9):2209–2215. 1.1.4

Amenta, P. S. (1961). Fusion of nucleoli in cells cultured from the heart of Triturus viridescens. *The Anatomical Record*. 3.3.1

Anastassova-Kristeva, M. (1977). The nucleolar cycle in man. *J Cell Sci*, 25:103–110. 1.2.2, 1.13, 3.3.1

Andersen, J. S., Lyon, C. E., Fox, A. H., Leung, A. K. L., Lam, Y. W., Steen, H., Mann, M., and Lamond, A. I. (2002). Directed proteomic analysis of the human nucleolus. *Curr Biol*, 12(1):1–11. 1.1.2, 2.1.2, 3.2, 5.1.3.3

Bai, B., Liu, H., and Laiho, M. (2014). Small RNA expression and deep sequencing analyses of the nucleolus reveal the presence of nucleolus-associated microRNAs. *FEBS OPEN BIO*, 4(C):441–449. 1.1.2

Barski, A., Cuddapah, S., Cui, K., Roh, T.-Y., Schones, D. E., Wang, Z., Wei, G., Chepelev, I., and Zhao, K. (2007). High-Resolution Profiling of Histone Methylations in the Human Genome. *Cell*, 129(4):823–837. 2.1.4.2

Bazett-Jones, D. P., Leblanc, B., Herfort, M., and Moss, T. (1994). Short-range DNA looping by the Xenopus HMG-box transcription factor, xUBF. *Science*, 264(5162):1134–1137. 1.1.5

Bell, S. P., Learned, R. M., Jantzen, H. M., and Tjian, R. (1988). Functional cooperativity between transcription factors UBF1 and SL1 mediates human ribosomal RNA synthesis. *Science*, 241(4870):1192–1197. 1.1.5

Bemiller, P. M. and Lee, L. H. (1978). Nucleolar changes in senescing WI-38 cells. *Mech Ageing Dev*, 8(6):417–427. 1.2.2, 3.3.1

Bemiller, P. M. and Miller, J. E. (1979). Cytological changes senescing WI-38 cells: a statistical analysis. *Mech Ageing Dev*, 10(1-2):1–15. 1.2.2, 3.3.1

Bernhard, W., Haguenau, F., and Oberling, C. (1952). L'ultra-structure du nucléole de quelques cellules animales, révélée par le microscope électronique. *Experientia*. 1.1.2

Bhorjee, J. S. and Pederson, T. (1973). Chromatin: its isolation from cultured mammalian cells with particular reference to contamination by nuclear ribnucleoprotein particles. *Biochemistry*, 12(14):2766–2773. 2.1.2, 3.2, 5.1.3.3

Bickmore, W. A. (2013). The Spatial Organization of the Human Genome. *Annual Review of Genomics and Human Genetics*, 14(1):67–84. 1.1.3, 3.3.2, **??**

Birnstiel, M. L., Wallace, H., Sirlin, J. L., and Fischberg, M. (1966). Localization of the ribosomal DNA complements in the nucleolar organizer region of Xenopus laevis. *National Cancer Institute monograph*, 23:431–447. 1.1.2

Blackburn, E. H. and Gall, J. G. (1978). A tandemly repeated sequence at the termini of the extrachromosomal ribosomal RNA genes in Tetrahymena. *Journal of Molecular Biology*, 120(1):33–53. 1.2.1

Blagosklonny, M. V. and Pardee, A. B. (2002). The restriction point of the cell cycle. *Cell Cycle*, 1(2):103–110. 1.2.1

Bodem, J., Dobreva, G., Hoffmann-Rohrer, U., Iben, S., Zentgraf, H., Delius, H., Vingron, M., and Grummt, I. (2000). TIF-IA, the factor mediating growth-dependent control of ribosomal RNA synthesis, is the mammalian homolog of yeast Rrn3p. *EMBO reports*, 1(2):171–175. 1.1.2

Bodnar, A. G., Ouellette, M., Frolkis, M., Holt, S. E., Chiu, C. P., Morin, G. B., Harley, C. B., Shay, J. W., Lichtsteiner, S., and Wright, W. E. (1998). Extension of life-span by introduction of telomerase into normal human cells. *Science*, 279(5349):349–352. 1.2.1

Boggs, B. A., Cheung, P., Heard, E., Spector, D. L., Chinault, A. C., and Allis, C. D. (2001). Differentially methylated forms of histone H3 show unique association patterns with inactive human X chromosomes. *Nature Genetics*, 30(1):73–76. 3.3.2

Boisvert, F.-M., Koningsbruggen, S. v., Navascués, J., and Lamond, A. (2007). The multifunctional nucleolus. *Nat Rev Mol Cell Biol*, 8(7):574–585. 1.1.2, 1.1.2, 1.6

Bolzer, A., Kreth, G., Solovei, I., Koehler, D., Saracoglu, K., Fauth, C., Müller, S., Eils, R., Cremer, C., Speicher, M. R., and Cremer, T. (2005). Three-Dimensional Maps of All Chromosomes in Human Male Fibroblast Nuclei and Prometaphase Rosettes. *Plos Biol*, 3(5):e157. 1.1.1, 1.1

Bourgeois, C. A., Laquerriere, F., Hemon, D., Hubert, J., and Bouteille, M. (1985). New data on the in situ position of the inactive X chromosome in the interphase nucleus of human fibroblasts. *Hum Genet*, 69(2):122–129. 3.3.2

Boveri, T. (1909). Die Blastomerenkerne von Ascaris megalocephala und die Theorie der Chromosomenindividualität. 1.1.1

Brangwynne, C. P., Mitchison, T. J., and Hyman, A. A. (2011). Active liquid-like behavior of nucleoli determines their size and shape in Xenopus laevis oocytes. *Proc Natl Acad Sci USA*, 108(11):4334–4339. 1.2.2, 3.3.1

Bridger, J. M., Boyle, S., Kill, I. R., and Bickmore, W. A. (2000). Re-modelling of nuclear architecture in quiescent and senescent human fibroblasts. *Curr Biol*, 10(3):149–152. (document), 1.2.2, 2.1.1, 3.1, 3.3.2

Britten, R. J. and Kohne, D. E. (1968). Repeated sequences in DNA. Hundreds of thousands of copies of DNA sequences have been incorporated into the genomes of higher organisms. *Science*, 161(3841):529–540. 1.1.4

Brown, D. D. and Gurdon, J. B. (1964). Absence of ribosomal RNA synthesis in the anucleolate mutant of xenopus laevis. *Proceedings of the National Academy of Sciences of the United States of America*, 51:139–146. 1.1.2

Busch, H., Muramatsu, M., Adams, H., Steele, W. J., Liau, M. C., and Smetana, K. (1963). Isolation of nucleoli. *Exp Cell Res*, 24:SUPPL9:150–63. 2.1.2, 3.2

Caburet, S., Conti, C., Schurra, C., Lebofsky, R., Edelstein, S. J., and Bensimon, A. (2005). Human ribosomal RNA gene arrays display a broad range of palindromic structures. *Genome research*, 15(8):1079–1085. 1.1.5

Camps, J., Wangsa, D., Falke, M., Brown, M., Case, C. M., Erdos, M. R., and Ried, T. (2014). Loss of lamin B1 results in prolongation of S phase and decondensation of chromosome territories. *The FASEB Journal*, 28(8):3423–3434. 3.3.2

Candido, E. P., Reeves, R., and Davie, J. R. (1978). Sodium butyrate inhibits histone deacetylation in cultured cells. *Cell*, 14(1):105–113. 2.1.3

Caudron-Herger, M., Pankert, T., Seiler, J., Németh, A., Voit, R., Grummt, I., and Rippe, K. (2015). Alu element-containing RNAs maintain nucleolar structure and function. *The EMBO Journal*, 34(22):2758–2774. 1.1.2

Chandra, T., Ewels, P. A., Schoenfelder, S., Furlan-Magaril, M., Wingett, S. W., Kirschner, K., Thuret, J.-Y., Andrews, S., Fraser, P., and Reik, W. (2015). Global Reorganization of the Nuclear Landscape in Senescent Cells. *CellReports*, 10(4):1–13. 3.3.2

Chen, Q. and Ames, B. N. (1994). Senescence-like growth arrest induced by hydrogen peroxide in human diploid fibroblast F65 cells. *Proceedings of the National Academy of Sciences of the United States of America*, 91(10):4130–4134. 1.2.1

Ching, R. W., Ahmed, K., Boutros, P. C., Penn, L. Z., and Bazett-Jones, D. P. (2013). Identifying gene locus associations with promyelocytic leukemia nuclear bodies using immuno-TRAP. *J Cell Biol*, 201(2):325–335. 1.1.1

Chuang, C. H. and Belmont, A. S. (2007). Moving chromatin within the interphase nucleus-controlled transitions? *Seminars in cell & developmental biology*. 3.1

Cooke, H. J. and Smith, B. A. (1986). Variability at the Telomeres of the Human X/Y Pseudoautosomal Region. *Cold Spring Harbor Symposia on Quantitative Biology*, 51(0):213–219. 1.2.1

Coppé, J.-P., Desprez, P.-Y., Krtolica, A., and Campisi, J. (2010). The senescence-associated secretory phenotype: the dark side of tumor suppression. *Annual review of pathology*, 5:99–118. 1.2.1

Coppé, J.-P., Patil, C. K., Rodier, F., Sun, Y., Muñoz, D. P., Goldstein, J., Nelson, P. S., Desprez, P.-Y., and Campisi, J. (2008). Senescence-Associated Secretory Phenotypes Reveal Cell-Nonautonomous Functions of Oncogenic RAS and the p53 Tumor Suppressor. *Plos Biol*, 6(12):e301. **??**, **??**

Corpet, A. and Stucki, M. (2014). Chromatin maintenance and dynamics in senescence: a spotlight on SAHF formation and the epigenome of senescent cells. *Chromosoma*, 123(5):423–436. 3.1

Couté, Y., Burgess, J. A., Diaz, J.-J., Chichester, C., Lisacek, F., Greco, A., and Sanchez, J.-C. (2006). Deciphering the human nucleolar proteome. *Mass Spectrometry Reviews*, 25(2):215–234. 1.1.2

Cremer, M., von Hase, J., Volm, T., Brero, A., Kreth, G., Walter, J., Fischer, C., Solovei, I., Cremer, C., and Cremer, T. (2001). Non-random radial higher-order chromatin arrangements in nuclei of diploid human cells. *Chromosome Research*, 9(7):541–567. 1.1.3

Cremer, T. and Cremer, M. (2010). Chromosome Territories. *Cold Spring Harbor Perspectives in Biology*, 2(3):a003889–a003889. 1.1.1

Cruickshanks, H. A., McBryan, T., Nelson, D. M., VanderKraats, N. D., Shah, P. P., van Tuyn, J., Rai, T. S., Brock, C., Donahue, G., Dunican, D. S., Drotar, M. E., Meehan, R. R., Edwards, J. R., Berger, S. L., and Adams, P. D. (2013). Cruickshanks 2012 ncb. *Nature cell biology*, 15(12):1495–1506. 3.3.2, **??**

d'Adda di Fagagna, F., Reaper, P. M., Clay-Farrace, L., Fiegler, H., Carr, P., von Zglinicki, T., Saretzki, G., Carter, N. P., and Jackson, S. P. (2003). A DNA damage checkpoint response in telomere-initiated senescence. *Nature*, 426(6963):194–198. 1.2.1

de Koning, A. P. J., Gu, W., Castoe, T. A., Batzer, M. A., and Pollock, D. D. (2011). Repetitive Elements May Comprise Over Two-Thirds of the Human Genome. *PLoS Genet*, 7(12):e1002384. 1.1.4

Dekker, J., Rippe, K., Dekker, M., and Kleckner, N. (2002). Capturing chromosome conformation. *Science*, 295(5558):1306–1311. 1.1.1

Dev, V. G., Tantravahi, R., Miller, D. A., and Miller, O. J. (1977). Nucleolus organizers in Mus musculus subspecies and in the RAG mouse cell line. *Genetics*, 86(2 Pt. 1):389–398. 1.1.5

Diesch, J., Hannan, R. D., and Sanij, E. (2015). Genome wide mapping of UBF binding-sites in mouse and human cell lines. *GDATA*, 3(C):103–105. 1.1.5

Dietzel, S., Jauch, A., Kienle, D., Qu, G., Holtgreve-Grez, H., Eils, R., Münkel, C., Bittner, M., Meltzer, P. S., Trent, J. M., and Cremer, T. (1998). Separate and variably shaped chromosome arm domains are disclosed by chromosome arm painting in human cell nuclei. *Chromosome Research*, 6(1):25–33. 1.1.1

Dillinger, S., Garea, A. V., Deutzmann, R., and Németh, A. (2014). Analysis of histone posttranslational modifications from nucleolus-associated chromatin by mass spectrometry. *Methods Mol Biol*, 1094:277–293. 2.1.3, 3.2

Dimri, G. P., Lee, X., Basile, G., Acosta, M., Scott, G., Roskelley, C., Medrano, E. E., Linskens, M., Rubelj, I., and Pereira-Smith, O. (1995). A biomarker that identifies senescent human cells in culture and in aging skin in vivo. *Proc Natl Acad Sci USA*, 92(20):9363–9367. 1.2.1, 2.1.1.1, **??**, **??**, 5.3.6

Djebali, S., Davis, C. A., Merkel, A., Dobin, A., Lassmann, T., Mortazavi, A., Tanzer, A., Lagarde, J., Lin, W., Schlesinger, F., Xue, C., Marinov, G. K., Khatun, J., Williams, B. A., Zaleski, C., Rozowsky, J., Röder, M., Kokocinski, F., Abdelhamid, R. F., Alioto, T., Antoshechkin, I., Baer, M. T., Bar, N. S., Batut, P., Bell, K., Bell, I., Chakrabortty, S., Chen, X., Chrast, J., Curado, J., Derrien, T., Drenkow, J., Dumais, E., Dumais, J., Duttagupta, R., Falconnet, E., Fastuca, M., Fejes-Toth, K., Ferreira, P., Foissac, S., Fullwood, M. J., Gao, H., Gonzalez, D., Gordon, A., Gunawardena, H., Howald, C., Jha, S., Johnson, R., Kapranov, P., King, B., Kingswood, C., Luo, O. J., Park, E., Persaud, K., Preall, J. B., Ribeca, P., Risk, B., Robyr, D., Sammeth, M., Schaffer, L., See, L.-H., Shahab, A., Skancke, J., Suzuki, A. M., Takahashi, H., Tilgner, H., Trout, D., Walters, N., Wang, H., Wrobel, J., Yu, Y., Ruan, X., Hayashizaki, Y., Harrow, J., Gerstein, M., Hubbard, T., Reymond, A., Antonarakis, S. E., Hannon, G., Giddings, M. C., Ruan, Y., Wold, B., Carninci, P., Guigó, R., and Gingeras, T. R. (2012). Landscape of transcription in human cells. *Nature*, 489(7414):101–108. 1.1.2, 1.6, 2.1.2

Egelhofer, T. A., Minoda, A., Klugman, S., Lee, K., Kolasinska-Zwierz, P., Alekseyenko, A. A., Cheung, M.-S., Day, D. S., Gadel, S., Gorchakov, A. A., Gu, T., Kharchenko, P. V., Kuan, S., Latorre, I., Linder-Basso, D., Luu, Y., Ngo, Q., Perry, M., Rechtsteiner, A., Riddle, N. C., Schwartz, Y. B., Shanower, G. A., Vielle, A., Ahringer, J., Elgin, S. C. R., Kuroda, M. I., Pirrotta, V., Ren, B., Strome, S., Park, P. J., Karpen, G. H., Hawkins, R. D., and Lieb, J. D. (2010). An assessment of histone-modification antibody quality. *Nat Struct Mol Biol*, 18(1):91–93. 3.3.2

Even-Faitelson, L., Hassan-Zadeh, V., Baghestani, Z., and Bazett-Jones, D. P. (2015). Coming to terms with chromatin structure. *Chromosoma*. 1.1.3

Farley, K. I., Surovtseva, Y., Merkel, J., and Baserga, S. J. (2015). Determinants of mammalian nucleolar architecture. *Chromosoma*, 124(3):323–331. 3.3.1

Filion, G. J., van Bemmel, J. G., Braunschweig, U., Talhout, W., Kind, J., Ward, L. D., Brugman, W., de Castro, I. J., Kerkhoven, R. M., Bussemaker, H. J., and van Steensel, B. (2010). Systematic protein location mapping reveals five principal chromatin types in Drosophila cells. *Cell*, 143(2):212–224. 1.1.3

Floutsakou, I., Agrawal, S., Nguyen, T. T., Seoighe, C., Ganley, A. R. D., and McStay, B. (2013). The shared genomic architecture of human nucleolar organizer regions. *Genome research*. 1.1.5, 1.8, 2.1.4.4, 2.1.4.4, 4.14

Fontana, F. (1781). Treatise on the venom of the viper, on the American poisons, and on the cherry laurel, and some other vegetable poisons : to which are annexed, observations on the primitive structure of the animal body, different experiments on the reproduction of the nerves, and a description of a new canal of the eye ... / translated from the original French of Felix Fontana. Vol. 1. 1.1.2, 1.4

Fraser, J., Williamson, I., Bickmore, W. A., and Dostie, J. (2015). An Overview of Genome Organization and How We Got There: from FISH to Hi-C. *Microbiology and molecular biology reviews : MMBR*, 79(3):347–372. 1.1.1

Freund, A., Laberge, R.-M., Demaria, M., and Campisi, J. (2012). Lamin B1 loss is a senescence-associated biomarker. *Mol Biol Cell*, 23(11):2066–2075. 1.2.2

Funayama, R., Saito, M., Tanobe, H., and Ishikawa, F. (2006). Loss of linker histone H1 in cellular senescence. *J Cell Biol*, 175(6):869–880. 3.1

Gagné, R., Laberge, C., and Tanguay, R. (1973). Aspect cytologique et localisation intranucléaire de l'hétérochromatine constitutive des chromosomes C9 chez l'homme. *Chromosoma*. 1.1.3

Gall, J. G., Tsvetkov, A., Wu, Z., and Murphy, C. (1995). Is the sphere organelle/coiled body a universal nuclear component? *Developmental genetics*, 16(1):25–35. 3.3.1

Gonzalez, I. L. and Sylvester, J. E. (1995). Complete sequence of the 43-kb human ribosomal DNA repeat: analysis of the intergenic spacer. *Genomics*, 27(2):320–328. 1.1.5, 1.1.5

Görisch, S. M., Lichter, P., and Rippe, K. (2005). Mobility of multi-subunit complexes in the nucleus: accessibility and dynamics of chromatin subcompartments. *Histochemistry and Cell Biology*, 123(3):217–228. 3.1

Greig, G. M. and Willard, H. F. (1992). β satellite DNA: characterization and localization of two subfamilies from the distal and proximal short arms of the human acrocentric chromosomes. *Genomics*. 1.1.5

Grozdanov, P., Georgiev, O., and Karagyozov, L. (2003). Complete sequence of the 45-kb mouse ribosomal DNA repeat: analysis of the intergenic spacer. *Genomics*, 82(6):637–643. 1.1.5, 4.16

Grummt, I. (2003). Life on a planet of its own: regulation of RNA polymerase I transcription in the nucleolus. *Genes Dev*, 17(14):1691–1702. 1.1.2

Guelen, L., Pagie, L., Brasset, E., Meuleman, W., Faza, M. B., Talhout, W., Eussen, B. H., de Klein, A., Wessels, L., de Laat, W., and van Steensel, B. (2008). Domain organization of human chromosomes revealed by mapping of nuclear lamina interactions. *Nature*, 453(7197):948–951. 1.1.1, 1.1.3

Guillén, A. K. Z., Hirai, Y., Tanoue, T., and Hirai, H. (2004). Transcriptional repression mechanisms of nucleolus organizer regions (NORs) in humans and chimpanzees. *Chromosome Research*, 12(3):225–237. 1.1.5

Haltiner, M. M., Smale, S. T., and Tjian, R. (1986). Two distinct promoter elements in the human rRNA gene identified by linker scanning mutagenesis. *Mol Cell Biol*, 6(1):227–235. 1.1.5

Hamdane, N., Herdman, C., Mars, J.-C., Stefanovsky, V., Tremblay, M. G., and Moss, T. (2015). Depletion of the cisplatin targeted HMGB-box factor UBF selectively induces p53-independent apoptotic death in transformed cells. *Oncotarget*, 6(29):27519–27536. 2.2, 4.11

Hamdane, N., Stefanovsky, V. Y., Tremblay, M. G., Németh, A., Paquet, E., Lessard, F., Sanij, E., Hannan, R., and Moss, T. (2014). Conditional Inactivation of Upstream Binding Factor Reveals Its Epigenetic Functions and the Existence of a Somatic Nucleolar Precursor Body. *PLoS Genet*, 10(8):e1004505. (document), 1.1.5, 2.2, 2.2.2, 2.2.2, 2.2.3, 3.4, 4.11

Hamperl, S., Wittner, M., Babl, V., Perez-Fernandez, J., Tschochner, H., and Griesenbeck, J. (2013). Chromatin states at ribosomal DNA loci. *Biochimica et Biophysica Acta (BBA) - Gene Regulatory Mechanisms*, 1829(3-4):405–417. 1.1.5

Harley, C. B., Futcher, A. B., and Greider, C. W. (1990). Telomeres shorten during ageing of human fibroblasts. *Nature*, 345(6274):458–460. 1.2.1, **??**

Hayashi-Takanaka, Y., Yamagata, K., Wakayama, T., Stasevich, T. J., Kainuma, T., Tsurimoto, T., Tachibana, M., Shinkai, Y., Kurumizaka, H., Nozaki, N., and Kimura, H. (2011). Tracking epigenetic histone modifications in single cells using Fab-based live endogenous modification labeling. *Nucleic Acids Research*, 39(15):6475–6488. 3.3.2, 4.8

Hayflick (1965). The limited in vitro lifetime of human diploid cell strains. *Exp Cell Res*, 37:614–636. (document), **??**

Hayflick and Moorhead (1961). The serial cultivation of human diploid cell strains. *Exp Cell Res*, 25:585–621. 1.2.1, 2.1.1.1

Heard, E., Rougeulle, C., Arnaud, D., Avner, P., and Allis, C. D. (2001). Methylation of histone H3 at Lys-9 is an early mark on the X chromosome during X inactivation. *Cell*. 3.3.2

Hein, N., Sanij, E., Quin, J., Hannan, K. M., Ganley, A., and Hannan, R. D. (2011). The Nucleolus and Ribosomal Genes in Aging and Senescence. (document)

Heitz, E. (1931). Die ursache der gesetzmässigen zahl, lage, form und grösse pflanzlicher nukleolen. *Planta*. 1.1.2

Heliot, L., Kaplan, H., Lucas, L., Klein, C., Beorchia, A., Doco-Fenzy, M., Menager, M., Thiry, M., O'Donohue, M. F., and Ploton, D. (1997). Electron tomography of metaphase nucleolar organizer regions: evidence for a twisted-loop organization. *Mol Biol Cell*, 8(11):2199–2216. 1.1.5

Henderson, A. S., Warburton, D., and Atwood, K. C. (1972). Location of ribosomal DNA in the human chromosome complement. *Proceedings of the National Academy of Sciences of the United States of America*, 69(11):3394–3398. 1.1.2, 1.1.5

Hsu, T. C., Spirito, S. E., and Pardue, M. L. (1975). Distribution of 18+28S ribosomal genes in mammalian genomes. *Chromosoma*, 53(1):25–36. 1.2.2

Jantzen, H. M., Admon, A., Bell, S. P., and Tjian, R. (1990). Nucleolar transcription factor hUBF contains a DNA-binding motif with homology to HMG proteins. *Nature*, 344(6269):830–836. 1.1.2, 1.1.5

Jantzen, H. M., Chow, A. M., and King, D. S. (1992). Multiple domains of the RNA polymerase I activator hUBF interact with the TATA-binding protein complex hSL1 to mediate transcription. *Genes & Development*. 1.1.5

Johmura, Y., Shimada, M., Misaki, T., Naiki-Ito, A., Miyoshi, H., Motoyama, N., Ohtani, N., Hara, E., Nakamura, M., Morita, A., Takahashi, S., and Nakanishi, M. (2014). Necessary and Sufficient Rolefor a Mitosis Skip in Senescence Induction. *Mol Cell*, pages 1–12. 1.2.1

Johnson, D. S., Mortazavi, A., Myers, R. M., and Wold, B. (2007). Genome-wide mapping of in vivo protein-DNA interactions. *Science*, 316(5830):1497–1502. 1.1.1

Kharchenko, P. V., Alekseyenko, A. A., Schwartz, Y. B., Minoda, A., Riddle, N. C., Ernst, J., Sabo, P. J., Larschan, E., Gorchakov, A. A., Gu, T., Linder-Basso, D., Plachetka, A., Shanower, G., Tolstorukov, M. Y., Luquette, L. J., Xi, R., Jung, Y. L., Park, R. W., Bishop, E. P., Canfield, T. P., Sandstrom, R., Thurman, R. E., MacAlpine, D. M., Stamatoyannopoulos, J. A., Kellis, M., Elgin, S. C. R., Kuroda, M. I., Pirrotta, V., Karpen, G. H., and Park, P. J. (2011). Comprehensive analysis of the chromatin landscape in Drosophila melanogaster. *Nature*, 471(7339):480–485. 1.1.3

Kim, S. H., Koroleva, O. A., Lewandowska, D., Pendle, A. F., Clark, G. P., Simpson, C. G., Shaw, P. J., and Brown, J. W. S. (2009). Aberrant mRNA Transcripts and the Nonsense-Mediated Decay Proteins UPF2 and UPF3 Are Enriched in the Arabidopsis Nucleolus. *The Plant Cell*, 21(7):2045–2057. 1.1.2

Kim, S. H., Spensley, M., Choi, S. K., Calixto, C. P. G., Pendle, A. F., Koroleva, O., Shaw, P. J., and Brown, J. W. S. (2010). Plant U13 orthologues and orphan snoRNAs identified by RNomics of RNA from Arabidopsis nucleoli. *Nucleic Acids Research*, 38(9):3054–3067. 1.1.2

Kind, J., Pagie, L., Ortabozkoyun, H., Boyle, S., de Vries, S. S., Janssen, H., Amendola, M., Nolen, L. D., Bickmore, W. A., and van Steensel, B. (2013). Single-cell dynamics of genome-nuclear lamina interactions. *Cell*, 153(1):178–192. 1.1.3, 3.2

Kind, J. and van Steensel, B. (2010). Genome&nuclear lamina interactions and gene regulation. *Current Opinion in Cell Biology*, 22(3):320–325. 1.1.3

Kit, S. (1961). Equilibrium sedimentation in density gradients of DNA preparations from animal tissues. *Journal of Molecular Biology*, 3(6):711–IN2. 1.1.4

Kosar, M., Bartkova, J., Hubackova, S., Hodny, Z., Lukas, J., and Bartek, J. (2014). Senescence-associated heterochromatin foci are dispensable for cellular senescence, occur in a cell type- and insult-dependent manner and follow expression of p16 ink4a. *Cell Cycle*, 10(3):457–468. 1.2.2, 3.1, **??**

Kuilman, T., Michaloglou, C., Mooi, W. J., and Peeper, D. S. (2010). The essence of senescence. *Genes Dev*, 24(22):2463–2479. 1.2.1

Learned, R. M., Cordes, S., and Tjian, R. (1985). Purification and characterization of a transcription factor that confers promoter specificity to human RNA polymerase I. *Molecular and Cellular Biology*. 1.1.2

Learned, R. M., Learned, T. K., Haltiner, M. M., and Tjian, R. T. (1986). Human rRNA transcription is modulated by the coordinate binding of two factors to an upstream control element. *Cell*. 1.1.5

Lee, B. Y., Han, J. A., Im, J. S., Morrone, A., Johung, K., Goodwin, E. C., Kleijer, W. J., DiMaio, D., and Hwang, E. S. (2006). Senescence-associated beta-galactosidase is lysosomal beta-galactosidase. *Aging cell*, 5(2):187–195. 1.2.1

Lehnertz, B., Ueda, Y., Derijck, A. A. H. A., Braunschweig, U., Perez-Burgos, L., Kubicek, S., Chen, T., Li, E., Jenuwein, T., and Peters, A. H. F. M. (2003). Suv39h-Mediated Histone H3 Lysine 9 Methylation Directs DNA Methylation to Major Satellite Repeats at Pericentric Heterochromatin. *Current Biology*, 13(14):1192–1200. 2.43

Lieberman-Aiden, E., van Berkum, N. L., Williams, L., Imakaev, M., Ragoczy, T., Telling, A., Amit, I., Lajoie, B. R., Sabo, P. J., Dorschner, M. O., Sandstrom, R., Bernstein, B., Bender, M. A., Groudine, M., Gnirke, A., Stamatoyannopoulos, J., Mirny, L. A., Lander, E. S., and Dekker, J. (2009). Comprehensive mapping of long-range interactions reveals folding principles of the human genome. *Science*, 326(5950):289–293. 1.1.1

López-Flores, I. and Garrido-Ramos, M. A. (2012). The repetitive DNA content of eukaryotic genomes. *Genome dynamics*, 7:1–28. 1.1.4, 1.7

López-Otín, C., Blasco, M. A., Partridge, L., Serrano, M., and Kroemer, G. (2013). The hallmarks of aging. *Cell*, 153(6):1194–1217. 1.2.1

Mais, C., Wright, J. E., Prieto, J.-L., Raggett, S. L., and McStay, B. (2005). UBF-binding site arrays form pseudo-NORs and sequester the RNA polymerase I transcription machinery. *Genes & Development*, 19(1):50–64. 1.1.5, 4.16

Mao, Z., Ke, Z., Gorbunova, V., and Seluanov, A. (2012). Replicatively senescent cells are arrested in G1 and G2 phases. *Aging*. 1.2.1

Matera, A. G., Frey, M. R., Margelot, K., and Wolin, S. L. (1995). A perinucleolar compartment contains several RNA polymerase III transcripts as well as the polypyrimidine tract-binding protein, hnRNP I. *The Journal of Cell Biology*, 129(5):1181–1193. 3.1

Matera, A. G., Izaguire-Sierra, M., Praveen, K., and Rajendra, T. K. (2009). Review Feature. *Developmental Cell*, 17(5):639–647. 1.3

McClintock, B. (1934). The relation of a particular chromosomal element to the development of the nucleoli in Zea mays. *Zeitschrift für Zellforschung und mikroskopische Anatomie*. 1.1.2

McConkey, E. H. and Hopkins, J. W. (1964). The relationship of the nucleolus to the synthesis of ribosomal RNA in HeLa cells. *Proceedings of the National Academy of Sciences of the United States of America*, 51:1197–1204. 1.1.2

McConnell, B. B., Starborg, M., Brookes, S., and Peters, G. (1998). Inhibitors of cyclin-dependent kinases induce features of replicative senescence in early passage human diploid fibroblasts. *Current Biology*, 8(6):351–354. 1.2.1

McStay, B., Frazier, M. W., and Reeder, R. H. (1991). xUBF contains a novel dimerization domain essential for RNA polymerase I transcription. *Genes & Development*, 5(11):1957–1968. 1.1.5

McStay, B. and Grummt, I. (2008). The epigenetics of rRNA genes: from molecular to chromosome biology. *Annu Rev Cell Dev Biol*, 24:131–157. 1.1.5, 1.1.5, 1.1.5, 1.9, 1.10

Mehta, I., Figgitt, M., Clements, C., Kill, I., and Bridger, J. (2007). Alterations to nuclear architecture and genome behavior in senescent cells. *Ann N Y Acad Sci*, 1100:250–263. (document)

Miller, O. L. and Beatty, B. R. (1969). Visualization of nucleolar genes. *Science*, 164(3882):955–957. 1.1.2

Milo, R., Jorgensen, P., Moran, U., Weber, G., and Springer, M. (2009). BioNumbers–the database of key numbers in molecular and cell biology. *Nucleic Acids Research*, 38(Database):D750–D753. 3.3.1

Montgomery, T. H. (1898). Comparative Cytological Studies with Especial Regard to the Morphology of the Nucleolus. 1.1.2

Monty, K. J., Litt, M., Kay, E. R., and Dounce, A. L. (1956). Isolation and properties of liver cell nucleoli. *The Journal of biophysical and biochemical cytology*, 2(2):127–145. 1.1.2, 2.1.2, 3.2

Moorefield, B. and Greene, E. A. (2000). RNA polymerase I transcription factor Rrn3 is functionally conserved between yeast and human. In *Proc Natl Acad Sci USA*. 1.1.2

Mosgoeller, W. (2004). *Nucleolar Ultrastructure in vertebrates*. The nucleolus. Landes Bioscience. 1.1.2

Moskalev, A. A., Aliper, A. M., Smit-McBride, Z., Buzdin, A., and Zhavoronkov, A. (2014). Genetics and epigenetics of aging and longevity. *Cell Cycle*, 13(7). 1.2.1

Moss, T. and Stefanovsky, V. Y. (1995). Promotion and regulation of ribosomal transcription in eukaryotes by RNA polymerase 1. *Progress Nucl Acid Res Mol Biol*. 1.1.5

Moss, T. and Stefanovsky, V. Y. (2002). At the center of eukaryotic life. *Cell*, 109(5):545–548. 1.1.2

Muñoz-Espín, D. and Serrano, M. (2014). Cellular senescence: from physiologyto pathology. *Nat Rev Mol Cell Biol*, 15(7):482–496. 1.2.1, 1.2.1, 1.11

Muramatsu, M., Smetana, K., and Busch, H. (1963). Quantitative aspects of isolation of nucleoli of the Walker carcinosarcoma and liver of the rat. *Cancer Research*. 1.1.2, 5.1.3.3

Nandakumar, V., Kelbauskas, L., Johnson, R., and Meldrum, D. (2010). Quantitative characterization of preneoplastic progression using single-cell computed tomography and three-dimensional karyometry. *Cytometry*, 79A(1):25–34. 3.3.1

Narita, M., Nũnez, S., Heard, E., Narita, M., Lin, A. W., Hearn, S. A., Spector, D. L., Hannon, G. J., and Lowe, S. W. (2003). Rb-mediated heterochromatin formation and silencing of E2F target genes during cellular senescence. *Cell*, 113(6):703–716. 1.2.2, 3.1, **??**, **??**

Nelson, G., Wordsworth, J., Wang, C., Jurk, D., Lawless, C., Martin-Ruiz, C., and von Zglinicki, T. (2012). A senescent cell bystander effect: senescence-induced senescence. *Aging cell*, 11(2):345–349. 1.2.1

Németh, A., Conesa, A., Santoyo-Lopez, J., Medina, I., Montaner, D., Péterfia, B., Solovei, I., Cremer, T., Dopazo, J., and Längst, G. (2010). Initial genomics of the human nucleolus. *PLoS Genet*, 6(3):e1000889. (document), 1.1.1, 1.1.2, 1.6, 1.1.3, 2.1.1, 2.1.4.2, 2.1.4.4, 2.1.5, 3.1, 3.2, 3.2, 3.3.4, 3.4, 6.1, 6.1, 7

Németh, A. and Längst, G. (2011). Genome organization in and around the nucleolus. *Trends Genet*, 27(4):149–156. 1.1.3, 1.1.5

Nichols, W. W., Murphy, D. G., Cristofalo, V. J., Toji, L. H., Greene, A. E., and Dwight, S. A. (1977). Characterization of a new human diploid cell strain, IMR-90. *Science*, 196(4285):60–63. 4.11

Nishimura, K., Kumazawa, T., Kuroda, T., Katagiri, N., Tsuchiya, M., Goto, N., Furumai, R., Murayama, A., Yanagisawa, J., and Kimura, K. (2015). Perturbation of Ribosome Biogenesis Drives Cells into Senescence through 5S RNP-Mediated p53 Activation. *CellReports*, 10(8):1310–1323. 3.3.3, **??**

Nizami, Z., Deryusheva, S., and Gall, J. G. (2010). The Cajal Body and Histone Locus Body. *Cold Spring Harbor Perspectives in Biology*, 2(7):a000653–a000653. 1.1.1

Ochs, R. L. and Press, R. I. (1992). Centromere autoantigens are associated with the nucleolus. *Exp Cell Res*, 200(2):339–350. 3.1

Olovnikov, A. M. (1973). A theory of marginotomy. The incomplete copying of template margin in enzymic synthesis of polynucleotides and biological significance of the phenomenon. *Journal of theoretical biology*, 41(1):181–190. 1.2.1

O'Sullivan, A. C., Sullivan, G. J., and McStay, B. (2002). UBF binding in vivo is not restricted to regulatory sequences within the vertebrate ribosomal DNA repeat. *Mol Cell Biol*, 22(2):657–668. 1.1.5

O'Sullivan, R. J., Kubicek, S., Schreiber, S. L., and Karlseder, J. (2010). Reduced histone biosynthesis and chromatin changes arising from a damage signal at telomeres. *Nat Struct Mol Biol*, 17(10):1218–1225. **??**

Pardee, A. B. (1974). A restriction point for control of normal animal cell proliferation. *Proceedings of the National Academy of Sciences of the United States of America*, 71(4):1286–1290. 1.2.1

Parrinello, S., Samper, E., Krtolica, A., Goldstein, J., Melov, S., and Campisi, J. (2003). Oxygen sensitivity severely limits the replicative lifespan of murine fibroblasts. *Nature cell biology*, 5(8):741–747. 1.2.1

Pederson, T. (1998). The plurifunctional nucleolus. *Nucleic Acids Research*, 26(17):3871–3876. 1.1.2, 1.1.2

Perry, R. P. (1962). The cellular sites of synthesis of ribosomal and 4S RNA. *Proceedings of the National Academy of Sciences of the United States of America*, 48(12):2179. 1.1.2

Pickersgill, H., Kalverda, B., de Wit, E., Talhout, W., Fornerod, M., and van Steensel, B. (2006). Characterization of the Drosophila melanogaster genome at the nuclear lamina. *Nature Genetics*, 38(9):1005–1014. 1.1.1

Pool, T. B., Heitman, T. O., and Buck, M. A. (1982). Quantitative morphological analysis of proliferating and nonproliferating subpopulations of IMR90 fibroblasts during aging in vitro. *American Journal of Anatomy*. 3.3.1

Prieto, J.-L. and McStay, B. (2008). Pseudo-NORs: a novel model for studying nucleoli. *Biochimica et biophysica acta*, 1783(11):2116–2123. 1.1.5

Putnam, C. D., Copenhaver, G. P., and Denton, M. L. (1994). The RNA polymerase I transactivator upstream binding factor requires its dimerization domain and high-mobility-group (HMG) box 1 to bend, wrap, and positively supercoil enhancer DNA. *Molecular and Cellular Biology*. 1.1.5

Rabl, C. (1885). *Morphologisches Jahrbuch*. Bd. X. 1.1.1

Ragoczy, T., Telling, A., Scalzo, D., Kooperberg, C., and Groudine, M. (2015). Functional redundancy in the nuclear compartmentalization of the late-replicating genome. *Nucleus*, 5(6):626–635. 1.1.3

Rai, T. S. and Adams, P. D. (2012). Lessons from senescence: Chromatin maintenance in non-proliferating cells. *Biochimica et Biophysica Acta (BBA) - Gene Regulatory Mechanisms*, 1819(3-4):322–331. 1.2.2

Ramirez, R. D., Morales, C. P., Herbert, B.-S., Rohde, J. M., Passons, C., Shay, J. W., and Wright, W. E. (2001). Putative telomere-independent mechanisms of replicative aging reflect inadequate growth conditions. *Genes & Development*. 1.2.1

Rao, S. S. P., Huntley, M. H., Durand, N. C., Stamenova, E. K., Bochkov, I. D., Robinson, J. T., Sanborn, A. L., Machol, I., Omer, A. D., Lander, E. S., and Aiden, E. L. (2014). A 3D Map of the Human Genome at Kilobase Resolution Reveals Principles of Chromatin Looping. *Cell*, pages 1–16. 1.1.1

Raska, I., Dundr, M., Koberna, K., Melcák, I., Risueño, M. C., and Török, I. (1995). Does the synthesis of ribosomal RNA take place within nucleolar fibrillar centers or dense fibrillar components? A critical appraisal. *Journal of Structural Biology*, 114(1):1–22. 1.1.2

Recher, L., Whitescarver, J., and Briggs, L. (1969). The fine structure of a nucleolar constituent. *Journal of ultrastructure research*, 29(1):1–14. 1.1.2

Reeder, R. H. and Roeder, R. G. (1972). Ribosomal RNA synthesis in isolated nuclei. *Journal of Molecular Biology*, 67(3):433–441. 1.1.2

Robinett, C. C., Straight, A., Li, G., and Willhelm, C. (1996). In vivo localization of DNA sequences and visualization of large-scale chromatin organization using lac operator/repressor recognition. *The Journal of Cell Biology*. 3.1

Rodier, F., Coppé, J.-P., Patil, C. K., Hoeijmakers, W. A. M., Muñoz, D. P., Raza, S. R., Freund, A., Campeau, E., Davalos, A. R., and Campisi, J. (2009). Persistent DNA damage signalling triggers senescence-associated inflammatory cytokine secretion. *Nature cell biology*, 11(8):973–979. 1.2.1

Roeder, R. G. and Rutter, W. J. (1969). Multiple forms of DNA-dependent RNA polymerase in eukaryotic organisms. *Nature*, 224(5216):234–237. 1.1.2

Ronneberger, O., Baddeley, D., Scheipl, F., Verveer, P. J., Burkhardt, H., Cremer, C., Fahrmeir, L., Cremer, T., and Joffe, B. (2008). Spatial quantitative analysis of fluorescently labeled nuclear structures: Problems, methods, pitfalls. *Chromosome Research*, 16(3):523–562. 5.5.4

Rosenfeld, J. A., Wang, Z., Schones, D. E., Zhao, K., DeSalle, R., and Zhang, M. Q. (2009). Determination of enriched histone modifications in non-genic portions of the human genome. *BMC Genomics*, 10(1):143. 2.1.4.2

Rothbart, S. B., Dickson, B. M., Raab, J. R., Grzybowski, A. T., Krajewski, K., Guo, A. H., Shanle, E. K., Josefowicz, S. Z., Fuchs, S. M., Allis, C. D., Magnuson, T. R., Ruthenburg, A. J., and Strahl, B. D. (2015). An Interactive Database for the Assessment of Histone Antibody Specificity. *Molecular Cell*, 59(3):502–511. 3.3.2

Roussel, P., André, C., and Comai, L. (1996). The rDNA transcription machinery is assembled during mitosis in active NORs and absent in inactive NORs. *The Journal of Cell Biology*. 1.1.5

Roussel, P., André, C., Masson, C., Géraud, G., and Hernandez-Verdun, D. (1993). Localization of the RNA polymerase I transcription factor hUBF during the cell cycle. *J Cell Sci*, 104 (Pt 2):327–337. 1.1.5

Russell, J. and Zomerdijk, J. C. B. M. (2005). RNA-polymerase-I-directed rDNA transcription, life and works. *Trends in Biochemical Sciences*, 30(2):87–96. 1.1.2

Sadaie, M., Salama, R., Carroll, T., Tomimatsu, K., Chandra, T., Young, A. R. J., Narita, M., Perez-Mancera, P. A., Bennett, D. C., Chong, H., Kimura, H., and Narita, M. (2013). Redistribution of the Lamin B1 genomic binding profile affects rearrangement of heterochromatic domains and SAHF formation during senescence. *Genes & Development*, 27(16):1800–1808. 1.2.2, 2.1.5, 2.1.5, 3.2, 3.3.4, 4.14, 6.3, 6.4, 6.5, 6.6, 6.7, 6.8, 6.9, 6.10, 6.11

Saitoh, Y. and Laemmli, U. K. (1994). Metaphase chromosome structure: bands arise from a differential folding path of the highly AT-rich scaffold. *Cell*, 76(4):609–622. 1.1.5

Sakai, K., Ohta, T., Minoshima, S., Kudoh, J., Wang, Y., de Jong, P. J., and Shimizu, N. (1995). Human ribosomal RNA gene cluster: identification of the proximal end containing a novel tandem repeat sequence. *Genomics*, 26(3):521–526. 1.1.5

Salama, R., Sadaie, M., Hoare, M., and Narita, M. (2014). Cellular senescence and its effector programs. *Genes & Development*, 28(2):99–114. 1.2.1, 1.2.1

Sanij, E., Diesch, J., Lesmana, A., Poortinga, G., Hein, N., Lidgerwood, G., Cameron, D. P., Ellul, J., Goodall, G. J., Wong, L. H., Dhillon, A. S., Hamdane, N., Rothblum, L. I., Pearson, R. B., Haviv, I., Moss, T., and Hannan, R. D. (2015). A novel role for the Pol I transcription factor UBTF in maintaining genome stability through the regulation of highly transcribed Pol II genes. *Genome research*, 25(2):201–212. 1.1.5

Sanij, E., Poortinga, G., Sharkey, K., Hung, S., Holloway, T. P., Quin, J., Robb, E., Wong, L. H., Thomas, W. G., Stefanovsky, V., Moss, T., Rothblum, L., Hannan, K. M., McArthur, G. A., Pearson, R. B., and Hannan, R. D. (2008). UBF levels determine the number of active ribosomal RNA genes in mammals. *J Cell Biol*, 183(7):1259–1274. 1.1.5

Saurin, A. J., Shiels, C., and Williamson, J. (1998). The human polycomb group complex associates with pericentromeric heterochromatin to form a novel nuclear domain. *The Journal of Cell Biology*. 1.1.1

Scherl, A., Couté, Y., Déon, C., Callé, A., Kindbeiter, K., Sanchez, J.-C., Greco, A., Hochstrasser, D., and Diaz, J.-J. (2002). Functional proteomic analysis of human nucleolus. *Mol Biol Cell*, 13(11):4100–4109. 1.1.2

Schmickel, R. D. (1973). Quantitation of human ribosomal DNA: hybridization of human DNA with ribosomal RNA for quantitation and fractionation. *Pediatric research*, 7(1):5–12. 1.1.5

Scholzen, T. and Gerdes, J. (2000). The Ki-67 protein: from the known and the unknown. *J Cell Physiol*, 182(3):311–322. 2.1.1.1

Schwarzacher, H. G. and Wachtler, F. (1983). Nucleolus organizer regions and nucleoli. *Human genetics*. 1.4

Serrano, M., Lin, A. W., McCurrach, M. E., Beach, D., and Lowe, S. W. (1997). Oncogenic ras provokes premature cell senescence associated with accumulation of p53 and p16INK4a. *Cell*, 88(5):593–602. **??**

Shah, P. P., Donahue, G., Otte, G. L., Capell, B. C., Nelson, D. M., Cao, K., Aggarwala, V., Cruickshanks, H. A., Rai, T. S., McBryan, T., Gregory, B. D., Adams, P. D., and Berger, S. L. (2013). Lamin B1 depletion in senescent cells triggers large-scale changes in gene expression and the chromatin landscape. *Genes & Development*, 27(16):1787–1799. 3.3.2, **??**

Shimi, T., Butin-Israeli, V., Adam, S. A., Hamanaka, R. B., Goldman, A. E., Lucas, C. A., Shumaker, D. K., Kosak, S. T., Chandel, N. S., and Goldman, R. D. (2011). The role of nuclear lamin B1 in cell proliferation and senescence. *Genes & Development*, 25(24):2579–2593. 1.2.2

Sirri, V., Hernandez-Verdun, D., and Roussel, P. (2002). Cyclin-dependent kinases govern formation and maintenance of the nucleolus. *J Cell Biol*, 156(6):969–981. 1.1.2

Sirri, V., Urcuqui-Inchima, S., Roussel, P., and Hernandez-Verdun, D. (2007). Nucleolus: the fascinating nuclear body. *Histochemistry and Cell Biology*, 129(1):13–31. 1.5

Sogo, J. M., Ness, P. J., Widmer, R. M., Parish, R. W., and Koller, T. (1984). Psoralen-crosslinking of DNA as a probe for the structure of active nucleolar chromatin. *Journal of Molecular Biology*, 178(4):897–919. 1.1.5

Spector, D. L. (2006). SnapShot: Cellular Bodies. *Cell*, 127(5):1071.e1–1071.e2. 1.1.1

Spiegelman, S. and Ritossa, F. M. (1965). Localization of DNA complementary to ribosomal RNA in the nucleolus organizer region of drosophila melanogaster. *Proceedings of the National Academy of Sciences of the United States of America*, 53:737–745. 1.1.2

Stahl, A., Hartung, M., Vagner-Capodano, A. M., and Fouet, C. (1976). Chromosomal constitution of nucleolus-associated chromatin in man. *Hum Genet*, 35(1):27–34. 1.1.3

Stefanovsky, V. Y., Pelletier, G., Bazett-Jones, D. P., Crane-Robinson, C., and Moss, T. (2001). DNA looping in the RNA polymerase I enhancesome is the result of non-cooperative in-phase bending by two UBF molecules. *Nucleic Acids Research*, 29(15):3241–3247. 1.1.5

Stults, D. M., Killen, M. W., Pierce, H. H., and Pierce, A. J. (2008). Genomic architecture and inheritance of human ribosomal RNA gene clusters. *Genome research*, 18(1):13–18. 1.1.5

Sullivan, G. J., Bridger, J. M., Cuthbert, A. P., Newbold, R. F., Bickmore, W. A., and McStay, B. (2001). Human acrocentric chromosomes with transcriptionally silent nucleolar organizer regions associate with nucleoli. *EMBO J*, 20(11):2867–2874. 2.1.2, 3.2, 5.1.3.1

Swanson, E. C., Manning, B., Zhang, H., and Lawrence, J. B. (2013). Higher-order unfolding of satellite heterochromatin is a consistent and early event in cell senescence. *J Cell Biol*, 203(6):929–942. 1.2.2, 2.1.1.1, 2.1.4.4, 3.3.2, 3.3.3, **??**, **??**

Swift, H. (1963). Cytochemical studies on nuclear fine structure. *Experimental Cell Research*. 1.1.2

Valentin, G. G. (1836). Repertorium für Anatomie und Physiologie. Kritische Darstellung fremder und Ergebnisse eigener Forschung, von G. Valentin. 1.1.2

van Koningsbruggen, S., Gierlinski, M., Schofield, P., Martin, D., Barton, G. J., Ariyurek, Y., den Dunnen, J. T., and Lamond, A. I. (2010). High-resolution whole-genome sequencing reveals that specific chromatin domains from most human chromosomes associate with nucleoli. *Mol Biol Cell*, 21(21):3735–3748. (document), 1.1.1, 1.1.2, 1.1.3, 2.1.1, 3.1, 3.2, 3.4, 6.1

van Steensel, B. and Dekker, J. (2010). Genomics tools for unraveling chromosome architecture. *Nat Biotechnol*, 28(10):1089–1095. 1.2

Vincent, W. S. (1952). The Isolation and Chemical Properties of the Nucleoli of Starfish Oocytes. *Proceedings of the National Academy of Sciences of the United States of America*, 38(2):139–145. 1.1.2, 2.1.2, 3.2

Vincent, W. S., Baltus, E., Lovlie, A., and Mundell, R. E. (1966). Proteins and nucleic acids of starfish oocyte nucleoli and ribosomes. *National Cancer Institute monograph*, 23:235–253. 1.1.2

Wang, Z., Zang, C., Rosenfeld, J. A., Schones, D. E., Barski, A., Cuddapah, S., Cui, K., Roh, T.-Y., Peng, W., Zhang, M. Q., and Zhao, K. (2008). Combinatorial patterns of histone acetylations and methylations in the human genome. *Nature Genetics*, 40(7):897–903. 2.1.4.2, 2.1.4.2

Waye, J. S. and Willard, H. F. (1989). Human beta satellite DNA: genomic organization and sequence definition of a class of highly repetitive tandem DNA. *Proceedings of the National Academy of Sciences of the United States of America*, 86(16):6250–6254. 1.1.4

Williamson, I., Berlivet, S., Eskeland, R., Boyle, S., Illingworth, R. S., Paquette, D., Dostie, J., and Bickmore, W. A. (2014). Spatial genome organization: contrasting views from chromosome conformation capture and fluorescence in situ hybridization. *Genes Dev*, 28(24):2778–2791. 3.3.4

Workman, C., Jensen, L. J., Jarmer, H., Berka, R., Gautier, L., Nielser, H. B., Saxild, H.-H., Nielsen, C., Brunak, S., and Knudsen, S. (2002). A new non-linear normalization method for reducing variability in DNA microarray experiments. *Genome Biology*, 3(9):research0048. 5.1.3.4

Zentner, G. E., Saiakhova, A., Manaenkov, P., Adams, M. D., and Scacheri, P. C. (2011). Integrative genomic analysis of human ribosomal DNA. *Nucleic Acids Research*, 39(12):4949–4960. 1.1.5

Zhang, L.-F., Huynh, K. D., and Lee, J. T. (2007). Perinucleolar Targeting of the Inactive X during S Phase: Evidence for a Role in the Maintenance of Silencing. *Cell*, 129(4):693–706. 3.3.2

Zhang, W., Li, J., Suzuki, K., Qu, J., Wang, P., Zhou, J., Liu, X., Ren, R., Xu, X., Ocampo, A., Yuan, T., Yang, J., Li, Y., Shi, L., Guan, D., Pan, H., Duan, S., Ding, Z., Li, M., Yi, F., Bai, R., Wang, Y., Chen, C., Yang, F., Li, X., Wang, Z., Aizawa, E., Goebl, A., Soligalla, R. D., Reddy, P., Esteban, C. R., Tang, F., Liu, G.-H., and Belmonte, J. C. I. (2015). Aging stem cells. A Werner syndrome stem cell model unveils heterochromatin alterations as a driver of human aging. *Science*, 348(6239):1160–1163. 2.1.4.3, 3.3.2, 5.4.3.2

Zillner, K., Komatsu, J., Filarsky, K., Kalepu, R., Bensimon, A., and Németh, A. (2015). Active human nucleolar organizer regions are interspersed with inactive rDNA repeats in normal and tumor cells. *Epigenomics*, 7(3):363–378. 1.1.5, 2.1.4.4